Université de Liège
Faculté des Sciences Appliquées

Symmetry and Pressure

A theoretical and experimental approach of the distortion under pressure

Dissertation présentée en vue
de l'obtention du grade de
Docteur en Sciences Appliquées

présentée par

Hugues Libotte

Année académique 2006-2007

A Clément, Cassandre et Sabine.
A Agnès et Francis.

Contents

Acknowledgments

« Il ne faut pas craindre d'avancer lentement, il faut seulement craindre de s'arrêter.»

Proverbe alsacien.

« Au-delà de la complexité réside la simplicité.»

A. Einstein

Like every thesis, this work would not be possible without the support and the confidence of many people. These words are certainly not sufficient to describe the kindness of people throughout my doctoral studies. The very first person I would like to thank is Prof. J.-P. Gaspard. Indeed he agreed to supervise my work in these special conditions. I would never have succeeded in this project without his invaluable advice and patience.

I also benefited from a very close and strong collaborative spirit in the ESRF teams of ID24 and ID27 beamlines. I wish to express my gratitude to Drs S. Pascarelli, G. Aquilanti, T. Le Bihan, M. Mezouar and W. Crichton and Mr S. Bauchau. I would also like to thank Prof. A San Miguel from the University of Lyon for his scientific and friendly support.

My interest in Physics was kindled at high school by the inspirational lectures of Mr M. Moureau. He is there somewhere at the source of this thesis.

Also, I would like to thank Prof. F. Grandjean, Ph. Lambin, Ph. Vanderbemden, B. Vanderheyden and Y. Lyon for agreeing to be part of the jury of my PhD thesis.

I would like also to acknowledge not only the attentiveness, support and patience of Sabine, Cassandre and Clément but also the time taken to read and correct this manuscript. Finally I am grateful to my parents for their enduring support and the values they passed on to me.

Résumé

La brisure de symétrie est un phénomène couramment rencontré dans le tableau périodique. L'objet de cette thèse est l'étude de cette distorsion et de son évolution sous pression. Un modèle théorique simple est développé sur base de la méthode des liaisons fortes afin de faire ressortir les moteurs physiques de telles distorsions. La particularité de notre modèle réside dans le traitement explicite du terme répulsif. Ce travail prouve en effet que celui-ci joue un rôle fondamental dans l'existence ou non de structures distordues. De telles brisures de symétrie peuvent être induites par de légères instabilités structurales ou encore par des instabilités électroniques - il s'agit alors de la bien connue distorsion de Peierls. L'origine de ces distorsions peut aussi se trouver dans des phénomènes expérimentaux parasites tels que la non-hydrostaticité dans une cellule haute pression. Notre modèle permet d'interpréter efficacement les données expérimentales collectées à l'ESRF par diffraction et absorption de rayon X sur $GaSb$, GaP, $InAs$, Am et Br_2 sous pression. Notre approche théorique est alors appliquée de façon plus générale dans le but de mettre en évidence les systématiques structurales gouvernant le comportement des semi-conducteurs III-V, des clathrates de type-II dopés et enfin des halogènes.

Abstract

Symmetry-breaking is often found in the periodic table. The aim of this thesis is to study the structural distortion and its evolution under pressure. A simple theoretical model is developed using the tight binding approach in order to highlight and understand the physical driving forces of such distortions. The distinctive feature of our model lies in the explicit treatment of the repulsive term. This work proves that this term is fundamental to the existence - or not - of the Peierls distortion. Such symmetry breaking can be induced by slight structural or electronic instabilities - the later is the well-known Peierls distortion. The origin of the distortion can also be linked to experimental parasitic effects such as uniaxial stress in a high pressure cell. Our model is able to efficiently explain the experimental data collected at the ESRF by X-ray diffraction and absorption of $GaSb$, GaP, $InAs$, Am and Br_2 under pressure. Our theoretical approach is then generalised in order to describe the structural systematics driving the behaviour of III-V semiconductors, alkali-doped type-II clathrates and finally halogens.

Chapter 1

Introduction

Pressure is the thermodynamical variable which exists with one of the wider range of orders of magnitude : from the deep space vacuum to the interior of neutron stars, pressure varies by almost 60 orders of magnitude. The laboratory setups allow to reach several hundreds of GPa (see figure 1.1), the density of condensed matter is then reduced by more than one order of magnitude.

Many fields of physics have interests in - the improvement of - the high-pressure techniques: geophysics and astrophysics for the study of the earth and big planets internal structure, chemistry and material sciences for novel material syntheses such as ultra-hard or superconducting materials, biosciences, ...

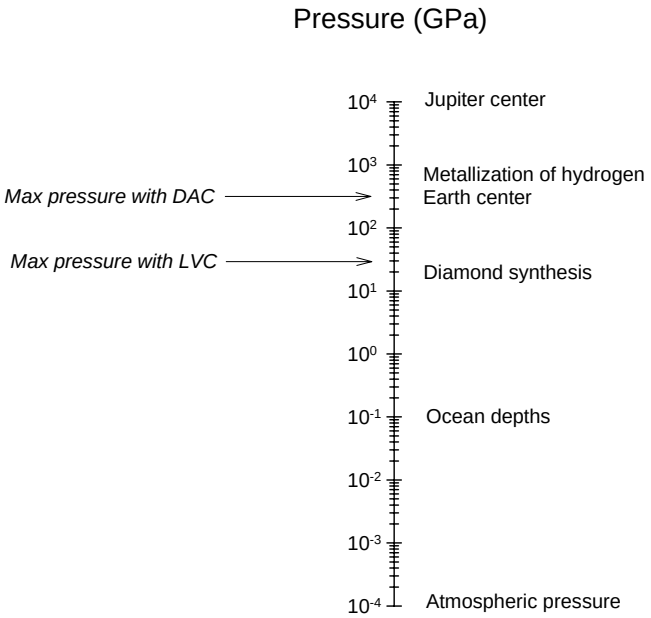

Figure 1.1: Some reference pressures of our environment and limits of the experimental setups used in this thesis. DAC and LVC stand for Diamond Anvil Cell and Paris-Edinburgh Large Volume Cell, respectively.

In condensed matter physics, high pressures play an important role. Indeed, the interatomic distances can be varied in a large domain inducing interesting behaviors such as large variations of the electronic properties (semiconductor or insulator to metal transition), structural phase

transitions (dissociation of molecular entities, deep symmetry modifications), chemical reactions which would not be possible at ambient pressure, ... No other parameter affects so drastically the properties of condensed matter: pressure is the key tool to modify the chemical bond and shed some light on its very nature.

The experimental study of matter under severe conditions of pressure began in the middle of the 17^{th} century by the study of the compressibility of liquids and gases. The most striking discovery was done by T. Andrews in 1869 [1] of the critical phenomena in gases. However, until the beginning of the 20^{th} century, the accessible pressure range was limited up to 300 MPa for technical reasons. In 1905, P. Bridgman [2] renewed pressure generation and routinely reached between 5 to 10 GPa with an original high-pressure cell design. Pressures as high as 40 to 50 GPa were reached using tungsten carbide cells in specific experiments. Many physical properties of matter under pressure were then studied by Bridgman : electrical resistivity, compressibility and melting of metals, viscosity of fluids, ... In 1946, the Nobel prize of physics was awarded to P. Bridgman "for the invention of an apparatus to produce extremely high pressures, and for the discoveries he made therewith in the field of high pressure physics"[1]. At that time, mainly indirect methods were used to detect and characterize structural changes in the material such as the optical properties [3], resistivity measurements [4], differential thermal analysis [5, 6].

Nowadays, the atomic structures and their behaviour under high pressure and/or high temperature can be studied using more straight forward methods such as X-ray diffraction [7], X-ray absorption spectroscopy (EXAFS[2]) [8], Raman scattering[9], ...

Systematic experimental studies have been performed and a complete picture of the behaviour of the elements and simple compounds emerges [10], completed by numerous theoretical approaches, mostly by *ab initio* methods [11].

The aim of this thesis is to measure and understand the symmetry-breaking mechanisms occurring throughout the periodic table under ambient conditions and their evolution under pressure. The origin of such distortions can be either driven by an electronic instability, the so-called Peierls distortion, or by a mechanical instability analogous to the Euler buckling in classical mechanics. Our approach is twofold : experimental and theoretical.

We performed a series of experiments based on two structural analysis techniques widely used in the high pressure field : X-ray diffraction and EXAFS. They probe the long range and the short range order of matter respectively. Such experiments under pressure are particularly efficient when combined with the outstanding quality of the beam of a third-generation synchrotron source like the ESRF (high brilliance, large spectral band, small source size and small divergence). We applied these techniques to four classes of covalent systems :

1. III-V semiconductors ($GaSb$, $InAs$ and GaP)
2. Halogens (Br_2) under pressure
3. Transuranians (Am) under pressure and
4. Clathrates endohedrally doped with Na. In opposition to the previous items, this system corresponds to the expanded metals or "negative pressures".

In all these cases, we mainly focus our attention on the symmetry changes induced by pressure.

After a short overview of the experimental tools used in this thesis given in chapter 2, some distortion processes occurring in group IV and III-V semiconductors are described in chapter 3. Nowadays their structural systematics is well established but several points still need to be

[1] http://nobelprize.org/nobel_prizes/physics/laureates/1946/

[2] Extended X-ray Absorption Fine Structure

addressed. We study compounds with increasing ionicity from Si to $InAs$ passing through $GaSb$ and GaP. In particular we stress on the effects of non-hydrostaticity (uniaxial stress) on the sequence of phases. The influence of ionicity on the relative phase stability is also discussed.

In chapter 4, the behaviour of bromine under pressure is described. Using a combined X-ray diffraction and absorption experiment, we study the metallization and the molecular dissociation process in halogens. The scaling rule describing the behaviour of the halogen family is studied in the light of our new experimental evidence.

As Am has a pivotal position in the actinide series, its high-pressure structures are studied in chapter 5 by X-ray diffraction. The (de)localization of the f-electrons is also discussed through the actinide series. A particular attention is given to the link between electronic localization and crystallographic structure.

After a short description of the clathrate structures, the distortion occurring in the alkali-doped clathrates is considered in chapter 6. In this case, the endohedral alkali atoms form a diamond sub-lattice which can be considered as an *expanded* structure. It has been shown experimentally that, in such conditions, the alkali atoms do not stay at the center of the clathrate cages. The distortion amplitude through the whole family of $X_8@Y-34$ compounds ($X = Li$, Na or K and $Y = C$, Si, Ge or Sn) is studied using both our semi-empirical model and *ab initio* calculations.

Chapter 7 is devoted to the theoretical models. In a simple and general framework, we discuss the central concept in this thesis, i.e. the quantum mechanical spontaneous symmetry breaking mechanism. This distortion process, also called Peierls distortion, leads to the octet rule followed by the elemental structures of the right hand side of the periodic table The distortion amplitude is reduced or disappears under pressure. We analyze this mechanism in detail using a semi-empirical tight binding mechanism.

Chapter 8 is the conclusion of this thesis. We also draw the possible tracks for future works.

The appendices summarize relevant structural data, basics of X-ray physics and some other theoretical aspects.

Chapter 2

Experimental methods

2.1 Introduction

The experimental study of matter under extreme conditions of temperature and pressure began in the middle of the 17^{th} century. However, until the beginning of the 20^{th} century, the accessible pressure range was very limited for technical reasons to less than 1 GPa. In 1905, P. Bridgman [2] built his own high-pressure cell design[1] and tackled many different aspects of matter under pressure: resistivity, compressibility, melting, ... In 1946, P. Bridgman received the Nobel prize for its outstanding results in high pressure physics.

Many different technologies are required to perform extreme-condition experiments : high-pressure and high-temperature generation and metrology, X-ray generation and detection, ... All along this work, we specifically use three methods :

- *X-ray Diffraction* (ADXRD [2])
- *X-ray Absorption*
  - *EXAFS* [3]
  - *XANES* [4].

These three methods are complementary in the structural study of matter under pressure as they are respectively a long (*ADXRD*) and short (*EXAFS* and *XANES*) range probe of the atomic arrangements. These methods applied to the very specific case of extreme-condition experiments are much better optimized with the high brilliance of the X-ray beam of dedicated beamlines on third-generation synchrotron facilities [5].

The whole experimental part of this thesis was performed at the ESRF[6]. X-ray diffraction and *EXAFS*/*XANES* facilities are accessible on the ID27 [7] and ID24 beamlines, respectively. The description of these two beamlines is given in the appendix A.6. The improvements in quality of the high pressure experiments and the continuous extension of the accessible pressure and temperature ranges are linked to the constant progress of the high-pressure cells, X-ray optics and detectors.

[1] Pressure as high as 40 to 50 GPa were reached using tungsten carbide cell in specific experiments.
[2] Angle-Dispersive X-Ray powder Diffraction
[3] Extended X-ray Absorption Fine Structure
[4] X-ray Absorption Near-Edge Structure
[5] In all the modern synchrotron facilities (ESRF, Spring8, Diamond, Soleil, ...), such beamlines now exist.
[6] European Synchrotron Radiation Facility
[7] Formerly ID30

2.1.1 High-pressure cells

The development of high-pressure cells was initiated by P. Bridgman during the first half of the 20^{th} century [12, 13]. The basic principle is the following: as the pressure is given by relation (2.1), it simply requires to drastically reduce the surface. The cells were originally based on two opposed tungsten carbide anvils that were pressed one against the other with a lever-arm. Nowadays, many different methods are used to apply the force between the anvils including gas or oil membranes. The reduction of the sample area, S, allows to get a very high value of the pressure, P, applied on the sample from a moderated force, F. More details can be found in references [14, 15]. Beside Other methods such as shock waves are also available to perform high pressure experiments. Beside those opposed anvil technology, other methods obviously exist to generate static (multi-anvil cells [16, 17]) or dynamic pressure (shock waves [18]) but they are out of the scope of this thesis.

$$P = \frac{F}{S} \tag{2.1}$$

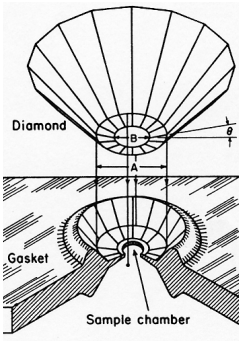

Figure 2.1: Illustration of the position of the sample in the DAC. It is contained in the gasket hole which has to be perfectly centered on the diamond axis. The culet of the diamond is the flat area compressing the gasket and the sample.

- *Diamond Anvil Cells*[8] This type of cell was developed in the late 50's by Weir, Lippincott, Van Valkenburg and Bunting [14, 19]. They are built around two cone-shaped diamonds. The first one is mounted on a moving piston in front of the other one fixed on the cylinder. They have to be perfectly aligned in order to avoid excess of strain which could induce their destruction. Diamond is preferred as they have high mechanical strength combined with a wide transparent optical domain (X-ray but also infra-red and visible light). The sample is obviously placed between the two diamonds inside a metallic gasket as illustrated in figure 2.1. Once the cell is closed, the piston is mechanically pressed. The pressure accessible from this kind of cell is of the order of 200 GPa. Obviously this value can be modulated by the force applied on the membrane but also by the size of the diamond culets (from 100 to 750 μm of diameter). In such an experimental set-up, the volume of the sample is very small (few hundred μm^3) which is one of the main drawback of the method. This drawback is also an advantage when the synthesis of the studied material is difficult as for monocrystals or when the sample is radioactive. Many different systems [20, 21, 22] based on this principle have been designed and few of them are illustrated in figure 2.2.

  In order to generate good hydrostatic conditions, a pressure transmitting medium is usually mandatory within the gasket. Otherwise uniaxial stress will be induced inside the sample

[8] DAC

as illustrated in section 3.8. This pressure transmitting medium is placed around the sample in the gasket hole. Different media can be used solid (NaCl, KCl, ...), liquid or gas. boron nitride, silicon oil, ethanol-methanol mixture, nitrogen, argon (solid à 1.3 GPa) or even helium [15].

Extreme conditions experiments combining high temperature and high pressure are also allowed within these cells. It is possible to heat the sample using either resistive or laser heating methods. In the first case, the system is heated up by a simple Joule effect applied either internally[9] or externally around the cell itself. When the laser (see figure 2.3) is used, the beam has to be concentrated on the sample at the same location as the X-ray beam which requires a precise optical design and alignment procedure. Using these methods, a temperature of more than 4000 K is achievable. At the opposite, the cells can be placed in a cryostat to study low temperature behaviour down to liquid helium temperature.

Figure 2.2: Different types of DAC among which Le Toullec, Diacell, Chervin and Akahama types.

- *Paris-Edinburgh press* is a large volume cell[10]. In this case, the high-pressure cell is made with two tungsten carbide or sintered diamond anvils as illustrated in figure 2.6. The sample is contained in a gasket placed between these two anvils. The structure of this gasket is quite complex (see figure 2.5). This gasket allows to get good hydrostatic conditions mainly due to the boron nitride cylinder. The carbon container allows to heat the sample by Joule effect directly.

  The pressure range accessible from this cell is obviously limited in comparison to the diamond anvil cell. Depending on the anvil used it may reach 25 GPa routinely. The volume sample is much higher (up to 100 mm^3) than in a diamond anvil cell : the quality of the collected spectra is thus improved even if the exit angle of the beam limits the observable part of the diffraction rings (see figure 2.4). The complex sample environment can be rejected using the Soller's slits [24, 25, 26] or numerical methods [27].

The accessible pressure and temperature range is not the only parameter driving the continuous developments of the experimental tools. The quality of the collected data is also guaranteed thanks the improvement of the experimental conditions (pressure or temperature gradient, non-hydrostaticity, gasket contribution in the spectra, ...) in order to obtain the right observation of the sample behaviour avoiding as much as possible any parasitic effect.

[9] On a specifically-designed gasket or even incorporated in the diamonds in the case of designer type anvils[23].
[10] LVC

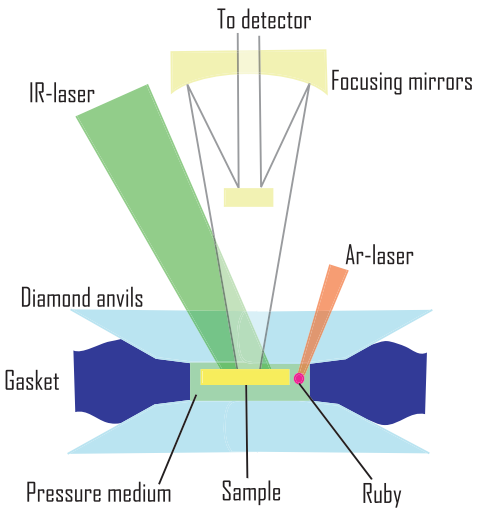

Figure 2.3: Schematic view of the laser heating setup in a diamond anvil cell. The sample is assumed to absorb most of the laser radiation. The laser beam is defocused - if needed - in order to heat up a reasonable sample area. The temperature is estimated by collecting the incandescent light coming from a point of the sample. The emission and absorption of incandescent light by the pressure-transmitting medium and the diamond is assumed to be negligible at least in a first approximation. The pressure is measured from the unheated ruby.

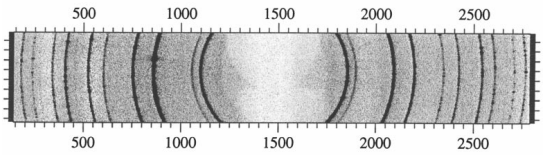

Figure 2.4: Diffraction pattern of the zinc-blende phase of InSb obtained with the LVC at the ESRF.

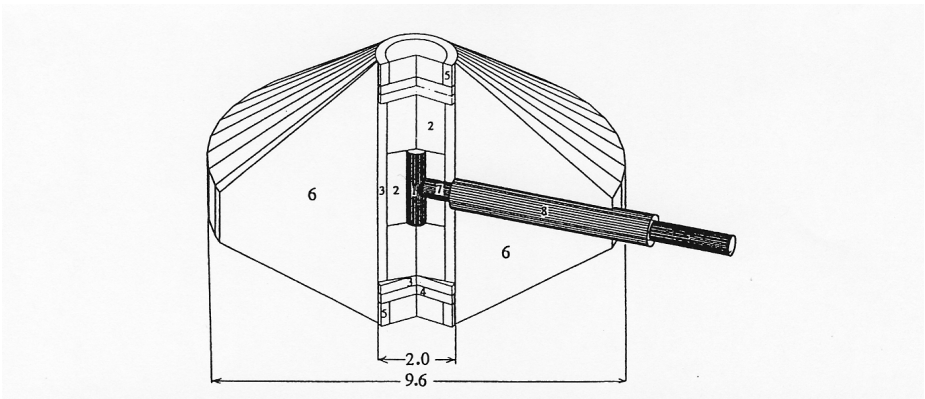

Figure 2.5: Cutaway view of the gasket assembly. (1) sample with a diameter of 0.5 mm, (2) boron nitride, (3) high-resistivity graphite furnace, (4) molybdenum foil, (5) stainless steel electrical feedthrough, (6) boron-epoxy insulating gasket, (7) thermocouple and (8) ceramic sheath. The dimensions are in mm.

2.1.2 Detectors

Depending on the application, different types of X-ray detectors are used[11]. For *ADXRD*, a two-dimensional detector is preferred in order to get a complete image of the diffraction rings

[11] Each of them have their technical limits : incident photon energy, spatial resolution, dynamic range, energy resolution capabilities, ...

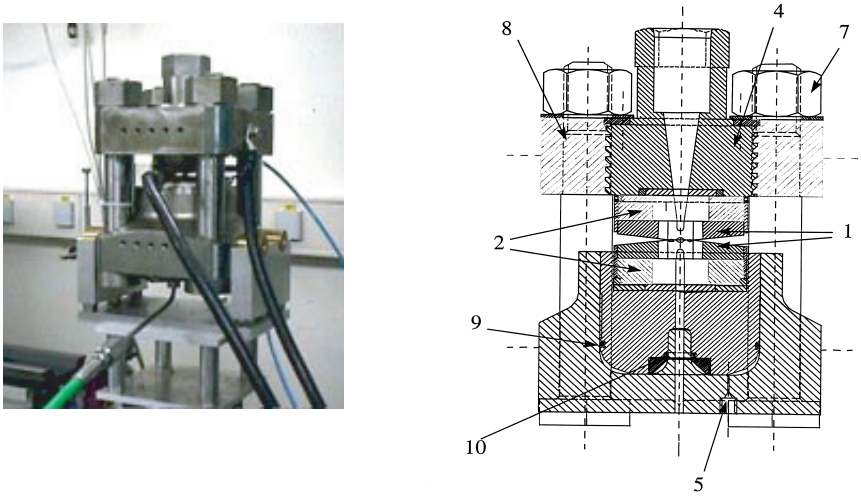

Figure 2.6: Picture and drawing of the Paris-Edinburgh press on the ID30/27 beamline at the ESRF. (1) anvil, (2) seat, (3) piston, (4) cylinder head, (5) pressure input, (6) column, (7) nut, (8) plate , (9) and (10) gaskets.

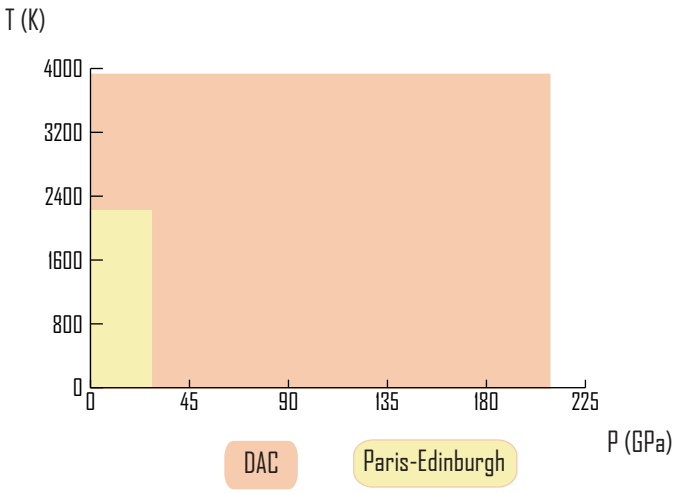

Figure 2.7: Schematic description of the P-T range accessible with the different techniques.

(image plate, CCD or CMOS optically coupled systems, ...). In the energy-dispersive mode, the diffraction setup requires a detector with an energy-resolution capability such as nitrogen-cooled *Ge* solid-state or *Si*-PIN sensors. Standard EXAFS experiments may also require such detectors for fluorescence detection[12]. EXAFS in the transmission geometry generally makes use of ionization chambers. However for high-pressure experiments and also time-resolved experiments, the dispersive EXAFS setup is often preferred. In this case a polychromator crystal produces an energy-direction correlation which is transformed into an energy-position correlation using a position-sensitive detector, such as CCD sensor. Data can then be collected simultaneously for the full energy range under study.

[12]Beamline LUCIA in the Swiss Light Source and BM29 at ESRF.

2.1.3 Metrology of high pressure and high temperature

Metrology of the experimental conditions is a key point in the high-pressure and high-temperature experiments. One of the possible methods for pressure measurement is to use an internal calibrant such as NaCl, KCl, CsCl, Au, Cu, Ta, ... [28] This is a reference material which is included inside the cell, sometimes mixed with the sample itself. The pressure behaviour of this calibrant is considered as a reference [29].

The calibrant has to be carefully selected in order to avoid overlapping of its diffraction peaks and the ones of the sample. The related chemical reactivity under pressure has also to be considered. The calibrant can also be located separately from the sample to avoid diffraction peaks overlap, but the possible gradient pressure may induce discrepancies between the measurement and the actual pressure on the sample. Moreover, in the case of EXAFS experiments, the simultaneous use of X-ray diffraction is required to follow the evolution of the calibrant lattice parameter.

The other famous method is the ruby fluorescence measurement. In this case, a small ruby crystallite is included in the cell. An optical window is obviously required in this case[13]. If the ruby crystal is illuminated by a blue (or green) laser beam, the electronic levels of the chromium ions are excited. When they fall down it induces a two-peak fluorescence shape (see figure 2.8). The position of these peaks as a function of pressure, P in $Mbar$, is tabulated and gives the experimental pressure [30, 31, 32] :

$$P = \frac{2.74\lambda_0}{7.665}\left[\left(\frac{\lambda_P}{\lambda_0}\right)^{7.665} - 1\right] \tag{2.2}$$

where λ_0 is the wavelength of the R_1 fluorescence peak of ruby measured at zero pressure and expressed in nm ($\lambda_0 = 694.29$ nm), and λ_P is the actual wavelength. The precision of the ruby method makes it unuseful for the lower pressures (≤ 1 GPa). Up to 10 GPa, Holzapfel *et al.* [33] shows that the accuracy of the method is about 1 %. The accuracy is reduced with increasing pressure down to around 5% at 100 GPa.

If both pressure and temperature are applied on the sample, a second measurement is required to determine the experimental (P, T) conditions. Due to the gasket complexity of the LVC, a direct measurement, using thermocouple, for example, is not trivial. Moreover similarly to pressure gradients, temperature gradients exist inside the cell.

When a thermocouple is used, it is placed against the diamond[14] or directly inside the sample container in the case of large volume cell. This is the simplest method but the estimation of the temperature difference between the thermocouple and the sample itself has first to be studied with reference cases. These differences are due to the thermal resistances of the materials around the sample.

It is also possible to measure the temperature directly within the DAC using the black-body emission of the sample. Measuring the radiated spectrum from the sample allows to estimate the temperature inside the sample. However, the influence of the actual emissivity of the sample needs to be calibrated. The temperature is estimated by fitting the theoretical Planck law with the experimental data.

An alternative non-invasive method consists of two reference materials mixed with the sample itself. By crossing the measured lattice parameters of both reference materials (Au and NaCl for example) with their equations of state, it is possible to calculate the temperature and pressure values [34].

[13] The standard Paris-Edinburgh press has not such an optical access.

[14] The thermal conductivity of diamond is roughly 4.5 times higher than the one of copper.

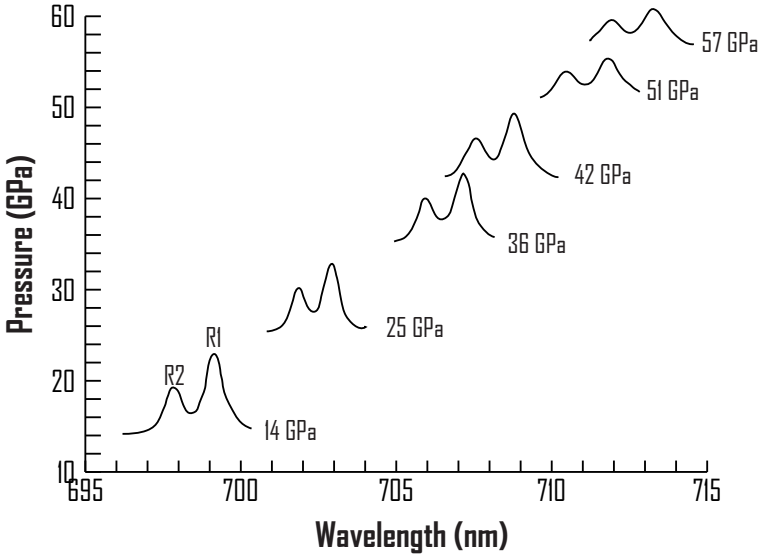

Figure 2.8: Schematic evolution of the fluorescence curve of ruby under pressure. The two-peak shape is shifted to lower wavelength with increasing pressure. Measurement of the R_1 and R_2 wavelengths allows to extract the value of pressure.

Even in well-designed pressure cells, gradients of pressure and temperature inevitably exist. This induces non-homogeneous behaviour of the sample (dispersion of the lattice parameter values, local phase transition, ...). Moreover pressure and temperature are not always measured exactly at the same location as X-ray beam goes through the sample. Therefore, discrepancies between the structural information coming from the sample and the (P-T) data may occur. This problem remains a major concern of extreme condition experiments.

It is also important to mention that parasitic effects like non-hydrostaticity, microstrains due to phase transitions, ... may induce unexpected behaviour of the sample and have to be clearly identified and avoided if possible. A trick to reduce microstrains is to temporarily and moderately rise the temperature of the sample: by reducing the internal stress it results in higher quality spectra during room temperature experiments. This point is experimentally and theoretically addressed in sections 3.4 and 3.8 respectively. The β-Sn phase of gallium antimonide is found to be unstable in favour of the orthorhombic *Imma* structure [35]. However this distortion is experimentally studied[36] and the distortion appears to be tightly linked to the amount of uniaxial stress applied on the sample. This distortion mechanism is theoretically illustrated in the case of silicon [37].

2.2 Experimental developments

During this thesis, I collaborated to experimental developments performed on the ID30 - now ID27 - beamline. A new set-up for collecting high-resolution ADXRD data was developed and tested : a Paris-Edinburgh large-volume cell is coupled with a fast imaging-plate system [27]. This is described in the next paper. This combination of technologies allows to reduce the acquisition time and thus to study light elements.

In the initial set-up, the sample surroundings gives a non-negligible contribution to the total signal. As the Rietveld refinement procedure can not be efficiently applied with this parasitic contribution, a numerical method of background subtraction was studied. In practice

two exposures are taken: one in through the sample and its environment and the other through the environment only. A least-square fit of the subtracted spectra is applied in order to remove the contribution of the surroundings from the final spectrum. Keeping some structure due to the gasket signal, the remaining signal has to be carefully process during the Rietveld refinement[38] in order to avoid any misunderstanding.

Improvements of the set-up are continuous: the set up of the Soller slits (illustrated in figure 2.9) is the ultimate improvement of the set-up in order to physically remove the signal coming from the surroundings of the sample [24, 26].

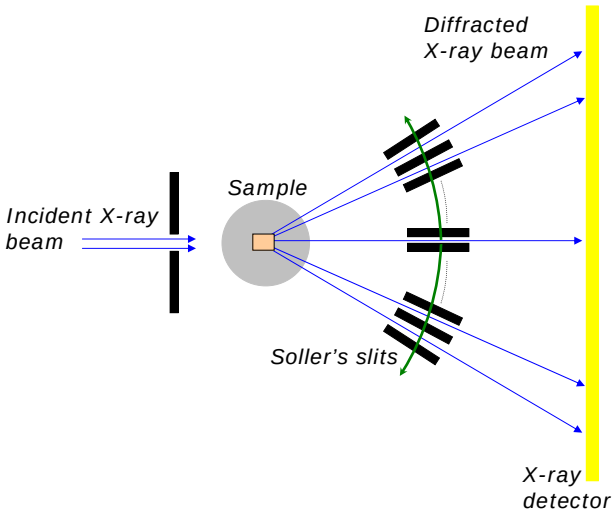

Figure 2.9: Schematic description of the diffraction setup with the Soller's slits. The principle of the method is to limit the *active* area (in orange) of the sample (in grey) by a strong collimation. The collimators are illustrated in black. Finally, in order to obtain the full angular spectrum, the Soller's slits are oscillating continuously.

2.3 Conclusion

This chapter is dedicated to the main technological aspects of the high-pressure experiments. Furthermore the experimental developments performed on the high-resolution angle-dispersive X-ray diffraction set-up are presented. The papers of Mezouar, Schultz and co-workers [27, ?] illustrates the efficiency of the ID27 set-up for high-pressure and high-temperature experiments. One of the first experiments performed with this equipment is described in detail in section 3.4. It underlines the two main capabilities of such an equipment : generating highly-hydrostatic conditions and collecting high-quality X-ray diffraction patterns.

The simultaneous use of two methods to study matter under pressure is one of the latest advances in the structural investigations of matter under pressure. In this thesis both *EXAFS* (for short range) and *ADXRD* (for long range) experiments were simultaneously performed to understand the slight distortion, chemical ordering and metallization of materials under pressure occurring in III-V semiconductors(see section 3.6) or halogens (see section 4.3).

Even if high-pressure experiments are difficult, the accessible pressure and temperature ranges are continuously extended. The same improvements are carried out on the collected data quality through the improvement of the X-ray beam properties, X-ray optics, the detector sensibility, ... However some historical goals are not yet reached such as metallization and molecular dissociation of hydrogen. New fields also appears such as the study of amorphization and incommensurate structures under pressure or chemical synthesis, ... Nowadays high pressure and high temperature experiments have not yet reached neither their technical nor scientific limits.

J. Synchrotron Rad. (1999). **6**, 1115–1119

Paris–Edinburgh large-volume cell coupled with a fast imaging-plate system for structural investigation at high pressure and high temperature

M. Mezouar,* T. Le Bihan, H. Libotte, Y. Le Godec and D. Häusermann

European Synchrotron Radiation Facility, BP 220, 38000 Grenoble, France.
E-mail: mezouar@esrf.fr

(*Received 7 December 1998; accepted 4 August 1999*)

A new set-up for collecting high-quality data suitable for structural refinement at high pressure and high temperature has been developed on beamline ID30 at the ESRF. The possibility of using high X-ray energies, high brilliance of third-generation sources and a new fast imaging-plate detector interfaced to the Paris–Edinburgh large-volume press has lead to a significant reduction of acquisition time and improvement of the quality of the data. The feasibility of angle-dispersive X-ray diffraction experiments at high pressure and high temperature, even on light elements, has been demonstrated.

Keywords: high pressure; high temperature; Paris–Edinburgh cell; image plates; Rietveld refinement; InSb; BN.

1. Introduction

X-ray powder diffraction experiments at high pressure and high temperature are of great interest in different domains of research such as material science or geophysics. However, the quality of the information on the crystal structure and its evolution under high pressure is limited by several experimental factors: pressure gradients, preferred orientations due to imperfect sample re-crystallization, X-ray sources and detecting systems. The Paris–Edinburgh large-volume cell (Besson *et al.*, 1992) has demonstrated its capability to generate hydrostatic pressure and low-temperature gradients (Mezouar, 1997; Besson *et al.*, 1996) and is commonly used on several synchrotron sources, in energy-dispersive X-ray diffraction mode (EDX), for precise determination of PT phase diagrams (Grima *et al.*, 1995; Mezouar *et al.*, 1996). However, for full structural refinement (Rietveld refinement; Rietveld, 1969), which needs accurate determination of the diffraction intensities, the use of EDX is restricted. Indeed, the diffracted signal needs, in that case, to be corrected for the energy dependence of the brilliance of the X-ray source, response of the detector and absorption of the sample. Moreover, the single-point detector used in EDX mode intercepts only a small part of the diffracted signal and cannot take into account preferred orientations in the sample which are often present at high pressure.

Angle-dispersive X-ray diffraction (ADX) with monochromatic beam and image-plate system, which provides a large surface of detection, high resolution and wide dynamic range, represents an important alternative. This detecting system has already been successfully interfaced to diamond anvil cells (Shimomura *et al.*, 1992; Nelmes *et al.*, 1992) and to large-volume cells (Chen *et al.*, 1997, 1998). However, an important limitation, mentioned by Chen *et al.* (1997, 1998), is the large acquisition time needed for generating an exploitable image. This limitation has recently been overcome by the use of a new on-line fast imaging-plate detector (Thoms *et al.*, 1998) and the high brilliance of third-generation sources. This paper is dedicated to a detailed description of this new set-up for structural investigation at high pressure and high temperature installed on the high-pressure beamline ID30 at the ESRF. Two examples have been selected to illustrate the potential of this new device: the high-pressure and high-temperature behaviour of indium antimonide (high-Z compound) and boron nitride (low-Z compound).

2. Experimental method

2.1. *The large-volume Paris–Edinburgh press in ADX mode*

A schematic view of the high-pressure beamline ID30 at the European Synchrotron Radiation Facility (ESRF) in large-volume configuration is presented in Fig. 1. The Paris–Edinburgh press is mounted on an x-y-z translation stage which allows very precise positioning relative to the incident beam (within 1 μm). Monochromatic X-ray beams with wavelengths down to $\lambda = 0.15$ Å ($E = 100$ keV) are selected using a Si(111) channel-cut monochromator and collimated down to $50 \times 50\ \mu m^2$ by two sets of tungsten carbide slits. The precise alignment of the sample relative to the beam is performed in monochromatic mode by monitoring the X-ray absorption signal, using a silicon photodiode located between the Paris–Edinburgh press and the

detector. This photodiode is mounted on a translation stage and can be positioned in the X-ray beam at any time during the experiment. In particular, this device allows a rapid checking (<2 min) of the alignment after each compression or heating of the sample. Angle-dispersive data are collected using image plates mounted on the new *fastscan* detector (Thoms *et al.*, 1998). This new detector allows the collection of high-quality data in less than 1 min, which is at least one order of magnitude faster than other imaging-plate systems. The sample-to-detector distance is precisely determined using the diffraction pattern from a silicon powder located at the sample position. The diffraction images are corrected for spatial distortions and the portion of the Debye–Scherrer rings are integrated using the soft-

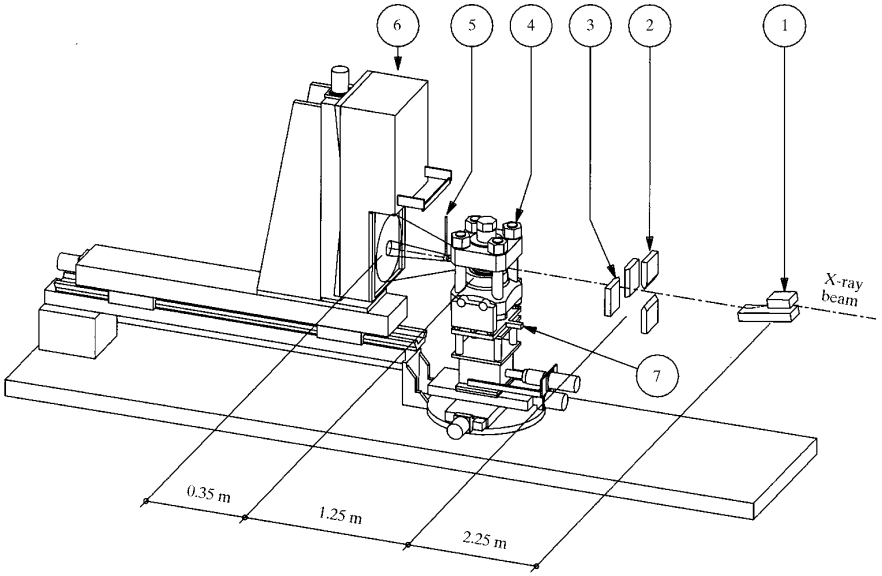

Figure 1
Layout of the high-pressure beamline ID30 at the European Synchrotron Radiation Facility (ESRF) in large-volume press configuration. 1: Si(111) channel-cut monochromator; 2–3: tungsten carbide slits, horizontal and vertical limits; 4: Paris–Edinburgh large-volume press; 5: beam stop; 6: fast-scan detector.

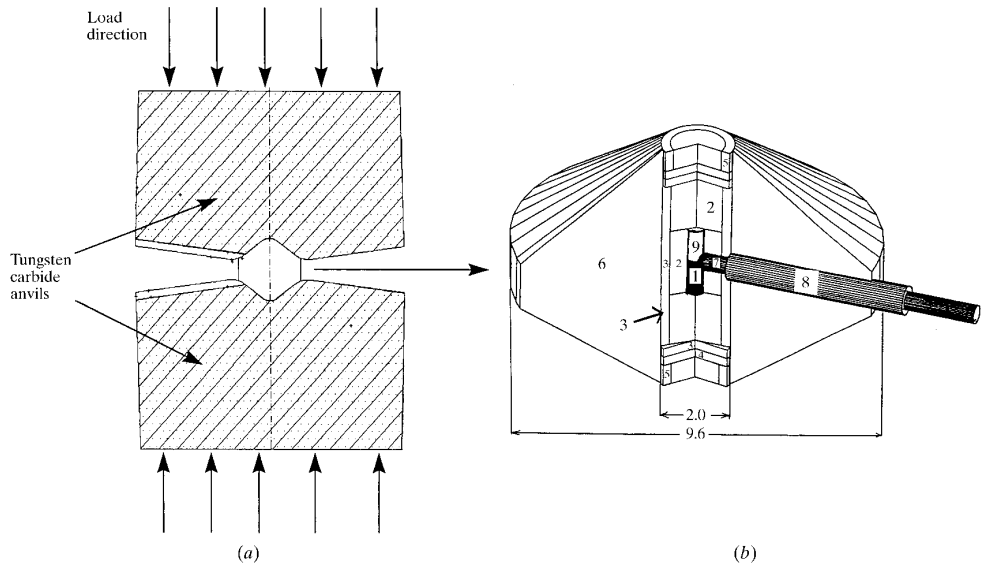

Figure 2
(*a*) High-pressure chamber. (*b*) Sample assembly. Cutaway view of the sample assembly between conoidal anvils (dimensions are in mm). 1: Sample; 2: boron nitride capsule; 3: high-resistivity graphite furnace, 4: molybdenum foil; 5: stainless-steel electrical feedthrough; 6: boron-epoxy (5:1) insulator gasket; 7: swaged chromel-alumel thermocouple; 8: ceramic sheath; 9: pressure calibrant

ware package *Fit2D* (Hammersley, 1997). Structural analyses are performed by full Rietveld refinement using the program *GSAS* (Larson & Dreele, 1994).

2.2. *Sample environment*

The sample assembly presented in Fig. 2 is contained between two supported tungsten carbide anvils with a quasi-conical profile which insures quasi-hydrostatic conditions (Makarenko, 1995) and a wide opening angle of 15°. The powder sample of height 2 mm and diameter 0.5 mm is encapsulated in a hexagonal boron nitride (h-BN) cylinder which is used as a pressure-transmitting medium. Temperatures up to 1900 K are generated by a graphite heater which is placed between the anvils and controlled by a thermocouple located at the centre of the sample assembly. In the present work a *K*-type (chromel-alumel) thermocouple was used to measure a maximum temperature of T = 1000 K. The position of the thermocouple inside the sample assembly was precisely determined using the X-ray transmission signal monitored by the silicon based photodiode. A minimum distance of 300 µm was fixed between the thermocouple tips and the X-ray beam to prevent diffraction from it. Boron-epoxy (5:1 in mass) was used as the compressing medium between the anvils. The pressure was measured *in situ* from the variation of the cell dimensions of NaCl powder as an internal calibrant, and calculated from the equation of state of Decker (1971). The location of the pressure calibrant in the sample assembly depends on the type of experiment. In the present work, in order to avoid additional peaks in the diffraction patterns, the NaCl pressure standard was positioned above the sample with an h-BN spacer in between. For each pressure–temperature (*PT*) point investigated, a diffraction image of the pressure calibrant was collected by slightly moving down the Paris–Edinburgh press. An efficient water-cooling system mounted on the tungsten carbide anvils was used to reduce the variation of the pressure on heating to less than 2% at the maximum temperature.

3. Method

3.1. *High-Z compounds*

To illustrate the potential of this new set-up we have investigated the high-pressure high-temperature behaviour of indium antimonide. Among the III–V semiconductors, indium antimonide has been one of the most extensively studied experimentally (Jayaraman *et al.*, 1961; Minomura *et al.*, 1966; McWhan & Marezio, 1966; Vanderborgh *et al.*, 1989; Nelmes *et al.*, 1993; Nelmes & McMahon, 1996) and theoretically (Zhang & Cohen, 1987; Guo *et al.*, 1993) under variable pressure and temperature. However, significant uncertainties remain in its high-pressure phase diagram. According to Mezouar *et al.* (1996), in the *PT* region defined in Fig. 3, InSb exhibits three solid modifications. At ambient conditions, InSb has the zinc blende-type structure and transforms under pressure to a metallic phase. The corresponding structure has been determined as orthorhombic with space group *Cmcm* (Nelmes *et al.*, 1993). The pressure–temperature domain of stability of this solid phase is noted IV in Fig. 3. At high temperature, another solid–solid phase transition (domain III in Fig. 3) has been firstly detected by resistivity measurements (Banus & Lavine, 1969) and numerous X-ray diffraction experiments have been performed. However, the data available on the crystal structure of this solid phase are still conflicting. Indeed, Banus & Lavine (1969) have determined the structure as tetragonal with space group $I4_1/amd$, whereas this phase has been identified as orthorhombic with space

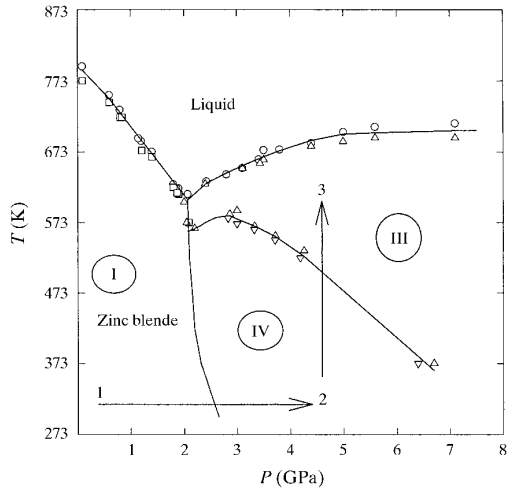

Figure 3
Phase diagram of InSb according to Mezouar *et al.* (1996). The thermodynamic path followed in this work: 1, ambient conditions; 2, P = 4.7 GPa, T = 373 K; 3, P = 4.7 GPa, T = 623 K.

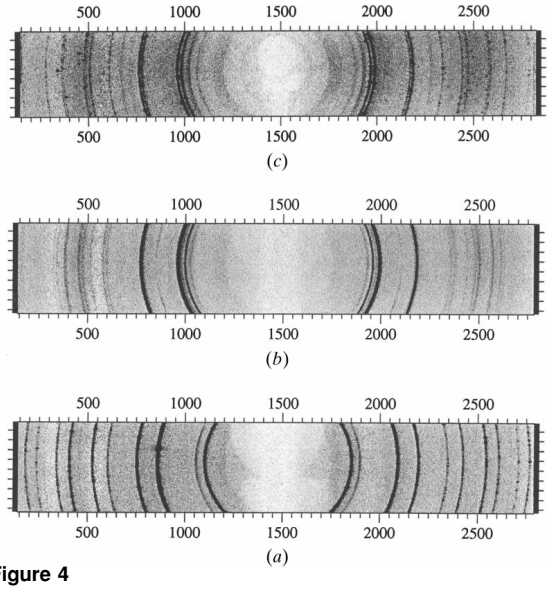

Figure 4
ADX diffraction patterns of the high-pressure high-temperature phase of InSb. (*a*) Position 1 in Fig. 3. (*b*) Position 2 in Fig. 3. (*c*) Position 3 in Fig. 3.

group *Pmmm* or *Pmmn* by Yu *et al.* (1978), and orthorhombic with space group *Immm* by Mezouar *et al.* (1996) and Nelmes & McMahon (1996).

In the present study we have re-examined the structure of solid III (*i.e.* corresponding to domain III in Fig. 3) *in situ* using our angle-dispersive powder diffraction set-up. The optimum wavelength in terms of contrast between the sample and its environment, and photon flux, was found at $\lambda = 0.1494$ Å. Indeed, for the high-Z compounds like InSb, the large difference in scattering power between the sample and its surroundings (boron gasket, graphite heater, h-BN capsule) increases strongly with the X-ray energy. At 83 keV the extra peaks from the sample environment indicated by asterisks in Fig. 5 are very weak and can be neglected. To reach the *PT* domain of the phase III, the pressure was slowly increased at room temperature in steps of 0.1 GPa from the solid I to the pure solid IV. At this point the temperature was raised carefully in steps of 10 K up to the pure solid III (*i.e.* free from solid IV). At each *PT* point the evolution of the diffraction pattern was checked in order to follow structural changes in real time. The sequence of transitions is shown in Figs. 4(*a*), 4(*b*) and 4(*c*). The transition from solid IV to solid III is accompanied by significant changes: the number of diffraction peaks decreases strongly which indicates a transition to a structure with higher symmetry. The diffraction pattern in Fig. 4(*c*) presents more spotty Debye–Scherrer rings due to recrystallization effects near the melting curve.

The data were of sufficient quality to allow us to clearly identify the crystal structure of the solid III as tetragonal with space group $I\bar{4}m2$ (β-tin-type structure) and to perform a full structural refinement. Several other space groups have been tested. In particular, all the previously proposed symmetries (I_{41}/amd, *Pmmm*, *Pmmn*, *Immm*) have been tried, and exhibit important deviations from the observed profile. The variables in the refinement were the lattice parameters a and c, a scale factor, three peak-shape parameters, an isotropic thermal motion parameter and a preferred orientation parameter. The result is presented in Fig. 5 and shows that the agreement between observed and calculated profiles is excellent. Indeed, the R_{wp} factor ($R_{wp} = \{\Sigma w_i[y_i(\text{obs}) - y_i(\text{calc})]^2/\Sigma w_i[y_i(\text{obs})]^2\}^{1/2}$) and the $R_F{}^2$ factor [$R_F{}^2 = \Sigma|F_{hkl}(\text{obs})^2 - F_{hkl}(\text{calc})^2|/F_{hkl}(\text{obs})^2$] which represent the deviation from the observed intensities and structure factors, respectively, became 0.05 and 0.04. The refined cell parameters are $a = b = 5.7462 \pm 0.0003$ Å and $c = 3.1434 \pm 0.0003$ Å at $P = 4.7$ GPa and $T = 603$ K

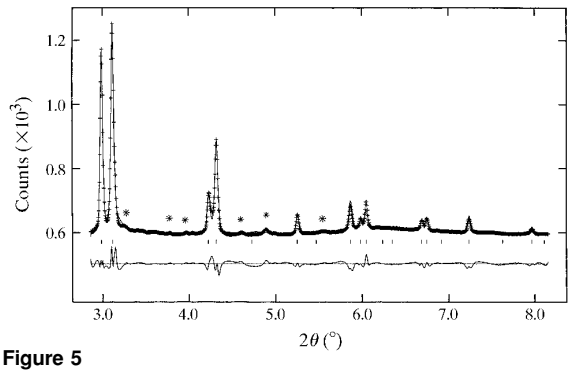

Figure 5
Rietveld refinement of a disordered β-tin structure (space group $I\bar{4}m2$) to the integrated profile of InSb obtained at $P = 4.7$ GPa and $T = 603$ K. The tick marks under the profile indicate the reflections allowed for this space group. Asterisks: contamination peaks from the sample environment.

3.2. *Low-Z compounds*

As described in §2.2, the sample environment is mainly composed of boron and carbon which have a low X-ray scattering power. However, for low-Z samples the extraction of the diffracted signal still remains difficult because, in that case, scattered signals coming from the surrounding material and from the sample are of the same order of magnitude. The subtraction method used to solve this problem is illustrated in Fig. 6. The selected example concerns the rhombohedral phase of boron nitride (space group $R3m$) which is a metastable solid modification of this compound. The sample consists of a powder of CVD-produced bulk pyrolytic r-BN, having a density of 2.26 g cm^{-3} and containing less than 5% volume of h-BN impurities. In order to avoid chemical reaction between the h-BN capsule and r-BN, the sample was pre-compacted and loaded directly into the graphite heater. The wavelength was fixed at $\lambda = 0.2232$ Å, and the pressure and temperature conditions of the experiment were $P = 5$ GPa and $T = 573$ K. Fig. 6 shows diffraction patterns from the sample and its surroundings, and of the surroundings only, taken by slightly translating the press in the direction perpendicular to the X-ray beam. The signal from the sample is extracted by subtracting these two diffraction patterns, after scaling. The corresponding two-dimensional images have been obtained in only 30 s. This exposure time was selected to fully use the dynamic range (14 bits) of the image plate. The

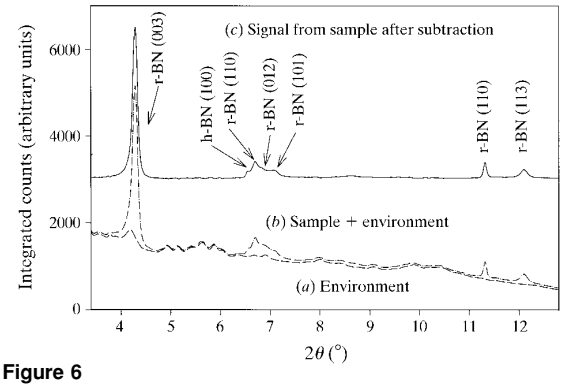

Figure 6
Integrated spectra of rhombohedral boron nitride (r-BN). (*a*) r-BN and the pressure medium at 5 GPa and 2473 K; (*b*) only the pressure medium close to the sample; (*c*) final spectrum of the sample after subtraction of the sample environment. The corresponding images were collected in 30 s using 55.5 keV radiation. Miller indices (*hkl*) of the r-BN sample and h-BN impurities are indicated.

quality of subtraction has been improved by the use of high-energy photons (E = 55.5 keV) which considerably limit the self-absorption by the sample. The refined cell parameters of r-BN at P = 5 GPa and T = 473 K are a = 2.493 ± 0.001 Å and c = 9.135 ± 0.001 Å. They have been determined by fitting the diffraction peaks positions to a pseudo-Voigt function using the program *Fit2D*.

4. Conclusions

A fast imaging plate is interfaced to a Paris–Edinburgh press for the rapid collection of *in situ* X-ray powder diffraction data suitable for structural refinement at high pressure and high temperature. Indeed, this is the first large-volume press mounted on a third-generation synchrotron source. Moreover, this set-up is interfaced to a fast on-line detector, which is at least ten times faster than other imaging-plate systems. This new set-up allows structural phase transformations to be followed very precisely over a wide range of pressure and temperature, and several experiments have already been successfully performed. The structure of InSb III has been unambiguously determined and the feasibility of ADX experiments, even on light elements, has been demonstrated.

We are grateful to Stany Bauchau for his technical help. One of the authors (HL) would like to thank J. P. Gaspard from the University of Liege for all support provided during his stay at the ESRF.

References

Banus, M. D. & Lavine, M. C. (1969). *J. Appl. Phys.* **40**, 409–413.
Besson, J. M., Grima, P., Gauthier, M., Itié, J. P., Mezouar, M., Häusermann, D. & Hanfland, M. (1996). *Phys. Status Solidi B*, **198**, 419–425.
Besson, J. M., Nelmes, R. J., Hamel, G., Loveday, J. S., Weill, G. & Hull, S. (1992). *Physica B*, **180/181**, 907–913.
Chen, J., Kikegawa, T., Shimomura, O. & Iwasaki, H. (1997). *J. Synchrotron Rad.* **4**, 21–27.
Chen, J., Parise, J. B., Li, R., Weidner, D. J. & Vaughan, M. (1998). *Properties of Earth and Planetary Materials at High Pressure and Temperature, Geophysical Monograph 101*, edited by M. H. Manghani & T. Yagi, pp. 139–144. Washington DC: AGU.
Decker, D. L. (1971). *J. Appl. Phys.* **42**, 3239–3243.
Grima, P., Polian, A., Gauthier, M., Itié, J. P., Mezouar, M., Weill, G. & Besson, J. M. (1995). *J. Chem. Solids*, **56**, 525–530.
Guo, G. Y., Crain, J., Blaha, P. & Temmerman, W. M. (1993). *Phys. Rev. B*, **47**(9), 4841.
Hammersley, A. (1997). *Fit2D*. ESRF, Grenoble, France.
Jayaraman, A., Newton, R. C. & Kennedy, G. C. (1961). *Nature (London)*, **191**, 1290–1291.
Larson, A. & Von Dreele, B. (1994). *GSAS*. Los Alamos Laboratory, Los Alamos, NM 87545, USA.
Makarenko, I. (1995). Private communication.
McWhan, D. B. & Marezio, M. (1966). *J. Chem. Phys.* **45**(7), 2508–2511.
Mezouar, M. (1997). PhD thesis, Université Denis Diderot Paris VII, France.
Mezouar, M., Besson, J. M., Syfosse, G., Itié, J. P., Häusermann, D. & Hanfland, M. (1996). *Phys. Status Solidi B*, **198**, 403–410.
Minomura, S., Okai, B., Nagasaki, H. & Tanuma, I. (1966). *Phys. Lett.* **21**(3), 272–273.
Nelmes, R. J., Hatton, P. D., McMahon, M. I., Piltz, R. O., Crain, J., Cernik, R. J. & Bushnell-Wye, G. (1992). *Rev. Sci. Instrum.* **63**, 1039–1043.
Nelmes, R. J. & McMahon, M. I. (1996). *Phys. Rev. Lett.* **77**, 663–666.
Nelmes, R. J., McMahon, M. I., Hatton, P. D., Crain, J. & Piltz, R. O. (1993). *Phys. Rev. B*, **47**, 35–54.
Rietveld, H. M. (1969). *J. Appl. Cryst.* **2**, 65–71.
Shimomura, O., Takemura, K., Fujihisa, H., Fujii, Y., Ohishi, Y., Kikegawa, T., Amemiya, Y. & Matsushita, T. (1992). *Rev. Sci. Instrum.* **63**, 967–971.
Thoms, M., Bauchau, S., Kunz, M., Le Bihan, T., Mezouar, M., Häusermann, D. & Strawbridge, D. (1998). *Nucl. Instrum. Methods*, A**413**, 175–180.
Vanderborgh, C. A., Vohra, Y. K. & Ruoff, A. L. (1989). *Phys. Rev. B*, **40**(18), 12450–12456.
Yu, S. C., Spain, I. L. & Skelton, E. F. (1978). *J. Appl. Phys.* **49**(9), 4741–4745.
Zhang, S. B. & Cohen, M. L. (1987). *Phys. Rev. B*, **35**(14), 7604–7610.

Chapter 3

III-V semiconductors under pressure

3.1 Introduction

Semiconductors of groups IVa and IIIa-Va are of major interest in the electronic industry since the second half of the 20^{th} century. They are based on a tetrahedral environment (diamond, zincblende or würtzite) which undergoes a structural phase transition under pressure. The main parameters of group IVa and IIIa-Va semiconductors to be studied in the 60's are the electrical conductivity[39] and the optical reflectivity [40]. However, in 1963, Jamieson started *in situ* structural studies using diffraction technique [7]. Since those early experiments and for a long time, semiconductors of groups IVa and IIIa-Va were thought to exhibit a simple transition scheme under pressure. Such a transition is assumed to induce an increase of the coordination number keeping highly-symmetric structures: a first transition to a sixfold coordinated structure (β-Sn or $NaCl$) and finally to an eightfold coordinated structure ($CsCl$) as illustrated in figure 3.1.

The initial and - too - simple view of their phase diagrams was completely reappraised in the 90's [10, 41, 42] as described in the next section. This was possible thanks to the improvements of high-pressure techniques and synchrotron sources. The interest for behaviour of IIIa-Va semiconductor under pressure is still very sustained as their phase diagrams are still under question. Today the key point concerns the distortion processes resulting in low-symmetry structures[1]. Chemical ordering is also one of the structural parameters under question. ADXRD and EXAFS experiments allow the quantitative observation of chemical order and slight symmetry breaking leading to distorted structures. *Ab initio* methods also come to complete the panel of techniques used to analyze the high pressure behaviour of semiconductors. They usually compare total energy of selected structures but recently the theoretical study of the phonon instabilities also suggests candidate structures.

This thesis is focused on three semiconductors : $GaSb$, GaP and $InAs$. The choice of these three semiconductors has been dictated by their relative position on the ionicity scale. Since a long time, it is well known that the structural trends of the IIIa-Va semiconductors under pressure are efficiently classified as a function of their ionicity. However, structural details are still under question. We will underline several discrepancies between the latest systematics and our experimental evidence. The effects of the uniaxial stress on the symmetry breaking are brought to the fore in the case of $GaSb$ but also of silicon.

The structural information concerning the crystallographic structures met in this thesis are summarized in appendix C.

[1] Those distorted structures are originated from the $NaCl$, β-Sn and $CsCl$ structures.

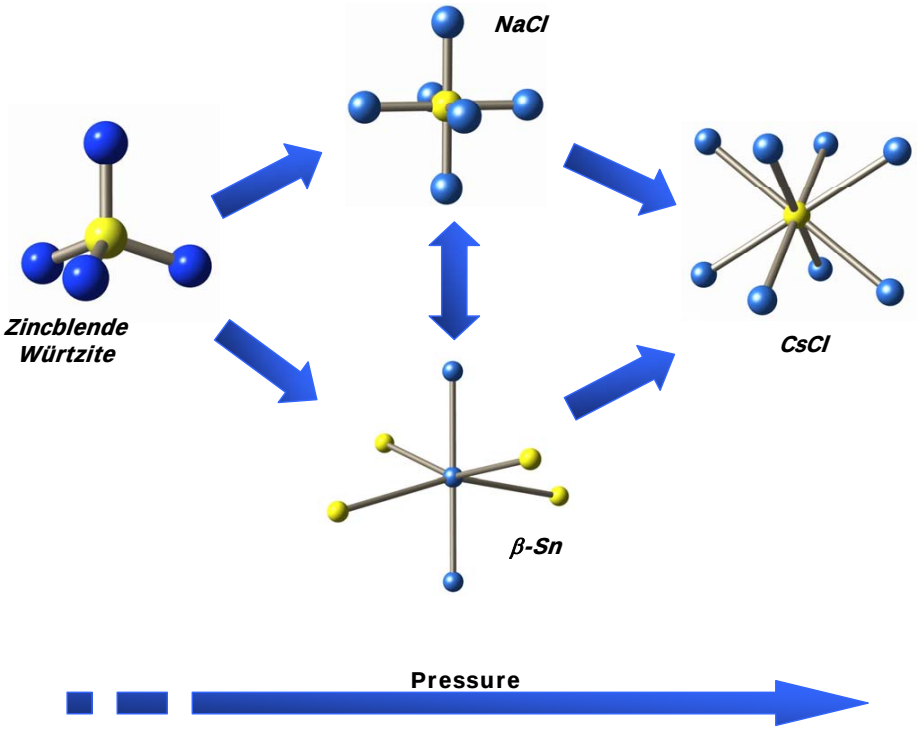

Figure 3.1: Simplified structural trend of the III-V semiconductors. When compressed, the initial tetrahedral environment collapses, giving rise to a sixfold coordinated structure. When the applied pressure is further increased, the structure becomes even more compact with a higher number of neighbours like in $CsCl$.

Compound	f_i	Tetrahedral		$Cinn.$	$NaCl$ type		$\beta - Sn$ type		$CsCl$ type	
		ZB	W		$NaCl$	$Cmcm$	$\beta - Sn$	$Imma$	$CsCl$	$dis - CsCl$
Si	0	+	-	-	-	-	+	+		
Ge	0	+	-	-	-	-	+	+		
Sn	0	+	-	-	-	-	+	-		
GaSb	0.169	+	-	-	-	-	-	+	+	-
AlSb	0.230	+	-	-	-	+	-	-		
InSb	0.294	+	-	-	-	+	-	-	+	-
GaAs	0.316	+	-	+	-	+	-	-	-	+
GaP	0.371	+	-	-	-	+	-	-	-	+
AlAs	0.375	+	-	-	-	-	-	-		
AlP	0.425	+	-	-	-	-	-	-		
InAs	0.450	+	-	-	+	+	-	-	-	+
InP	0.506	+	-	-	+	+	-	-	-	+
GaN	0.780	-	+	-	+	-	-	-		
AlN	0.794	-	+	-	+	-	-	-		
InN	0.853	-	+	-	+	-	-	-		

Table 3.1: Structures observed at various pressure following Ozolins *et al.* [42]. ZB, W, Cinn. and dis-$CsCl$ respectively stand for zincblende, würtzite, cinnabar and distorted $CsCl$. f_i is the Phillips ionicity.

3.2 Ionicity

The ionicity of a compound, f_i, is one of the fundamental parameter in the III-V systematics. In the early work of Phillips [43], this influence was clearly point out even if only three structures were considered : zinc-blende, β-Sn and $NaCl$. Even if this simplified phase diagram (see figure 3.3) is now completely revisited by the works of Ozolins *et al.* [41] and Kim *et al.* [42], the ionicity value allows to classify semiconductors exhibiting a common behaviour as shown in table 3.1.

- The würtzite structure happens only for the more ionic compounds (the nitride semiconductors).
- The $NaCl$ structure also appears only for the more ionic compounds.
- The $\beta - Sn$ structure only appears for the less ionic III-V semiconductors.

The concept of ionicity itself is also the subject of endless discussions. If a compound AB is considered, the charge transfer from atom A to B depends on the relative electronegativity of the atoms, X_A and X_B. Different definitions of the ionicity value, f_i, exist. Even if the values themselves differ from a definition to the other, the principle and the resulting classification remain almost identical.

- Pauling gave a first expression of the ionicity [44]:

$$f_i = 1 - e^{-\frac{(X_A - X_B)^2}{4}} \tag{3.1}$$

- Phillips [43] developed another approach based on a ionic and covalent gap, respectively E_i and E_c. They are linked to the actual gap, E_g, by $E_g^2 = E_i^2 + E_c^2$. Based on these virtual gaps, we get another definition of the ionicity :

$$f_i = \frac{E_i^2}{E_g^2} \tag{3.2}$$

  Based on the Phillips definition, Van Vechten [45] made an extensive study of the possible correlation between ionicity and volume reduction at phase transition, $\Delta V_{I,II}$. Even if the structure identification was not totally correct, he clearly points out that

$$-\frac{\Delta V_{I,II}}{V_I(P)} = 0.209 - 0.056 f_i \tag{3.3}$$

  where $V_I(P)$ is the volume of the initial phase at the transition pressure, P. It was also clearly determinesd that this kind of relationship does not exist if the ambient volume, $V_I(0)$, is considered.

  Chelikowsky and Burdett studied the consistency of the ionicity scale of Phillips and Van Vechten [46] with an *ab initio* approach [47]. They found a very nice agreement between the two points of view. In their paper, they also define an new ionicity scale based on the charge transfer, ΔQ.

$$f_i(\Delta Q) = \frac{4 - N_c}{4} + \alpha \Delta Q \tag{3.4}$$

  where N_c is the number of valence electrons. α is a arbitrary parameter whose value is chosen to get the same ionicity value for $GaAs$ in both scales.

- In his book Harrison [48] gives the following description of the charge transfer in III-V semiconductors. The ionicity, f_i, is directly derived from the polarity of the bond, α_p, using the s and p energy levels of the atoms i, $\epsilon_s^{(i)}$ and $\epsilon_p^{(i)}$ respectively.

$$f_i^2 = 1 - \left(1 - \alpha_p^2\right)^{\frac{3}{2}} \tag{3.5}$$

with

$$\alpha_p = \frac{V_3}{\sqrt{V_2^2 + V_3^2}} \tag{3.6}$$

where

$$\epsilon_h^{(i)} = \frac{\epsilon_s^{(i)} + 3\epsilon_p^{(i)}}{4} \tag{3.7}$$

$$V_3 = \frac{\epsilon_h^{(2)} - \epsilon_h^{(1)}}{2} \tag{3.8}$$

$$V_2 = \frac{1}{4}\left(-\beta_{ss\sigma} + 2\sqrt{3}\beta_{sp\sigma} + 3\beta_{pp\sigma}\right) \tag{3.9}$$

The effective charge, Z^*, is thus simply given by

$$Z^* = 4\alpha_p - \Delta Z \tag{3.10}$$

with ΔZ =0, 1, 2 and 3 for elements of groups 14, 15, 16 and 17, respectively.

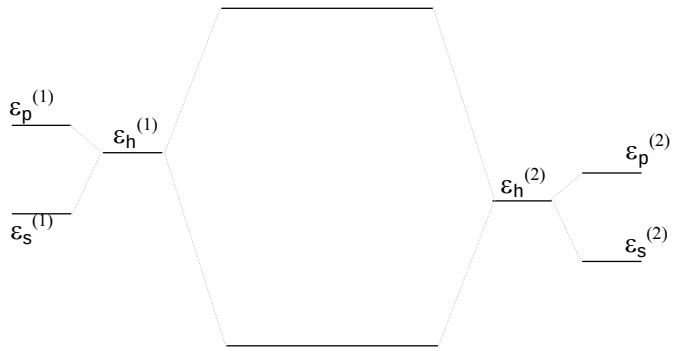

Figure 3.2: Illustration of the electronic levels in the model of Harrison for binary tetrahedral semiconductors.

3.3 The structural trend at the end of the 20^{th} century

Jamieson [7] and Phillips [46, 43, 49] introduced a first systematics of III-V semiconductors under pressure based on the ionicity of the compound (see figure 3.3). Their systematics was contradicted by both experimental and theoretical works. The Nelmes and McMahon group performed systematic exploration of the groups IVa, IIIa-Va and IIa-VIa semiconductors using the high-resolution capabilities of the combined synchrotron and DAC setups. Their results are summarized in a review paper [10]. At the same time, many *ab initio* calculations of total energy and phonon modes were performed. The review paper of Mujica *et al.* [11] is the reference for the theoretical works performed on $A^N B^{(8-N)}$ semiconductors.

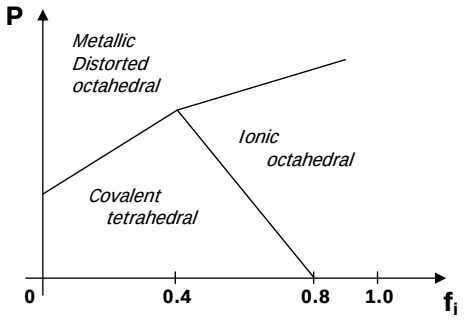

Figure 3.3: Structural trend of the IIIa-Va semiconductors as predicted by Phillips [46]. f_i is the ionicity of the compound.

Ozolins and Zunger [42] first argued the systematic absence of $NaCl$-type and β-Sn-type, high pressure phases in covalent and ionic semiconductors, respectively. They observed soft phonon modes with imaginary frequencies for the less ionic compounds. They conclude that the NaCl structure is dynamically stable only for $InAs$, InP and the nitrides (AlN, GaN and InN)[2]. The phonon instability which exists in the original NaCl structure is geometrically compatible with a symmetry-breaking mechanism giving rise to the $Cmcm$ structure, in agreement with the experimental observations of Nelmes *et al.* [50]. The dynamical stability of the $CsCl$ structure is considered [41]: the phonon instabilities suggest distortion schemes leading to $AuCd$ and $InBi$-type structures.

Nelmes *et al.* [50], Ozolins *et al.* [42] and Kim *et al.* [41] summarized the structural trends at the end of the 20^{th} century. However, their systematics does not take into account the experimental evidence of the β-Sn structure in $GaSb$ [36] and $InSb$ [27]. The short range chemical order could play some role. The influence of ionicity on the short-range chemical order is also addressed in this thesis in the case of $GaSb$ and GaP.

3.4 GaSb

$GaSb$ is the least ionic semiconductor in the IIIa-Va family. It is widely used in photovoltaic cells, laser diodes and photodetectors. The ZB lattice parameter under ambient conditions is 6.09 Å. The first study of $GaSb$ under pressure was performed by Minomura and Drickhamer in 1962 [39]. They indicated an insulator-to-metal transition around 9 GPa, now revised to 7.5 GPa. $GaSb$-II structure was first identified to be β-Sn by Jamieson [7] and by Weir and co-workers [51]. They observed a second transition at 27.8 GPa to a $GaSb$-III structure. This structure is supposed to have a simple hexagonal structure. A further transition was reported at 61 GPa to an unknown structure.

In 1994, McMahon *et al.* [35] studied the diffraction pattern of $GaSb$-II and found additional diffraction peaks. This lead to the reassessment of the structure: the best Rietveld [38] fit is obtained with a disordered $Imma$ structure. This experiment does not exhibit any transition around 28 GPa. Another transition is observed around 67 GPa but the structure was not identified. In 2001, the chemical order of $GaSb$-II was studied by Vanpeteghem *et al.* [52] which underline the lack of complete short-range chemical order.

$GaSb$ is an interesting compound to study the evolution of the structural trends from covalent group-IVa semiconductors to binary IIIa-Va semiconductors. As ionicity is a key parameter of the

[2]In this case, the structure under ambient pressure is the würtzite structure.

III-V systematics, it is important to study the effect of a slight charge transfer on the structure and chemical ordering of *GaSb*. This is performed both experimentally and theoretically in the next papers [36, 53, 37].

ZB (*GaSb*-I)		
↓		
d-Imma (*GaSb*-II)	7.6 GPa [35]	$\frac{\Delta V}{V} = 18.3$ %
or		
β-Sn (*GaSb*-II) [36]		
↓		
SH	27.8 GPa [51]	
↓		
Pmm2	61.0 GPa [51]	
↓		
(?)	63-71 GPa [10]	

Table 3.2: Sequence of phases in *GaSb* under pressure.

We performed angle dispersive X-ray diffraction experiments [36] in a diamond anvil cell using different pressure-transmitting media and in a large volume cell (Paris-Edinburgh type). By varying the stress state around the sample, it is possible to understand the physical origin of the structural distortion from β-*Sn* to *Imma* suggested by Nelmes *et al.* [50]. Indeed the β-*Sn* structure was also clearly identified in *InSb* [27] which also has a low ionic character. We compare this distortion process to the reduction of the β-*Sn*-to-*Imma* transition pressure observed in silicon under uniaxial compression in section 3.8 [37].

The ionicity - or charge transfer - obviously has an influence on the possible chemical disorder. In the case of *InSb*, the X-ray scattering properties of In and Sb are very similar as they roughly have the same number of electrons. It is thus difficult to study the chemical ordering using ADXRD. As *Ga* and *Sb* do not belong to the same row of the periodic table, the diffraction pattern of *GaSb* gives us indication about the long range chemical ordering as mentioned in reference [36]. Chemical disorder is not so energetically unfavourable in the case of the low ionic compounds such as *GaSb*. We also study this point using *ab initio* calculations within the DFT framework [53].

phys. stat. sol. (b) **211**, 395 (1999)

Subject classification: 62.50.+p; 61.10.Nz; 64.30.+t; 64.70.Kb; S7.13

The Effect of Micro-Strain and Pressure Medium on the High-Pressure Phase of GaSb

M. Mezouar[1]) (a), H. Libotte (a), S. Députier (b), T. Le Bihan (a), and D. Häusermann (a)

(a) European Synchrotron Radiation Facility, B.P. 220, F-38000 Grenoble, France

(b) Laboratoire de Chimie du Solide et Inorganique Moléculaire, UMR CNRS-Université 6511, Campus de Beaulieu, F-35042 Rennes Cedex, France

(Received August 14, 1998; in revised form September 17, 1998)

Angle dispersive X-ray diffraction experiments have been performed in a diamond anvil cell using different pressure media and a large volume cell (Paris-Edinburgh cell) in order to determine the effect of pressure–temperature conditions on the high-pressure phase of the binary compound gallium antimonide GaSb. In particular, fine analysis of the diffraction patterns obtained at high pressure and/or temperature have clearly evidenced the importance of the pressure medium and of micro-strains which considerably modified the structure at high pressure.

1. Introduction

Among the III–V semiconductors, gallium antimonide has been the most extensively studied one at high pressure [1 to 7]. However, significant uncertainties remain on the determination of the crystallographic structure of its high-pressure phase. Indeed, X-ray powder diffraction studies in energy dispersive mode have firstly [5] led to a site-ordered β-tin-like structure as in the case of germanium and silicon at pressure of 7 GPa. Using an improved method, i.e. angle-dispersive diffraction with image-plate detector, the structure of the high-pressure phase was found orthorhombic with space group Imma [6]. In both cases, the diffraction pattern used to determine the symmetry and space group has been obtained at pressure above 18 GPa in a diamond anvil cell using the mixing ethanol–methanol as pressure transmitting medium which is not perfectly hydrostatic above 11 GPa. The aim of this paper is to find out the thermodynamically stable structure of GaSb at high pressure and, more important, to determine the exact role played by the pressure medium, micro-strains and temperature.

2. Experimental Method

2.1 Sample preparation

The binary phase GaSb was prepared by direct combination of the elements. The starting materials were antimony as powder and gallium as ingots, both with minimum purity 99.9%. The elements were intimately mixed (total sample about 500 mg), placed in

[1]) Corresponding author: Tel.: +33 4 76 88 27 75, Fax: +33 4 76 88 27 84, e-mail: mezouar@esrf.fr

a silica tube which was evacuated to 0.133 Pa, sealed under vacuum and placed in a resistance furnace. The sample was first annealed at this temperature for 48 hours and subsequently cooled to 600 °C and annealed at this temperature for 48 hours. Numerous grindings, cold pressing and re-annealings at the same temperature of 600 °C for a few days were needed to ensure homogeneity and reach thermodynamic equilibrium. Finally, the sample was quenched in ice water.

The pellet was pulverised and analysed using X-ray powder diffraction (CPS 120 INEL) equipped with a position sensitive detector covering 102° in 2θ (elemental silicon was taken to determine a cubic spline calibration function to describe the 2θ versus channel number function).

2.2 DAC and large volume cell experiments

The samples were loaded in a membrane type diamond anvil cell (DAC) [8] (with 650 μm-diameter central flats). In order to exhibit the effect of non-hydrostaticity on the process of phase transformations, two different loadings have been performed: one with nitrogen as pressure-transmitting medium and one without any pressure medium. The pressure was measured on-line using the ruby-fluorescence technique [9]. In parallel and in order to examine the effect of temperature on the process of strain relaxation, we have performed a high-pressure high-temperature experiment using the large volume Paris-Edinburgh cell [10]. The Paris-Edinburgh press is a device commonly used for the precise determination of pressure–temperature phase diagrams [11,12] using energy dispersive X-ray diffraction. Recently, this set-up has been interfaced to the new fast imaging plate detector [13] for the rapid collection of *in situ* X-ray powder diffraction data suitable for structural refinement at high pressure and high temperature. This new set-up is described in detail in [14].

The wavelength of the incident X-ray beam was fixed at 0.4211 Å for DAC experiments and 0.2371 Å for the large volume cell experiment using a silicon (111) channel cut monochromator and collimated down to $50 \times 50\ \mu m^2$ by two sets of tungsten carbide slits. The angle-dispersive data were collected on the high brilliance beamline ID30 at the European Synchrotron Radiation Facility (ESRF). These data were corrected for spatial distortions, and the full ring profiles were integrated using the software package Fit2D [15]. Structural analysis has been performed by full Rietveld refinement using the program GSAS [16].

3. Results and Discussion

Fig. 1 shows two integrated patterns of the pure high-pressure phase of GaSb obtained at $P = 12$ GPa and $T = 300$ K in a membrane type DAC. The diffraction patterns a and b correspond to the cell loaded with nitrogen as pressure transmitting medium and to a cell without any pressure medium, respectively, and show clearly that the resolution is degraded when pressure gradients are present. For instance, the two peaks which form the doublet at $2\theta = 13.5°$ can only be separated under hydrostatic conditions (Fig. 1a). However, the line width still remains abnormally high (0.3° at $2\theta = 9.5°$) which means that the resolution is also affected by the large strain energy accumulated inside the grains during the compression.

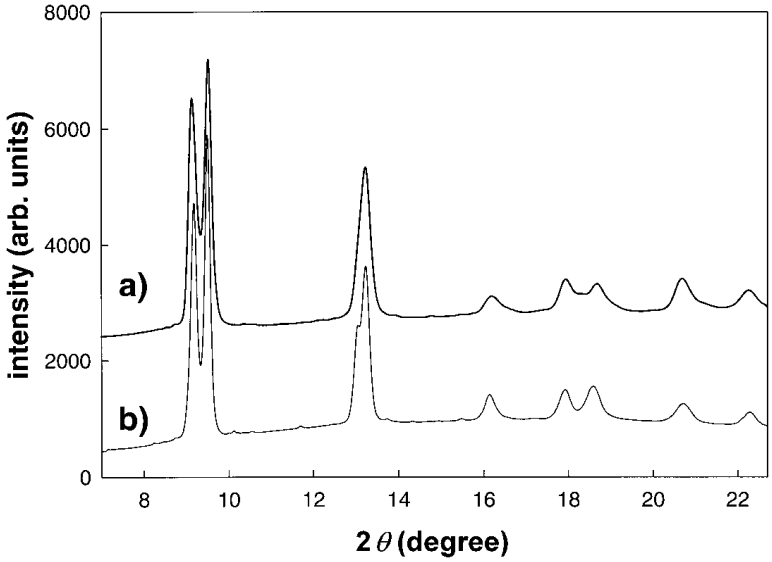

Fig. 1. ADX diffraction patterns of the high-pressure phase of GaSb at 11 GPa, a) with nitrogen as pressure transmitting medium, b) without pressure medium

Another important effect is visible in Figs. 2a and b which represent enlargements of the integrated diagrams Figs. 1a and b in the region of 2θ between 15.7° and 23°. An asymmetry of the peak profiles is observed (shoulders indicated by the arrows in Fig. 2a) which is unambiguously due to the pressure gradients. In a previous study [6], the presence of the shoulders has been detected at the same 2θ positions, and fine crystallographic analysis (Rietveld refinement) has led to propose that GaSb does not have the site-ordered (diatomic) β-tin-like structure [5] but a disordered orthorhombic structure with space group Imma. The present work shows clearly that the Imma

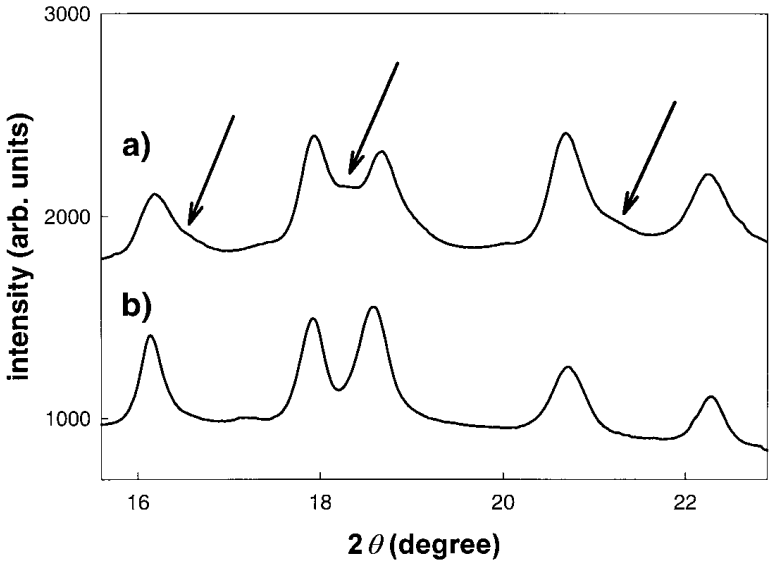

Fig. 2. Enlargement of the ADX diffraction patterns shown in Figs. 1a, b in the region of 2θ between 15.7° and 23°. The arrows indicate the shoulders induced by non-hydrostatic conditions

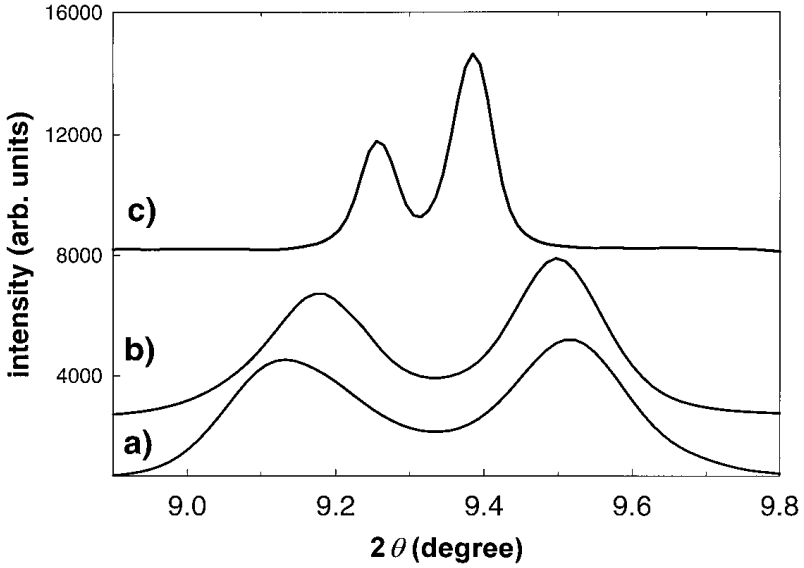

Fig. 3. ADX diffraction patterns of the high-pressure phase of GaSb in the region of 2θ between 8.9° and 9.8°, a) in a DAC without pressure medium, b) in a DAC with nitrogen as pressure transmitting medium, and c) in the Paris-Edinburgh cell at $P = 7$ GPa and $T = 500$ K

structure is only stabilized under non-hydrostatic conditions. This stabilization can be explained by the proximity of the minima of the Gibbs free energy function for those two solid phases.

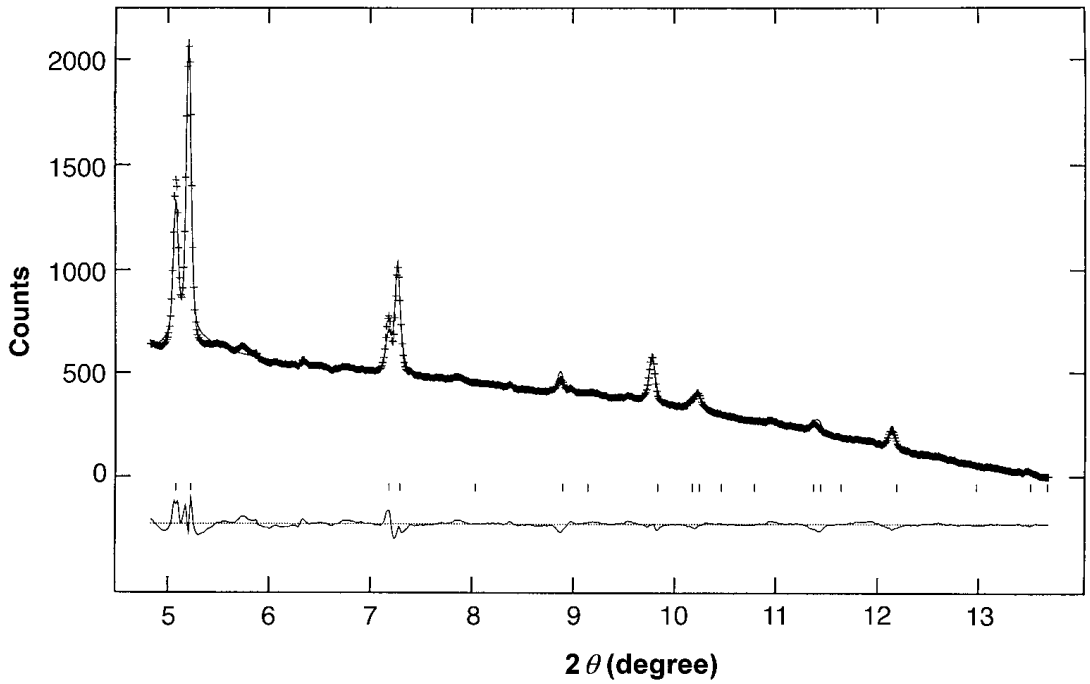

Fig. 4. Rietveld refinement of a disordered β-tin structure (space group $I\bar{4}m2$) to the integrated profile obtained at $P = 7$ GPa and $T = 500$ K in the Paris-Edinburgh cell. The tick marks under the profile indicate the reflections allowed for this space group

As described above, the width and the shape of the diffraction peaks are strongly affected by the nature of the pressure medium which can induce pressure gradients and also by the strain energy accumulated inside the crystallites during the compression. In order to avoid those problems and to recover the resolution suitable for least square refinement, the pressurised sample has been heated up to 500 K using the Paris-Edinburgh cell. Fig. 3 shows the effect of the temperature on the diffraction lines around $2\theta = 9.5°$. A strong reduction of the line width is observed during the heating of the sample due to the annealing of the micro-strain and pressure gradients. In this condition, the resolution is increased by a factor two and makes Rietveld refinement [17] more reliable.

In agreement with previous work [6], the (110) and (311) reflections which are characteristic of the site ordered β-tin-like structure are absent from the observed profile. Therefore, the Rietveld refinement has been performed using the disordered β-tin structure (space group $I\bar{4}m2$) with 50:50 occupancy of each site by Ga and Sb. The variables in this refinement were the lattice parameters a and c, a scale factor, three peak-shape parameters, an isotropic thermal motion parameter and a preferred orientation parameter. The result is presented in Fig. 4 and shows that the agreement between observed and calculated profile is excellent ($R(F^2) = 3.1\%$). The cell parameters are $a = b = 5.299$ Å and $c = 2.960$ Å at $P = 7$ GPa and $T = 500$ K. The fitted profile for the previously proposed [6] disordered Imma structure is shown in Fig. 5 and exhibits important deviations to the observed profile. Indeed, numerous allowed reflections indicated by the tick marks are absent (the most evident non-existent reflections are indicated by arrows in Fig. 5).

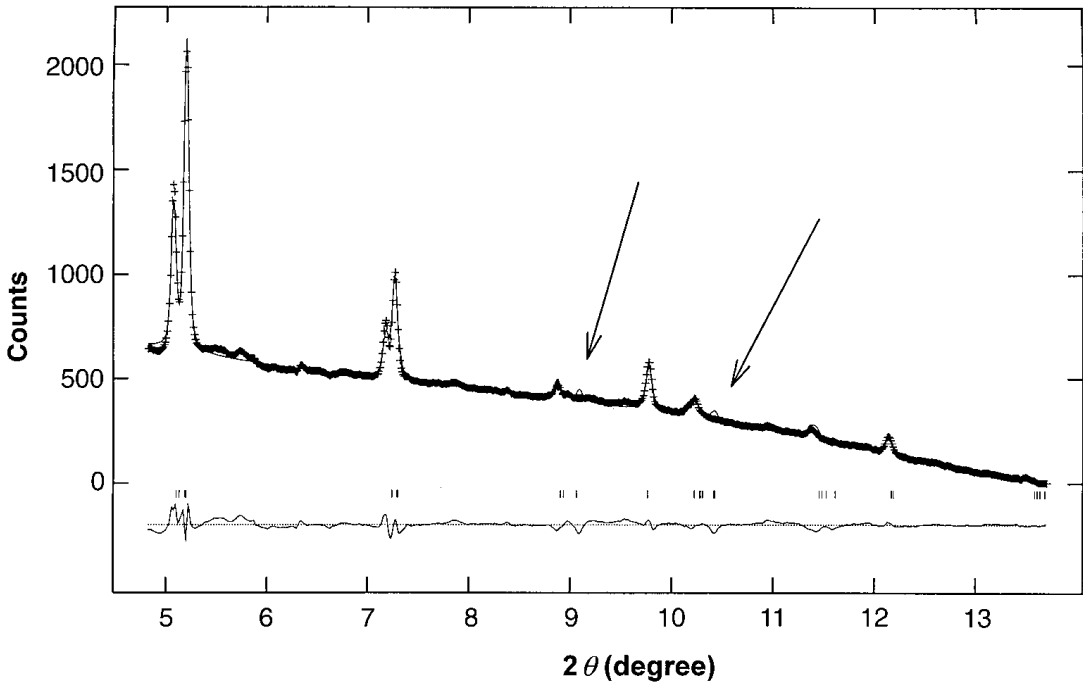

Fig. 5. Rietveld fit of the Imma structure to the integrated profile obtained at $P = 7$ GPa and $T = 500$ K. The tick marks under the profile indicate the reflections allowed for this space group. The arrows indicate the clear discrepancy between calculated and observed profiles

4. Conclusion

General effect of pressure conditions has been examined by redundant experiments (DAC, LV cell). The main conclusion is that stress conditions which strongly depend on the experimental method can induce different solid phases which can be persistent in a wide region of pressure and temperature. It has been shown that the stable high-pressure phase of GaSb (obtained under hydrostatic conditions) has the site-disordered β-tin structure.

Acknowledgements We gratefully acknowledge very helpful discussions with R.J. Nelmes and M.I. McMahon from the Department of Physics (University of Edinburgh, U.K.) and A. San Miguel from the University Claude Bernard (Lyon, France). One of the authors (H. L.) would like to thank J. P. Gaspard from the University of Liege for all supports provided during his stay at the ESRF.

References

[1] S. MINOMURA and H.G. DRICKHAMER, J. Phys. Chem. Solids **23**, 451 (1962).
[2] J.C. JAMIESON, Science **139**, 845 (1963).
[3] A. JAYARAMAN, W. KLEMENT, and G.C. KENNEDY, Phys. Rev. **130**, 540 (1963).
[4] S.C. YU and I.L. SPAIN, Solid State Commun. **25**, 49 (1978).
[5] S.T. WEIR, Y.K. VOHRA, and A.L. RUOFF, Phys. Rev. B **36**, 4543 (1987).
[6] M.I. MCMAHON, R.J. NELMES, N.G. WRIGHT, and D.R. ALLAN, Phys. Rev. B **50**, 13047 (1994).
[7] A. SAN MIGUEL, A. POLIAN, and J.P. ITIÉ, High Pressure Res. **10**, 416 (1992).
[8] R. LE TOULLEC, J.P. PINCEAUX, and P. LOUBEYRE, High Pressure Res. **1**, 77 (1998).
[9] R.A. FORMAN, G.J. PIERMARINI, J.D. BARNETT, and S. BLOCK, Science **176**, 284 (1972).
[10] J.M. BESSON, R.J. NELMES, G. HAMEL, J.S. LOVEDAY, G. WEILL, and S. HULL, Physica B **180/181**, 907 (1992).
[11] P. GRIMA, A. POLIAN, M. GAUTHIER, J. P. ITIÉ, M. MEZOUAR, G. WEILL, and J.M. BESSON, J. Phys. Chem. Solids **56**, 525 (1995).
[12] M. MEZOUAR, J.M. BESSON, G. SYFOSSE, J. P. ITIÉ, D. HÄUSERMANN, and M. HANFLAND, phys. stat. sol. (b) **198**, 403 (1996).
[13] M. THOMS, S. BAUCHAU, M. KUNZ, T. LE BIHAN, M. MEZOUAR, D. HÄUSERMANN, and D. STRAWBRIDGE, Nuclear Instrum. and Methods A **413**, 175 (1998).
[14] M. MEZOUAR, T. LE BIHAN, Y. LE GODEC, H. LIBOTTE, M. THOMS, and D. HÄUSERMANN, Paris-Edinburgh large volume cell coupled with a fast imaging plate system for structural investigation at high pressure and high temperature, in preparation.
[15] A. HAMMERSLEY, Fit2D, ESRF annual report (1997).
[16] A. LARSON and B. VON DREELE, GSAS, Los Alamos Laboratory (1994).
[17] H. M. RIETVELD, J. Appl. Cryst. **2**, 65 (1969).

EUROPHYSICS LETTERS 15 August 2003

Europhys. Lett., **63** (4), pp. 545–548 (2003)

Ab initio study of the site ordering in the GaSb β-Sn phase

H. Libotte[1] and J. P. Gaspard[1]

[1] *Condensed Matter Physics Laboratory, University of Liège, B5 B-4000, Sart-Tilman, Belgium*

(received 3 April 2003; accepted in final form 17 June 2003)

PACS. 62.50.+p – High-pressure and shock-wave effects in solids and liquids.
PACS. 64.60.Cn – Order-disorder transformations; statistical mechanics of model systems.
PACS. 64.70.Kb – Solid-solid transitions.

Abstract. – Site ordering of the β-Sn phase of GaSb is studied in the framework of the density functional formalism. Different order configurations are compared in order to elucidate the local structure of the β-Sn phase of GaSb. This theoretical work confirms the latest EXAFS results where a local chemical disorder was observed.

From the early days of high-pressure research, III-V semiconductors have been intensively studied. The β-tin phase [1–3] was of major importance through all the high-pressure semiconductor systematics. However, this point was revised and distorted structures were theoretically and experimentally proposed instead of the usual β-tin phase [4, 5]. Another new parameter in the III-V systematics is the chemical order. In the diatomic ordered β-Sn phase the first shell of neighbours of a cation (anion) contains four anions (cations) and two cations (anions). Obviously, these homoatomic bonds are not energetically favorable. Therefore, the disorder rate should have an influence on the β-Sn phase stability. The description of the chemical ordering in III-V semiconductors under pressure is a new matter of interest that has emerged recently [6, 7].

GaSb is the least ionic III-V semiconductor. It is commonly used in optoelectronical devices such as infrared laser and light emitting diodes. GaSb lies at the frontier between the covalent group-IV semicondutors, *e.g.* Si, and more ionic binary compounds, *e.g.* InAs. Its behaviour is therefore really interesting in order to understand the physics of binary semiconductors under pressure. Experimentally, the first high-pressure phase of GaSb under highly hydrostatic conditions is site-disordered β-Sn [8, 9], even if other distorted structures were also observed [10]. This disordered β-Sn phase is compatible with the dynamical phonon calculations [11] which showed that the true diatomic β-Sn phase does not exist for the ionic III-V semiconductors.

The aim of this letter is to study the short-range ordering of the GaSb β-Sn phase using *ab initio* methods. The calculations were performed using the AbInit package [12] within the framework of the density functional formalism. The pseudopotentials of Hartwigsen, Goedecker and Hutter [13] were used with the Ceperley-Alder [14] form of the local-density approximation. In order to resolve the small enthalpy differences between site-disordered structures, high-quality Brillouin-zone integrations were needed [15]. Ordered zinc-blende and β-Sn structures were, respectively, studied with $4 \times 4 \times 4$ and $8 \times 8 \times 16$ k-point meshes. The

TABLE I – *Structural parameters of the zinc-blende phase resulting from the fit of the calculated $E(V)$ points by a third-order Murnaghan equation of state.*

Parameter	This work	Previous work [8]
a (Å)	5.979	6.095
B_0 (GPa)	57.3	54.9
B_0'	4.22	4.78

disorder effects were examined within macro-cells of 108 atoms. Here, $6\times6\times6$ k-point meshes were used. For each calculation, we chose an energy cutoff of 15 Ha. A careful convergence study was performed in order to check the accuracy of our calculations. For the ordered zinc-blende structure, the third-order Murnaghan equation-of-state fit of the calculated $E(V)$ points is summarized in table I. A complete $E(V)$ curve is calculated for each order and disorder configuration of the zinc-blende and the β-Sn phases using the third-order Murnaghan equation of state. For each point, a structural optimization was performed in order to relax the internal atomic forces at constant volume and to find the stable $\frac{c}{a}$ ratio for this volume. At 9 GPa the calculated value of 0.54 is very close to the experimental value of 0.556 [7].

The first case to study is obviously the site-ordered diatomic β-tin phase with space group $I\bar{4}m2$ and Ga atom on the $2(a)$ site and Sb atom on the $2(c)$ site. Conversely, there is the completely site-disordered quasimonoatomic phase. In this case, each site has an equal probability to be occupied by a Ga atom or a Sb atom. Progressive disordering of the β-tin phase is also studied. For each macro-cell configuration, the numbers of gallium and antimony atoms are obviously equal in order to conserve the stoichiometry of the compound. In the following, the notation $(x : 100-x)$ is used to describe the chemical order rate. This means that the $2(a)$ site has an occupancy of x% of Sb atoms and $(100-x)$% of Ga atoms and that the $2(c)$ site has an occupancy of x% of Ga atoms and $(100-x)$% of In atoms. Three intermediate chemical order rates were also considered: the $(12.5 : 87.5)$, $(25 : 75)$ and $(37.5 : 62.5)$ occupancies. For

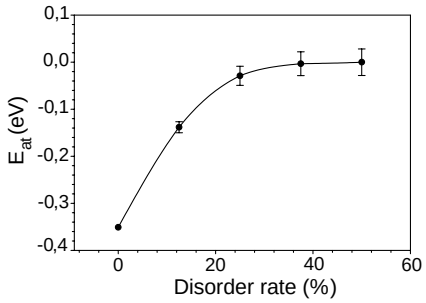

Fig. 1

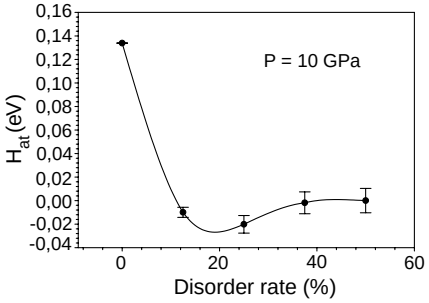

Fig. 2

Fig. 1 – Energy curve as a function of the chemical disorder rate, x, for the zinc-blende phase under zero pressure. The stable structure is a $(0 : 100)$ configuration. This curve can be plotted for any pressure up to the structural phase transition. In all these cases, the stable structure is the ordered configuration. The line is the fit of the calculated points using spline curves.

Fig. 2 – Enthalpy curve as a function of the chemical disorder rate, x, at 10 GPa. The stable structure is a $(19 : 81)$ configuration. This curve can be plotted for any pressure in the range from 8 up to 20 GPa. In all these cases, the stable structure is the $(20 \pm 5 : 80 \pm 5)$ configuration. The line is the fit of the calculated points using spline curves.

each order rate, the energy calculation is performed on ten different configurations randomly generated according to the stoichiometry and order rate constraints. The resulting energies are averaged in order to lower the influence of a special configuration.

Our method is applied both to the zinc-blende and the β-Sn phases under pressure. Concerning the zinc-blende phase, fig. 1 shows the energy per atom as a function of the disorder rate at zero pressure. The minimum of this curve clearly corresponds to the chemically ordered structure, *i.e.* the (0 : 100) configuration. The enthalpy curve shape does not change if a pressure is applied. In fig. 2, the atomic enthalpy is given as a function of the chemical disorder at a pressure of 10 GPa for the β-Sn phase. It is clear from this figure that the stable phase at 10 GPa is around the (19 : 81) occupancy β-tin phase. Moreover, our calculations show that the disorder is not significantly influenced by pressure at least for the pressure range considered here, *i.e.* up to 20 GPa. All our conclusions are in fair agreement with the latest EXAFS results [7], where $(25 \pm 10 : 75 \pm 10)$ and $(38 \pm 10 : 62 \pm 10)$ configurations are, respectively, reported at 8.6 GPa and 11 GPa. The error bars in figs. 1 and 2 show the standard deviation of the ten configurations for the considered order rate. It is clear that this standard deviation increases with the disorder rate as the number of different atomic surrounding configurations also increases with the disorder rate. Therefore, the statistical averaging of our method becomes less efficient. However, the physical interpretation of our curve does not change. It is clear that the error bars are small enough not to influence significantly the position of the enthalpy minimum. The transition from zinc-blende to β-Sn is calculated to be 5.6 GPa which is in good agreement with experimental values of 7.0 GPa [10].

In conclusion, the stable structure of the first GaSb high-pressure phase is not a completely site-disordered β-Sn phase. There is a certain amount of short-range ordering. Indeed the stable configuration seems to be very close to the (20 : 80) configuration. This chemical disorder is needed in order to fully stabilize the β-Sn phase of GaSb. By this way, our calculations give a theoretical confirmation of the latest experimental observations [7]. The evolution of the chemical order rate with ionicity and pressure should be further studied through the III-V family both by experimental and theoretical means in order to get a complete description of the III-V behaviour under pressure.

* * *

We gratefully acknowledge Prof. Ph. Ghosez (University of Liège, Belgium) and Drs. S. Pascarelli and G. Aquilanti (ESRF, France) for invaluable discussions. This work is supported by FNRS Grant No. 9.4565.96F.

REFERENCES

[1] Jamieson J. C., *Science*, **139** (1963) 845.
[2] Yu S. C. and Spain I. L., *Solid State Commun.*, **25** (1978) 49.
[3] Weir S. T., Vohra Y. K. and Ruoff A. L., *Phys. Rev. B*, **36** (1987) 4543.
[4] Nelmes R. J. and McMahon M. I., *Semiconductors and Semimetals*, Vol. **54** (Academic Press) 1998, p. 145.
[5] Nelmes R. J., McMahon M. I. and Belmonte S. A., *Phys. Rev. Lett.*, **79** (1997) 3668.
[6] Ackland G. J., *Phys. Rev. Lett.*, **86** (2001) 5301.
[7] Vanpeteghem C. B., Nelmes R. J., Allan D. R., McMahon M. I., Sapelkin A. V. and Bayliss S. C., *Phys. Status Solidi B*, **223** (2001) 405.
[8] Mezouar M., Libotte H., Députier S., Le Bihan T. and Hausermann D., *Phys. Status Solidi B*, **211** (1999) 395.

[9] LIBOTTE H. and GASPARD J.-P., *Phys. Rev. B*, **62** (2000) 7110.
[10] MCMAHON M. I., NELMES R. J., WRIGHT N. G. and ALLAN D. R., *Phys. Rev. B*, **50** (1994) 13047.
[11] OZOLINS V. and ZUNGER A., *Phys. Rev. Lett.*, **82** (1999) 767.
[12] The ABINIT code is a common project of the Universite Catholique de Louvain, Corning Incorporated, University of Liège and other contributors (URL: `http://www.abinit.org`).
[13] HARTWIGSEN C., GOEDECKER S. and HUTTER J., *Phys. Rev. B*, **58** (1998) 3641.
[14] CEPERLEY D. M. and ALDER B. J., *Phys. Rev. Lett.*, **45** (1980) 566.
[15] MONKHORST H. J. and PACK J. D., *Phys. Rev. B*, **13** (1976) 5189.

3.5 InAs

InAs is one of the most ionic zincblende III-V semiconductors (see table 3.1) and thus its behaviour is very interesting to study the influence of charge transfer by comparison with *GaSb*. Due to its high electronic mobility, it is used in high-speed optical communication systems. At ambient pressure it crystallizes in the zincblende structure with a lattice parameter of 6.05 Å. *InAs* was studied in 1962 by Minomura *et al.* [39] who measured its electrical resistivity under pressure. The transition pressure to the *NaCl* structure was located around 7 GPa in 1963 by Jamieson [7] using the diffraction technique. This was confirmed by Vohra *et al.* in 1985 [54]. They also reported a transition to a β-Sn structure at 17 GPa. In 1995, Nelmes *et al.* reported the same first transition to the site-ordered *NaCl* structure [55]. However, they observed that this phase is stable on a very limited pressure range : at 9 GPa extra diffraction peaks appear. This new structure was clearly identified to have the *Cmcm* symmetry. No other transitions were observed up to 46 GPa. The *ab initio* simulations of Mujica in 1997 confirmed that the stability range of the *NaCl* structure is very narrow [56]. They also mentioned a further transition around 24 GPa from *Cmcm* to *Immm*.

ZB (InAs-I)		
↓		
NaCl (InAs-II)	7 GPa [55]	
↓		
Cmcm	9 GPa [10]	$\frac{\Delta V}{V} = 0$ %
		stable upto 46 GPa

Table 3.3: Sequence of phases in InAs under pressure.

In 2002, Pascarelli *et al.* [57] reported the same ZB-to-*Cmcm* transition using a combined combined EXAFS and ADXRD experiment. The transition around 24 GPa was not observed. The next transition is observed at 35 GPa from *Cmcm* to a lower-symmetry structure[58]. Rietveld refinement [38] of the collected spectra combined with a XAS study allow to conclude that this new structure has the *Pmma* symmetry [59, 60] in agreement with the theoretical analysis of Ozolins *et al.* [42]. The *ZB* and *Cmcm* structures are identified to be site-ordered whereas *Pmma* is site-disordered. This work is the first experimental evidence of the absence of the *CsCl* structure in the phase diagram of InAs at high pressure.

In the *low* pressure range, the *Cmcm* structure is observed but also the *NaCl* structure which clearly has a limited stability pressure range. We develop a theoretical approach of the distortion mechanism occurring in the *NaCl* structure using the experimental data reported in [58]. This model - presented in the next paper - also allows to discuss the effect of charge transfer on the relative stability of the *ZB*, *NaCl* and *Cmcm* structures [61].

Symmetry breaking of ionic semiconductors under pressure: the case of InAs

H. Libotte[1], G. Aquilanti[2], S. Pascarelli[2] and J.P. Gaspard[1]

[1] Condensed Matter Physics Lab., University of Liège, B5, B-4000, Sart-Tilman, Belgium.

[2] European Synchrotron Radiation Facility, F-38043 Grenoble, France.

PACS numbers: 61.50.Lt, 61.50.Ah, 61.66.Fn

Abstract. The structure of InAs under high pressure is studied by X-ray diffraction. An *NaCl*-to-*Cmcm* distortion under pressure in InAs is found to be similar to other ionic III-V semiconductors behaviour. We suggest the physical mechanism responsible for this breaking of symmetry using a semi-empirical quantum mechanical model. In addition, the stabilizing role of the ionicity with respect to the *NaCl* structure is also discussed.

1. Introduction

Under hydrostatic pressure, symmetry-lowering transitions have been observed in different materials such as alkali metals [1, 2, 3, 4], group-IV and III-V semiconductors [5, 6]. Semiconductors show an open structure at ambient pressure (diamond, zinc blende (ZB), würtzite, CN=4). Earlier studies [7] have shown that the coordination number increases from 4 to 4+2 (β-Sn structure) for the more covalent compounds and from 4 to 6 ($NaCl$ structure) for the more ionic compounds. Recently, it has been shown that the first or the second high-pressure phase can be less symmetrical than initially assumed. Indeed the systematics of the ionic III-V semiconductors under pressure have been reassessed [8, 9]. The existence of the β-Sn and $NaCl$ structures for most III-V semiconductors has been shown to depend on the ionicity of the compound [10]. Moreover, the stability of the $CsCl$ structure was also discussed with reference to dynamical instabilities [9].

The $NaCl$-to-$Cmcm$ transition under pressure have been experimentally observed in several semiconductors [11] and a number of *ab initio* calculations confirmed these observations [12, 9]. InAs is one of the most ionic III-V semiconductors [13]. The calculations of Mujica and Needs [12] have been unable to separate the stability ranges of $NaCl$ and $Cmcm$ structures. Recently, a study combining X-ray diffraction and X-ray absorption study [14, 6, 15] showed that two distorted structures are stable in the phase diagram of InAs under pressure: $Cmcm$ and $Pmma$. The latest observed structural sequence is thus [16, 6] $ZB \rightarrow$NaCl$\rightarrow Cmcm \rightarrow Pmma$.

The aim of this paper is twofold : first the structural parameters of the high pressure phases of InAs are extracted in the range (0, 40) GPa through detailed refinement of the ADXRD data collected within a diamond anvil cell [6, 15]. Second, a general mechanism of the symmetry-lowering that occurs in III-V semiconductors under pressure is discussed as a function of the ionicity of the compound. The experimental results obtained for InAs by angle-dispersive X-ray diffraction (ADXRD) are explained using the semi-empirical quantum mechanical model.

The paper is organized as follows: in the first section we report the structural results of an ADXRD experiment at high pressure on InAs. In the next section a tight-binding (TB) based theoretical model is described. The theoretical predictions are compared to the experimental results of ADXRD. The physical trends responsible for the behaviour of InAs under pressure are finally discussed and several conclusions concerning the systematics of III-V semiconductors under pressure are drawn.

2. Experimental results

ADXRD data on powdered InAs were recorded at the beamline ID30 of European Synchrotron Radiation Facility (ESRF, Grenoble). The measurements have been performed using nitrogen as pressure transmitting medium. The experimental setup is described in a previous paper [15] focused on the observation of the phase transitions

Phase	$B_0(GPa)$	$B_0'(GPa)$	$\frac{V}{V_{0,ZB}}\|_{P=0}$
ZB	62.7 ± 2.0	6.5 ± 1.0	1.0
$NaCl$	67.6 ± 1.0	6.5 ± 1.0	0.824
$Cmcm$	152 ± 10	7.0 ± 1.0	0.761

Table 1. Structural parameters of the high-pressure EoS of InAs for ZB, $NaCl$ and $Cmcm$ structures.

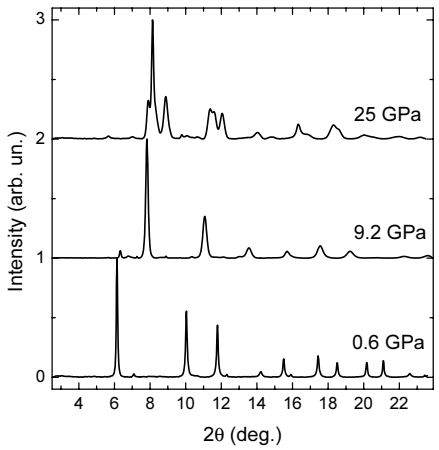

Figure 1. Selected diffraction patterns of InAs at 0.6 (ZB structure), 9.2 ($NaCl$ structure) and 25 GPa ($Cmcm$ structure). [15]

and on the description of the symmetry properties of the structures. In this paper, we present the results of a Rietveld refinement of the diffracted patterns giving the lattice parameters and atomic coordinates. Moreover, the equations of state of the new phases are established. Figure 1 shows the diffraction patterns recorded at 0.6 GPa, 9.2 GPa and 25 GPa corresponding to InAs in the ZB, $NaCl$ and $Cmcm$ structures, respectively.

Since the semi-empirical model described in the following sections is used to explain the $NaCl$-to-$Cmcm$ distortion, the structural parameters presented here are relative to the structures of InAs up to the $Cmcm$ phase. Figure 2 shows the volume per unit cell as a function of pressure normalized to the volume at room pressure.

In the ZB-to-$NaCl$ phase transition we observe a huge volume discontinuity of ∼18%, consistent with a change in the coordination number, while no measurable volume discontinuity is associated to the $NaCl$ to $Cmcm$ phase transition. The experimental P-V points were fitted using the third-order Birch-Murnaghan equation of state. The relative parameters B_0, B_0' and $\frac{V}{V_0}|_{P=0}$ are reported in table 1.

The best refinements from 13.5 to 31 GPa result in an orthorhombic unit cell in spacegroup $Cmcm$. Figures 3 and 4 show the structural parameters of InAs as a function of pressure. From 34 to 42 GPa we have fitted the data using a mixed $Cmcm$ and $Pmma$ phase. The $Pmma$ parameters are not reported here. The $Cmcm$ structure is an orthorhombic distortion of the $NaCl$ structure. In fact, the best refinements for the data

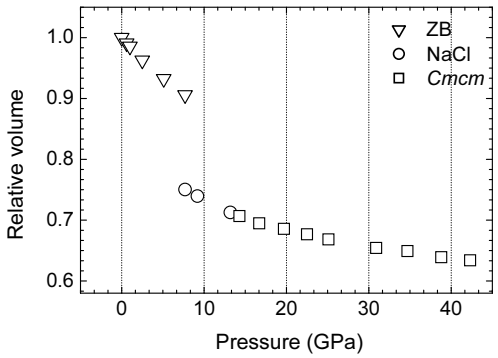

Figure 2. Relative volume of InAs versus pressure for data recorded using nitrogen as pressure transmitting medium. A change in atomic volume of $\sim 18\%$ is associated with the ZB-to-$NaCl$ transition. No volume discontinuity is observed in the $NaCl$-to-$Cmcm$ phase transition.

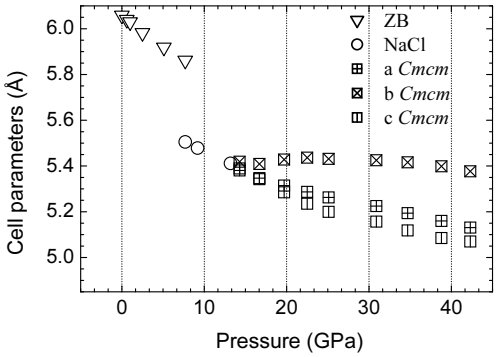

Figure 3. Unit cell parameters versus pressure of ZB, $NaCl$ and $Cmcm$ structures of InAs.

points at 13.5 and 16.7 GPa give a nearly cubic cell symmetry. As the pressure increases, the orthorhombic distortion becomes more and more pronounced. The In and As atoms are located on sites *4(c)* of spacegroup $Cmcm$, i.e. $(0,\, y_1,\, \frac{1}{4})$ and $(0,\, y_2,\, \frac{1}{4})$ respectively. The deviation of y_1 and y_2 from $\frac{3}{4}$ and $\frac{1}{4}$ (values that correspond to the $NaCl$ structure) is a further indication of the increase of the distortion of the $Cmcm$ structure with respect to $NaCl$ as a function of pressure. This is illustrated in figure 4. In the following, we use two parameters related to the sum and the difference of the fractional coordinates y_1 and y_2 i.e. $u = \frac{1}{2}\left[(y_1 + y_2) - 1\right]$ and $\delta = \frac{1}{2}\left[(y_1 - y_2) - \frac{1}{2}\right]$. Their physical meaning is discussed in the next section. They vanishes for the undistorted $NaCl$ structure.

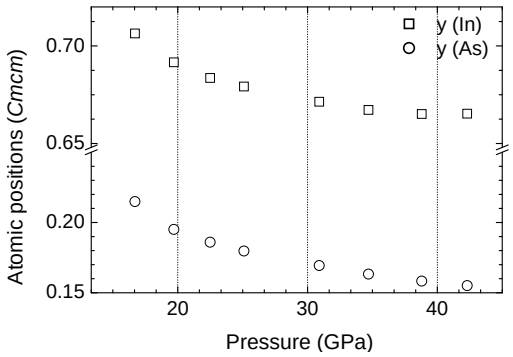

Figure 4. y values of In and As in the *Cmcm* structure as a function of pressure with $x = 0$ and $z = \frac{1}{4}$.

3. Theoretical model

3.1. Description of the total energy calculations

A simple model may account for the qualitative structural evolution of the covalent and ionocovalent structures under pressure. Let us assume that the total energy of an ionic semiconductor can be written as a sum of three contributions [17] : the band energy, the repulsive energy and the ionic energy.

$$E_{tot} = \int_{-\infty}^{E_F} E n_p(E) dE + \sum_{i<j} \frac{V_0}{r_{ij}^p} + \alpha_M \frac{Q^2}{4\pi\epsilon_0} \frac{1}{r} \tag{1}$$

where E_F and $n_p(E)$ are the Fermi level and the p-electron density of states. α_M is the Madelung constant for a given structure and Q the electronic charge of the ions. V_0 and p are the parameters of the repulsive interaction : the higher the p value, the harder the repulsion and V_0 characterizes its strength. r_{ij} is the distance between atoms i and j.

In order to calculate E_{tot} for the high-pressure structures of InAs, i.e. $NaCl$ and $Cmcm$, tight-binding calculations on a minimum basis including p orbitals only are enough to explain the distortion. The lower energy s electrons do not contribute significantly to the difference of cohesive energy as the related states are filled. The integral in (1) involving the p-electron density of states, $n_p(E)$, is approximated using a moments' expansion [18, 19], limited to the fourth-moment of the density of states, i.e. two shells of neighbors are considered in the calculation of the cohesive energy. This is analogous to the Gauss quadrature technique. The resonance integrals between the p orbitals, $\beta(r)$, are assumed to vary as an inverse power of the interatomic distance:

$$\beta(r) = \frac{\beta_0}{r^q} \tag{2}$$

where β_0 and q are the physical parameters of the resonant interaction. Usually, the q value is between 2 and 3 [21].

The parameters of our model (β_0, q, V_0, p) are obtained by fitting the theoretical model to the experimental equation of states, i.e. the bulk modulus, B_0, its pressure

derivative, B'_0, and the zero-pressure lattice parameter, a_0 of the different phases, obtained from our ADXRD data and reported in Table 1. Finally as the Madelung constant depends on the structure in a complex way it has to be computed numerically. We used the GULP [22] software to evaluate the Madelung constant as a function of the distortion parameters, λ and θ.

3.2. NaCl-to-Cmcm transition

The *Cmcm* structure is as an orthorhombic distortion of the $NaCl$ structure in which the $x-y$ planes slide on each other to create a zig-zag chain along the z-direction characterized by the distortion parameter u (see figure 5) or the θ angle related to u by the relation $u = \frac{1}{2}tan\theta$. A second distortion occurs if $\Delta y = y_1 - y_2$ differs from 0.5 and leads to a zig-zag along the x-direction. On the basis of the Rietveld refinement of our ADXRD data, the second distortion was shown to be very small (see fig. 4); the λ value is as low as -0.00175 at 20 GPa. Therefore, it is neglected in our calculations and we first assumed that the unit cell remains cubic at the transition. These two approximations allowed us to explain the mechanism of the $NaCl$-to-*Cmcm* phase transition using a one-parameter model, i. e. the angle θ shown in figure 5. This distortion mechanism is similar to an Euler buckling along the z-axis. The Madelung contribution does not play a major role at this level and it will be omitted in this section.

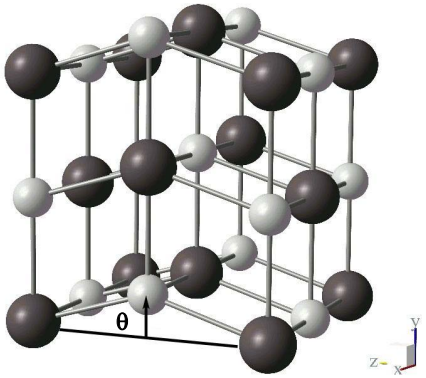

Figure 5. Idealized distorted $NaCl$ structure used to model the *Cmcm* structure with a single parameter θ.

Within this model, the *Cmcm* and $NaCl$ phases can be treated on the same footing, with two parameters $\frac{a}{2}$, and θ (see Fig. 5). The $NaCl$ structure is a special case of the *Cmcm* structure for $\theta = 0$. In the $NaCl$ structure, the first six neighbors are at the same distance $\frac{a}{2}$. When the distortion occurs, the nearest four neighbors stay at the same distance $d_1 = \frac{a}{2}$ and two neighbors show an interatomic distance $d_2 = \frac{a}{2}\sqrt{1+\tan^2\theta} \simeq \frac{a}{2}(1+\theta^2)$ to the second order in θ. The atomic volume is independent of θ and equal to $v_{at} = a^3/8$.

An expansion up to the fourth-moment of the density of states is required as it is the lowest order moment that includes the θ angle. Since the valence angles are close to 90^o the total energy can be calculated at the fourth level with only the $pp\sigma$ interactions, the $pp\pi$ interactions being negligible. We use Kanamori's expression [23] to calculate the moments μ_2 and μ_4 of the p-electron density of states. We write

$$\mu_2 = 4\frac{\beta_0^2}{a^{2q}} + 2\frac{\beta_0^2}{a^{2q}} cos^{2q}\theta \tag{3}$$

$$\mu_4 = \frac{\beta_0^4}{a^{4q}}\Big[12 + 2cos^{4q}\theta + 4cos^{4q}\theta cos^2 2\theta + 8sin^4\theta cos^{2q}\theta + 16sin^2\theta cos^{2q}\theta\Big] \tag{4}$$

The covalent energy, E_{cov}, is simply given by

$$E_{cov} = -\sqrt{\frac{\mu_2^3}{\mu_4}} \tag{5}$$

From this formula we observe that the curvature at $\theta = 0$ changes sugn when the volume decreases. This is best shown by the expansion of the total energy to the second order that can be written as

$$E_{tot}(a,\theta) = -2\sqrt{3}\frac{\beta_0}{a^q} + 6\frac{V_0}{2a^p} + \theta^2\left(\frac{2q\beta_0}{\sqrt{3}a^q} - \frac{pV_0}{2a^p}\right) \tag{6}$$

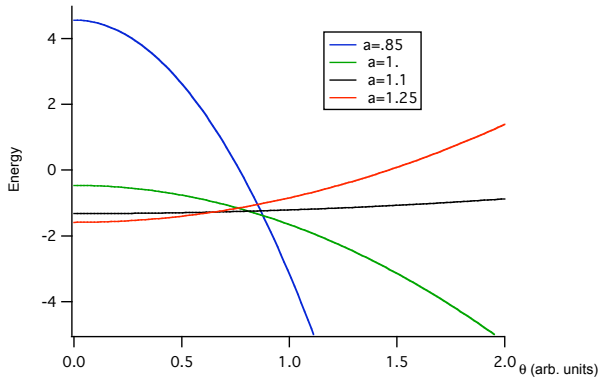

Figure 6. Total energy as a function of the angle θ for different values of the lattice parameter a.

The coefficient of the θ^2 term is positive for large values of the atomic volume v_{at} and changes sign for small volumes as illustrated in figure 6. When the angular distortion occurs, both the repulsive and attractive contributions are reduced as the interatomic distances are increased. This is illustrated in figure 6 for the attractive energy. The competition between these contributions defines if the distorted structure is stable with pressure.

The a and θ parameters at ambient pressure are obtained by minimizing the total energy as a function of both a and θ. The values at the equilibrium are then given by

$$a^{p-q} = \frac{\sqrt{3}pV_0}{2q\beta_0} \tag{7}$$

$$\theta \quad = 0 \tag{8}$$

When the volume is reduced, i.e. by applying pressure, the undistorted structure becomes unstable because the coefficient of θ^2 becomes negative. The critical value, a_{crit}, is given by:

$$a_{crit}^{p-q} = \frac{\sqrt{3}pV_0}{4q\beta_0} \tag{9}$$

Based on this simple description the compression ratio between the $NaCl$ lattice parameter at ambient pressure and at the transition is $\left(\frac{1}{2}\right)^{\frac{1}{p-q}}$.

Up to now we have shown that the distortion may occur under pressure in the absence of ionic contribution. The ionic contribution does not directly affect the occurrence or not of the distortion. The observed phase diagram mostly depends on the structures, such as zinc-blende, that are in competition with the $NaCl$ structure.

To account for the orthorhombic distortion, a second parameter, λ, has to be included in the structural description in addition to the angular distortion already mentioned. This is the second breaking of symmetry observed in the high-pressure behaviour of InAs. The orthorhombic distortion can be simply described assuming that the three lattice parameters are respectively given by a, $a(1-\lambda)$ and $a(1+\lambda)$. Thus, there are three different resonance integrals, β_a, β_θ and β_c in the $Cmcm$ structures. They are respectively related to the three axes x, y and z. They are given as a function of the lattice parameters and the angular distortion arising in the $Cmcm$ structure.

$$\beta_a = \frac{\beta_{pp\sigma}}{r_{Cmcm}^q} \tag{10}$$

$$\beta_\theta = \frac{\beta_{pp\sigma}}{r_{Cmcm}^q}\left[\frac{cos\theta}{1-\lambda}\right]^q \tag{11}$$

$$\beta_c = \frac{\beta_{pp\sigma}}{r_{Cmcm}^q}\left[\frac{1}{1+\lambda}\right]^q \tag{12}$$

where $r_{Cmcm} = \frac{a}{2}$. The second and fourth moments of the density of states write:

$$\mu_2 = 2\beta_a^2 + 2\beta_\theta^2 + 2\beta_c^2 \tag{13}$$

$$\mu_4 = 6\beta_a^4 + 6\beta_c^4 + 2\beta_\theta^4 + 4\beta_\theta^4 cos^2(2\theta) + 16\beta_\theta^2\beta_c^2 sin^2\theta + 8\beta_\theta^2\beta_c^2 sin^4\theta \tag{14}$$

In order to get the complete expression of the total energy for the $Cmcm$ phase, the Madelung contribution has to be added.

$$E_{tot} = -\sqrt{\frac{\mu_2^3}{\mu_4}} + V_0\frac{1}{r_{Cmcm}^p}\left[\left(\frac{1}{1+\lambda}\right)^p + 1 + \left(\frac{cos\theta}{1-\lambda}\right)^p\right] - \frac{1}{4\pi\epsilon_0}\alpha_{Cmcm}\frac{Q^2}{r_{Cmcm}} \tag{15}$$

A series expansion of expression (15) is performed in order to analyze the behaviour of both angular and orthorhombic distortions as a function of the atomic volume.

$$E_{tot} = -2\sqrt{3}\frac{\beta_0}{a^q} + 6\frac{V_0}{2a^p} + \theta^2\left(\frac{2q\beta_0}{\sqrt{3}a^q} - \frac{pV_0}{2a^p}\right) + \lambda^2\left[\frac{2\sqrt{3}q(\frac{2}{3}q-1)\beta_0}{3a^q} - \frac{p(p+1)V_0}{a^p}\right] - \frac{1}{2\pi\epsilon_0}\alpha_{Cmcm}\frac{Q^2}{a} \quad (16)$$

Clearly both distortions are favoured with volume reduction.

4. Discussion

We have built a model that allows to describe the *NaCl*-to-*Cmcm* distortion in both covalent and ionocovalent III-V semiconductors. We use two parameters : the buckling angle θ that accounts for the shift of the x-y plane and the orthorhombic distortion parameter λ. The stable structure, i.e. the couple (θ, λ), at a given value of the relative atomic volume, $\frac{V}{V_{0,ZB}}$ is calculated by minimizing equations (15) at constant volume for the covalent and ionocovalent structures respectively. The evolution of the resulting distortion angles, θ, as a function of the relative atomic volume are illustrated in figure 7. The parameters used for the tight-binding model are given in tables 2. These parameters are obtained by fitting the experimental $V(P)$ curves using equation (15) with and without charge transfer.

Figures 7 show the displacement of the minimum of the *Cmcm* energy as a function of the volume reduction. It clearly illustrates the appearance of the distortion when the volume is reduced, i.e. when the pressure is applied. The *ab-initio* calculations of Mujica and Needs give an evolution of the angle of distortion very similar to our predictions [12]. Figures 9 shows the evolution of the (θ, λ) energy curves as a function of the relative volume. The minimum of the energy is clearly located at $(0, 0)$ when the volume is high enough. However, when the atomic volume is reduced, the distortion appears and the minimum of the curve moves towards to a distorted structure. Again in this case our tight-binding results are in fair agreement with the *ab initio* calculation of Mujica and Needs [12].

The *NaCl*-to-*Cmcm* transition is a clearly second-order transition. It occurs at 12.5 GPa when the Madelung term is taken into account. These transition pressures were determined from the $E(V)$ curves of both phases. When the Madelung term is not included in the calculation, the transition pressure is much lower. This is illustrated in figure 8 where the evolution of the transition pressure is given as a function of the charge transfer, $\frac{Q}{e}$. It is clear from this figure that the occurrence of the buckling of the chemical bond is not directly linked to the ionicity of the compound. However, the transition may occur at very different pressure depending on the charge transfer between anion and cation. This indicates that the *NaCl* structure can be masked by other more stable phases, i.e. zinc-blende, if the transition pressure to the *Cmcm* structure is low enough.

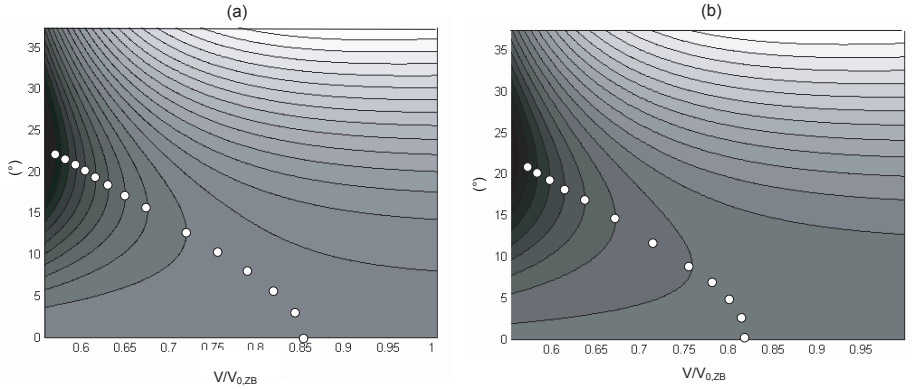

Figure 7. Isoenergy curves of the energy of the $Cmcm/NaCl$ structures as a function of the distortion angle θ and the relative atomic volume, $\frac{V}{V_{0,ZB}}$ when the Madelung term is not included (a), and when the Madelung term is taken into account (b). The charge transfer, Q, is assumed to be 0.39. In both cases the distortion clearly appears to become stable when the volume is reduced. The white dots are guide for the eye in order to locate the stable θ angle for given values of the reduced volume.

$Q \neq 0$			$Q = 0$	
$\frac{p}{q}$	$\frac{V_0}{r_{0,ZB}^p}\ (eV)$	$\frac{Q}{e}$	$\frac{p}{q}$	$\frac{V_0}{r_{0,ZB}^p}\ (eV)$
3.5	0.373	0.39	3.7	0.438

Table 2. Values of the electronic parameters obtained from the fit of our model to the experimental $V(P)$ curve for each structure in competition using relation 15.

Compound	Ionicity [21]	Crystallographic structures and related transition pressures
InP	0.398	ZB $\overrightarrow{_{9.8GPa}}$ NaCl $\overrightarrow{_{28GPa}}$ *Cmcm*
InAs	0.396	ZB $\overrightarrow{_{9.2GPa}}$ NaCl $\overrightarrow{_{13.5GPa}}$ *Cmcm*
GaP	0.317	ZB $\overrightarrow{_{24GPa}}$ *Cmcm*
GaAs	0.321	ZB $\overrightarrow{_{17.3GPa}}$ *Cmcm*

Table 3. Experimental data for GaAs, GaP, InAs and InP

This is in agreement with the experimental data related to other III-V semiconductors. InP and InAs, the more ionic semiconductors, exhibit $NaCl$ structure in their phase diagrams [10, 11, 14] whereas GaP and $GaAs$ do not.

5. Conclusion

In this paper we determine the structural parameters for the $NaCl$ and $Cmcm$ phases of InAs up to 40 GPa. A general mechanism of symmetry lowering of highly symmetric (cubic $NaCl$) structures is described and applied to covalent and ionocovalent III-V semiconductors. The description of this phenomenon is based on a simple TB model that

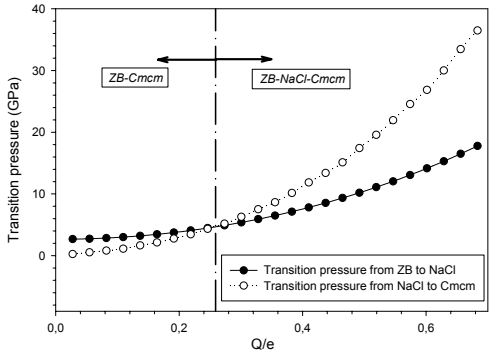

Figure 8. Evolution of the transition pressures as a function of the charge transfer, $\frac{Q}{e}$. *ZB* energy is calculated with the same model.

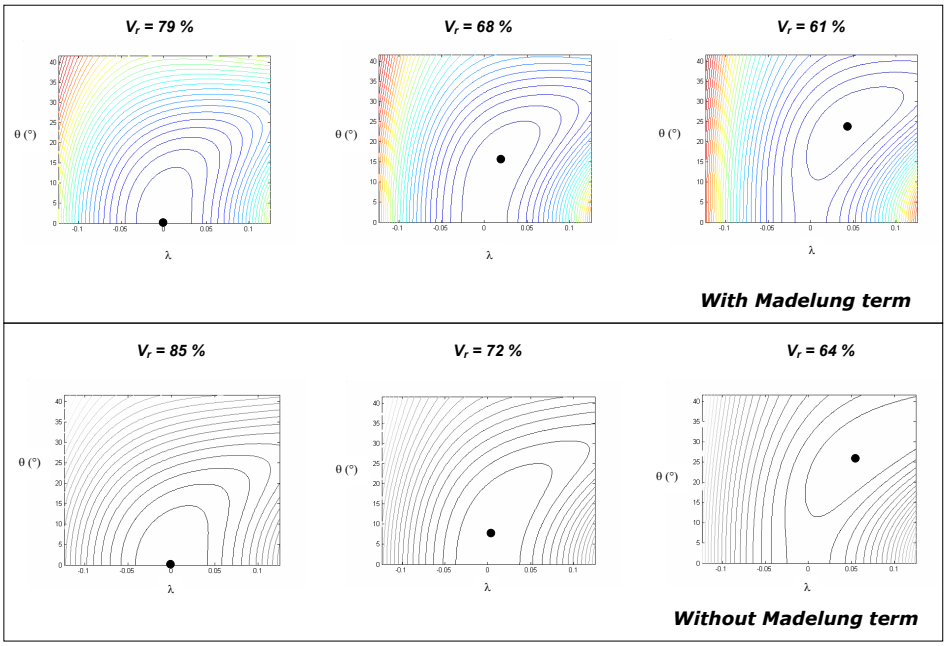

Figure 9. Energy curve of the distorted structures. The distortion parameters (λ, θ) are given for different values of the reduced volume, V_r. The black dot illustrates the stable set of parameters at the considered reduced volume. The charge transfer is assumed to be 0.39.

allows identification of the physical parameters responsible of the distortion mechanism. We show that, independently of the degree of ionicity, the undistorted NaCl structure becomes unstable with increasing pressure. For completeness, we discuss the effect of the ionic contribution on the occurrence of the distorted phase. The $NaCl$ structure may occur only in highly ionic systems. This explains the qualitative difference observed in the phase diagrams of ionic and covalent III-V semiconductors. In the case of InAs, the ionicity is high enough to stabilize the $NaCl$ phase on a limited pressure range; that

Symmetry breaking of ionic semiconductors under pressure: the case of InAs 12

is, between 9.2 and 13.5 GPa.

6. acknowledgments

The FNRS and the EU (NoE FAME) are gratefully acknowledged.

[1] N. E. Christensen and D. L. Novikov, *Sol. State Comm.*, **119** (2001) 477.
[2] J. B. Neaton and N. W. Ashcroft, *Nature*, **400** (1999) 141.
[3] U. Schwarz, K. Takemura, M. Hanfland, and K. Syassen, *Phys. Rev. Lett.*, **81** (1998) 2711.
[4] G. G. N. Angilella, F. Siringo, and R. Pucci, *Eur. Phys. J. B*, **32** (2003) 323.
[5] M. I. McMahon and R. J. Nelmes, *Phys. Rev. B*, **47** (1993) R8337.
[6] S. Pascarelli, G. Aquilanti, W. A. Crichton, T. Le Bihan, M. Mezouar, S. De Panfilis, J. P. Itié and A. Polian, *Europhys. Lett.*, **61** (2003) 554.
[7] J. C. Phillips, Bonds and Bands in Semiconductors (Academic Press, New York, 1974).
[8] K. Kim, V. Ozoliņš, and A. Zunger, *Phys. Rev. B*, **60** (1999) R8449.
[9] V. Ozoliņš and A. Zunger, *Phys. Rev. Lett.*, **82** (1999) 767.
[10] R. J. Nelmes and M. I. McMahon, Semiconductors and Semimetals, **54**, Academic Press (1998).
[11] R. J. Nelmes, M. I. McMahon, and S. A. Belmonte, *Phys. Rev. Lett.*, **79** (1997) 3668.
[12] A. Mujica and R. J. Needs, *Phys. Rev. B*, **55** (1997) 9659.
[13] Y. K. Vohra, S. T. Weir, and A. L. Ruoff, *Phys. Rev. B*, **31** (1985) 7344.
[14] S. Pascarelli, G. Aquilanti, W. A. Crichton, T. Le Bihan, S. De Panfilis, E. Fabiani, M. Mezouar, J. P. Itié, and A. Polian, *High Press. Res.*, **22** (2002) 331.
[15] G. Aquilanti, W. A. Crichton, T. Le Bihan, and S. Pascarelli, *Nucl. Instrum. Methods B*, **200** (2003) 90.
[16] R. J. Nelmes, M. I. McMahon, N. G. Wright, D. R. Allan, H. Liu, and J. S. Loveday, *J. Phys. Chem. Solids*, **56** (1995) 539.
[17] J.A. Majewski and P. Vogl, *Phys. Rev. B*, **35** (1987) 9666.
[18] J. P. Gaspard and F. Cyrot-Lackmann, *J. Phys. C* **6** (1973) 3077.
[19] R. Haydock, V.Heine, and M. J. Kelly, *J. Phys. C* **8** (1975) 2591.
[20] J. Stoer and R. Bulirsch, Introduction to Numerical Analysis, Springer-Verlag, New-York (1980).
[21] W. A. Harrison, Electronic Structure and the Properties of Solids, Freeman, San Francisco (1980).
[22] J. D. Gale, *JCS Faraday Trans.*, **93** (1997) 629.
[23] J. Kanamori, *Progr. Theoret. Phys.*, **35** (1966) 16.

3.6 GaP

GaP has an intermediate ionicity between *InAs* and *GaSb*. It is usually used in high temperature diodes and transistors[3]. Under ambient conditions, it has the *ZB* structure with a lattice parameter of 5.45 Å. In 1974, Onodera *et al.* [62] reported the first high pressure phase transition at 22 GPa. But the first diffraction experiment was only performed in 1978 by Yu *et al.* [63] with the same value of the transition pressure. However, no clear description of the structure was given before the works of Baublitz and Ruoff in 1982 using an EDX setup [64]. They observed a transition to a β-Sn structure confirmed by Hu *et al.* [65] in 1984 even if unassigned peaks were observed in both cases. In 1989, Itié *et al.* performed a XAS experiment compatible with a β-Sn structure [66].

ZB (GaP-I)		
↓		
d-Cmcm (GaP-II)	24 GPa [50]	$\frac{\Delta V}{V} = 14$ %
		stable upto 52 GPa

Table 3.4: Sequence of phases in GaP under pressure.

In 1997, a new ADXRD experiment of Nelmes *et al.* [50] suggested a *Cmcm* symmetry that takes into account the originally unassigned peaks and shoulders. The atomic ordering was also described to be chemically disordered. Following these experimental works, *ab initio* simulations were initiated by Mujica *et al.* [56, 67] in 1997 and 1998. They underlined that the enthalpy of different structures are very close to each other. They also suggested possible structures never reported in the experimental works such as *Immm*, *Imm*2 or SC16.

Due to its medium ionicity within the III-V family, *GaP* has to be studied in order to elucidate the relative stability of the *NaCl* and *β-Sn* phases. Both of them were observed in the past but according to the new systematics, neither *NaCl* nor *β-Sn* should be observed. We performed a combined ADXRD-EXAFS experiment in order to clearly identify the *GaP*-II structure. The issue of chemical ordering is adressed and the influence of the ionicity discussed [68].

[3] Up to 650 K.

High pressure phase of GaP: structure and chemical ordering

G. Aquilanti,[1,*] H. Libotte,[2] W. A. Crichton,[1] S. Pascarelli,[1] A. Trapananti,[1] and J.-P. Itié[3]

[1]*European Synchrotron Radiation Facility,*
rue 6 Jules Horowitz - B.P. 220 38043 Grenoble Cedex 09 - France
[2]*Département de Physique, B5, Université de Liège, B4000 Sart-Tilman, Belgique*
[3]*Synchrotron SOLEIL, L'Orme des Merisiers,*
St Aubin, BP 48, F-91192 Gif-sur-Yvette, France

(Dated: June 19, 2007)

Abstract

The present paper concerns a combined X-ray diffraction and absorption study of gallium phosphide (GaP) at high pressure up to 39 GPa. The aim of this study is twofold: to clarify the nature of the high pressure phase using X-ray diffraction and to determine the degree and the evolution of the short range chemical order using X-ray absorption. The analysis of X-ray diffraction shows that GaP transforms to a *Cmcm* structure and the absence of the "difference reflections" indicates that the *Cmcm* structure lacks long-range chemical order. In this system the EXAFS is compatible with the hypothesis of a chemically ordered *Cmcm* local environment. The comparison between the XANES region of the spectra and multiple scattering calculations confirms this hypothesis clearly showing that the *Cmcm* is short-range chemically ordered. The local environment of Ga is given by 6 P atoms and short-range Ga-Ga interactions are not likely to occur in this system at least up to 39 GPa. This result shows that even in a compound with a relatively low ionicity of the bonds, this parameter dictates the short-range interactions up to very high pressures.

I. INTRODUCTION

Angle dispersive x-ray diffraction (ADXRD) applied to high pressure structural studies has led to a reevaluation of the high pressure phase diagram of many materials[1]. At the same time developments in theoretical calculations have allowed to explain the reason of the occurrence of certain high pressure structures and also to predict the occurrence of new stable high pressure phases[2–5]. A typical case of this scenario is the reformulation of the structural sequences as a function of pressure of the octect compounds $A^{(n)}B^{(8-n)}$. The unanimously accepted structural sequence for these compounds was the direct transformation from the open fourfold coordinated zincblende (ZB) structure to the quasi-sixfold β-Sn structure, or, first to the sixfold NaCl and then to the β-Sn depending on the ionicity of the bonds[6]. In the light of the new systematics, the NaCl structure was found to be stable for a narrow energy range and the β-Sn was found not to occur in any of the III-V and II-VI systems at high pressure and room temperature[7], although a β-Sn structure has been observed in the more covalent GaSb[8] and in InSb[9] after heating at high pressure. The actual phases were found to have lower symmetry orthorhombic structures with space groups *Cmcm* or *Imm2* and *Imma*. Although the occurrence of the orthorhombic structures has been assessed by ADXRD and their occurrence seems to be systematic for the octet compounds and in particular for the III-V semiconductors[7], the determination of the site-ordering of the high pressure phases still remains a matter of debate. The determination of the site-ordering of those systems, such as InSb and GaAs, where the two atomic species have very similar scattering power, becomes difficult at high pressures for diffraction techniques, due to important peak broadening. For GaP, where Ga and P have very different scattering powers, ADXRD evidenced a long-range site-disorder at high pressure[7]. However, the fact that the average structure is site-disordered does not exclude the possibility of ordering over a short-range scale.

The local atomic environment yields information on fundamental interactions between atoms. Therefore, only information on local chemical order allows to verify theoretical methods that yield to the formulation of models used to reproduce the thermodynamic and structural properties of matter. In this context, X-ray absorption spectroscopy (XAS) can have an important and complementary role to diffraction techniques because, probing selectively the local environment around the photoabsorber atom, it is able to distinguish chemical-order from chemical-disorder over a short length scale.

The first structural studies of GaP showed that the high pressure phase had a β-Sn structure[10,11]. A following XAFS study[12] used a model based on the β-Sn structure to fit the experimental data of GaP at high pressure and found that the local environment was well reproduced with such a model, given by 4 P and 2 Ga atoms as first and second neighbors. A more recent experiment using ADXRD has shown that the actual high pressure structure of GaP has a *Cmcm* symmetry with a clear lack of long-range chemical order[7]. A first-principle study of the high pressure structural properties on several III-V compounds[3] has demonstrated that after a first phase transition to an SC16 phase, the latter becomes unstable to the β-Sn structure at 20.3 GPa and to the *Cmcm* at 20.4 GPa. However, as pressure is further increased, the β-Sn structure becomes more stable than *Cmcm*. This overview of previous work suggests conflicting results regarding the nature of the high pressure phase of GaP. In particular, it is worth noting that the structural model based on the β-Sn symmetry, which has been debated, still allowed a good fitting of EXAFS data[12].

In this contribution we present an experimental study combining ADXRD and XAS of GaP at high pressure up to 39 GPa. The aim of this work is to elucidate the high pressure phase of GaP and in particular to give an insight on the short-range chemical ordering. The paper is organized as follows: in section II we describe the experimental details of the ADXRD and XAS experiments. In section III we show the data and their qualitative evolution with pressure. In section IV we present the results deriving from full Rietveld refinement for the ADXRD data and from the EXAFS analysis for the XAS data. In section V we give details of the full multiple scattering calculations of the x-ray absorption near-edge structure (XANES) for the high pressure phase of GaP and we show the comparison with the experimental data. Finally, in section VI we discuss the results and give several conclusions.

II. EXPERIMENTAL

The XRD and XAS experiments have been both carried out at the European Synchrotron Radiation Facility at beamlines ID30 and ID24 respectively. The pressure was generated using a Le Toullec-type and a Chervin-type diamond anvil cells for the XRD and XAS experiments respectively, equipped with standard diamonds of 320 μm diameter flat. A fine powder of GaP ground from polycrystalline stock (Alfa Aesar, purity 99.999%) was loaded

in a stainless steel gasket with a hole of 120 μm of diameter and an initial thickness of 30 μm together with a 4:1 mixture of methanol:ethanol as pressure transmitting medium and a ruby sphere for the pressure measurements[13]. The data were recorded at room temperature. The maximum pressure reached was 39 GPa. For the XRD experiment the wavelength selection was made using a Si (111) monochromator tuned to $\lambda = 0.3738$ Å. Patterns were recorded using a MAR345 image plate detector with 100 μm pixel resolution. The sample-detector distance was calibrated by a Si-filled gasket at the sample position. Two-dimensional image plate data were corrected for spatial distortion and integrated with FiT2D to produce a 2θ-I pattern[14].

The XAS data were recorded at the gallium K-edge (E = 10.367 keV). The beam was focussed horizontally by a curved polychromator Si(111) crystal in a Bragg geometry and vertically with a bent Si mirror placed at 2.8 mrad respect to the direct beam[15]. The Bragg diffraction peaks arising from the diamond anvils were removed from the energy range of interest by changing the orientation of the diamond anvil cell and following in real time the intensity of the transmitted beam on a 2-dimensional detector. In this case the Bragg reflections limited the k range of the spectra to ~ 11 Å^{-1}. Although we performed two distinct experiments, the loading conditions (diamonds flats, sample thickness, pressure transmitting medium) were kept the most similar as possible for the two experiments. The only remarkable difference between the two loadings was the position of the ruby sphere that was placed in the center and off-center of the sample for the XRD and XAS experiments respectively. This was necessary for the XAS experiment to avoid any interaction between the x-ray beam and the ruby, detrimental to the data quality.

III. DATA EVOLUTION WITH PRESSURE

Figure 1 shows some ADXRD data at selected pressures. At room pressure GaP crystallizes in a ZB structure. The onset of the phase transition is at 31 GPa with the appearance of new Bragg reflections at $2\theta \sim 9°$ and 12.7°, indicated by arrows in the pattern at 32 GPa of Fig. 1. At 39 GPa the transition is almost complete although the (111) reflection corresponding to the ZB structure at $2\theta \sim 7°$ is still detectable. Figure 2 shows some XAS data at some selected pressures and the extracted kχ(k) signals. For this set of data we observe that the onset of the phase transition is at 26 GPa and at 31 GPa the transition is

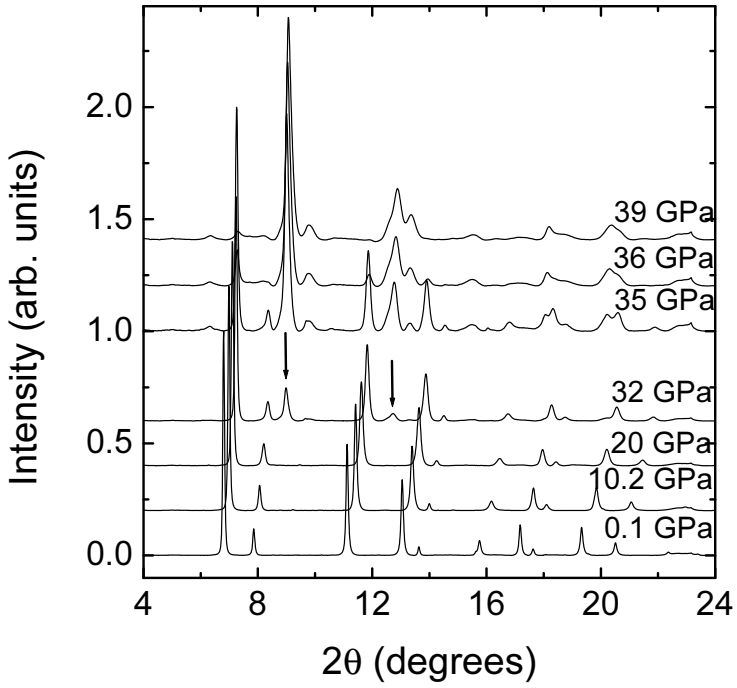

FIG. 1: Background subtracted XRD data at selected pressures. The arrows indicate the new Bragg reflections relative to the high pressure phase of GaP (GaP-II).

complete.

The difference in the transition pressure depends on the position of the ruby chip for the pressure measurements. In the XAS data the chip has been placed off center to avoid any interaction between the x-ray beam and the sample resulting in a erroneous normalization of the XAS spectra. As a consequence of this, the pressure is underestimated for the XAS data points. The change in the main frequency of the oscillations from 1.3 GPa to 39 GPa reflects the different local environment around Ga when going from a ZB structure with 4 P first neighbors to a structure with different local symmetry. The data at 28 GPa well describes the mixture of the two phases.

IV. QUANTITATIVE ANALYSIS

The experimental spectra were analyzed using the Rietveld refinement method[16]. The full-profile refinement was performed using the GSAS[17] package. The background of the spectra was fitted using Chebyshev polynomials of the first kind. The peak profile fitting

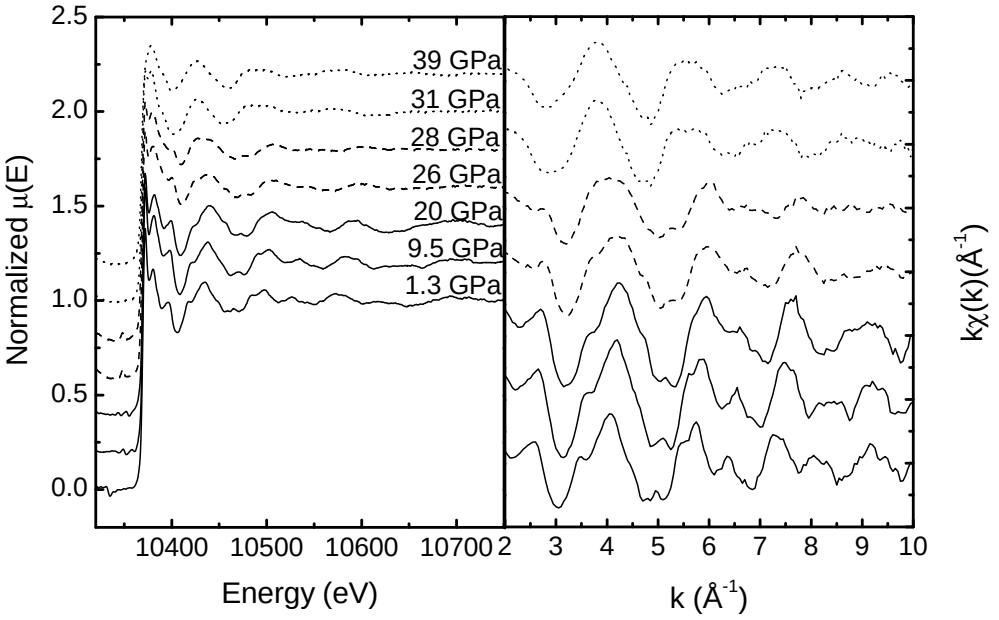

FIG. 2: *Left panel:* Normalized XAS spectra of GaP at selected pressures. *Right panel:* corresponding extracted kχ(k) EXAFS signals. The spectra drawn in continous line correspond to the GaP-I, in dashed line to the mixed GaP-I/GaP-II, and the dotted line to the GaP-II.

was based on pseudo-Voigt functions. Moreover, preferred orientation correction was taken into account using the spherical harmonics functions.

The EXAFS data analysis has been performed using the codes from the UWXAFS package[18]. The experimental XAFS functions χ(k), were obtained after subtracting the embedded-atom absorption background from the measured absorption coefficient and normalizing by the edge step using the program ATHENA[19]. Phase shifts for photoabsorber and backscatterer atoms have been calculated by FEFF8[20] using a self-consistent energy dependent exchange correlation Hedin-Lundqvist potential. Structural data for the GaP phases used by the ATOMS program[21] to prepare the input for FEFF8 were taken from ref. 22 for the ZB structure, from the Rietveld refinement of ADXRD data for the *Cmcm* structure and from the structural parameters of Itié *et al.*[12] for the β-Sn.

A. GaP-I

The ADXRD data from ambient pressure to 30.2 GPa were Rietveld refined in order to obtain the variation of the cell parameter of GaP in the ZB structure as a function of pressure. Figure 3*a)* shows the data and the Rietveld fit of the data at 12.6 GPa. The lattice parameter measured at ambient pressure was 5.455 Å.

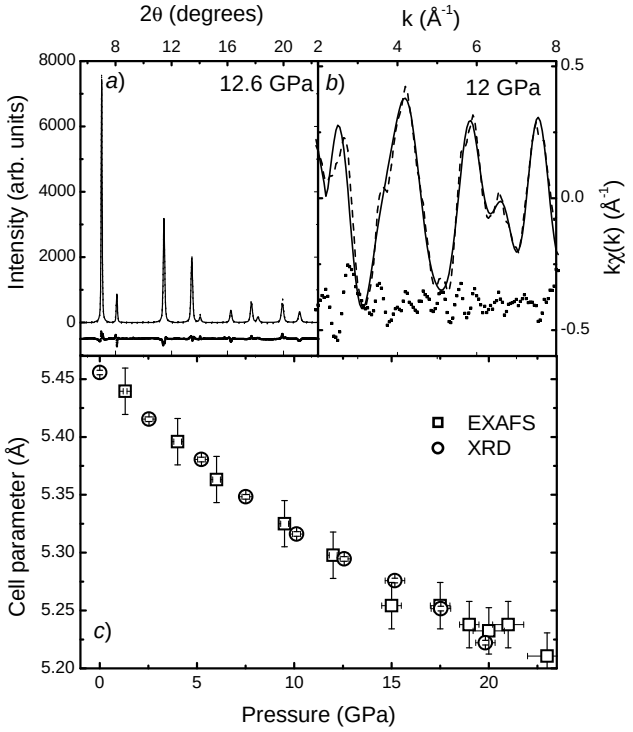

FIG. 3: *a)* Rietveld fit of XRD data at 12.6 GPa. *b)* XAS data and fit (dashed and continous lines respectively) at 12 GPa. The bottom dotted line is the residual function. *c)* Evolution as a function of pressure of the cell parameters of GaP-I as obtained from Rietveld refinement (circles) and calculated from the bond distances values obtained from the EXAFS analysis (squares).

The EXAFS data from 0.4 GPa to 23 GPa were also fitted using the structural model based on a ZB structure obtained from diffraction. The k-range of the experimental EXAFS function χ(k) limited the number of structural parameters that could be left free during the minimization procedure. The fits were performed using the theoretical signals relative to single scattering between the photoabsorber and the first 3 neighbors shells constraining the distances to the crystallographic structure. Figure 3*b)* shows the XAS data and the fit

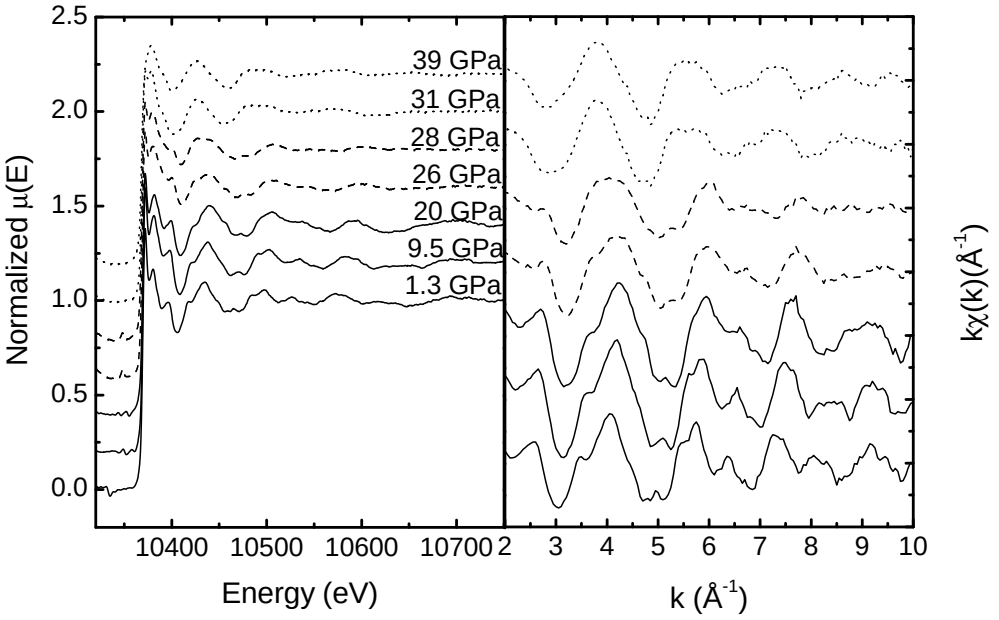

FIG. 2: *Left panel:* Normalized XAS spectra of GaP at selected pressures. *Right panel:* corresponding extracted kχ(k) EXAFS signals. The spectra drawn in continous line correspond to the GaP-I, in dashed line to the mixed GaP-I/GaP-II, and the dotted line to the GaP-II.

was based on pseudo-Voigt functions. Moreover, preferred orientation correction was taken into account using the spherical harmonics functions.

The EXAFS data analysis has been performed using the codes from the UWXAFS package[18]. The experimental XAFS functions χ(k), were obtained after subtracting the embedded-atom absorption background from the measured absorption coefficient and normalizing by the edge step using the program ATHENA[19]. Phase shifts for photoabsorber and backscatterer atoms have been calculated by FEFF8[20] using a self-consistent energy dependent exchange correlation Hedin-Lundqvist potential. Structural data for the GaP phases used by the ATOMS program[21] to prepare the input for FEFF8 were taken from ref. 22 for the ZB structure, from the Rietveld refinement of ADXRD data for the *Cmcm* structure and from the structural parameters of Itié *et al.*[12] for the β-Sn.

A. GaP-I

The ADXRD data from ambient pressure to 30.2 GPa were Rietveld refined in order to obtain the variation of the cell parameter of GaP in the ZB structure as a function of pressure. Figure 3*a)* shows the data and the Rietveld fit of the data at 12.6 GPa. The lattice parameter measured at ambient pressure was 5.455 Å.

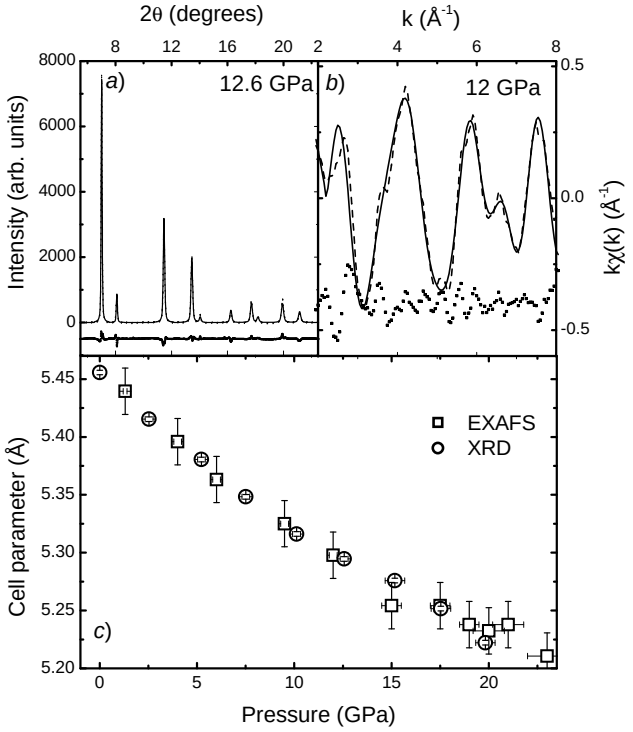

FIG. 3: *a)* Rietveld fit of XRD data at 12.6 GPa. *b)* XAS data and fit (dashed and continous lines respectively) at 12 GPa. The bottom dotted line is the residual function. *c)* Evolution as a function of pressure of the cell parameters of GaP-I as obtained from Rietveld refinement (circles) and calculated from the bond distances values obtained from the EXAFS analysis (squares).

The EXAFS data from 0.4 GPa to 23 GPa were also fitted using the structural model based on a ZB structure obtained from diffraction. The k-range of the experimental EXAFS function χ(k) limited the number of structural parameters that could be left free during the minimization procedure. The fits were performed using the theoretical signals relative to single scattering between the photoabsorber and the first 3 neighbors shells constraining the distances to the crystallographic structure. Figure 3*b)* shows the XAS data and the fit

at 12 GPa. Figure 3*c)* shows the evolution as a function of pressure of the cell parameter of GaP-I as obtained from the Rietveld refinement (circles) and calculated from the bond distances values obtained from the EXAFS analysis.

B. GaP-II

The ADXRD data at 39 GPa show that the GaP-I to GaP-II transition is almost complete although the (111) reflection of the ZB can still be identified at $\sim 7°$. The pattern at 39 GPa could be indexed using a *Cmcm* phase and a ZB fraction below 10 %. The resulting fit is illustrated in Fig. 4.

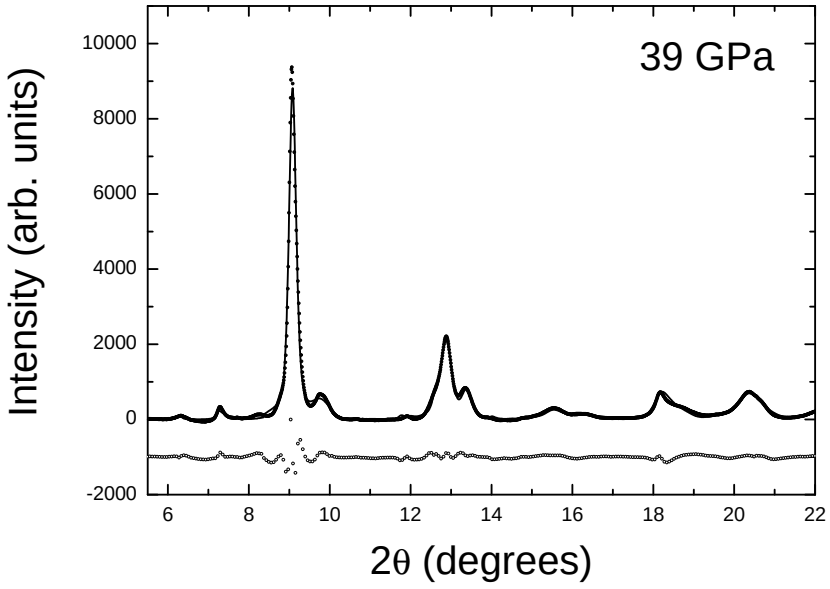

FIG. 4: Rietveld fit (continous line) of the experimental spectrum (dotted line) at 39 GPa. The bottom curve is the residual function. Two phases are taken into account: the ZB and the *Cmcm*.

The lattice parameter of the ZB structure at 39 GPa is 5.080(4) Å. The refinement of the *Cmcm* phase at 39 GPa gives a = 4.679(5) Å, b = 4.933(6) Å and c = 4.728(5) Å. The internal coordinates are y(Ga/P) = 0.661(7), y(Ga/P) = 0.189(7). The absence of the (111) reflection and the weakness of the (110) at $2\theta \sim 6.3°$ suggest that the structure lack of long-range site order.

The analysis of the EXAFS data of GaP in the high pressure region presents an intriguing scenario. In fact, the EXAFS data reported in ref. 12 could be fitted using a model based

on a β-Sn structure for GaP-II that was the only structural model proposed at that time. Nevertheless, in the present work we claim, in agreement with Nelmes *et al.*[7], that the structure is not β-Sn, but has a *Cmcm* symmetry. We use EXAFS to distinguish β-Sn from *Cmcm*, assuming for the latter a chemically ordered environment. We shall then show from XANES analysis that this assumption is correct.

The local environment of Ga in GaP in an ordered *Cmcm* structure as from the structural parameters reported in this work and in a β-Sn structure as reported by Itié *et al.*[12] are given in table I. While in the β-Sn structure the photoabsorber presents two well defined shells of

β-Sn			***Cmcm***		
atom	dist. (Å)	deg.	atom	dist. (Å)	deg.
P	2.41	4	P	2.33	1
Ga	2.44	2	P	2.34	2
			P	2.48	2
			P	2.60	1

TABLE I: Atomic cluster surrounding the Ga atom for GaP in β-Sn and *Cmcm* structures within a distance of 2.7 Å.

P and Ga respectively in the *Cmcm* structure the photoabsorber is surrounded by 6 P atoms at distances between 2.33 Å and 2.60 Å. In Fig. 5*a)* we show the calculated k$\chi(k)$ signals relative to the single scattering Ga-P signal at 2.41 Å and to the Ga-Ga signal at 2.44 Å corresponding to the β-Sn local environment. The lower curve represents the sum of the two signals. Figure 5*b)* shows the calculated k$\chi(k)$ signals relative to the Ga-P single scattering signals at the four different distances reported in table I and the lower curve represents the sum. In Fig. 5*c)* the two sum curves are compared directly. It is interesting to notice that up to k $\simeq$ 6 Å^{-1}, besides a small difference in the overall amplitude, the two calculated curves present a similar main frequency, whereas at higher k the difference between the two curves becomes more important and a fitting over the shown k-range should be able to discriminate between the two models. The two compared curves are the sum of calculated k$\chi(k)$ signals where no Debye-Waller factor is included and no fitting is performed.

On the basis of the calculations of the theoretical signals discussed above the fitting of the data at 37.5 GPa was performed using the two structural models. All the results are

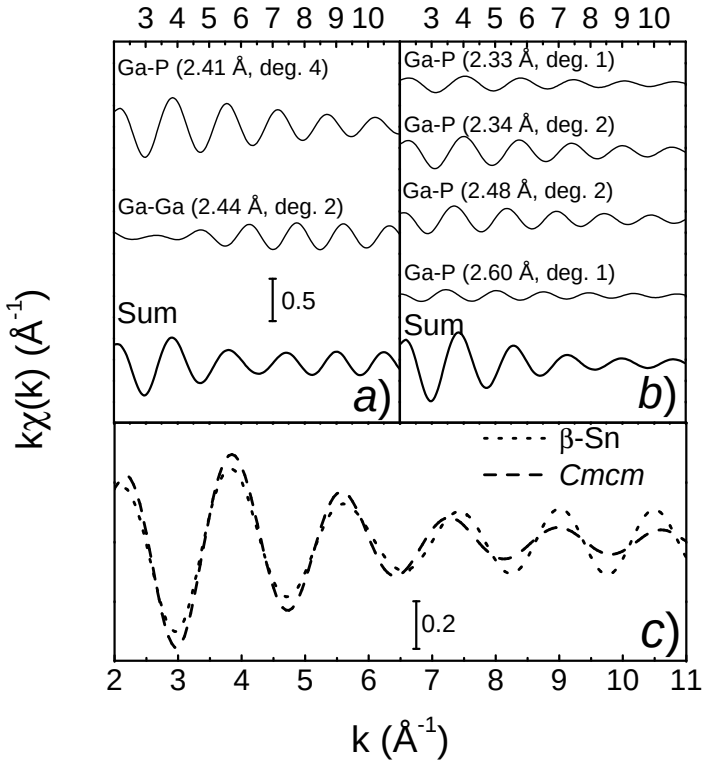

FIG. 5: *a)* Calculated k$\chi(k)$ relative to the Ga-P single scattering at 2.41 Å and to the Ga-Ga at 2.44 Å corresponding to the β-Sn local environment. The lower curve represent the sum of the two signals. *b)* Calculated k$\chi(k)$ relative to the Ga-P single scattering at the four different distances reported in table I corresponding to the *Cmcm* local environment. The lower curve represents the sum. *c)* Comparison between the two sum curves.

summarized in table II. For the β-Sn model two scattering signals were used, corresponding to 4 P atoms at 2.41 Å and 2 Ga atoms at 2.44 Å as nearest neighbors. Leaving the Ga-P and the Ga-Ga distances together with their relative Debye-Waller factors as free parameters (fit β-free on table II) yields Ga-P and Ga-Ga distances not compatible with a β-Sn structure and non physical values for the Debye-Waller factors. In order to guarantee a local environment compatible with a β-Sn structure we constrained the two distances Ga-P and Ga-Ga to vary with the same ΔR (fit β-constrained on table II) and we left the Debye-Waller factors as free parameters. In this case the Ga-Ga signal is over-damped leading to a zero contribution of such a signal in the fitting of the experimental XAFS.

For the *Cmcm* model we have approximated the distribution of the first 6 P atoms as

two groups of 3 atoms at two different distances [1]. The structural parameters are reported in table II. Figure 6 reports the fit using the *Cmcm* models. Although the residual function

	R_{Ga-P} (Å)	σ^2_{Ga-P} (Å^2)	N_P	R_{Ga-Ga} (Å)	σ^2_{Ga-Ga} (Å^2)	N_{Ga}	$\mathcal{R}$-factor
β-free	2.35(1)	-0.004(1)	4	2.32(1)	-0.002(1)	2	1.5%
β-constrained	2.38(1)	0.005(1)	4	2.41(1)	0.2(2)	2	2.5%
Cmcm	2.34(1)	0.006(2)	3				1.5%
	2.44(2)	0.007(3)	3				

TABLE II: Structural parameters obtained from the fitting of the experimental data at 39 GPa using the model based on the β-Sn and *Cmcm* structures.

(Figure 6) left panel, bottom curve) contains frequencies associated to higher distances shells and to multiple scattering contributions, the first peak of the Fourier transform is well reproduced by the best-fit calculation using 2 Ga-P single shells scattering signals. Therefore, the results of the fitting show that the β-Sn structure must be ruled out and GaP crystallizes with a *Cmcm* symmetry above 30 GPa. In order to confirm our results we also performed an additional analysis of the XANES part of the absorption spectra.

V. XANES SIMULATIONS

The low energy part of a XAS spectrum (XANES region) is extremely sensitive to the structural details around the absorbing site such as overall symmetry, distances and bond angles, and therefore a full retrieval of the geometrical structure within 6-7 Å from the absorbing site can in principle be obtained from the experimental XANES spectra. However, the quantitative analysis of this region presents difficulties mainly related to the theoretical approximation in the treatment of the potential and the need for heavy time consuming algorithms to calculate the absorption cross section in the framework of a full multiple scattering approach. Therefore, we have compared qualitatively our data to *ab-initio* simulations obtained by performing full multiple scattering calculations using the FEFF8 package[20].

[1] Although at this pressure a fraction of the ZB phase may still be present, as evidenced by ADXRD, the addition of the ZB contribution does not affect the fitting, when the *Cmcm* model is used.

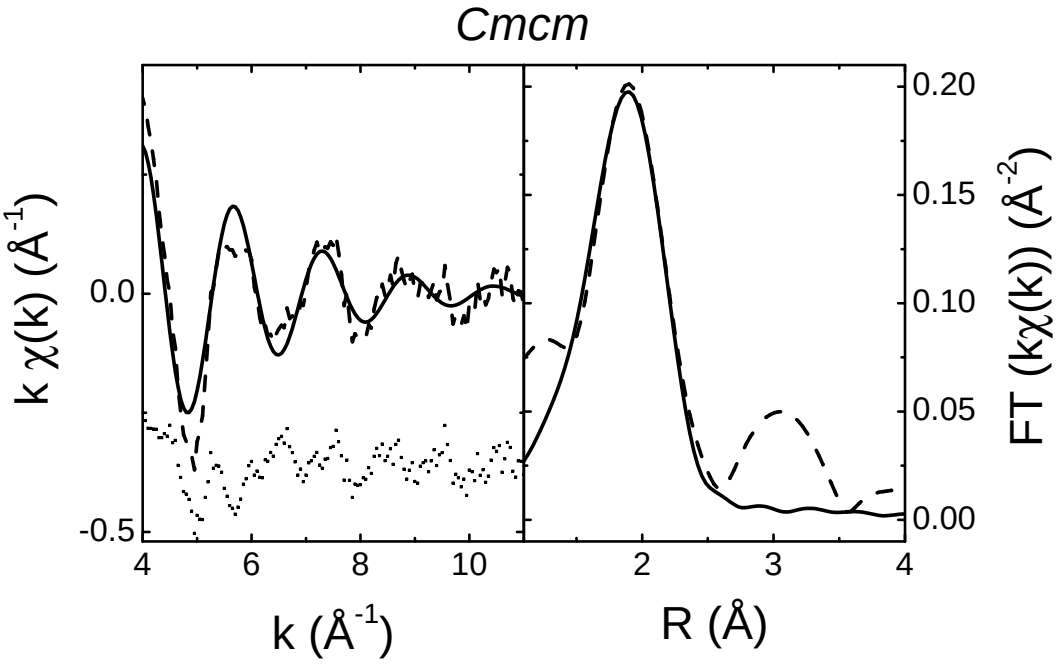

FIG. 6: *Left panel:* Comparison between the experimental EXAFS spectrum at 37.5 GPa (dashed curve) and the best-fit calculation (solid curve) corresponding to a *Cmcm* environment. The bottom dotted curve shows the residual function. *Right panel:* Comparison between the modulus of the Fourier transform of the experimental EXAFS spectrum at 37.5 GPa (dashed curve) and the modulus of the Fourier transform of the best-fit calculation (solid curve).

A. Method of calculation

We used a self-consistent energy dependent exchange correlation Hedin-Lundqvist potential to simulate the XANES of the high pressure GaP. Self-consistency was obtained by successively calculating the electron density of states, electron density and Fermi level at each stage of the calculation within a cluster centered on the atom of 5.30 Å (56 atoms) and 5.15 Å (34 atoms) of radius for β-Sn and *Cmcm* structures respectively, and then iterating. Full multiple scattering XANES calculations up to a photoelectron wavevector value of k = 6 $Å^{-1}$ (corresponding to a photoelectron energy of about E $\sim$ 130 eV) were carried out for a larger cluster of atoms centered on the photoabsorber of a radius of 6.0 Å (69 atoms) and 6.7 Å (84 atoms) for for β-Sn and *Cmcm* structures respectively. All multiple-scattering paths within these clusters were summed to infinite order. Besides the structural informa-

tion defining the geometry of the cluster, the only external parameters used as input for the simulations were a constant experimental broadening and an offset in the energy scale. No thermal or static disorder factor was added to the simulations.

We performed simulations for the different observed high pressure phases for GaP: i.e. β-Sn and *Cmcm*. For the β-Sn structure the cluster was built using structural parameters calculated from the Ga-Ga and Ga-P bond distances obtained by Itié *et al.*[12] and assuming that those distances corresponded to a tetragonal cell of space group *I-4m2* with two internal atomic position at (0, 0, 0) and (0, 1/2, 1/4). The resulting cell parameters were $a = 4.663$ Å and $c = 2.44$ Å. For the *Cmcm* structure we built ordered as well as disordered clusters. In the former case the composition of each coordination shell was determined by the space group symmetry and by the cell internal site occupation of each atom, as defined by a long range site ordered structure and as obtained by the Rietveld refinement of the ADXRD data. In the latter case, chemically disordered local environments around the absorber atom were approached by randomly mixing the chemical composition of each coordination shell in the chemically ordered clusters. To obtain a simulated XANES spectrum that took into account a random disorder of the structure we used the following strategy. We ran first a FEFF calculation on two chemically disordered clusters: say $d1$ and $d2$. We averaged the two calculated spectra and obtained $ave2$ ($ave2 =< d1, d2 >$). On a third chemically disordered cluster we simulated a third XANES spectrum: say $d3$. We averaged the three spectra to obtain $ave3 =< d1, d2, d3 >$ and so on. Figure 7 shows (*left panel*) some selected average spectra $ave(n)$ and $ave(n-1)$ and the corresponding differences $ave(n) - ave(n-1)$ (*right panel*). After 25 spectra calculated on 25 randomly disordered clusters, the mean value of the points distribution of $ave(n) - ave(n-1)$ was always less than 10^{-3}.

This way of proceeding assumes rigid Ga-Ga and Ga-P bond lengths. In fact, the different dimensions of the Ga and P atoms as well as the different electronegativities of the Ga-Ga and Ga-P bonds lead inevitably to different Ga-Ga and Ga-P bond lengths (bond relaxation). To take into account and to verify whether and how the effect of the bond relaxation is relevant respect to the chemical mixing, we considered one of the 40 XANES simulations performed on one disordered cluster whose difference with the average of the 40 simulations was minimum. We relaxed the Ga-Ga and Ga-P distances of several amounts from $\Delta = \pm 0.01$ up to $\Delta = \pm 0.04$. For each value of the relaxation parameter we relaxed both *i)* the whole cluster, *ii)* only the atomic positions at a distance less than 3 Å from the photoasborber. To relax

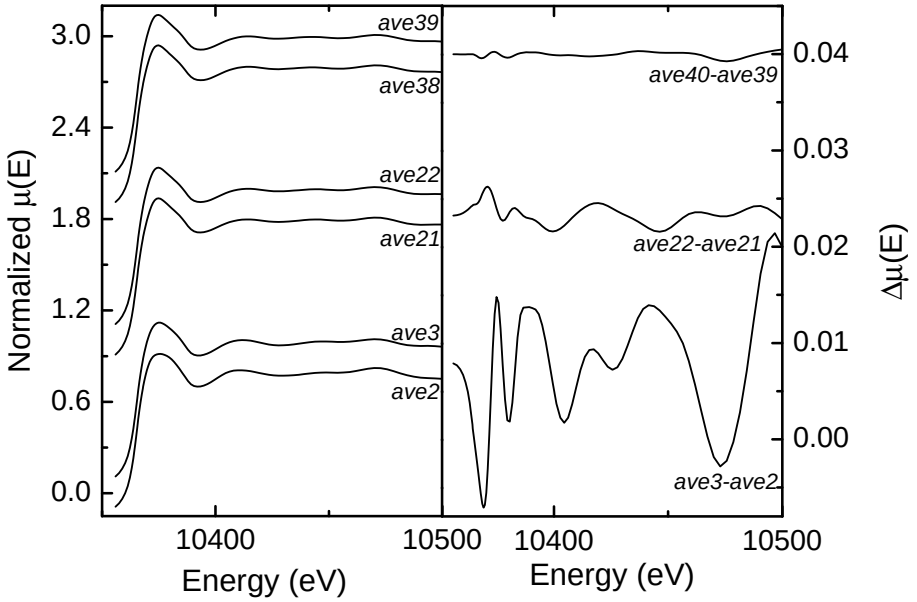

FIG. 7: *Left panel:* selected averaged spectra $ave(n)$ and $ave(n-1)$. *Right panel:* corresponding differences $ave(n) - ave(n-1)$. The mean value of the point distributions of the differences $ave(n) - ave(n-1)$ approaches to zero with the increasing number of clusters over which the averages are calculated.

the bond lengths of the requested quantity Δ we scaled the atomic coordinates of each atom such as

$$d_{Ga-Ga}^{relaxed} = d_{Ga-Ga} + \Delta$$

$$d_{Ga-P}^{relaxed} = d_{Ga-P} - \Delta$$

and such as to conserve the same bond directions as those of the non-relaxed cluster.

We found that the differences between the simulated spectra on the non-relaxed and relaxed clusters increase with the relaxation quantity Δ. For the same Δ, relaxation of the whole cluster or only for $r \leq 3$ Å from the photoabsorber, gave similar results, indicating that XANES spectra are affected mainly by the positions of the closest atoms. Figure 8 (*left panel*) shows from bottom to top the simulated spectra of GaP in the ordered *Cmcm* structure (*Cmcm*-ord), the average of 40 spectra calculated on 40 randomly disordered clusters (*ave40*), the simulated spectra on the randomly disordered cluster whose difference with the average *ave40* is minimum (*d1*) and the spectrum calculated on the same relaxed cluster (*d1rel*) (whole cluster relaxed, $\Delta = \pm 0.04$ Å). On the right panel of Fig. 8 we plot

the differences between the spectra of the left panel. The difference between the rigid and the relaxed cluster (*d1-d1rel*) is about 2% of the absorption jump, whereas the difference between the chemical disordered and ordered cluster (*(Cmcm-ord)-ave40*) reaches 15% of the absorption jump. Therefore this analysis shows that the relaxation of the bond lengths has a negligible effect respect to the chemical mixing. For this reason in the following sections we will always refer to the spectrum *ave40* as a model for GaP in the disordered *Cmcm* structure.

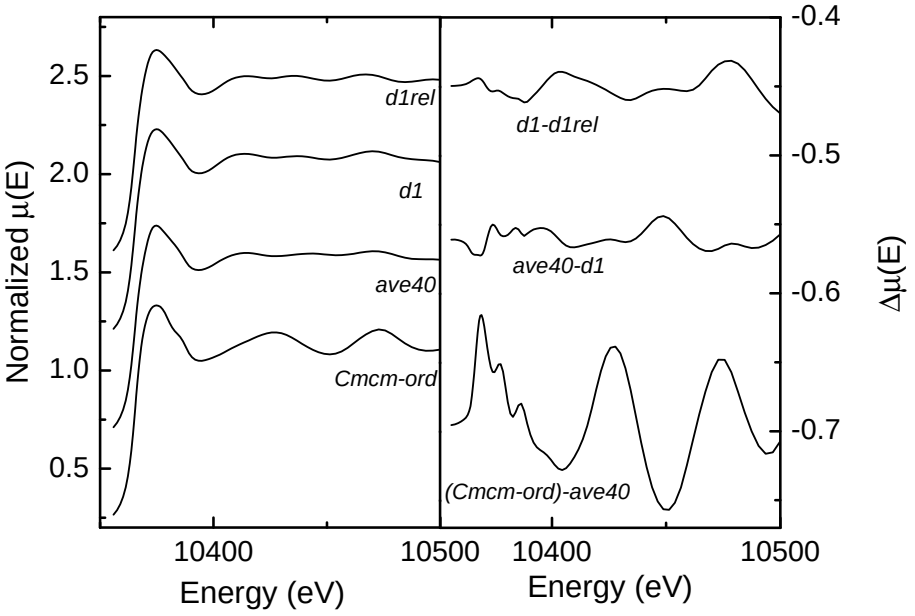

FIG. 8: *Left panel:* from bottom to top: simulated spectrum of GaP in the ordered *Cmcm* structure (*Cmcm*-ord). Average of 40 spectra calculated on 40 randomly disordered clusters (*ave40*). Simulated spectrum on a randomly disordered cluster whose difference with the average *ave40* is minimum (*d1*). Spectrum calculated on the same relaxed cluster (*d1rel*) (whole cluster relaxed, $\Delta = \pm 0.04$ Å). *Right panel:* Difference spectra: from bottom to top: ((*Cmcm*-ord)-*ave40*), *ave40-d1*, *d1-d1rel*.

B. Results

Figure 9 shows from bottom to top the simulated spectra of GaP in the β-Sn structure (spectrum *a*) and in the disordered and ordered *Cmcm* structures (spectra *b-d* and *b-o*).

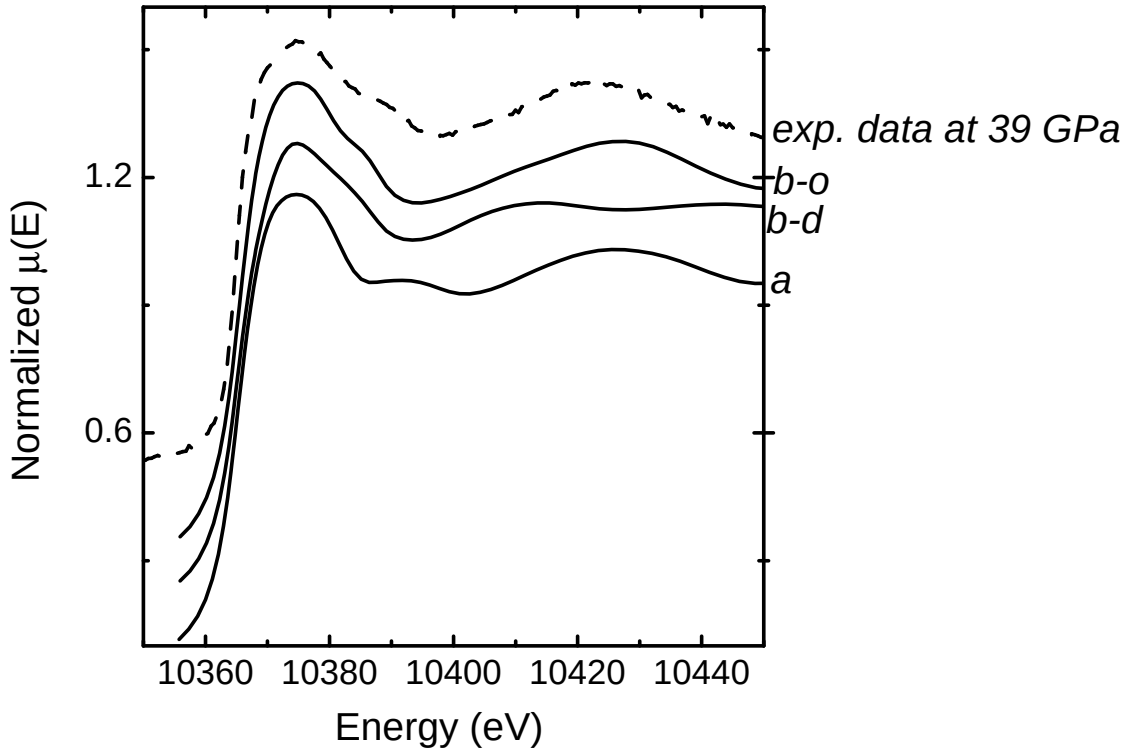

FIG. 9: *From bottom to top*: Simulated spectra of GaP in β-Sn structure (a), in disordered and ordered *Cmcm* structure (b-d and b-o) respectively, and the experimental XANES spectrum of GaP at 39 GPa. (dashed line).

At energies above 10400 eV the spectra a and b-o present similar features, while important variations can be observed just above the absorption edge. In particular the spectrum a presents a feature at $\sim$ 10390 eV that is not observed in any other simulated spectrum (nor in the experimental one). For the simulated spectra in the *Cmcm* structure, chemically mixing of each shell leads to important variations above 10390 eV. In fact, the chemical disorder (different atomic species are in the same positions) introduced with the random mixing of each coordination shell almost doubled the main frequency respect to the spectrum b-o and heavily reduced the amplitudes of the oscillations. The region just above the absorption edge presents as well differences although the shoulder at the right of the white line is common to the two spectra. The top spectrum of Fig. 9 represents the experimental XANES data at 39 GPa. The agreement with the spectrum b-o is striking considering the absence of adjustable parameters in the theory: all the features are well reproduced. The comparison

of the data with the simulated spectra excludes a chemical disorder around the Ga atom (due to the disagreement at energies above 10390 eV with spectrum *b*-*d*), and at the same time excludes the occurrence of the β-Sn structure (due to the disagreement just above the absorption edge). This result is consistent with recent XRD diffraction works[7] (including our own), which show chemical disorder on long range. Furthermore, it indicates that whereas chemical order is lost over many lattice cells, or is not detectable by long-range probing techniques (i.e. XRD), GaP on a local atomic scale does conserve a high degree of chemical order.

VI. CONCLUSIONS

In conclusion, we performed combined XRD and XAS measurements on GaP-II up to 39 GPa. XRD data showed that the GaP-II phase has a *Cmcm* symmetry in agreement with previous results. The absence of "difference reflections" indicates a lack of long range chemical order. The EXAFS analysis of data corresponding to GaP-II shows a local environment corresponding to a *Cmcm* structure. Full multiple scattering XANES calculations were used to analyze the local chemical ordering. Indeed, the comparison of the XANES spectra with multiple scattering calculation confirms unequivocally the occurrence of a *Cmcm* symmetry with a high degree of local chemical ordering. This means that, notwithstanding the low ionicity of this compound, this parameter dictates the short range interaction even at high pressures. The local environment of Ga in GaP-II is given by 6 P neighbors and short-range Ga-Ga interactions are not likely to occur in this system at least up to 39 GPa. We have also shown that the relaxation of Ga-P and Ga-Ga distances in the disordered clusters has a negligible effect on the XAS data with respect to that of chemical disorder.

Acknowledgments

We acknowledge the European Synchrotron Radiation Facility for provision of beamtime through the project HS2103. The experiment at ID30 has been performed during in-house research time. We are also grateful to Sebastien Pasternak for technical support during the

experiment at ID24.

---

* Electronic address: aquilanti@esrf.fr

[1] R. J. Nelmes and M. I. McMahon, J. Synchrotron Rad. **1**, 69 (1994).

[2] A. Mujica, R. J. Needs, and A. Munõz, Phys. Rev. B **52**, 8881 (1995).

[3] A. Mujica and R. J. Needs, Phys. Rev. B **55**, 9659 (1997).

[4] V. Ozoliņš and A. Zunger, Phys. Rev. Lett. **82**, 767 (1999).

[5] K. Kim, V. Ozoliņš, and A. Zunger, Phys. Rev. B **60**, 8449 (1999).

[6] J. C. Phillips, *Bond and Bands in Semiconductors* (Academic Press, New York and London, 1973).

[7] R. J. Nelmes, M. I. McMahon, and S. A. Belmonte, Phys. Rev. Lett. **79**, 3668 (1997).

[8] M. Mezouar, H. Libotte, S. Députier, T. Le Bihan, D. Häusermann, Phys. Status Solidi B **211**, 395 (1999).

[9] M. Mezouar, T. Le Bihan, H. Libotte, Y. Le Godec and D. Häusermann, J. Synchrotron Rad. **6**, 1115 (1999).

[10] M. Nelmes and A. L. Ruoff, J. Appl. Phys **53**, 6179 (1982).

[11] J. Z. Hu, D. R. Black, and I. L. Spain, Solid State Commun. **51**, 285 (1984).

[12] J. P. Itié, A. Polian, C. Jauberthie-Carillon, E. Dartyge, A. Fontaine, H. Tolentino, and G. Tourillon, Phys. Rev. B **40**, 9709 (1989).

[13] R. A. Forman, G. J. Piermarini, J. D. Barnett, and S. Block, Science **176**, 284 (1972).

[14] A. P. Hammersley, S. O. Svensson, A. Thompson, H. Graafsma, Å. Kvick, and J. P. Moy, Rev. Sci. Instrum. **66**, 2729 (1995).

[15] S. Pascarelli, O. Mathon, and G. Aquilanti, J. All. Comp. **362**, 33 (2004).

[16] H. M. Rietveld, Acta Cryst. **22**, 151 (1967).

[17] A. C. Larson and R. B. Von Dreele, Los Alamos National Laboratory Report LAUR 86-748 (2004).

[18] E. A. Stern, M. Newville, B. Ravel, Y. Yacoby, and D. Haskel, Physica B: Condensed Matter **208-209**, 117 (1995).

[19] B. Ravel and M. Newville, Physica Scripta p. To be published (2005).

[20] A. L. Ankudinov, B. Ravel, J. J. Rehr, and S. D. Conradson, Phys. Rev. B **58**, 7565 (1998).

[21] B. Ravel, J. Synchrotron Rad. **8**, 314 (2001).

[22] P. Deaus, U. Voland, and H. A. Schneider, Phys. Stat. Sol., Sect. A: Appl. Res. **80**, 29 (1983).

3.7 Stability range of the $NaCl$ structure

As illustrated in section 3.5 the transition pressure from the $NaCl$ to the $Cmcm$ structure increases with the charge transfer. We performed calculations in order to evaluate the stability range of the $NaCl$ structure. Figure 3.4 shows that there exists a limiting value of the charge transfer which determines the existence of the $NaCl$ structure. Above this value the $NaCl$ structure is stable on a limited pressure range. The more ionic the compound the wider the stability range. This conclusion is in agreement with the work of Ozolins *et al.*. Ionicity is the driving parameter of the structural systematics of III-V semiconductors. Both GaP and $InAs$ phase diagrams agree with this theoretical approach : an $NaCl$ structure is observed in $InAs$, the most ionic compound, and absent in GaP, the least ionic compound.

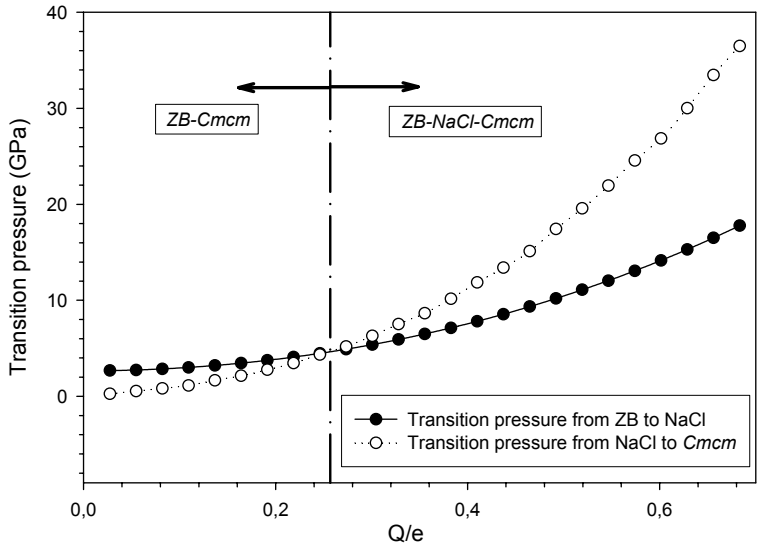

Figure 3.4: Evolution of the transition pressures, ZB-to-Cmcm and NaCl-to-Cmcm.

3.8 Non-hydrostatic effects

3.8.1 Introduction

High pressure experiments are assumed to be performed under hydrostatic conditions, i.e. isotropic pressure. However, the opposed anvils produce uniaxial force. The pressure transmitting medium[4] is required to insure a hydrostatic transmission of the pressure to the sample.

Non-hydrostatic contributions inevitably complicate the interpretation of the experiments under pressure. Even if the experimental set-ups are conceived to minimize them, they may have qualitative effects in special conditions[5]. With the advances of the high-resolution ADXRD, EXAFS, ...such effects become observable and quantifiable. The use of nitrogen, helium or argon allows to work at higher pressure keeping good experimental conditions. However, they require more complicated methods for the loading of the cell. Such parasitic effects have been ignored for a long time. The quantitative analysis of their influence on the high-pressure phase diagrams is limited to few examples [7, 69, 70, 71, 72, 27].

[4]This could be the sample itself

[5]Vitreous transition occurring in ethanol-methanol mixture or silicon oil used as pressure transmitting medium. Residual micro-strain after a first-order phase transition

The measurement of uniaxial stress has been deduced from the diffraction pattern by Singh and Kennedy [70, 71]. But even when the amount of uniaxial stress is known[6], it is complicated to theoretically calculate the precise energy differences between structures. Our own approach is based on a tight-binding model [37] which was the first step to the more accurate works using the LDA or GGA methods [73, 74, 75].

3.8.2 Macroscopic aspects

The first theoretical study of uniaxial stress was performed by Singh and Kennedy [70] in 1974. Singh updated the results in 1993 [71] based on the different possible geometrical setup of diffraction experiments. They efficiently applied a combination of the Hooke and Bragg laws to a set of randomly-oriented crystallites subject to the stress state given by

$$\sigma_{ij} = \begin{pmatrix} \sigma_1 & 0 & 0 \\ 0 & \sigma_1 & 0 \\ 0 & 0 & \sigma_3 \end{pmatrix} \tag{3.11}$$

From this expression, the fundamental parameter of the theory is defined as the uniaxial stress $t = \sigma_3 - \sigma_1$. In this case, the hydrostatic pressure is given by $\sigma_p = \left(\sigma_1 + \frac{t}{3}\right)$. For a given material, Hooke's law writes $\epsilon_{ij} = S_{ijkl}\sigma_{kl}$[7]. The total deformation related to the crystal plane, ϵ_{hkl}, is described as the sum of the hydrostatic compression, ϵ_p, and the uniaxial component, ϵ_d.

$$\epsilon(hkl) = \epsilon_p + \epsilon_d \tag{3.12}$$

This study is based on the two limiting cases characterized by either the same stress state in all the crystallites (Reuss limit) or the same strains (Voigt limit). The actual situation is obviously located between these cases. The main results of this work is the possibility to extract the maximum intensity of the uniaxial stress, t, from a plot of the experimental lattice strain, $\epsilon(hkl)$, against the parameter $\Gamma(hkl)$.

$$\Gamma(hkl) = \frac{h^2k^2 + k^2l^2 + l^2h^2}{(h^2 + k^2 + l^2)^2} \tag{3.13}$$

$$\epsilon(hkl) = \frac{a_{exp} - a_0}{a_0} \tag{3.14}$$

where a_0 and a_{exp} are the zero-pressure lattice parameter and the actual lattice parameter under pressure, respectively. In the case of the LVC experimental set-up [8] Singh and Kennedy showed that these two parameters are linked by the following equation

$$\epsilon(hkl) = \epsilon_p(hkl) - mK_1t + (1-m)t(K_2 + K_3\Gamma(hkl)) \tag{3.15}$$

where m defines the stress state of the sample[9], K_1, K_2 and K_3 are constant coefficients related to the considered material. The detailed expression is given in the paper of Singh [71] but this simplified version allows to highlight a linear relationship between $\epsilon(hkl)$ and $\Gamma(hkl)$. The slope of the $\epsilon(hkl)$-$\Gamma(hkl)$ line is directly related to the amplitude of the uniaxial stress. Obviously the value of this stress depends on the actual stress state, i.e. m. However, a maximum value of t can be computed.

[6] Through the analysis of the diffraction pattern.

[7] Using the Einstein summation convention.

[8] When the LVC experimental set-up is considered, the X-ray beam is perpendicular to the pressure axis. When a DAC set-up is considered, the X-ray beam is parallel to the pressure cell axis. The resulting expression for $\epsilon(hkl)$ as a function of $\Gamma(hkl)$ is more complicated as it depends on the diffraction angle. When the energy dispersive diffraction mode is selected, this angle is constant. The details are given in the paper of Singh[71].

[9] $m = 0$ is the iso-stress model whereas $m = 1$ is the iso-strain model

3.8.3 Tight-binding approach of the uniaxial stress

The starting point of this study is the structural distortion observed in $GaSb$ under pressure from the β-Sn to the $Imma$ structures [36]. Using different experimental conditions, non-hydrostaticity is identified to be the origin of the symmetry-breaking process. The theoretical description of the phenomenon is obviously mandatory in order to confirm this observation. As silicon exhibits both β-Sn and $Imma$ phases under hydrostatic conditions, it is a good candidate to illustrate the effects of uniaxial stress on the relative phase stability without any additional complexity brought in by ionicity.

PHYSICAL REVIEW B VOLUME 62, NUMBER 11 15 SEPTEMBER 2000-I

Pressure-induced distortion of the β-Sn phase in silicon: Effects of nonhydrostaticity

H. Libotte* and J.-P. Gaspard
Condensed Matter Physics, University of Liege (B5), B-4000 Sart-Tilman, Belgium
(Received 26 February 1999; revised manuscript received 24 January 2000)

Studies of phase transitions under pressure usually assume perfect hydrostatic conditions but it is far from being true in practice. Theoretical calculations based on a tight-binding model prove that nonhydrostatic conditions can significantly reduce the Si II to Si XI transition pressure. This distortion induced by nonhydrostaticity was already observed in high-pressure experiments (in the case of GaSb and InSb), and so this work is the theoretical confirmation of the possibility of such a phenomenon.

I. INTRODUCTION

The high-pressure behavior of silicon, germanium, and their isoelectronic compounds has been intensively studied for over 30 years[1–6] as it shows an interesting pressure-driven semiconductor-to-metal phase transition. All these experimental and theoretical works led to a structural systematics in which the β-Sn structure plays a key role for groups IV and III-V semiconductors as a first high-pressure phase.[7] However, this point was recently revised.[8–10] The β-Sn phase is only found in elemental semiconductors Sn, Si, and Ge whereas different orthorhombic distortions of the β-Sn structure are proposed for the III-V compounds. Moreover, distorted structures were observed[11] at intermediate pressures between the β-Sn structure and the hexagonal phase in the elemental semiconductors.

A perfect hydrostaticity is generally assumed in most theoretical studies as well as in high-pressure experiments with a pressure-transmitting medium. However, the pressure cells are usually uniaxial by construction and the hydrostaticity is determined by the efficiency of the pressure-transmitting medium and/or by the plastic properties of the material under study. In GaSb (Ref. 12) and InSb (Refs. 13 and 14) it was recently shown that the pressure-transmitting medium significantly influences the high-pressure phase structure. These experiments show that under hydrostatic conditions the β-Sn phase of GaSb and InSb is stable. However, in the absence of any pressure-transmitting medium, i.e., under highly uniaxial conditions, the stable phase is found to be orthorhombic. In order to confirm this observation, we performed total energy calculations using a tight-binding approximation with a repulsive potential. The relative phase stability of β-Sn and orthorhombic $Imma$ phases is studied as a function of pressure. The aim of this paper is to prove the importance of a deviation from hydrostatic conditions on the relative stability of phases under pressure.

II. METHOD OF CALCULATION

The relative stability of three phases of silicon is studied: diamond, β-Sn, and orthorhombic $Imma$. These phases are labeled Si I, Si II, and Si XI,[11] respectively. Actually the three structures can be described with an orthorhombic cell[15] using only three dimensionless parameters (Figs. 1 and 2 and Table I): the ratio of two lattice parameters c/a, b/a, and a fractional coordinate Δ.

In order to simulate nonhydrostatic conditions, we superimpose to the hydrostatic pressure a uniaxial stress successively along each of the three cell axes. These stress conditions simulate the nonhydrostatic transmission of pressure by the transmitting medium as well as the effects of residual microstrains after a phase transition. We show that a uniaxial stress along the a or b axis does not influence the relative phase stability. On the contrary, the stress along the c axis has significant effects that are discussed below.

For the sake of simplicity, the effect of a uniaxial stress along the c axis is studied on a single crystallite. Actually, as we will show later, it is the only component of the uniaxial stress that influences the relative stability of the phases.

The relative stability of two phases can be determined for given (hydrostatic) pressure and temperature conditions by a simple comparison of their Gibbs free energies $G=E+PV-TS$ per atom. Moreover, we neglect the entropic effects, i.e., the calculations are done at 0 K. Finally two terms are successively estimated: the internal energy, E, and the nonhydrostatic pressure term.

Our computational calculations are performed using a semiempirical tight-binding model in the two-center approximation. The total energy is the sum of a pairwise classical repulsion, E_{rep}, and an electronic contribution, E_{el}.

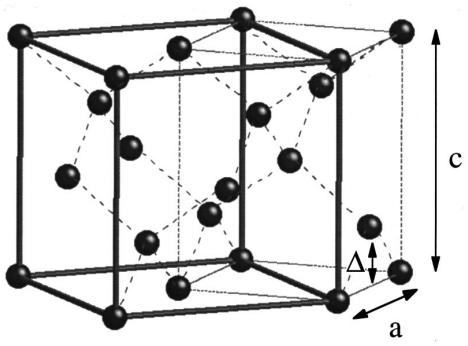

FIG. 1. Description of the diamond structure with a tetragonal cell. In the cubic system ($Fd\bar{3}m$), atoms are on the ($8a$) positions, whereas in the tetragonal system ($I4_1/amd$) they are on the ($4a$) positions with $c=\sqrt{2}a$. The thin dashed lines represent the covalent bonds between silicon atoms.

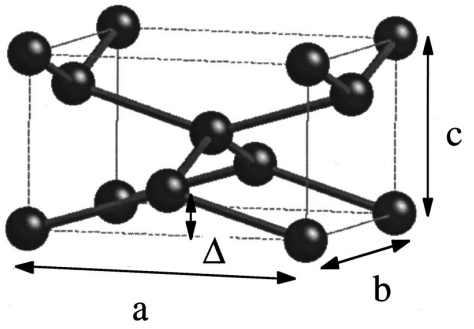

FIG. 2. Parameters used to describe the three structures studied in this work. *a*, *b*, and *c* are the lattice parameters. The atomic positions in the *Imma* orthorhombic structure are (0,0,0) and $(0,\frac{1}{2},\Delta)$.

The repulsive contribution is easy to compute and is given by

$$E_{\mathrm{rep}}=\sum_{i<j} V_{\mathrm{rep}}(r_{ij}), \tag{1}$$

where

$$V_{\mathrm{rep}}(r_{ij})=V_{\mathrm{rep},0}\left(\frac{r_{ij}}{r_0}\right)^{-p}, \tag{2}$$

r_{ij} is the distance between atom i and atom j, and r_0 is a constant taken as the interatomic distance[16] in the diamond phase of silicon at ambient pressure ($r_0=2.35$ Å). $V_{\mathrm{rep},0}$ and p are two of the semiempirical parameters adjusted to reproduce structural properties of silicon (see Sec. III).

The electronic energy is given by

$$E_{\mathrm{el}}=\int_{-\infty}^{E_F} En(E)dE \tag{3}$$

with the Fermi energy, E_F, defined by

$$N_{\mathrm{el}}=\int_{-\infty}^{E_F} n(E)dE, \tag{4}$$

where $n(E)$ is the electronic density of states and N_{el} is the number of electrons per atom. Useful techniques to estimate this integral quantity are the continued fraction[17] and recursion methods.[18]

TABLE I. Structural parameter values for the three phases (diamond, β-Sn, and orthorhombic *Imma*).

Structure	$\frac{b}{a}$	$\frac{c}{a}$	Δ
Diamond	1	$\sqrt{2}$	0.25
β-Sn	1	free [a]	0.25
Orthorhombic *Imma*	free	free	free

[a]This means that the parameter is not constrained by symmetry requirements.

The wave function of the complete system is developed on an atomic wave-function basis. The electronic Hamiltonian matrix can generally be written as

$$H_{\mathrm{el}}=\sum_{i,\mu} \epsilon_{i\mu}|\phi_{i\mu}\rangle\langle\phi_{i\mu}|+\sum_{i,\mu}\sum_{i\neq j,\nu} \beta_{ij}^{\mu\nu}|\phi_{i\mu}\rangle\langle\phi_{j\nu}|, \tag{5}$$

where $|\phi_{i\mu}\rangle$ is the atomic orbital located on site i of type μ ($\mu=s$, p_x, p_y, or p_z), $\epsilon_{i\mu}$ is the electronic level of $|\phi_{i\mu}\rangle$ (ϵ_s or ϵ_p), and $\beta_{ij}^{\mu\nu}$ is the resonance integral between $|\phi_{i\mu}\rangle$ and $|\phi_{j\nu}\rangle$. In this case, one $3s$ and three $3p$ (p_x, p_y, and p_z) atomic orbitals centered around each silicon atom are used. The zero of energies, ϵ_0, is taken at the center of gravity of s and p energy levels of silicon as

$$\epsilon_0=\frac{\epsilon_s+3\epsilon_p}{4}. \tag{6}$$

The interatomic interactions are assumed to be nonvanishing for nearest neighbors only. In addition, the atomic wave functions are supposed to be orthogonal, i.e., $\langle\phi_{i\mu}|\phi_{j\nu}\rangle=\delta_{ij}\delta_{\mu\nu}$, where δ is the Kronecker symbol.

The recursion method is basically the Lanczos algorithm[19] applied to the Hamiltonian matrix, H_{el}. It iteratively constructs a new basis where the Hamiltonian matrix H'_{el} is tridiagonal [see relation (7)]. The number of iterations depends on the level of approximation needed. In this work we stop the calculation after eight steps, which corresponds to considering four shells of neighbors (eighth-moment approximation). The diagonal and subdiagonal elements of the tridiagonal Hamiltonian matrix are the coefficients of the continued fraction, also called Green's function, given by relation (8),

$$H'_{\mathrm{el}}=\begin{pmatrix} a_1 & b_1 & 0 & & & \\ b_1 & a_2 & b_2 & 0 & & \cdots \\ 0 & b_2 & a_3 & b_3 & 0 & \\ & 0 & b_3 & a_4 & b_4 & 0 \\ \vdots & & & & \ddots & \end{pmatrix}, \tag{7}$$

$$R(z)=\cfrac{1}{z-a_1-\cfrac{b_1}{z-a_2-\cfrac{b_2}{z-\ldots}}}. \tag{8}$$

Practically, only a finite number of the Green's-function coefficients are calculated: four (a_i,b_i) pairs in this work. The continued fraction is truncated and the Green's function is therefore a ratio of two polynomials in z. The four zeros of the denominators and their weights are computed giving a set of discrete electronic energy levels. They are filled up to the Fermi level and the weighted sum of the occupied levels gives a very good approximation of the electronic contribution. Actually, this method corresponds to the four-points Gaussian integration applied to relation (3), which is known to be an efficient method for the calculations of integral properties.

The resonance integrals, $\beta_\lambda(r_{ij})$ (λ stands for the μ and ν indices and can be $ss\sigma$, $sp\sigma$, $pp\sigma$, or $pp\pi$), between neighboring atoms i and j distant of r_{ij} are assumed to have

TABLE II. Interatomic distances in diamond, β-Sn, and orthorhombic *Imma*. r_{1st}, r_{2nd}, ... are the interatomic distances between first, second, ... neighbors, respectively. N_{1st}, N_{2nd}, ... are the number of first, second, ... neighbors, respectively. All the atoms belonging to a sphere of radius 1.1 r_0 centered on a given silicon atom are written in italics.

Structure	r_{1st}	N_{1st}	r_{2nd}	N_{2nd}	r_{3rd}	N_{3rd}	r_{4th}	N_{4th}
Diamond [a]	*2.35*	*4*	3.84	12	4.50	12	5.43	6
β-Sn [b]	*2.42*	*4*	*2.57*	*2*	3.03	4	3.54	8
Orthorhombic *Imma* [b]	*2.37*	*2*	*2.47*	*2*	*2.56*	*2*	2.84	2

[a]At ambient pressure.

[b]At a pressure just above the transition pressure. Therefore, it is the longest distance between first or second neighbors that can be found in that phase as the higher the pressure, the shorter the distances.

the form proposed by Slater and Koster.[20] In addition, we assume a distance dependence given by

$$\beta_\lambda(r_{ij}) = \beta_{\lambda,0}\left(\frac{r_{ij}}{r_0}\right)^{-q}. \tag{9}$$

Now we are able to calculate the attractive part of the cohesive energy using Eq. (3). The repulsive energy between atoms i and j is added [Eq. (1)]. We assume that both attractive and repulsive energies vanish for interatomic distances greater than r_{cutoff}. This cutoff distance is taken as $1.1r_0$, which is greater than the second-neighbor distance in the β-Sn structure and the third-neighbor distance in the orthorhombic *Imma* structure (see Table II). Actually, it is the same shell of neighbors. By this way only the interactions between first neighbors are taken into account. This simplification can be justified by the strong screening effect due to the first shell of neighbors.

Now we have to add the pressure term to the internal energy in order to obtain the Gibbs free energy at 0 K. However, this form is only valid for hydrostatic conditions. In order to modify this term for nonhydrostatic compression, we use the general expression (10) largely used in thermomechanics—with the Einstein notation—to take into account the deformation contribution to G, the free energy per atom. σ_{ij} and ϵ_{ij} are the components of the stress and strain tensors, respectively. If we assume a hydrostatic compression ($\sigma_1=\sigma_2=\sigma_3$), this expression gives the well-known PV term,

$$\int_V \epsilon_{ij}\sigma_{ij}dV. \tag{10}$$

In a high-pressure experiment the stress state[21,22] of a crystallite can be written as Eq. (11) with a uniaxial stress $t=\sigma_3-\sigma_1$,

$$\sigma_{ij} = \begin{pmatrix} \sigma_1 & 0 & 0 \\ 0 & \sigma_1 & 0 \\ 0 & 0 & \sigma_3 \end{pmatrix}. \tag{11}$$

Assuming a homogeneous deformation into the sample and Eq. (11) for the stress tensor σ_{ij}, we can transform expression (10). The corrected Gibbs free energy per atom (12) is

$$G = E + PV + \gamma F_z c, \tag{12}$$

where γ (dimensionless) is the percentage of uniaxial stress and F_z the force along the c axis. F_z can be approximated by Pab, where a and b are the lattice parameters. The resulting additional stress is obviously limited by the von Mises criterion.[23] If $\gamma=0$, the nonhydrostatic pressure term vanishes and hydrostatic conditions are recovered.

Considering the equilibrium Gibbs free energy of the phases under study, we determine which one of them is the most stable. The calculation is proceeded in two steps. First we evaluate a, b, c, and Δ—with the constraints shown in Table I—from which the Gibbs free-energy minimum is obtained for both the β-Sn and orthorhombic *Imma* structures. Then the relative stability of these stable phases is directly determined by comparison.

III. RESULTS AND DISCUSSION

The parameters ϵ_s, ϵ_p, $\beta_{ss\sigma,0}$, $\beta_{sp\sigma,0}$, $\beta_{pp\sigma,0}$, $\beta_{pp\pi,0}$, $V_{\text{rep},0}$, and p are determined as follows. We fix $q=2$ as suggested by Harrison.[24] In order to determine the values of the parameters, we fit the cohesion energy, $E_{\text{coh,diam}}$, the bulk modulus at zero pressure, $B_{0,\text{diam}}$, the equilibrium volume of the diamond phase at zero pressure, $V_{0,\text{diam}}$, and the diamond-to-β-Sn transition pressure, $P_{\text{trans},I}$. Table III shows the comparison of the parameter values obtained in this work with previous ones. The structural parameters obtained here by calculations and their experimental counterparts are given in Table IV. In these calculations, the stable c/a ratios are found to be between 0.6 and 0.65. These val-

TABLE III. Comparison of tight-binding parameter values obtained in this work and in previous works for silicon.

Parameter	This work	Previous works
ϵ_s (eV)	-3.13	-4.20 [a]
ϵ_s (eV)	1.28	1.72 [a]
$\beta_{ss\sigma,0}$ (eV)	-1.55	-2.08 [a]
$\beta_{sp\sigma,0}$ (eV)	1.85	2.48 [a]
$\beta_{pp\sigma,0}$ (eV)	2.03	2.72 [a]
$\beta_{pp\pi,0}$ (eV)	-0.537	-0.72 [a]
$V_{\text{rep},0}$ (eV)	3.27	3.46 [b]
$\left(-r\frac{d\ln V_{\text{rep}}(r)}{dr}\right)_{r=r_0}$	5.07	6.18 [b]

[a]Reference 25.

[b]Reference 26.

TABLE IV. Comparison of tight-binding parameter values obtained in this work and in previous experimental works for silicon.

Parameter	This work	Previous works
$V_{0,\mathrm{diam}}$ (Å ^{3})	20.01	20.01 [a]
$B_{0,\mathrm{diam}}$ (GPa)	68.8	99.9 [c]
$E_{\mathrm{coh,diam}}$ (eV)	4.91	4.63 [d]
$P_{\mathrm{trans},I}$ (GPa)[e]	10	10.3 [b]
$\left(\frac{\Delta V}{V_0}\right)_I$ (%)[e]	14	23.8 [b]
$P_{\mathrm{trans},II}$ (GPa) [f]	27	$\approx$ 14 [c]

[a]Reference 16.
[b]Reference 11.
[c]Reference 28.
[d]Reference 27.
[e]From diamond to β-Sn.
[f]From β-Sn to orthorhombic *Imma*.

ues are very close to the experimental value of 0.55.[11]

Using these values, the energy curves $E(V)$ for the different phases are shown in Fig. 3. From the calculations it appears that the transition from the diamond to the β-Sn occurs at 10 GPa under hydrostatic conditions. All the values reported in Table III confirm that this model is qualitatively and even semiquantitatively correct.

We now show that nonhydrostaticity can induce a stabilization of a distorted phase. Therefore, we perform the calculation of the corrected free energy given by Eq. (12) for different values of γ to simulate an increasing uniaxial stress. For example, $E(V)$ curves are shown in Fig. 4 for the different phases and $\gamma=0.3$. A linear decrease of the transition pressure, P_t, with γ (see Figs. 5 and 6) is clearly observed.

The slope $dP_t/d\gamma$ is approximately -8.5 GPa. The conclusion is therefore obvious: nonhydrostatic conditions, i.e., a uniaxial stress along the *c* axis, modify the transition pressure between two very similar structures: the tetragonal β-Sn structure and an orthorhombic distortion with space group *Imma*.

It is very important to note that an uniaxial stress along the *a* or *b* axis was also considered. Nevertheless, the calculations clearly show that the relative phase stability is not influenced by these nonhydrostatic effects, i.e., no variation of the β-Sn-to-orthorhombic-*Imma* transition pressure is observed. These stress conditions only induce a tiny variation of the lattice parameters but do not change the crystal symmetry.

If we simply assume a complete random orientation of the crystallites, each of them feels a uniaxial stress component along the *c* axis. The intensity of this stress component belongs like the cosine of the angle between the *c* axis of the crystallite and the direction of the applied stress. Therefore, the spectra corresponding to this situation can be interpreted as the superposition of several spectra, each of them corresponding to a different stress state. The crystallites submitted to a strong enough uniaxial stress component along the *c* axis will undergo a phase transition from the β-Sn to the orthorhombic *Imma*. The other crystallites will obviously conserve their tetragonal symmetry. Now, the experimental spectra presented in the article of Mezouar *et al.*[12] can be easily explained. When a uniaxial stress is applied on the powdered sample, a fraction of the crystallites undergoes a β-Sn-to-*Imma* phase transition, which explains the presence of the peaks characteristic of the *Imma* phase, whereas the other part of the sample stays in the tetragonal symmetry. Moreover, depending on the orientation of each crystallite, the stress components along the *a* and *b* axes are different

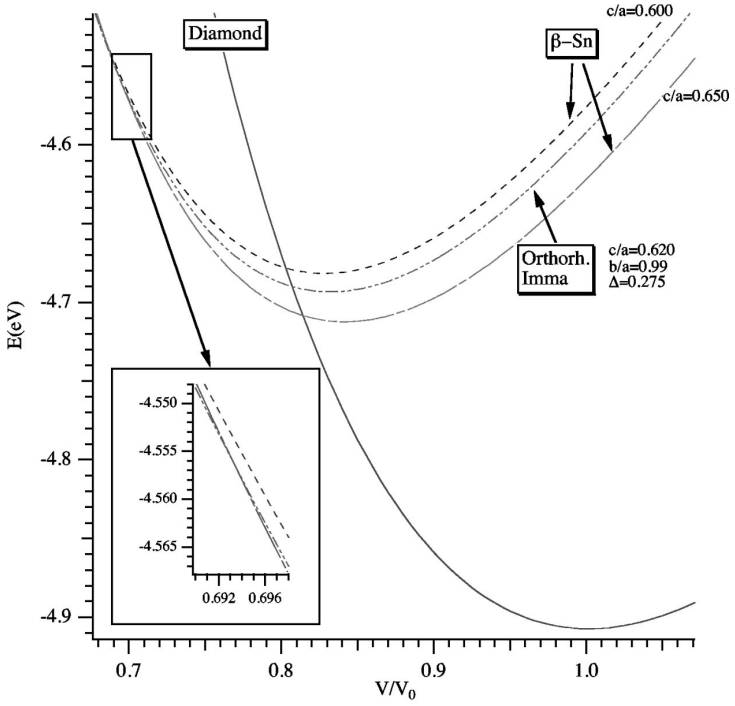

FIG. 3. $E(V)$ curves of the different phases (diamond, β-Sn, and orthorhombic *Imma*) for given sets of structural parameters c/a, b/a, and Δ under hydrostatic conditions ($\gamma=0$). The inset represents the transition zone where the orthorhombic *Imma* and β-Sn curves cross each other. V_0 is the equilibrium atomic volume at ambient conditions.

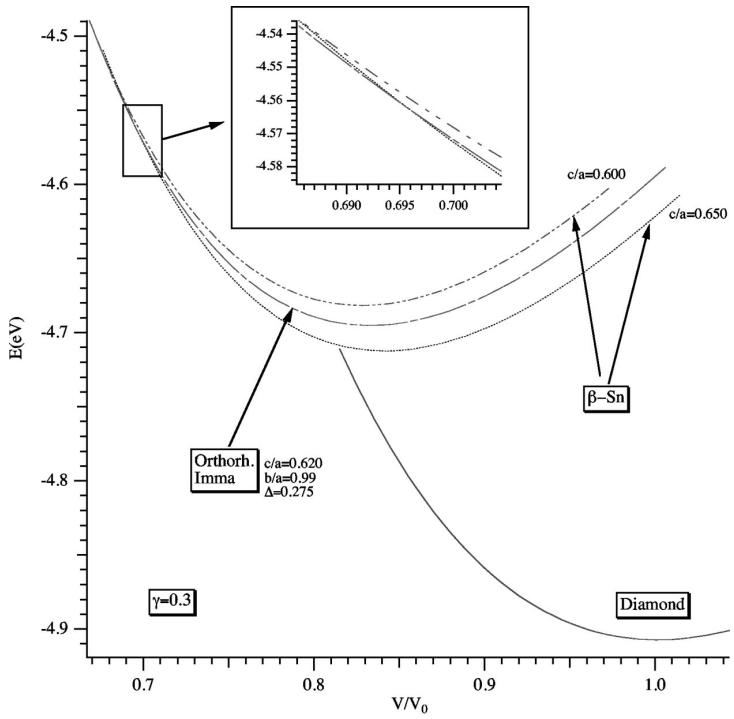

FIG. 4. $E(V)$ curves of the different phases (diamond, β-Sn, and orthorhombic *Imma*) for given sets of structural parameters c/a, b/a, and Δ under nonhydrostatic conditions ($\gamma=0.3$). The inset represents the transition zone where the orthorhombic *Imma* and β-Sn curves cross each other. V_0 is the equilibrium atomic volume at ambient conditions.

and so are the lattice parameters. Taking into account all these effects and the fact that the diffraction peaks of the β-Sn phase are very close to those of the *Imma* phase, the broad diffraction peaks experimentally observed are simply the superposition of the spectra corresponding to all these stress states. Therefore, this complicated situation can be interpreted as the stability of the *Imma* phase, but it is wrong. Actually, only a part of the sample has the orthorhombic structure and this transition is only due to the uniaxial stress.

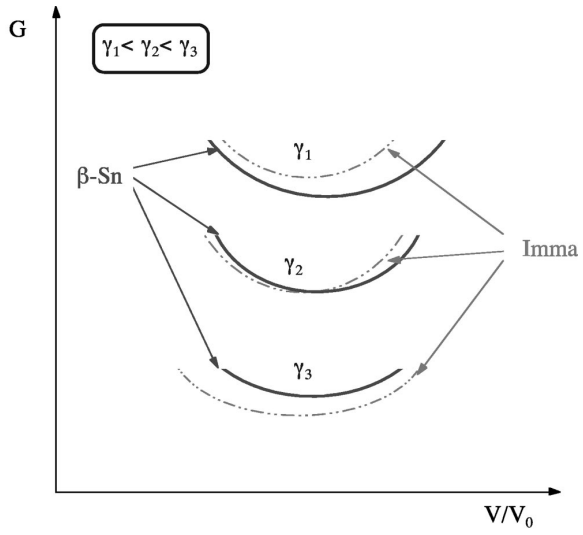

FIG. 5. Schematic view of the relative displacements of the β-Sn and orthorhombic *Imma* $E(V)$ curves for increasing values of the uniaxial stress parameter (γ) at a given pressure. The orthorhombic *Imma* energy curve goes down faster than the β-Sn curve. This corresponds to a progressive relative stabilization of the orthorhombic *Imma* phase, i.e., the β-Sn-to-orthorhombic-*Imma* transition pressure decreases with increasing γ values.

IV. CONCLUSION

The calculations presented here are the theoretical counterpart of an experimentally observed phenomenon: the stabilization of a distorted structure—orthorhombic *Imma*—under the influence of a nonhydrostatic compression in GaSb (Ref. 12) and InSb.[14] This experimental evidence indicates that our conclusions obtained for silicon should

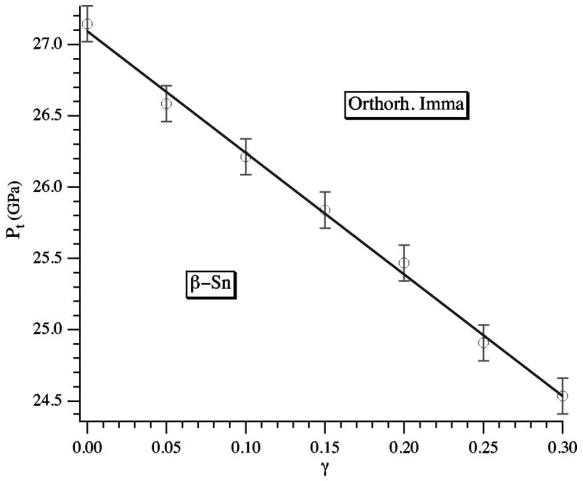

FIG. 6. Evolution of the β-Sn-to-orthorhombic-*Imma* transition pressure as a function of the uniaxial stress parameter γ. The slope is -8.5 GPa.

also apply to III-V semiconductors with a weak charge transfer. We do not claim that orthorhombic *Imma* phases or other distorted phases are only due to the nonhydrostatic conditions inside the sample, but we show they are stabilized in polycrystalline samples.

Therefore, with the advent of ultimate high-pressure studies, nonhydrostaticity—whose effects are already relevant in the 10 GPa range—can no longer be ignored. Thus it becomes essential to use a better, i.e., more hydrostatic, pressure-transmitting medium for the high-pressure experiments such as nitrogen, argon, helium, etc.

ACKNOWLEDGMENTS

We gratefully acknowledge Dr. J.-Y. Raty, M. Duflot, P. Henrotte (University of Liege, Belgium) and Dr. M. Mezouar (ESRF) for invaluable discussions. This work was supported by FNRS Grant No. 9.4565.96F.

*Corresponding author. Electronic address: h.libotte@cet.be

[1] S. Minomura and H. G. Drickhamer, J. Phys. Chem. Solids **23**, 451 (1961).
[2] A. Jayaraman, W. Klement, Jr., and J. C. Kennedy, Phys. Rev. **130**, 540 (1963).
[3] S. C. Yu, I. L. Spain, and E. F. Skelton, Solid State Commun. **25**, 49 (1978).
[4] H. Olijnyk, S. K. Sikka, and W. B. Holzapfel, Phys. Lett. **103A**, 137 (1984).
[5] J. Z. Hu, L. D. Merkle, C. S. Menoni, and I. L. Spain, Phys. Rev. B **34**, 4679 (1986).
[6] S. B. Zhang and M. L. Cohen, Phys. Rev. B **35**, 7604 (1987).
[7] J. C. Phillips, *Bonds and Bands in Semiconductors* (Academic Press, New York, 1973).
[8] M. I. McMahon and R. J. Nelmes, Phys. Status Solidi B **198**, 389 (1996).
[9] R. J. Nelmes, M. I. McMahon, and S. A. Belmonte, Phys. Rev. Lett. **79**, 3668 (1997).
[10] V. Ozolins and A. Zunger, Phys. Rev. Lett. **82**, 767 (1999).
[11] M. I. McMahon and R. J. Nelmes, Phys. Rev. B **47**, R8337 (1993).
[12] M. Mezouar, H. Libotte, S. Deputier, T. Le Bihan, and D. Hausermann, Phys. Status Solidi B **211**, 395 (1999).
[13] M. Mezouar, T. Le Bihan, H. Libotte, Y. Le Godec, and D. Hausermann, J. Synchrotron Radiat. **6**, 115 (1999).
[14] M. Mezouar and H. Libotte (unpublished).
[15] M. J. P. Musgrave, Proc. R. Soc. London **272**, 503 (1963).
[16] R. W. G. Wyckoff, *Crystal Structures* (Interscience Publishers, New York, 1963).
[17] T. J. Stieltjes, Ann. Fac. Sci. Univ. Toulouse Sci. Math. Sci. Phys. **8**, 1 (1894).
[18] R. Haydock, Solid State Phys. **35**, 215 (1980).
[19] C. Lanczos, J. Res. Natl. Bur. Stand. **45**, 255 (1950).
[20] J. C. Slater and G. F. Koster, Phys. Rev. **94**, 1498 (1954).
[21] A. K. Singh and G. C. Kennedy, J. Appl. Phys. **45**, 4686 (1974).
[22] A. K. Singh, J. Appl. Phys. **73**, 4278 (1993).
[23] R. von Mises, Z. Angew. Math. Mech. **8**, 161 (1928).
[24] W. Harrison, *Electronic Structure and the Properties of Solids* (Freeman, San Francisco, 1980).
[25] J. Robertson, Adv. Phys. **32**, 361 (1983).
[26] L. Goodwin, A. J. Skinner, and D. G. Pettifor, Europhys. Lett. **9**, 701 (1989).
[27] Ch. Kittel, *Introduction to Solid State Physics* (Wiley, New York, 1976).
[28] M. I. McMahon, R. J. Nelmes, N. G. Wright, and D. R. Allan, Phys. Rev. B **50**, 739 (1994).

3.8.4 Ab initio description of the uniaxial stress

In 2001, Cheng *et al.* [73] focused on the diamond-to-β-Sn phase transition in silicon under non-hydrostatic stress conditions. They applied a thermodynamic analysis similar to the usual enthalpy difference used in hydrostatic cases. As the uniaxial stress ($P_x = P_y \neq P_z$) is taken into account, they started their analysis from relation 3.16 which is directly derived from the second law of thermodynamics.

$$[(E_2 - E_1) + P_x(V_2 - V_1)] + \left[(P_z - P_x)\int_1^2 l_x l_y dl_z\right] = \Delta H + \bar{\Delta}W \leq 0 \tag{3.16}$$

If this condition is fulfilled, the transition from phase 1 to phase 2 takes place. The last term, called $\bar{\Delta}W$, is only equal to zero when hydrostatic conditions occur. The work performed during the transition, W, is given by

$$W = P_x\int_1^2 l_y l_z dl_x + P_y\int_1^2 l_x l_z dl_y + P_z\int_1^2 l_x l_y dl_z \tag{3.17}$$

where 1 and 2 are illustrating the limits of the lattice parameters of the phases 1 and 2, respectively. The stress state is simply given by three diagonal elements, P_x, P_y and P_z defined by

$$P_x = P_y = \frac{1}{a_{x,y}a_z}\frac{\partial E(a_x, a_y, a_z)}{\partial a_{x,y}} \tag{3.18}$$

$$P_z = \frac{1}{a_x a_y}\frac{\partial E(a_x, a_y, a_z)}{\partial a_z} \tag{3.19}$$

Even if the path selected for the integral quantity, $\bar{\Delta}W$, obviously has some influence on the result, they first selected the shortest one and found

$$\overline{\Delta}W = \frac{1}{3}(P_z - P_x)(a_{z,2} - a_{z,1})(a_{y,1}a_{x,2} + a_{x,1}a_{y,2} + 2a_{x,2}a_{y,2} + 2a_{x,1}a_{y,1}) \tag{3.20}$$

The evolution of the resulting transition pressure is roughly given by $P_z = 0.658P_x + 3.9$. For different paths giving respectively the maximum and minimum value of $\overline{\Delta}W$, the result is $0.710P_x + 3.3$ and $0.570P_x + 4.9$, respectively.

Based on the same method, Cheng [74] also studied five different phases of silicon : diamond, β-Sn, simple-hexagonal, simple-cubic, and hexagonal closed-packed structures. He clearly pointed out that uniaxial stress may drastically change the hydrostatic phase diagram. For given stress states, it is possible to observe direct phase transition from the diamond to the simple-hexagonal phase. Unfortunately, Cheng did not include $Imma$ in his study.

In 2006, Gàal-Nagy *et al.*[75] performed a similar study of the non-hydrostatic effects but they also studied the enthalpy barriers between the different phases. They obtained similar quantitative results as Cheng *et al.* even if there are few numerical discrepancies between the results.

3.8.5 Comparison with our LCAO model

Using the same model as exposed in our paper [37], the diamond-to-β-Sn transition is studied in order to evaluate our model in comparison with the latest *ab initio* calculations. As our model is based on the γ parameter, we have first to define P_x and P_z as a function of γ using

$$P_z = (1 + \gamma)P_x \tag{3.21}$$

In the previous works of Cheng *et al.* and Gaal-Nagy *et al.*, the results are usually summarized using a linear relation between P_x and P_z, i.e. $P_z = aP_x + b$. Figure 3.5 summarizes the previous works and our results in the $P_x - P_z$ plane. A fair agreement between all the results is clearly seen. Moreover, we define the average transition pressure, P_{trans},

$$P_z = \frac{2P_x + P_z}{3} \tag{3.22}$$

The evolution of P_{trans} as a function of γ is given in the same figure. The effect of uniaxial stress is clearly to reduce the transition pressure from diamond-to-β-Sn by a factor as high as 3.

The structural competition is drastically modified by a huge amount of uniaxial stress. In any case, this parasitic effect has to be avoided or, at least, minimized in order to get the most reliable observation of the phase diagram of matter under pressure.

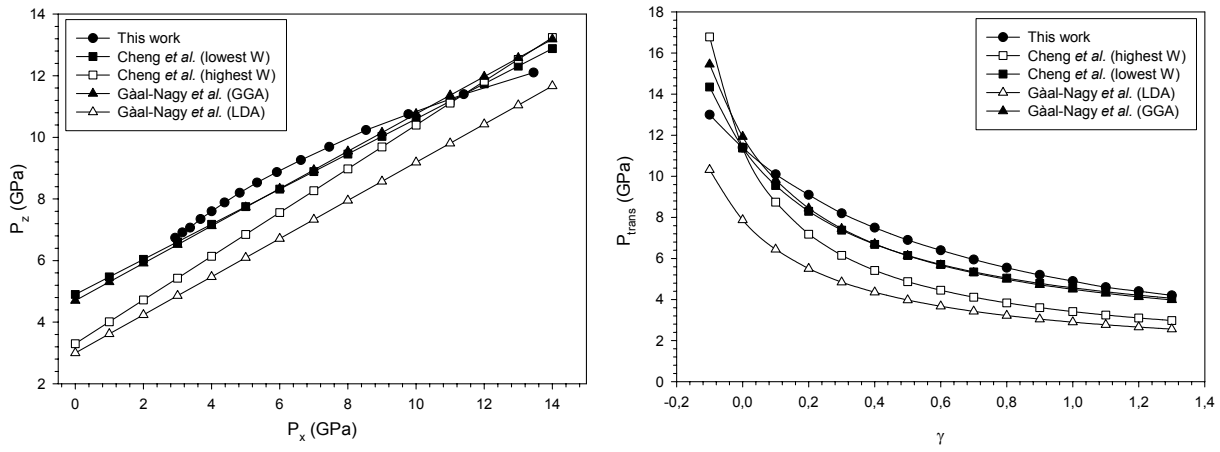

Figure 3.5: Comparison of our results with the previous works.

3.8.6 Conclusion

Nonhydrostaticity is a popular problem and is almost always present in high pressure experiments. The structural competition under non-hydrostatic stress state is a complicated problem to describe as illustrated in this section. The transition pressure is deeply influenced by the uniaxial stress but it is difficult to quantitatively compare experimental and theoretical results. Uniaxial effects on the cell symmetry are also under question as their evaluation requires the calculation of the stress energy which is a complicated task. Even if our approach is quite straightforward - even crude -, it is able to describe the physical mechanism of distortion under non-hydrostatic pressure. It gives results compatible with the LDA- or GGA-based calculations, emphasizing the physical and computational efficiencies of such a simple - but physical - model when a semi-quantitative study is required.

3.9 Conclusion : updated systematics of III-V semiconductors under pressure

The results presented in this thesis allow to complete and comment the structural systematics of III-V semiconductors under pressure. The basis of this set of experimental and theoretical

studies relies on only few questions :

- Does the diatomic β-Sn structure exist in the low-ionicity semiconductors?
- Does the $NaCl$ structure really disappear from the phase diagram of the more covalent semiconductors?
- What are the combined effects of ionicity and pressure on the chemical order?

High-resolution X-ray diffraction experiments using both LVC and DAC highlighted that the β-Sn structure is observed for $GaSb$ and $InSb$ contrary to the previous conclusions of Nelmes *et al.*. The origin of the discrepancies is clearly identified as the uniaxial stress state of the sample. A theoretical description of such a mechanism is given in the case of silicon. If the ionicity of the compound is increased, the β-Sn structure is no more observed. This is the limiting case of GaP. The usual $NaCl$ structure is also shown to be absent from the phase diagram of GaP as suggested by Ozolins. The distorted $Cmcm$ structure is preferred. The $NaCl$ structure only acquires a limited stability range for the most ionic semiconductors, such as $InAs$, before the transformation to the distorted $Cmcm$ structure. This competition between distorted and non-distorted structures is also efficiently described using our tight-binding approach.

Chemical ordering seems to be mainly driven by ionicity which likes charge alternation. $GaSb$-II is site-disordered whereas GaP-II is site-ordered. $GaSb$-II has the β-Sn structure which only exists in low-ionicity compounds : in a chemically-ordered structure two of the six first neighbours have the same chemical nature as the central atom. The chemical disorder is thus energetically less costly than in $NaCl$ or analogue structures. In the case of mid-ionic compounds, the chemical order is maintained in the $NaCl$ and $Cmcm$ structures. However, when the density of the pressurized structure becomes high enough, the charge transfer becomes negligible and chemical disorder may appear as in the $Pmma$ structure of $InAs$ [59, 60]. Combined XRD-XAS studies prove to be the key set-up for such experimental studies.

Chapter 4

Halogens

4.1 Introduction

Halogens are among the most simple crystals of diatomic molecules. At room temperature and pressure, fluorine and chlorine are gases, bromine is a liquid and iodine and astatine[1] are solids. Group 17 is therefore the only one through the periodic table group exhibiting all three states of matter at ambient conditions. Halogens are highly reactive : they can be harmful or lethal to biological organisms in sufficient quantities. Chlorine and iodine are both used as disinfectants for drinking water, swimming pools, sterilization processes in the food industry,... Moreover, they are supposed to be partially responsible of the destruction of the Earth ozone layer, due to the release of fluoro-carbons used as refrigerant fluids in cooling systems.

As halogens are prototypes of the behaviour of hydrogen[2] [76, 77], their behaviour under pressure has received much attention, both theoretically and experimentally [78, 79, 80, 81, 82, 83]. However in the case of hydrogen, the metallization and dissociation pressures are estimated to be - at least - as high as 350 GPa [84, 85] and up to now, hydrogen was never observed neither in its atomic state nor in its metallic state. The current knowledge of solid hydrogen is limited to the existence of three crystallographic forms: a close packed lattice of freely-rotating molecules (phase I), an incommensurate structure with a local orientational order due to a quantum orientational transition (phase II) [86], and above 150 GPa, phase III, which is stable up to at least 320 GPa. The determination of the structure of this phase is crucial for understanding the metallization of hydrogen but constitutes a great experimental challenge due to the extremely weak scattering power of the solid hydrogen sample. Such high pressures are still difficult to reach with the current high pressure set-up and halogens remain an interesting prototype. Furthermore, the study of halogens under pressure reveals unexpected phase transitions as discussed in section 4.2.

The experiments performed during this thesis and the related theoretical models are focused on the mechanism of metallization which still deserves further studies. Its relative position within the sequence of phases has to be elucidated.

In the solid state at low pressure, halogens form an orthorhombic molecular crystal made up of four X_2 molecules ($X = Cl, Br, I$) in a unit cell with space group $Cmca$ (phase I). The atoms are located at $(0, y, z)$. The molecules form zig-zag chains lying in parallel planes as illustrated in figure 4.1.

[1] Astatine is a radioactive element with a maximum lifetime of 8.3 hours for its ^{210}At isotope.

[2] The metallization of hydrogen under pressure is one of the major goals of high-pressure science : hydrogen is present in the big planets'interior but also in military applications. Moreover, hydrogen is the lightest element. Thus its study under pressure concentrates technical challenges of both high-pressure cell design and X-ray detection efficiency.

Historically, iodine - with its relatively low transition pressures, below 25 GPa - was the first halogen to be studied. For this reason iodine is widely documented as shown in the next section. However, even in this case, a new incommensurate structure has been recently discovered mainly thanks to experimental improvements. The physical mechanism of metallization of the molecular solid is the subject of many questions.

Let us underline that the relative behaviour of the intermolecular and intramolecular distances is deeply linked to the molecular dissociation process. Thus a combined experimental study[3] is particularly well suited for the study of the molecular character of the bond. Our interest is focused on bromine as its behaviour remains still unclear in terms of molecular dissociation and metallization. This also allows to discuss the scaling rule applied to the halogen family.

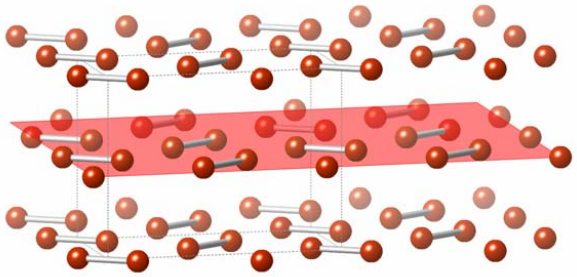

Figure 4.1: Crystallographic structure of iodine at ambient pressure. The crystal is made of parallel, weakly linked planes of molecules illustrated in red. Two successive planes are shifted with respect to each other.

Element	r_{gas} (Å)	r_{solid} (Å)
F_2	1.43	1.49
Cl_2	1.99	2.02
Br_2	2.28	2.27
I_2	2.66	2.72

Table 4.1: The nearly identical intermolecular distances of halogens in the gas and the solid phase indicate that no covalent bond appears between diatomic molecules.

4.2 Halogens under pressure

Halogens exhibit two behaviours under pressure : an insulator-to-metal transition and a molecular dissociation. The question of the simultaneity - or not - of these phenomena is an unsolved issue. Thus the mechanism of such transitions has focused much attention as it is a model of the hydrogen transitions. Until the beginning of the 21^{th} century, the assumed phase diagram of halogens was simple but a new structure[4] has been discovered recently [88, 89].

[3] EXAFS is used as a local probe of matter and diffraction as a long range probe. Both experiments are simultaneously performed.

[4] An incommensurate structure.

Element	a (Å)	b (Å)	c (Å)	y	z	B_0 (GPa)	B'_0
Cl_2	6.24	8.26	4.48	0.121	0.110	15.18	1.59
Br_2	6.67	8.72	4.48	0.138	0.112	15.64	2.21
I_2	7.136	9.784	4.686	0.154	0.117	13.73	2.88

Table 4.2: Structural parameters of I_2, Br_2 and Cl_2 from Wyckoff [87]. The zero pressure bulk moduli, B_0, and its derivative, B'_0 are found in reference [83].

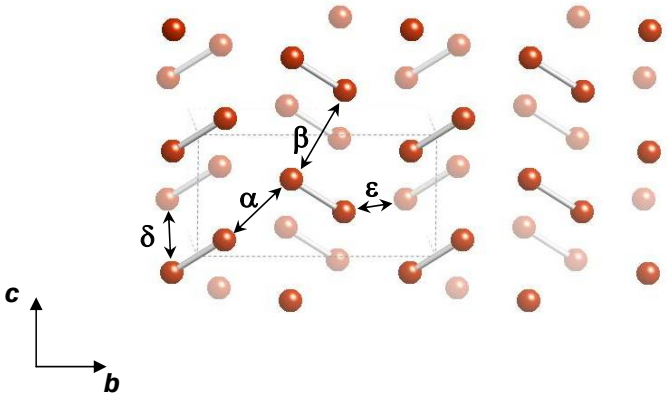

Figure 4.2: View of two molecular planes in the low pressure structure of halogens. The shaded atoms lie in the adjacent molecular plane halfway below. The unit cell is displayed with the dotted line. The different characteristic distances within the plane and between planes are illustrated.

4.2.1 Iodine

The studies on iodine started in the 60's [90]. The first electrical resistance measurements [91] illustrates a strange behaviour of its conductivity : the electrical resistivity of iodine drops by almost 10 orders of magnitude when pressure reaches 17 GPa (this is the first observed transition)[5]. It is related to the conductivity perpendicular to the molecule planes ($E_g^{perp} = 0$ et $E_g^{paral} = 0.11$). At about 22 GPa[6] the resistance along the molecular planes drastically drops. This is compatible to the zero-pressure data : iodine is an insulator with a resistivity perpendicular to the molecular planes about 10^4 higher than the resistivity within the planes. At intermediate pressures, iodine under pressure could be compared to graphite with a low cohesion between the planes and a strong anisotropy of the conductivity. However, in our paper [92] the values of these pressures are corrected to take into account the recalibration of pressure apparatus of Drickamer and co-workers. Based on the original data, the lowest transition, i.e. in-plane, is now located between 12 and 15 GPa and the second transition, i.e. between planes, between 17 and 19 GPa. If those values are correct, metallization would take place before the transition to the incommensurate phase, occurring at 23 GPa. These transport experiments were never verified: it would be interesting to perform them again.

The conductivity changes rise the question of the molecular dissociation. Indeed the conductivity may appear simultaneously with a structural phase transition or before it by a simple

[5] A corrected value is given at 13 GPa.
[6] A corrected value is given at 22 GPa.

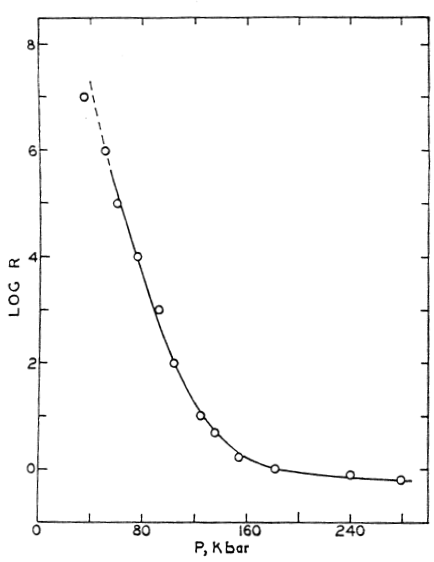

Figure 4.3: Electrical resistance as a function of pressure for iodine perpendicular to the *ac* plane (from reference [91]).

band overlapping in a solid which is still molecular. Theoretical models were developed in order to understand the observations. In 1964, Rosenberg [93] suggested a simplified model based on the Hückel approximation using only the $pp\pi$ and $pp\sigma$ interaction within the molecular planes. This results in an efficient two-band model able to describe the basis of the physical mechanism of such a metallization prior to the structural phase transition.

a (Å)	b (Å)	c (Å)
3.031	5.252	2.904

Table 4.3: Structural parameters of the high-pressure phase of I_2 ($Immm$) at 30 GPa.

The intramolecular distance, r_s and the angle of the zig-zag chain, θ, are simply given by

$$r_s = \sqrt{(by)^2 + (cz)^2} \tag{4.1}$$

$$\theta = tg^{-1}\left(\frac{by}{cz}\right) \tag{4.2}$$

As the electronic properties are tightly linked to the structural properties, several geometrical parameters are introduced:

$$\alpha = \sqrt{(\frac{c}{2})^2 + (\frac{b}{2} - 2yb)^2} \tag{4.3}$$

$$\beta = \sqrt{(c - 2zc)^2 + (2yb)^2} \tag{4.4}$$

$$\delta = \sqrt{(\frac{a}{2})^2 + (\frac{c}{2})^2} \tag{4.5}$$

$$\epsilon = \sqrt{(\frac{a}{2})^2 + (\frac{c}{2} - 2zc)^2} \tag{4.6}$$

$$\tag{4.7}$$

where α, ..., ϵ are the interatomic distances from the smallest one to the highest one. b and c are the lattice parameters in the molecule plane and a the lattice parameter perpendicular to the planes. yb and zc locate the atoms from the origin of the cell.

As the metallization process was unclear, further studies of the evolution of the band structure of iodine under pressure were made by Natsume *et al.* [94]. Even at high pressure, the s band remains separated from the p states. Based on an original model of Bersohn and Rosenberg [90, 93], Siringo *et al.* [80, 95, 96] studied the evolution of the band structure as a function of pressure with experimental structural data as input. They pointed out that the insulator-to-metal transition within the planes is associated to a band overlap. Their second step was to add the orbitals perpendicular to the planes, p_z. In such conditions there are two gaps Δ_{p_x,p_y} and Δ_{p_z}, respectively associated with the $p_x - p_y$ (in plane) orbitals and p_z orbitals (out of plane). The p_z gap reduces much faster than the first one as it has to be because it involves the weakest bonds[7]. It needs to be included in the description of the insulator-to-metal transition under pressure.

At the beginning of the 80^{th}, the structure of the high pressure phase of iodine was elucidated by Takemura et al.[79, 97]. The related structure is no more based on diatomic molecules. Thus this phase transition is directly related to the molecular dissociation. The structure is simpler than the I_2-I: it is based on an orthorhombic $Immm$ structure. The volume reduction associated with this transition is about 4%. Finally, Fujii *et al.* [98, 99] performed experiments at higher pressure. They observed a transition from the $Immm$ structure to a body-centered tetragonal ($I4/mmm$) at 43 GPa. The last transition occurs at 55 GPa to a face-centered cubic structure.

In 2002, Mukose *et al.* calculated the metallization pressure of iodine, bromine and chlorine. As established by Siringo *et al.* metallization takes place by an indirect gap closing. They report 10, 35 and 100 GPa for I_2, Br_2 and Cl_2, respectively. The experimental counterparts are 16, 60 and 165 GPa.

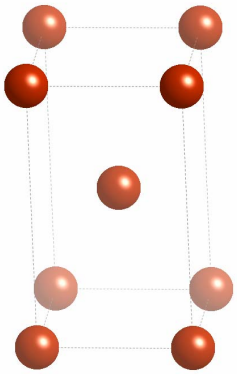

Figure 4.4: View of a first high-pressure phase of halogens with space group $Immm$.

The works of Takemura *et al.* [88] and Kume *et al.* [89] shed new light on the halogen behaviour: a new intermediate phase was identified, I-V. The structure is depicted in figure 4.5 (a). Its structure has been characterized in detail for iodine : the nearest interatomic distance is continuously distributed between the bond length of I_2 in the molecular crystal and the nearest interatomic distance in the atomic crystal as illustrated in figure 4.5 (b). This new transition occurs at 23 GPa for iodine [88]. The resulting sequence of phases is summarized in table 4.4.

[7] The interplanar spacing is higher than the intermolecular distance within the planes.

Cmca (*I*-I)		
↓		
Metallization	16 GPa	
↓		
Incommensurate (*I*-V)	23 GPa	
↓		
Immm (*I*-II)	30 GPa	
↓		
bct (*I*-III)	43 GPa	
↓		
fcc (*I*-IV)	55 GPa	Stable up to 276 GPa

Table 4.4: Sequence of phases in iodine under pressure at room temperature.

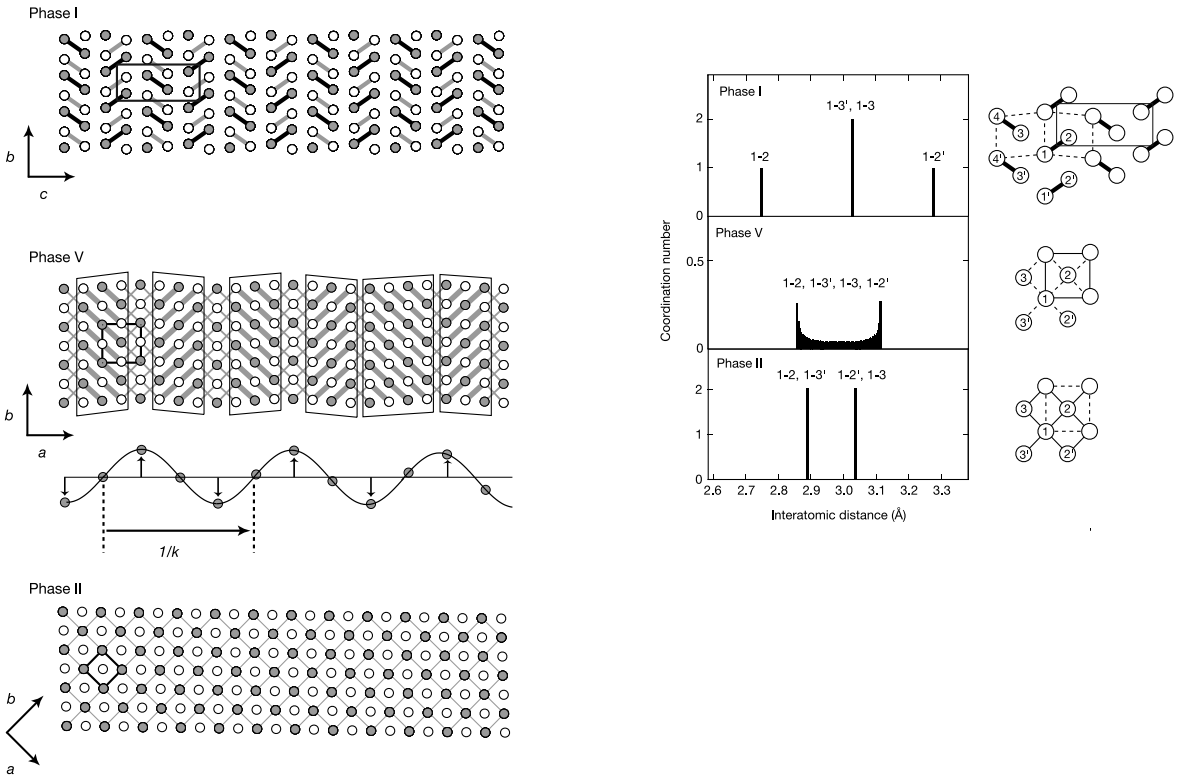

Figure 4.5: Figures adapted from the reference [88]. **Left panel**: structures of the phases I and II and of the incommensurate phase, phase V. Filled and open circles indicate respectively the atoms lying in the plane and in the adjacent plane halfway below. Diatomic I_2 molecules are the basic unit of the phase I but they disappear in the phase V. The interatomic distances are distributed in the range 2.86-3.11 Å. Thick lines: distances between 2.86 and 2.92 Å; thin lines: distances between 2.92 and 3.05 Å. The interatomic distances between 3.05 and 3.11 are not displayed for the sake of clarity. Domains with chains of three or four atoms are indicated by parallelograms. The incommensurate nature of the structure is also illustrated by the amplified atomic displacement. Bottom picture: structure of phase II. **Right panel**: distribution of the interatomic distances in the different structures.

4.2.2 Bromine

Bromine - and of course chlorine and fluorine - are much less studied than iodine as the transition pressures are higher. Fujii *et al.* [100] showed that the behaviour of bromine was similar to the

one of iodine : at 80 GPa, the initial molecular structure disappears in favour of a *Immm* structure. This value is in good agreement with the scaling rule of Fujihisa which is describe in the next section [81]. Some clue of metallization is detected at about 60 GPa where the surface of the sample begins to reflect light. However, Shimizu *et al.* [101] performed resistivity measurement under pressure and the metallization was not clearly identified. They assumed it takes place at the phase transition around 80 GPa.

A new phase of solid bromine was discovered at a pressure region above 80 GPa by Raman scattering. This phase was found to be the same as the iodine phase V with an incommensurate structure [88] which appears between the molecular phase I and the monoatomic phase II. The collected data also suggests that the monoatomic phase II only appears above 30 and 115 GPa for iodine and bromine, respectively [89]. The resulting phase diagram is summarized in table 4.5.

Cmca (*Br*-I)	
↓	
Metallization	60 GPa
↓	
Incommensurate	82 GPa
↓	
Immm (*Br*-II)	118 GPa

Table 4.5: Sequence of phases in iodine under pressure at room temperature.

In the framework of this thesis, it is worth to underline that Kume and co-workers [89] noticed a splitting of the Raman peaks around 25 GPa, pressure at which a discontinuity was observed in the evolution of the width of the Br K-edga white line peak [92]. This point is discussed in section 4.3. The peak splitting disappears around 60 GPa. Metallization is impossible to observe directly with Raman but a specific peak seems to be associated with such a phenomenon. According to the previously published results about electrical conductivity [102, 103, 81], the metallization of bromine is assumed to occur around 60-70 GPa, prior to the appearance of the incommensurate structure.

4.2.3 Scaling rule

A common behaviour for the whole halogen family emerges from the experimental data: not only the atomic volume but also the atomic coordinates follow a common trend. Following Düsing *et al.* [104], a structural parameter, Δ, is defined by

$$\Delta = \frac{\sqrt{(2b)^2 + c^2}}{4r_g} \tag{4.8}$$

where r_g is the intramolecular distance in the gas and b and c are the lattice paramters. When a critical value, Δ_c, is reached, the halogens become metallic. The value of Δ_c is scaled to iodine: the predicted metallization pressures of bromine and chlorine are then 58±6 and 140±30 GPa respectively. However, this result is not compatible with the latest results of Fujihisa *et al.* [81]. Based on their extended study of halogens , they suggested another scaling ratio, $\frac{Rd}{M}$ where R is the molar refractivity, M the molar weight and d the density. When this ratio is equal to 1, the material is metallic. Indeed at this density a strong delocalization of the electrons occurs. In the case of iodine, the gap-closes at 16 GPa, i.e. at $\frac{Rd}{M} = 0.9$.

Element	$\frac{Rd}{M}$
I_2	0.60
Br_2	0.44
Cl_2	0.34

Table 4.6: Herzfeld parameter at 0 GPa for I_2, Br_2 and Cl_2.

Based on this first approach, Fujihisa *et al.* introduced a new version of the scaling rule : the scaled volume, v_s, is defined by

$$v_s(P) = \frac{v_{at}(P)}{8r_s^3} \tag{4.9}$$

where v_{at} is the atomic volume and r_s the intramolecular distance in the solid. In this definition, r_s is assumed to be constant. This parameter is tightly linked to the molecular/atomic character of the solid. Miao and co-workers also gave a simplified equation of state for the halogens based on this scaled volume.

$$P \approx 4.4 \left(\frac{v_s(0)}{v_s(P)} \right)^{3.3} - 4.4 \tag{4.10}$$

At low compression, the sole intermolecular distances are reduced. From the experimental data of iodine, the critical values of the scaled volume are now defined by 1.37 and 1.29 corresponding to the gap closure and to molecular dissociation respectively. The metallization pressure of bromine is now assumed to be around 60 GPa. In the case of chlorine, the gap closure and the molecular dissociation are expected to occur around 165±30 GPa and 220±40 GPa respectively.

The discovery of the incommensurate structures in iodine and bromine and the pressure dependence of the intramolecular distances[8] require a revision of the current scaling rule applied to the halogens under pressure. Indeed, the pressures related to the molecular dissociation are now shifted up to 30 and 115 GPa for iodine and bromine respectively.

4.3 Experimental study of bromine under pressure

Even if the bromine behaviour is widely documented, open questions remain. Bromine still needs to be studied in order to establish an efficient scaling rule. We performed two XAS experiment [92, 105]. We measured the width of the unoccupied conduction band and the intramolecular distance as a function of pressure. Around 25 GPa there is a slope change in the evolution of the bandwidth. This result is compatible with the latest Raman experiments of Kume *et al.* [89]. As described in our first paper, we suggested that this modification is linked to the metallization of bromine even if the scaling rules were not in fair agreement with such an interpretation[9]. The observed transition pressure was also completely different from the one obtained by transport measurements [102, 103, 101].

The identification of the incommensurate structure relaunched the study of the famous scaling rule of halogens. By a combined X-ray diffraction and EXAFS studies, we focus on the molecular character of bromine under pressure through the relative evolution of the intermolecular and intramolecular distances. The progressive reduction of the intermolecular distances drives the two major transformations observed in halogens : metallization by a gap closure

[8] The related EXAFS measurements are discussed in the next section.

[9] It is worth to underline that the scaling rules were applied with success to the molecular dissociation. Concerning the metallization process, no convincing data exists

mechanism and molecular dissociation. Even if the incommensurate structure is not unique in the framework of elements under pressure[10], in the case of halogens, it is closely related to the molecular dissociation process. Our approach allows to study the evolution of the intramolecular distance. As this distance is involved in the scaling rule, our experiment should allow to reassess it.

[10] Uranium [106], Barium[107], Antimony[108], ... exhibit incommensurate structures in their phase diagrams.

Eur. Phys. J. B **17**, 227–233 (2000)

The European Physical Journal B
EDP Sciences

Bromine metallization studied by X-ray absorption spectroscopy

A. San Miguel[1,a], H. Libotte[2], J.P. Gaspard[2], M. Gauthier[3], J.P. Itié[3], and A. Polian[3]

[1] Département de Physique des Matériaux, Université Claude Bernard-Lyon 1, 69622 Villeurbanne Cedex, France
[2] Physique de la Matière Condensée, Université de Liège, B5, 4000, Sart-Tilman, Belgique
[3] Physique des Milieux Condensés, B77, Université P. et M. Curie, 4 place Jussieu, 75352 Paris Cedex 05, France

Received 20 March 2000

Abstract. Bromine has been studied up to a pressure of 110 GPa by X-ray absorption spectroscopy (XAS) at the bromine K-edge, that allows to measure the pressure evolution of the width of the unoccupied conduction band. At 25 ± 5 GPa we observe a slope change in the evolution of this width. Comparison with published calculations of the electronic density of states indicates that the physical origin of the slope change is compatible with the metallisation process. This is also confirmed by a simple tight binding calculation. In addition, the metallisation pressure value is in agreement with calculated ones. At 68 ± 5 GPa a discontinuity in the evolution of the width of the sigma antibonding band points out the onset of a phase transformation. This result is compatible with the observed phase transformation near 80 ± 5 GPa by X-ray diffraction that is associated with the molecular dissociation.

PACS. 61.10.Ht X-ray absorption spectroscopy: EXAFS, NEXAFS, XANES, etc. – 61.50.Ks Crystallographic aspects of phase transformations; pressure effects – 61.66.Bi Elemental solids

1 Introduction

The properties of molecular solids are of central interest, both from a theoretical point of view as well as for their applications, for example in astrophysical problems. Among molecular solids, those built from diatomic molecules like I_2, Br_2 or O_2 are of special interest with respect to the metallization process. In fact, they may be used as models for the metallization of solid hydrogen which, at the present state of theoretical calculations, may happen above 300 GPa at ambient temperature and is therefore still out of reach for static compression [1]. For these reasons a great deal of effort has been devoted in the last years to improving the understanding of the non metal-metal transition in simple molecular systems, in particular in solid [2–9] and liquid [10,11] halogens (I_2, Br_2, Cl_2).

Under ambient conditions, iodine is solid with an orthorhombic structure ($D_{2h}^{18} - Cmca$) [12]. At ambient temperature, chlorine and bromine crystallize with the application of low pressure in the same orthorhombic structure. This structure is layered with the molecules lying in planes disposed perpendicular to the a axis (Fig. 1). The distance between the closest bromine atoms lying in neighboring planes is comparable with the van der Waals diameter, indicating that, at low pressure, the interaction between planes is dominated by van der Waals type potentials. On the contrary, inside the molecule planes (the bc planes), the shortest intermolecular bond is significantly shorter than the van der Waals diameter and consequently these materials cannot be considered as purely

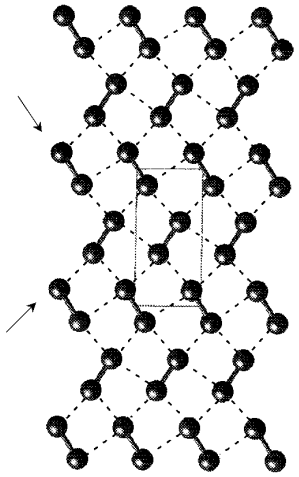

Fig. 1. Structure of one layer of the low pressure phase of solid halogens ($D_{2h}^{18} - Cmca$). The intra-molecular bonds are noted with a solid line. The two arrows point to the perpendicular directions where the Peirls type distortions are observed (see text). The unit cell is depicted. The full structure can be obtained by stacking the planes in the a direction (perpendicular to the layers) with an additional $(0, 1/2, 0)$ translation.

[a] e-mail: sanmigue@dpm.univ-lyon1.fr

molecular crystals. In fact, it has already been pointed out that in the absence of covalent intermolecular bonding, the structure of iodine should be simple cubic [13]. Nevertheless, because the intramolecular distance is much smaller than the inter-molecular ones, the low pressure phase of the halogens is referred to as a molecular crystal. The structure of the low pressure phase of solid halogens can be understood in terms of a Peierls distortion. Indeed, a partially filled p band is known to be unstable with respect to a periodic distortion, the wavelength of which depends on the number of p electrons [14,15]. For a 5/6 filled p band, if all the three directions of the space are equivalent, a distortion of the cubic cell is expected giving rise to a period of the distorted cell that is 6 times the period of the original simple cubic cell. In this paper this will be referred as a 6-merization. An alternative solution that breaks the symmetry is the layer structure of halogens, where the anisotropy gives rise to a Peierls distortion with a 4-merization in two orthogonal directions of the plane as shown in Figure 1. This opens a gap in the Fermi level.

X-ray diffraction studies show that iodine and bromine follow a first order pressure induced phase transformation towards a body-centered orthorhombic structure (D_{2h}^{25} – $Immm$). In this phase, the molecules lie in planes within which the intra and inter molecular distances are equal. To underline this fact, the formation of this 2-dimensional association has been called the monoatomic phase and the phase transformation "molecular dissociation". This has been observed to happen at 21 GPa [4,16] for iodine, near 80 GPa [8,17] for bromine, and it has been predicted to happen at 220 ± 40 GPa for chlorine [8].

Because of its lower transition pressure iodine has been extensively studied. Under ambient conditions, solid iodine is a semiconductor with an optical gap of 1.35 eV. From the detailed study of the transport and optical properties, Drickamer and co-workers [2,18] found that the onset of the metallic behavior takes place in the direction perpendicular to the layers *via* progressive gap closure and at a pressure lower than the dissociation pressure. In the layered direction the onset of a metallic behavior was also observed at a higher pressure that matches the dissociation pressure within the error bars. X-ray diffraction studies gave no evidence of structural changes associated with the onset of metallization [4,16,19,20]. The experimental results of Drickamer and co-workers are confirmed by semi-empirical tight binding calculations on the Bersohn-Rosenberg model for iodine [6]. In fact this simple model shows that the gap of the p_z band due to the weaker interaction between bc planes decreases more rapidly with pressure and closes at a lower pressure than the gap due to $p_x p_y$ orbitals inside the planes. The monoatomic iodine high pressure phase can be expected to be a "hole conductor" because of the $(4s)^2(4p)^5$ electronic configuration that provides seven valence electrons, that is to say, one hole. This is in agreement with band structure calculations in the high pressure phase [21] and is experimentally confirmed by transport measurements [22]. It is worthwhile to note that the value for the metallization pressure of iodine given by Riggleman and Drickamer [18] of 16 GPa – the value commonly found in the literature – must be corrected from the calibration of the pressure scale of the high pressure apparatus done afterwards by Drickamer [23]. This is shown in Figure 2, from where we deduce metallization pressures for iodine of 13 ± 2 GPa in the layers and 17 ± 2 GPa perpendicular to the layers. At higher pressures iodine follows a second order transformation to a body centered tetragonal phase at 43 GPa [24]. In this new phase the Peierls distortion of bc planes disappears and a planar square lattice is obtained. A first order transition to a face-centred cubic phase at 55 GPa was also reported [25] and this new phase remains stable at least up to 276 GPa [26].

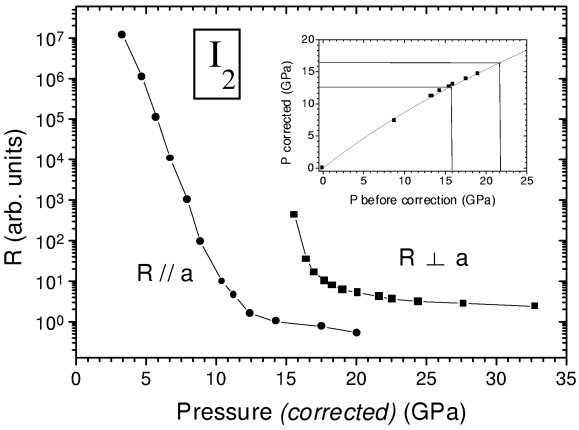

Fig. 2. Recalibration of the iodine electrical measurement of (A.S. Balchan, H.G. Drickamer, J. Chem. Phys. **34**, 1948 (1961); B.M. Riggleman, H.G. Drickamer, J. Chem, Phys. **38**, 2721 (1963)) from the pressure calibration given in (H.G. Dirckamer, Rev. Sci. Inst. **41**, 1667 (1974)). The inset shows the correspondence between the uncorrected and corrected pressure values and the correspondence between the metallization values given in the original papers (16 and 22 GPa) and the corrected ones (13 and 17 GPa).

A similar scheme of phase transformations can be expected for bromine and chlorine, but experimental or theoretical results are much scarcer than in the iodine case. We will restrict our discussion to the processes of metallization and of molecular dissociation. None of these transformations have been observed in chlorine where X-ray diffraction studies have been performed up to 45 GPa [27]. In bromine, the onset of the first order phase transformation associated with the molecular dissociation was evidenced by X-ray diffraction experiments [17] at 80 GPa. The structure refinement [8] of the low pressure phase gives the evolution of the interatomic distances with pressure. In the low pressure phase, the compression reduces the intermolecular distance whereas the intramolecular distances do not show a significant variation with pressure. At the phase transition edge (80 GPa) the difference between intra and inter molecular distances is only 8% (to be compared with 43% of difference at ambient conditions) but the equality between inter and intra

Table 1. Measured calculated and predicted transition pressures for the metallization and dissociation of solid halogens.

	P metallization (GPa)			P dissociation (GPa)	
	Exp.	Calc.	Predicted	Exp.	Predicted
Cl_2	-	$67^{\dagger}$	165^{+}	-	$220 \pm 40^{+}$
Br_2	$25 \pm 5^{*}$	$33^{\dagger}$, $35^{\S\S}$	60^{+}	$80 \pm 5^{\ddagger}$, $68 \pm 5^{*}$	$80 \pm 5^{+}$
I_2	$13 \pm 2^{\sharp}$	$15^{\dagger}$	16^{+}	$21 \pm 2^{\S}$	$21 \pm 2^{+}$

(*) This work.
(♯) Pressure calibration of the data of B.M. Riggleman, H.G. Drickamer, J. Chem. Phys. **38**, 2721 (1963) (see text for details).
(†) F. Siringo F. Piccitto, R. Pucci, High Pressure Research **3**, 162 (1990).
(+) Structural scaling rule of H. Fujihisa, Y. Fujii, K. Takemura, O. Shimomura, J. Phys. Chem. Solids **56**, 1439 (1995).
(‡) Y. Fujii, K. Hase, N. Hamaya, Y. Ohishi, A. Onodera, O. Shimomura, K. Takemura, Phys. Rev. Lett. **58**, 796 (1987).
(§) K. Takemura, S. Minomura, O. Shimomuran, Y. Fujii, Phys. Rev. Lett. **45**, 1881 (1980).
(§§) H. Miyagi, K. Yamguchi, H. Matsuo, K. Mukose, J. Phys. Condens. Matter **10**, 11203 (1998).

molecular distances only takes place in the high pressure phase after a volume reduction, $\Delta V/V$, of 3% at the phase transformation.

Our work was motivated by the lack of experimental data concerning the metallization process of bromine and in particular the value of the metallization pressure. In addition some predictions for the metallization pressure of bromine and chlorine [6,8,9] are in serious contradiction (see Tab. 1) giving values that differ by a factor two for bromine and even more for chlorine. In order to obtain a more complete description of the high pressure behavior of solid bromine we have performed X-ray absorption spectroscopy experiments at the Br K-edge up to a pressure of 110 GPa. X-ray absorption spectroscopy (XAS) [28] is a very powerful technique to explore local properties of matter. Information of the local structure and electronic structure can be obtained from the spectra. In the case of bromine, there is a very prominent peak feature just before of the jump of the bromine K-edge. This feature was extensively studied in the early days of EXAFS (Extended X-ray Absorption Fine Structure) and it was shown [29] through the angular dependence of the spectra taken on a bromine-on-graphite system, that this peak is due to electronic transition from the $1s$ electrons to unfilled $4p$ states associated with the σ-antibonding orbitals (σ^*). In the following we will refer to that peak as the $1s \rightarrow 4\sigma^*$ transition. Because of dipolar selection rules, the structures at the beginning of the bromine K-edge X-ray absorption spectra are the projection of the p-density of free states modified by the presence of the $1s$ core-hole. In bromine, the energy modification of the ground state by the creation of one hole in the $1s$ level has been evaluated to be 7.3 eV [30]. In the case of the bromine K-edge no quadrupolar contributions should be expected. Similarly to solid bromine there exists an important covalent coupling between bromine molecules giving rise to a $1s \rightarrow 4\sigma^*$ feature in the electronic spectrum corresponding to the transitions to the very narrow conduction band of solid bromine. The evolution of the electronic structure of bromine with density will be reflected in the features of the $1s \rightarrow 4\sigma^*$ peak and can be used as a fingerprint of phase transitions or electronic changes. It would also have been of major interest to follow the EXAFS signal with pressure. Unfortunately, as explained below, this was not accessible in this experiment.

2 Experimental

X-ray absorption spectra were taken at the energy dispersive XAS beamline (ID24) of the ESRF (European Synchrotron Radiation Facility). A specially profiled Bragg Si (111) crystal polychromator [31,32] was used in order to disperse the undulator white-beam around the Bromine K-edge energy (13.474 keV). Harmonic rejection was ensured by the double reflection of the white beam on the Kirkpatrick-Baez optics placed before the polychromator. The reflected beam by the polychromator was focussed on to the sample in the horizontal plane to approximately 150 μm and further slitted by the sample environment to 30 μm. In the vertical plane the beam was defined by slits to 50 μm. Due to of the very high pressure that was required, high focusing was an essential parameter in this experiment. The ID24 spectrometer allows focusing of 50 μm of the polychromatic beam for energies between 5 and 11 keV, but this value rapidly increases when going to higher energies due to the X-ray penetration in the curved polychromator crystal. More details concerning the ID24 spectrometer can be found elsewhere [33]. Pressure was generated using a membrane diamond anvil cell with a large angular aperture [34] in which bevelled diamonds with 100 μm diameter culets were mounted. Liquid bromine was introduced in to the hole of 30 μm diameter drilled in a rhenium gasket. The pressure transmitting media was the sample itself. Pressure was measured in situ through the luminescence of a ruby chip introduced with the sample [35] and special care was observed to avoid hydration of the sample during the loading process [36]. The loading was performed in a glove box under inert atmosphere. The intensity of the pre-edge feature of the XAS spectra was used to determine any possible chemical degradation of bromine. In fact, we have observed that when bromine has been exposed to air the intensity of the pre-edge feature decreases to more than half when compared to a pure sample. The diamond anvil cell was oriented with respect to the X-ray beam in order to avoid the presence of diamond diffraction glitches in the zone of interest around the absorption edge. The main experimental problem arises when reducing the size of the beam in the vertical direction by slitting. In fact, when the vertical dimension was less than 100 μm, very sharp structures in the X-ray beam appear in the signal. These structures are of the same magnitude as the signal of the EXAFS oscillations at 50 μm of slit size. Nevertheless, the intensity of the pre-edge feature is more than 10 times the amplitude

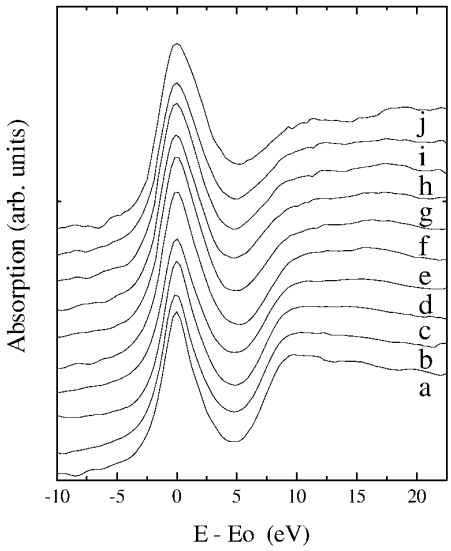

Fig. 3. Edge region of the X-ray absorption spectra of bromine at the K-edge as a function of pressure. The spectra have been shifted in the vertical direction for clarity. Labels correspond to the sample pressure : a (8.1 GPa), b (9.5 GPa), c (13.2 GPa), d (17.8 GPa), e (24.8 GPa), f (41 GPa), g (63 GPa), h (65 GPa), i (71 GPa), j (110 GPa). The energy origin has been arbitrarily fixed at the maximum of the pre-edge feature.

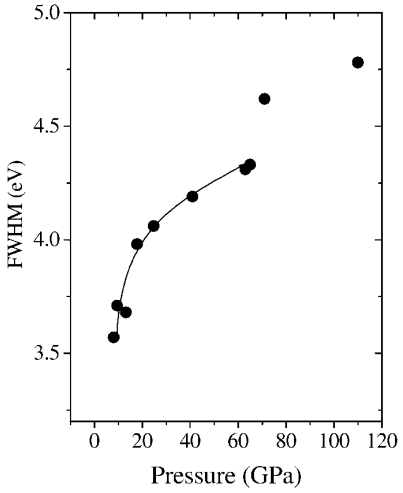

Fig. 4. Observed full-width-half-maximum of the evolution with pressure of the pre-edge peak ($1s \rightarrow 4\sigma^*$ band transition) as a function of pressure.

of the EXAFS oscillations and, being only slightly affected by the presence of these structures, it can be exploited. The origin of the spurious structures that appear at low vertical slitting is the strong coherence of the X-ray beam related to the small emittance of the ESRF electron beam. However, without this small emittance, it would have been difficult to attain the reduced horizontal beam size needed for the experiment. For each bromine spectra, a reference spectrum of KBr at the Br K-edge was taken in order to make the energy calibration by comparing with a spectrum obtained with a two crystal monochromator [37].

3 Results

In Figure 3 we show the edge region of the X-ray absorption spectra as a function of pressure. The energy origin was arbitrarily set at the maximum of the pre-edge feature. In our first spectrum taken at 8.1 GPa, we observe a difference between the 1s and the continuum energy levels, $\Delta E = E_{1s\rightarrow\infty} - E_{1s\rightarrow\sigma^*}$ of 7.3±0.5 eV a value that is in good agreement with other measured [38] and calculated [30] values (8 eV). We have taken as value for the $1s \rightarrow 4\sigma^*$ transition the maximum of the pre-edge feature and for the $1s \rightarrow \infty$ one, the value of the inflexion point at the edge. No clear trend was observed in the evolution of ΔE with pressure that seems to be constant within our sensitivity. This means that the relative position between the bottom of the conduction band and the continuum level (the minimum energy need to consider a photoelectron as a free propagating wave) is constant within this limit. This is in good agreement with band structure calculations performed on the low pressure phase of iodine [6,9]. It is possible to fit the pre-edge feature with a single Lorentzian function. We nevertheless observe a progressive (linear) degradation of this fitting when the pressure is applied to the sample. A fit with two Gaussian functions gives a good representation of the pre-edge feature for all pressures. In that case, the higher energy peak contribution to the pre-edge increases linearly with pressure going from 14% of the total area at the lowest pressure measured (8.1 GPa) up to 25% at 71 GPa. At 1.2 Mbar, both peaks contribute in a similar way to the total signal. This trend is also observed in the calculated density of states within the full-potential linear muffin-tin orbital method (FPLMTO) [9]. The pressure evolution of the FWHM of the pre-edge feature is a measure of the evolution of the width of the $4\sigma^*$ empty band. The measured evolution of this FWHM with respect to pressure is shown in Figure 4. It has been observed, for all the pressure domain explored, that a positive slope of the curve as is expected for a progressive augmentation of density. It is also obvious that up to 25 ± 5 GPa this slope is greater than that between 25 ± 5 and 63 ± 5 GPa. In addition, a clear discontinuity is observed in the evolution of the FWHM of the $1s \rightarrow 4\sigma^*$ feature at 68 ± 5 GPa. Such a discontinuity can only be related to a discontinuous change of the evolution of the electronic structure of bromine. The pressure at which it is observed, 68 ± 5 GPa, is slightly lower than the observed phase transformation pressure (80 ± 5 GPa) associated with the molecular dissociation [8,17]. It is closer to the metallization pressure for bromine (60 GPa) obtained from scaling rules [8]. Unfortunately there is a lack of experimental data that could allow to check if there is or not a further change – corresponding to the structural phase transformation – at 80 GPa. Nevertheless, all calculations and observations

show that the gap closure of iodine is progressive and without discontinuity and we expect the same trend for bromine. In that case, the observed discontinuity could only be associated to the molecular dissociation. The difference between our value for the dissociation pressure and the published one [8,17] can have different origins: i) an underestimation of the error bars (we recall here that bromine itself is serving as pressure transmission medium) ii) the different sensitivity to the phase transition of a local probe (X-ray absorption spectroscopy) and of a long range-order probe (X-ray diffraction). The experimental problems already reported prevent us from extracting quantitative structural information from the EXAFS or the XANES (X-ray Absorption Near Edge Structure) parts of the spectra. Nevertheless, it can be observed from Figure 3 that the XANES part (the region situated after the edge in the figure) progressively changes with pressure. This is an indication of an evolution of the local structure around the bromine atom related to the density reduction. Better data quality is needed for the extraction of quantitative information from this part of the spectra.

4 Model description

In order to obtain a physical explanation of the slope change of the FWHM of the XAS pre-edge feature that is observed at 25 ± 5 GPa, a semi-empirical tight-binding model is used.

The Fermi energy, E_{F} is defined by

$$N_{\mathrm{el}} = \int_{-\infty}^{E_{\mathrm{F}}} n_p(E)\mathrm{d}E \tag{1}$$

where $n_p(E)$ is the electronic density of states and N_{el} is the number of p electrons per atom (in the case of bromine, $N_{\mathrm{el}} = 5$). In a first approximation, the $4s$ levels are filled and therefore, they do not contribute to the band energy.

Our model description is based on a simplification of the real crystallographic structure. In a first approximation, the two directions in the molecular layers (the 4-merised direction shown by arrows in Fig. 1) are assumed to be independent. This is exact if the angles are equal to 90° and if only the $pp\sigma$-orbital interactions, which are the most important interatomic interactions, are taken into account ($pp\pi = 0$). Therefore, the electronic density of states is calculated for a 1-D chain of bromine atoms linked to their neighbours by one short bond (intramolecular) and three long bonds. In the z-direction, a simple linear chain of atoms linked by long bonds is considered.

Under these assumptions the tight-binding Hamiltonian writes

$$H_{\mathrm{el}}^{1D} = \sum_i \epsilon_p |\phi_i\rangle\langle\phi_i| + \sum_i \sum_{j\neq i} \beta_{pp\sigma}^{ij} |\phi_i\rangle\langle\phi_j| \tag{2}$$

where $|\phi_i\rangle$ is the p atomic orbital located on site i, ϵ_p is the p electronic level and $\beta_{pp\sigma}^{ij}$ is the resonance integral between $|\phi_i\rangle$ and $|\phi_j\rangle$.

The interatomic interactions are assumed to be non-vanishing for nearest neighbours only. In addition the atomic wave functions are supposed to be orthogonal, *i.e.* $\langle\phi_i|\phi_j\rangle = \delta_{ij}$ where δ is the Kronecker symbol.

The resonance integrals, $\beta_{pp\sigma}(r_{ij})$, between neighboring atoms i and j distant of r_{ij} are assumed to have the form proposed by Slater and Koster [39]. In addition we assume a distance dependence given by relation (3) where $q = 2$.

$$\beta_{pp\sigma}(r_{ij}) = \beta_{pp\sigma,0} \left(\frac{r_{ij}}{r_0}\right)^{-q}. \tag{3}$$

If the long bonds were of infinite length a three peak electronic spectrum would appear. Long bonds of finite length would give rise to three bands, the width of each one being equal to $2\beta_{pp\sigma}(r_L)$, with r_L the long bond length.

In order to evaluate the evolution of the conduction bandwidth as a function of pressure the interatomic distances have been taken from the experimental X-ray diffraction data [8]. The electronic parameters are chosen so as to reproduce the zero-pressure optical gap calculated by Siringo *et al.* [6]. The metallization pressure is found to be at about 50 GPa. The metallization occurs when the bottom of the antibonding σ^* conduction band crosses the top of valence p_z-band. This was already found in a more detailed calculation [6] and justifies our simple approach. Figure 5 shows the calculated width of the conduction band, $W(P)$, as a function of pressure as it should be observed by XAS. It is clear that the slope of the curve changes at the metallization pressure, P_{M}. This can be explained as follow.

Below P_{M}, *i.e.* before the band crossing, the conduction band width is simply the difference between the top and the bottom of the empty conduction band. Above P_{M}, *i.e.* after metallization has occurred, the situation is different: there is an overlap between the σ^* conduction band and the p_z-band. Therefore, the observed width of the conduction band is now the difference between the top of the σ^* conduction band and the Fermi level. This is shown in the schematic representation of the band structure of Figure 5.

5 Discussion and conclusions

Our model shows that the conduction bandwidth, as observed by XAS, has a slope discontinuity at a pressure at which the metallization occurs. Experimentally, the expected presence of pressure gradients and the effect of non-zero temperature produce a continuous change of the slope and this is precisely what it is observed experimentally at 25 ± 5 GPa. This value is in very good agreement with the calculated metallization pressure [7,9] and consequently does not agree with the one deduced from structural scaling rules (see Tab. 1). As the metallization process involves the inter-plane electronic interaction, it can

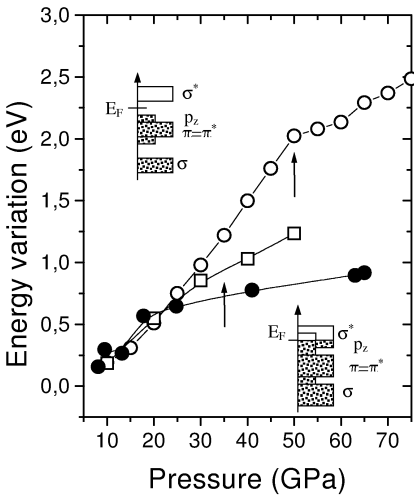

Fig. 5. Calculated (hollow symbols) and measured (filled symbols) FWHM evolution with pressure of the pre-edge peak ($1s \rightarrow 4\sigma^*$ band transition). Empty circles: within a simple tight binding calculation with the metallization pressure, P_M, that was arbitrarily set at 50 GPa (see text). Empty squares: from the electronic-DOS calculated in a full-potential linear muffin-tin orbital method and convoluted by a 0.4 eV Lorentzian function. In this case the gap closure was observed at 35 GPa. The arrow points to the metallization pressure, P_M, in the two cases corresponding to the introduction of the Fermi level in the $4\sigma^*$ band. Lines are only guides for the eye. For both calculations, the slope change corresponds to the metallization process. There are also shown the scheme of the electronic band structure before (top) and after (bottom) the metallisation.

be expected that the structural scaling rules that work remarkably well in the case of the dissociation process are not directly applicable to the metallization as it has been proposed [8]. In the same way, the electronic-DOS calculated by FPLMTO [9] also shows the same type of pressure non linear behaviour of the band-width of the σ^* conduction band from the metallization pressure (Fig. 5). In our simple model we have set arbitrarily the metallization pressure at a value of 50 GPa that is 15 GPa higher than in the FPLMTO calculation [9] and we have nevertheless obtained the slope change associated to the metallization process using the same structural data at the chosen metallization pressure. This confirms that within this model the slope change is well associated to electronic changes and not to the evolution of the compressibility of bromine. The absolute value of the band-width is difficult to compare with our experimental values that are affected by the core-hole width, the experimental resolution and pressure gradients.

It is worth to note that, in liquid iodine, a two step metallization process is observed [10] at a much lower pressure than for the solid phase (between 3 and 5 GPa). This reduced metallization pressure value indicates that an important loss of the lamellar character of the solid phase can be concluded, but at the same time, the persistence of a two step process in the liquid phase could indicate that the lamellar structure has not been totally destroyed. In other words, the Peierls distortion should then still be present in the liquid phase. This is in fact also observed in liquid elements like arsenic [40] and demonstrated theoretically. Indeed the Peierls distortion is a local effect [15] more than a long range effect. In addition, EXAFS measurements [11] show that the iodine intra-molecular distance increases slightly with pressure both in the solid and in the liquid phase, but much more rapidly for the last one. A simple tight binding computation of a Peierls distorted system shows a slight increase of the intra-molecular distance close to the dissociation pressure [41]. Consequently, the EXAFS results are also compatible with a persistence of the Peierls distortion in the liquid phase of the halogens, but significantly reduced with respect to the one of the solid phase at ambient conditions.

In conclusion, our X-ray absorption experiment shows that at 25 ± 5 GPa there is a slope change in the XAS FWHM of the pre-edge feature at the Br K-edge that can be interpreted as an evidence of the onset of the metallization process. A simple tight binding model allows us to assign the physical origin of this slope change in agreement with FPLMTO calculations [9]. The excellent agreement between the observed pressure value of 25 ± 5 GPa with the one calculated by Siringo *et al.* [7] and Miyagi *et al.* [9] reinforces the metallization assumption. Nevertheless this can not be considered as a complete proof of the metallization process because we can not give a proof of uniqueness of origin for the slope change of the FWHM and further measurements or calculations will be needed in order to verify our observation. At 68 ± 5 GPa a discontinuity in the evolution of the width of the empty conduction band points out the presence of a structural phase transformation. This transformation takes place at a pressure that is compatible with the observed phase transformation near 80 ± 5 GPa and that is associated with the molecular dissociation. In addition, we note that, to our knowledge, we have reached the highest pressure ever reported in a XAS experiment.

We are grateful to Prof. H. Miyagi (Osaka University) for providing us with the electronic-DOS files of his calculations [9].

References

1. K.A. Johnson, N.W. Ashcroft, Nature **403**, 632 (2000).
2. A.S. Balchan, H.G. Drickamer, J. Chem. Phys. **34**, 1948 (1961).
3. K. Syassen, K. Takemura, H. Tups, A. Otto, *Physics of solids under high pressure*, edited by J.S. Schilling, R.N. Shelton (North Holland Publishing Company, 1981), p. 125.
4. K. Takemura, Y. Fujii, S. Minomura, O. Shimomura, J.D. Axe, Phys. Rev. B **26**, 998 (1982).
5. M. Pasternak, J.N. Farrell, R.D. Taylor, Phys. Rev. Lett. **58**, 575 (1987).

6. F. Siringo, R. Pucci, N.H. March, Phys. Rev. B **37**, 2491 (1988); *ibid.* **38**, 9567 (1988).
7. F. Siringo, F. Piccitto, R. Pucci, High Pressure Research **3**, 162 (1990).
8. H. Fujihisa, Y. Fujii, K. Takemura, O. Shimomura, J. Phys. Chem. Solids **56**, 1439 (1995).
9. H. Miyagi, K. Yamguchi, H. Matsuo, K. Mukose, J. Phys Cond. Matter **10**, 11203 (1998).
10. V.V. Brazhkin, S.V. Popova, R.N. Voloshin, A.G. Umnov, High Pressure Research **6**, 363 (1992).
11. U. Buontempo, A. Filipponi, D. Martínez-García, P. Postorino, M. Mezouar, J.P. Itié, Phys. Rev. Lett. **80**, 1912 (1998).
12. F. van Bolhuis, P.B. Koster, T. Migechelsen, Acta Crystallog. **23**, 90 (1967).
13. K. Yamasaki, J. Phys. Soc. Jpn **17**, 1262 (1962).
14. J.-P. Gaspard, R. Céolin. Solid State Comm. **84**, 839 (1992).
15. J.-P. Gaspard, A. Pellegatti, F. Marinelli, C. Bichara, Phil. Mag. **77**, 727 (1998).
16. K. Takemura, S. Minomura, O. Shimomuran, Y. Fujii, Phys. Rev. Lett. **45**, 1881 (1980).
17. Y. Fujii, K. Hase, Y. Ohishi, H. Fujihisa, N. Hamaya, K. Takemura, O. Shimomura, T. Kikegawa, Y. Amemiya, T. Matshshita, Phys. Rev. Lett. **63**, 536 (1989).
18. B.M. Riggleman, H.G. Drickamer, J. Chem, Phys. **38**, 2721 (1963).
19. O. Shimomura, K. Takemura, Y. Fuji, S. Minomura, M. Mori, Y. Noda, Y. Yamada, Phys. Rev. B **18**, 715 (1978).
20. K. Takemura, Y. Fuji, S. Minomura, O. Shimomura, Solid State Comm. **30**, 131 (1979).
21. Y. Natsume, T. Suzuki, Solid State Comm. **44**, 1105 (1982).
22. T. Yamauchi, K. Shimizu, N. Takeshita, M. Ishizuka, K. Amaya, S. Endo, J. Phys. Soc. Jpn **63**, 2307 (1994).
23. H.G. Drickamer, Rev. Sci. Inst. **41**, 1667 (1974).
24. Y. Fujii, K. Hase, Y. Ohishi, N. Hamaya, A. Onodera, Solid State Comm. **59**, 85 (1986).
25. Y. Fujii, K. Hase, N. Hamaya, Y. Ohishi, A. Onodera, O. Shimomura, K. Takemura, Phys. Rev. Lett. **58**, 796 (1987).
26. R. Reichlin, A.K. McMahan, M. Ross, S. Martin, J. Hu, R.J. Hemley, J.K. Mao, Y. Wu, Phys. Rev. B **49**, 3725 (1994).
27. E.-Fr. Düsing, W.A. Grosshans, W.B. Holpzapfel, J. Phys. Colloq. France **45**, C8-203 (1984).
28. *X-ray Absorption*, edited by D.C. Konigsberger, R. Prins (Wiley, New York, 1988).
29. S.M. Heald, E.A. Stern, Phys. Rev. B **17**, 4069 (1978).
30. S.H. Chou, J.J. Rehr, A. Stern, E.R. Davidson, Phys. Rev. B **35**, 2604 (1987).
31. J. Pellicer-Porres, A. San Miguel, A. Fontaine, J. Synchrotron Radiation **5**, 1250 (1998).
32. A. San Miguel, M. Hagelstein, J. Borrel, G. Marot, M. Renier, J. Synchrotron Radiation **5**, 1396 (1998).
33. M. Hagelstein, A. San Miguel, A. Fontaine, J. Goulon, J. Phys. IV France **7**, C2-303 (1997).
34. J.C. Chervin, B. Canny, J.M. Besson, Ph. Pruzan, Rev. Sci. Instrum. **66**, 2595 (1995).
35. G. Piermanrini, S. Block, J.D. Barnett, R.A. Forman, J. App. Phys. **46**, 2774 (1975).
36. This problem is particularly relevant in the paper: J.P. Itié, M. Jean-Louis, E. Dartyge, A. Fontaine, A. Jucha, J. Phys. Colloq. France **47**, C8-897 (1986).
37. The reference spectrum was kindly provided by Pr. T. Murata (Kyoto University of Education).
38. T.A. Tyson, K.O. Hodgson, C.R. Natoli, M. Benfato, Phys. Rev. B **46**, 5997 (1992).
39. J.C. Slater, G.F. Koster, Phys. Rev. **94**, 1498 (1954).
40. R. Bellissent, C. Bergman, R. Céolin, J.-P. Gaspard, Phys. Rev. Lett. **59**, 661 (1987).
41. J.-P. Gaspard, private communication.

PRL 99, 015501 (2007) PHYSICAL REVIEW LETTERS week ending 6 JULY 2007

New Phase Transition of Solid Bromine under High Pressure

A. San-Miguel,[1] H. Libotte,[2] M. Gauthier,[3] G. Aquilanti,[4] S. Pascarelli,[4] and J.-P. Gaspard[2]

[1]*Université de Lyon, F-69000 Lyon, France and Université de Lyon 1, Laboratoire PMCN, CNRS, UMR 5586, F69622 Villeurbanne Cedex, France*

[2]*Physique de la Matière Condensée, Université de Liège, B-4000 Liège, Belgium*

[3]*IMPMC, CNRS UMR 7590, Université Pierre et Marie Curie, F-75352, Paris 6, Paris, France*

[4]*European Synchrotron Radiation Facility, BP220, F-38043 Grenoble, France*

(Received 26 March 2007; published 6 July 2007)

Solid bromine has been studied by x-ray absorption spectroscopy experiments up to a maximum pressure of 75 GPa. The data analysis of the extended fine structure reveals that the intramolecular distance first increases, reaching its maximum value at 25 ± 5 GPa. From this value the intramolecular distance abruptly begins to decrease evidencing a nonpreviously observed phase transformation taking place at 25 ± 5 GPa. A maximum variation of 0.08 Å is observed at 65 ± 5 GPa where again a phase transition occurs. This last transformation could correspond with the recently observed change to an incommensurate modulated phase. We discuss the possible generalization of the observed new phase transition at 25 ± 5 GPa to the case of the other halogens.

DOI: 10.1103/PhysRevLett.99.015501 PACS numbers: 61.50.Ks, 31.70.Ks, 61.10.Ht, 62.50.+p

We report x-ray absorption spectroscopy experiments showing the existence of a phase transition in solid diatomic bromine at 25 ± 5 GPa. Previous to this work the consensus has been that under compression of diatomic molecular solids, the intermolecular distances shrink and in a lesser extent the intramolecular distance increases or remains constant. Both distances become progressively comparable leading at a given pressure to molecular dissociation and metallization through one or more phase transformations [1–4]. At the dissociation pressure both the intermolecular and intramolecular distances are the same. The high resolution of our experiments shows that the intramolecular distance of bromine initially increases up to 25 GPa as expected. However, at 25 GPa the intramolecular distance suddenly begins to decrease up to 65 ± 5 GPa. This sudden change in sign of the pressure induced bond distance modification is attributed to a new type of phase transition, which to our knowledge is observed here for the first time. This result should modify the way we understand dissociation and metallization in diatomic solids at high pressure and could have significant theoretical impact on the investigation of these phenomena in solid H_2, or other molecular solids which are of central interest, both from a theoretical point of view as well as for their implications, for example, in astrophysical problems.

The heavier halogens (Br_2, I_2), constitute model systems for the study of simple molecular solids under high pressure as the necessary pressures for metallization or dissociation are typically a factor of 10 to 100 smaller than for H_2. The low pressure solid phase of the halogens is an orthorhombic molecular crystal (D_{2h}^{18} or *Cmca*) made of layers of molecules (see Fig. 1). Each layer is constituted of in-plane molecules in a zigzag arrangement. During the first stages of compression, the predominant effect on the structural arrangement is the reduction of the interlayer distances as observed by x-ray diffraction experiments ([5], and references therein). A consistent picture of the high pressure evolution of halogens (Cl_2, Br_2 , and I_2) was developed by Fujihisa *et al.* [5] following the high pressure x-ray diffraction investigation of iodine and bromine [6–9]. They observed that the pressure evolution of the structural parameters of the three halogens scaled well as a function of a reduced atomic volume defined as $v_r = v_{at}/(8r_s^3)$, with r_s being the interatomic distance of the molecule in the solid state. An important fact to keep in mind is that in this definition r_s was considered constant.

It was equally found that the dissociation pressure of bromine and iodine takes place at a limiting value of $v_r = 1.29$, which corresponds well with their respective observed transitions pressures at that time at 21 and 80 GPa. Further transitions to more compact structures have been identified at higher pressures [10].

Semimetallization through gap closure was predicted to take place at $v_r = 1.37$ based on a value of 16 GPa for iodine. This gives a prediction of 60 GPa for the semimetallization pressure of bromine, which is in good agree-

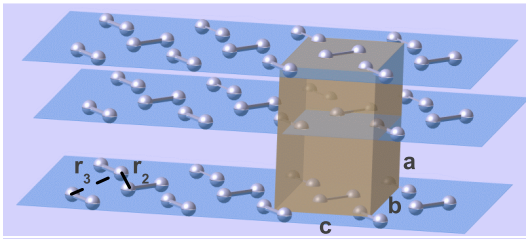

FIG. 1 (color online). View of the structure of the low pressure phase of bromine (*Cmca*, space group No. 64). The layered structure is emphasized and the unit cell is depicted. The EXAFS measurements here presented have allowed us to follow the pressure evolution of the intramolecular distance and the next-neighbor distances, r_2 and r_3.

PRL 99, 015501 (2007) PHYSICAL REVIEW LETTERS week ending 6 JULY 2007

ment with electrical conductivity experiments [11]. In fact, electrical conduction experiments in iodine [12,13] show that the electrical resistivity drops down abruptly from 0 to 13 GPa in the direction perpendicular to the I_2 layers and from 0 to 18 GPa in the layers' directions as it has been discussed in [14]. Different calculations [5,13–15] indicate that the interlayer interaction is responsible for the progressive gap closure through orbital resonance.

Recent investigations have shown the presence of an intermediate incommensurate modulated phase [2,16] leading to a revision of the halogens' phase diagram. This intermediate phase has been well characterized in the case of iodine [2], showing nearest interatomic distances continuously distributed between the bond length of I_2 in the molecular crystal and the nearest interatomic distance in the fully dissociated monatomic crystal. The transition to the incommensurate modulated phase takes place at about 23 GPa for iodine and 84 GPa for bromine. The dissociation pressures are pushed further to pressures of about 30 and 115 GPa for iodine and bromine, respectively [16].

The observation of an evolution of the intramolecular distance in iodine at the first stages of compression [17] will modify the values of the key parameter of reduced atomic volume. This, added to the discovery of the intermediate incommensurate phase and the shift of the different transition pressures, calls for a revision of our image of the high pressure evolution of halogens. In this Letter we show that the bromine intramolecular distance not only significantly evolves with pressure, but also its variation shows a sharp discontinuity at 25 GPa, which evidences a phase transition. The consequence on the case of iodine will be discussed.

Our experiments were performed at the ID24 energy dispersive extended x-ray-absorption fine structure spectroscopy (EXAFS) beam line [18,19] of the European Synchrotron Radiation Facility (ESRF, Grenoble, France) using a specially designed optics [20,21]. The x-ray beam with an energy window around the bromine K edge, was focused both in the horizontal and vertical planes to reach a 10×10 μm^2 spot. Pressure was applied using a diamond anvil cell at room temperature. The solid sample was loaded in the cell at liquid nitrogen temperature in an argon atmosphere to avoid sample contamination. Two different experiments were performed. In the first one, pressure was calibrated from the bromine equation of state [5] monitoring the (111) and (112) diffraction peaks. In this experiment a maximum pressure of 61 GPa was reached. In the second experiment the evolution of the full width at half maximum of the Br K edge near-edge peak was used for the pressure calibration [14] and a maximum pressure of 75 GPa was attained. In all experiments ruby chips were included for pressure calibration, but their signals were not found. No pressure transmitting medium was introduced. The noncontamination of the sample was easily checked visually as the color of bromine evolves from red to yellow when it is in contact with air. A further check comes from the preedge peak (see Fig. 2), the intensity of which rapidly decreases with contamination. In contrast with our previous work on bromine [14], both the x-ray-absorption near-edge structure (XANES) and EXAFS part of the spectra were obtained.

The x-ray absorption Br K edge preedge strong peak (see inset of Fig. 2) corresponds to the transition of the photoelectron to the first nonoccupied states in the electronic density of states. These states derive from the σ^* antibonding energy level of the Br_2 molecule [22]. Figure 2 shows the evolution of the FWHM of this peak as a function of pressure. The already observed discontinuity in the slope of this feature at 25 GPa [14] is then confirmed by both experiments and is even better defined. We observe in Fig. 2 a further change in the evolution of the FWHM at 65 ± 5 GPa. The x-ray absorption preedge peak is followed at higher photoelectron energies in the spectra by the Br K edge absorption jump. We have followed the position of the Br K edge at the inflexion point of the absorption jump. Its evolution with pressure is linear with a value at ambient pressure of 13 471 eV and a slope of 0.02 eV GPa^{-1}.

The EXAFS oscillations were extracted by usual technics and are shown in Fig. 3(a) for some selected data. The most important contribution to the signal is due to the single scattering path of the photoelectron inside the molecule. With increasing pressure, contributions from second and higher neighboring shells become progressively important. Our data analysis includes the *ab initio* calculation of the atomic scattering amplitude and phase shift for each scattering path using the FEFF [23] code and the fit with the structural model of bromine using the FEFFIT code [24]. In addition, we have constrained our data analysis so that the atomic volume at the measured pressure corresponds, within the error bars, to the one measured by x-ray diffraction [5]. The obtained fits, shown in Fig. 3(a), are remarkably satisfactory up to 68 GPa. The interatomic distances

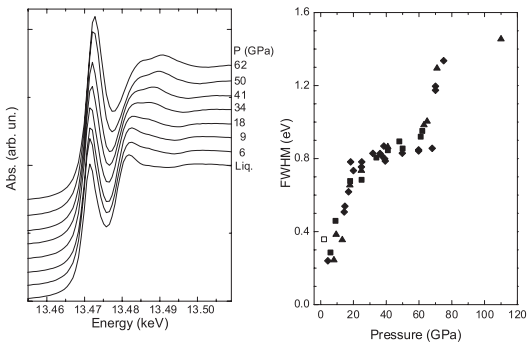

FIG. 2. Left panel: Pressure evolution of the bromine near-edge x-ray absorption fine structure at the Br K edge. Right panel: evolution of the FWHM of the preedge peak. The open square is for a single crystal signal and the filled symbols correspond to powder data obtained in three different experiments, including the one of Ref. [14] (triangles).

PRL 99, 015501 (2007) PHYSICAL REVIEW LETTERS week ending 6 JULY 2007

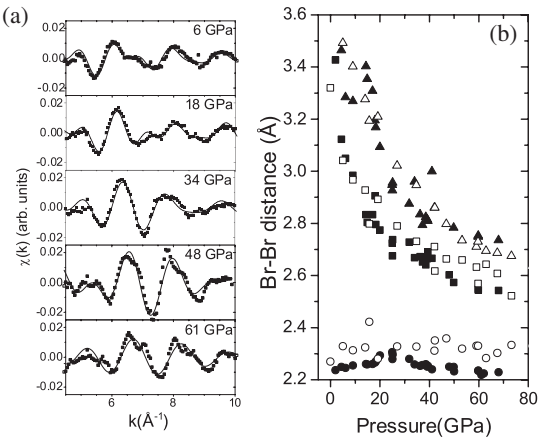

FIG. 3. Panel (a): EXAFS oscillations at the bromine K edge as a function of pressure (dots) and their fit (lines) with the structural model (see text). The k-range extension is limited by the presence of x-ray diffraction glitches from the single crystal diamond anvils (not shown). Panel (b): bromine molecular distance evolution with pressure obtained from the analysis of the EXAFS data from our two separate experiments (filled markers) compared to the x-ray diffraction results from [5] (open markers). Different symbols are for the intramolecular distance and the r_2 and r_3 distances.

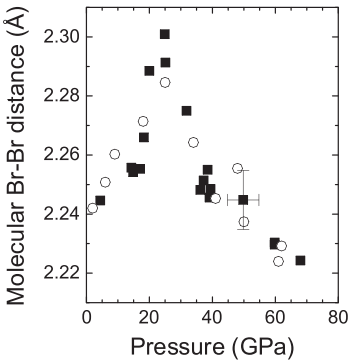

FIG. 4. Intramolecular distance evolution obtained by EXAFS analysis. The different symbols hold for the two different experiments. The maximum elongation of the Br_2 molecule is obtained at 25 ± 5 GPa, where a phase transition takes place.

obtained from the EXAFS fits are shown in Fig. 3(b) and compared with the ones obtained by x-ray diffraction by Fujihisa *et al.* [5].

The fitting constraint on the atomic volume leads to a coupling between the EXAFS results on the second and third neighbor distances, that appear to be in very good agreement with the x-ray diffraction data [5]. There is no geometrical constraint on the first neighbor distance, for which the EXAFS is more sensitive. Within the error bars, there is agreement between the results from the two techniques. EXAFS being a local probe, the nearest neighbor distances are determined with a very high accuracy, whereas the second and third neighbor distances are more scattered. Figure 4 shows only the bromine intramolecular distances as obtained from our EXAFS experiments. The agreement between our two EXAFS experiments is remarkable. It appears here clearly that contrary to what has been shown in all previous works, the bromine intramolecular distance evolves with pressure. But more remarkable, the bromine molecule elongates by about 0.06 Å from room pressure up to 25 GPa, and then it contracts of about 0.08 Å up to 68 GPa. Such a small variation could not be detected in the previous x-ray diffraction experiment since the errors in the determination of the molecular distance were comparable with the variations observed in the present study. All fits up to 68 GPa were reliable within the same structural model corresponding to the molecular *Cmca* phase. We recall here that strong changes in the x-ray absorption preedge peak are observed at 65 ± 5 GPa. For pressures above this value, we have tested different structural models in the EXAFS fit: (i) the body-centered orthorhombic *Imma* phase corresponding to the molecule dissociation observed in bromine at 115 GPa and in iodine at 30 GPa; (ii) the recently discovered incommensurably modulated high pressure phase of iodine [2] observed before dissociation. All attempts of improvement of the EXAFS fits within these models failed. However, a good fit could be obtained using a simple model that considered two different Br-Br distances at 2.22 and 2.56 Å. A mixture of the *Cmca* phase with either of the above mentioned high pressure structures could agree with this last fit. In fact, as it can be seen in Fig. 2, the data at 70 and 75 GPa correspond to a zone of rapid change of the preedge peak shape, which can be assigned to a phase transition domain. The combination of our EXAFS and near-edge observations is reasonably compatible with a structural phase transformation at 65 ± 5 GPa, implying important changes in the electronic structure.

Kume *et al.* [16] pointed out the appearance of a new Raman band (called X by them) at 60 GPa in bromine that within the error bars is consistent with our results. A pressure transformation at 65 ± 5 GPa is considerably below the transition pressure towards the modulated phase (84 GPa). We speculate that the nature of this phase transformation makes it more sensitive to local probes as Raman and x-ray-absorption spectroscopy (XAS).

Let us now return to the unusual behavior of the bromine interatomic distance within the *Cmca* phase. The increase of the intramolecular distance with pressure that is observed up to 25 GPa is the one expected for such an anisotropic system. In fact, a linear dilation of the iodine intramolecular distance with pressure is exactly what was also measured in solid and liquid iodine using EXAFS [17] and is characteristic of other anisotropic systems [25]. The sudden change appearing at 25 GPa clearly points out to the onset of a phase transformation and is supported by Raman experiments that show the splitting of some modes at 25 GPa [16] and by the discontinuity in the width of the XAS preedge peak. However, there is no discontinuous

PRL 99, 015501 (2007) PHYSICAL REVIEW LETTERS week ending 6 JULY 2007

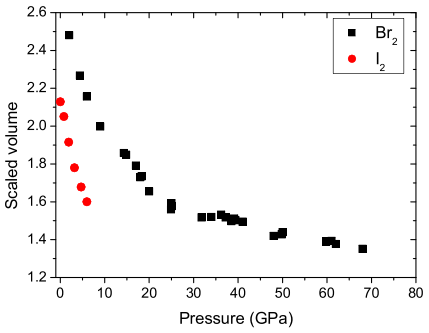

FIG. 5 (color online). Pressure evolution of the scaled volume (see text) of solid iodine and bromine. The atomic volumes are obtained from Ref. [5]. The pressure dependence of the intramolecular distance of iodine are from Ref. [17] and of bromine from this work.

evolution of the next-neighbor measured EXAFS distances as well as in the published x-ray diffraction structural parameters [5]. To try to get some more insight on the phase transformation at 25 GPa, let us turn to the reduced volume concept.

In Fig. 5, we compare the pressure evolution of the reduced volume of bromine and iodine as a function of pressure. The atomic volume values are the ones given in Ref. [5]. We have considered in both cases the pressure dependence of the molecular distance as obtained in the present work for bromine and the ones for iodine from Ref. [17]. In that way the reduced volume is here defined as $v_r = v_{at}/(8r_m^3)$, with r_m the molecular distance at the given pressure. The phase transition observed at 25 GPa for bromine translates into a sudden reduction of the pressure derivative of v_r taking place at $v_r = 1.5$. This reduction is representative to an evolution toward a reduced molecular character. From the figure we cannot exclude the presence of a small plateau in v_r appearing at 25 GPa.

In the case of iodine, the measured interatomic distances only allow us to determine its reduced volume up to a maximum value of $v_r = 1.6$, just above the phase transition limit of bromine. If we extrapolate the reduced volume values for iodine, the value of $v_r = 1.5$ would be attained in iodine at approximately 8–10 GPa. Interestingly, in the pressure dependence of the Raman spectra of bromine and iodine, Kume *et al.* [16] show that the crossover of the $A_g(S)$ and $B_{3g}(S)$ modes and a splitting of the $A_g(L)$ and $B_{3g}(L)$ modes takes place in the domain 25–32 GPa for bromine and at about 10 GPa for iodine.

In conclusion, EXAFS and XANES data show the existence of a phase transition in solid bromine at 25 ± 5 GPa. The phase transformation is associated with variations of the molecular character of the structure of Br_2. The pressure dependence of a reduced volume compared to published Raman data [16], shows that the intramolecular evolution with pressure described here could be a more general behavior applying to other molecular systems as the other halogens and particularly iodine. The exact nature of the observed phase transition, which appears to be associated with modifications in the electronic structure, remains to be clarified.

[1] K. A. Johnson and N. W. Ashcroft, Nature (London) **403**, 632 (2000).
[2] K. Takemura, K. Sato, H. Fujihisa, and M. Onoda, Nature (London) **423**, 971 (2003).
[3] M. I. Eremets, R. J. Hemley, H. K. Mao, and E. Gregoryanz, Nature (London) **411**, 170 (2001).
[4] R. J. Hemley, Annu. Rev. Phys. Chem. **51**, 763 (2000).
[5] H. Fujihisa, Y. Fujii, K. Takemura, and O. Shimomura, J. Phys. Chem. Solids **56**, 1439 (1995).
[6] K. Takemura, S. Minomura, O. Shimomura, and Y. Fujii, Phys. Rev. Lett. **45**, 1881 (1980).
[7] K. Takemura, S. Minomura, O. Shimomura, Y. Fujii, and J. D. Axe, Phys. Rev. B **26**, 998 (1982).
[8] Y. Fujii, K. Hase, N. Hamaya, Y. Ohishi, and A. Onodera, Phys. Rev. Lett. **58**, 796 (1987).
[9] Y. Fujii, K. Hase, Y. Ohishi, H. Fujihisa, N. Hamaya, K. Takemura, O. Shimomura, T. Kikegawa, Y. Amemiya, and T. Matsushita, Phys. Rev. Lett. **63**, 536 (1989).
[10] R. Reichlin, A. K. McMahan, M. Ross, S. Martin, J. Hu, R. J. Hemley, H.-k. Mao, and Y. Wu, Phys. Rev. B **49**, 3725 (1994).
[11] K. Shimizu, K. Amaya, and S. Endo, in *High Pressure Science and Technology: Proceedings of the Joint XV AIRAPT and XXXIII EHPRG International Conference, Warsaw, Poland, 1995* (World Scientific, Singapore, 1996), p. 498.
[12] A. S. Balchan and H. G. Drickamer, J. Chem. Phys. **34**, 1948 (1961).
[13] B. M. Riggleman and H. G. Drickamer, J. Chem. Phys. **38**, 2721 (1963).
[14] A. San-Miguel, H. Libotte, J. P. Gaspard, M. Gauthier, A. Polian, and J. P. Itié, Eur. Phys. J. B **17**, 227 (2000).
[15] F. Siringo, F. Piccitto, and R. Pucci, High Press. Res. **3**, 162 (1990).
[16] T. Kume, T. Hiraoka, Y. Ohya, S. Sasaki, and H. Shimizu, Phys. Rev. Lett. **94**, 065506 (2005).
[17] U. Buontempo, A. Filipponi, D. Martínez-García, P. Postorino, M. Mezouar, and J. P. Itié, Phys. Rev. Lett. **80**, 1912 (1998).
[18] M. Hagelstein, A. San Miguel, A. Fontaine, and J. Goulon, J. Phys. IV (France) **7**, 303 (1997).
[19] S. Pascarelli *et al.*, J. Synchrotron Radiat. **6**, 146 (1999).
[20] J. Pellicer-Porres, A. San-Miguel, and A. Fontaine, J. Synchrotron Radiat. **5**, 1250 (1998).
[21] S. Pascarelli, O. Mathon, M. Munoz, Mairs, and J. Susini, J. Synchrotron Radiat. **13**, 351 (2006).
[22] S. M. Heald and E. A. Stern, Phys. Rev. B **17**, 4069 (1978).
[23] A. L. Ankudinov, B. Ravel, J. J. Rehr, and S. D. Conradson, Phys. Rev. B **58**, 7565 (1998).
[24] M. Newville, B. Ravel, D. Haskel, J. J. Rehr, E. A. Stern, and Y. Yacoby, Physica (Amsterdam) **208B–209B**, 154 (1995).
[25] J. Pellicer-Porres, A. Segura, V. Munoz, and A. San-Miguel, Phys. Rev. B **60**, 3757 (1999).

4.4 Conclusion

The precise study of the intramolecular distance in bromine under pressure allows us to redefine the scaling parameter used in the halogen systematics. Indeed, Fujihisa and co-workers initially assumed that the intramolecular distance is constant but our experimental results underline it is not. This scaling rule is reassessed as illustrated in our paper. The intramolecular distance exhibits a maximum around 25 GPa corresponding to a new phase transition in bromine. Even if the phase transition mechanism is not identified, the molecular character of bromine is clearly affected. These conclusions are in good agreement with the results of Kume *et al.* using Raman spectroscopy. The transition to the incommensurate structure is also observed around 65 GPa.

Even if the structure of this new phase is not elucidated, a new limiting value of the scaled volume is introduced: $v_s = 1.5$. In the case of iodine, a similar transition should occur at about 10 GPa. This point calls further studies in order to confirm the new scaling rule.

Our results about the evolution of the intramolecular distance combined with the latest results of Kume and co-workers concerning the incommensurate structure deeply modify the current view of the behaviour of halogen group under pressure. The electronic and crystallographic structures of the new phase need to be clarified.

Chapter 5

Actinides

5.1 Introduction

Actinides are important elements not only because of their nuclear properties but also because of the fundamental issues related to their ground state properties and their pressure evolution. The most exciting element is americium that has a pivotal position in the series. The structural behaviour of the actinide elements - the so-called $5f$-electron series - is tightly linked to the behaviour of the f-electrons (table 5.1) [109, 110]. These elements can be classified in two groups. The light actinides (Ac, Th, Pa, U, Np, and Pu) have delocalized $5f$ electrons involved in the metallic bonding at atmospheric pressure and exhibit a small volume (see figure 5.1) decreasing with the number of electrons and unusual low-symmetry structures: even if Ac and Th have the FCC structure, the crystal structure of the next four elements (Pa, U, Np, and Pu) show an increasing complexity[1]. In contrast, the heavy actinides, also called transplutonium metals, have localized $5f$ electrons and display symmetrical structures. From Am to Cf, the elements exhibit high symmetry and close-packed structures. In this case the localized $5f$ electrons play a minor role in the chemical bonding. In this regard they mimic the lanthanide metals.

Ac	Th	Pa	U
$5f^0 6d^1 7s^2$	$5f^0 6d^2 7s^2$	$5f^2 6d^1 7s^2$	$5f^3 6d^1 7s^2$
Np	Pu	Am	Cm
$5f^4 6d^1 7s^2$	$5f^6 6d^0 7s^2$	$5f^7 6d^0 7s^2$	$5f^7 6d^1 7s^2$
Bk	Cf	Es	Fm
$5f^9 6d^0 7s^2$	$5f^{10} 6d^0 7s^2$	$5f^{11} 6d^0 7s^2$	$5f^{12} 6d^0 7s^2$
Md	No	Lr	Rf
$5f^{13} 6d^0 7s^2$	$5f^{14} 6d^0 7s^2$	$5f^{14} 7s^2 7p^1$	$5f^{14} 6d^2 7s^2$

Table 5.1: The electronic configuration of the actinide elements.

The light actinides, up to Pu, behave like the non-magnetic transition metals with a parabolic evolution of the Wigner-Seitz radii as a function of the number of f-electrons. This situation is described by a Friedel model (rectangular density of electronic states) similar to the one applied

[1] Pu has a monoclinic unit cell with 16 atoms.

to the transition elements [111]. At the opposite, the volume of transplutonium elements is roughly constant similarly to the lanthanides.

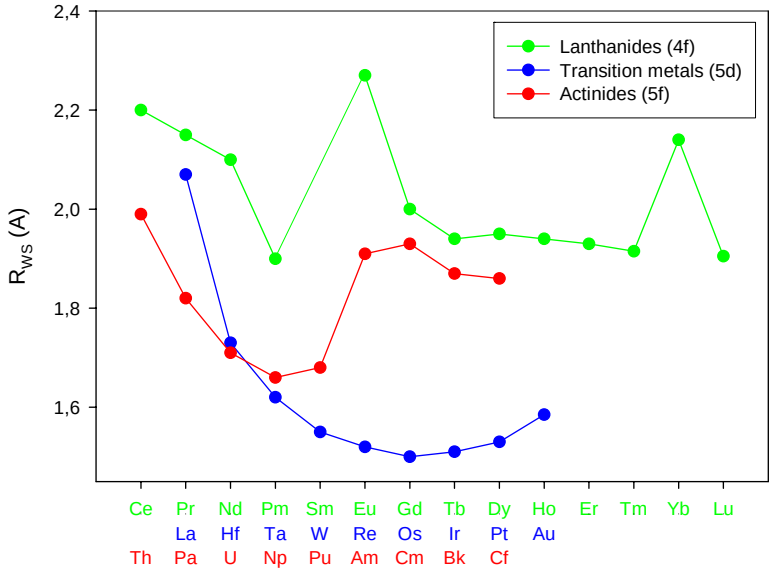

Figure 5.1: The Wigner-Seitz radii, R_{WS}, for the $5d$, $4f$ and $5f$-electron elements. R_{WS} and the atomic volume, V_{at} are related by $V_{at} = \frac{4\pi}{3} R_{WS}^3$. The parabolic behaviour of the Th-Pu series is the proof that the f-electrons are itinerant.

The f-electron elements are difficult to describe within the LDA approximation, and it is clearly impossible for the heavy actinides. Indeed the on-site interaction between the f electrons is strong enough to overcome the kinetic energy [110, 112]. Thus theoretical study of the actinides is far more difficult when the electrons are strongly correlated.

Americium plays a special role as the previous elements have delocalized f electrons and it is the first among the actinides to have localized $5f$ electrons. The f-electrons of the lanthanide and actinide elements are greatly affected by pressure. In some of the early lanthanide metals, it is interesting to note that after acquiring $4f$-electron character in their bonding by applying high pressures, they adopt some of the same low-symmetry structures exhibited by the protactinium-plutonium metals that have itinerant $5f$ electrons. The discontinuity in the volume at Am could be explained by the removal of some of the $5f$ contribution to the chemical bonding, i.e. by the localization of the $5f$ electrons. This raises the question of whether applying pressure on americium and the following transplutonium metals significantly changes their bonding properties. As these actinides have more spatially extended f-electrons than their lanthanide counterparts, it should be easier to force their $5f$electrons to contribute to bonding by applying pressure i. e. they may be more sensitive to the effects of pressure than their lanthanide counterparts.

5.2 Americium under pressure

We analyzed in detail the different structures of americium under hydrostatic pressure in a collaborative work including the teams of scientists from Oak Ridge National Laboratory, the European Institute of Transuranium Elements of Karlsruhe and the ESRF. Americium displays significant structural differences at atmospheric pressure between its near neighbour, Plutonium and its lanthanide homologue, Europium. In the next two papers we present the structural

analysis, by X-ray diffraction, of americium up to 100 GPa. The main interest is located in the localization - or delocalization - process of the f-electrons and the symmetry of the structures.

5.3 Covalent bonding in narrow band systems : the Friedel Model

The transition metals are characterized by a narrow and partially filled d-band which drives their cohesive properties. A simple treatment was proposed by Friedel [111] assuming a constant density of states (see figure 5.2). With a density of state, n_d , given by (5.1)

$$n_d(E) = \frac{10}{W} \tag{5.1}$$

the resulting electronic energy, (in absolute value) simply writes

$$E_a = 5\frac{N_d}{10}\left(1 - \frac{N_d}{10}\right)W \tag{5.2}$$

where N_d is the number of d electrons and W is the electronic bandwidth. The maximum of the cohesive energy is obtained for a half-filled band. This parabolic shape for the cohesive energy is experimentally observed for $4d$ and $5d$ elements[2] but not for the $3d$ series where the late transition metals are magnetic and correlation effects as have to be taken into account. Let us recall that a second-moment argument shows that the bandwidth is roughly given by

$$W \propto \sqrt{Z}\beta \tag{5.3}$$

where Z is the number of neighbours and β is the resonance integral. The atomic volumes show the opposite trend with a minimum for the half filled band.

Light actinides behave the same way : the atomic volume show a parabolic trend up to Pu (see fig. 5.1).

The density of states is modellized by

$$n_f(E) = \frac{14}{W} \tag{5.4}$$

and the electronic energy writes

$$E_a = 7\frac{N_f}{14}\left(1 - \frac{N_f}{14}\right)W \tag{5.5}$$

5.4 Roman to gothic transition

In addition, a distortion of a closed packed structure may produce an energy gain. Indeed, if a gap of width G, originating from a Peierls distortion, appears in the rectangular density of states, as illustrated in figure 5.2, the resulting electronic energy is given by

$$E_a = -7(W - G)\frac{N_F}{14}\left(\frac{W}{W - G} - \frac{N_F}{14}\right) \tag{5.6}$$

[2]Finally, the body centered cubic (BCC) structure appears to be more stable for a half-filled d-band than the face centered cubic (FCC) structure. This is linked to the strong bimodal shape of the related BCC density of states with a weak density of states at the Fermi level in comparison with the FCC structure. However, at high temperature, the entropic contribution is favourable to the FCC structure. The structural sequence is thus FCC-HCP-BCC-HCP-FCC.

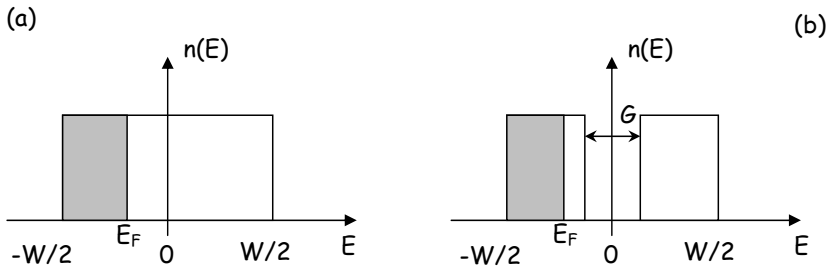

Figure 5.2: Schematic description of the electronic density of states of the Friedel d-band without (a) and with (b) a gap. The width of the gap is G.

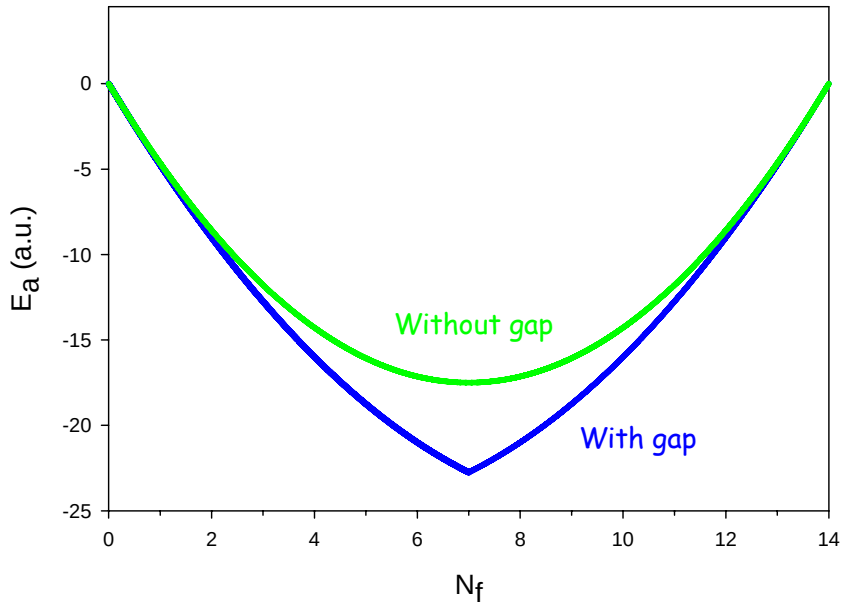

Figure 5.3: Electronic energy related to the densities of states given in figure 5.2. (Roman to gothic transition).

for $0 \leq N_f \leq 7$ and a similar expression for $7 \leq N_f \leq 14$ (see figure 5.4). Assuming that the bandwidth is the same in the two cases, W, the distorted structure is more stable: the maximum energy difference is $\frac{7}{4}G$.

It can be shown that the effect is enhanced in narrow bands.

Experimentally, it is observed that the early actinides are distorted, and so does americium when pressure is applied. It transforms from a strongly correlated system into a delocalized (or itinerant) electron system.

When the electronic band are very narrow, electron-electron correlations have to be taken into account, i.e. for the partially-localized electrons. As mentioned in the introduction, this point can not be performed within the LDA formalism. In the late 70's Friedel and co-workers [113, 114], described a perturbation approach within the tight-binding scheme. However, their works have never been continued, to our knowledge.

If the intraatomic correlation coefficient, U, is added to our model, we have the following

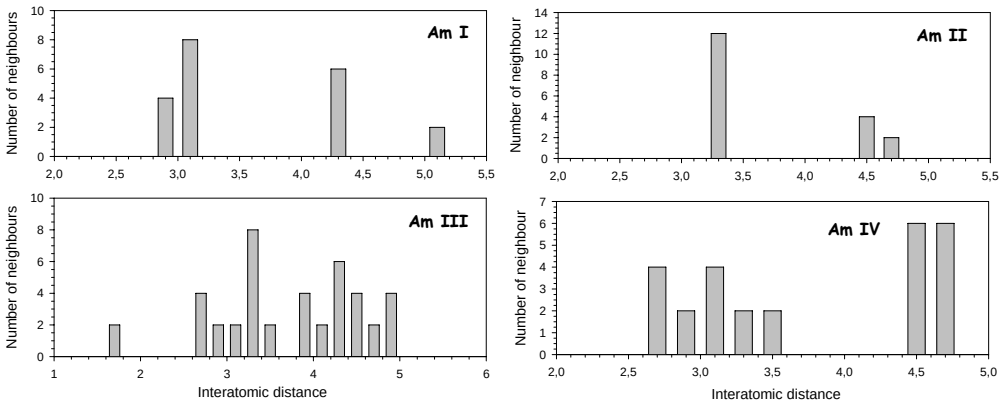

Figure 5.4: Histograms of the number of neighbours as a function of the interatomic distances. $Am-I$ and $Am-II$ are more symmetric than $Am-III$ and $Am-IV$ where the interatomic distance distribution is much wider.

relation to the second order in $\frac{U}{\beta_0}$:

$$E = -\sqrt{Z}\beta_0 r^{-q} + ZV_0 r^{-p} + P\gamma r^3 - K_u \frac{U^2}{\beta_0} r^q \tag{5.7}$$

The last term of this expression is similar to a negative pressure if $q = 3$. So pressure and electronic correlation have opposite influences. This is compatible with our structural observation of Am-III and Am-IV, respectively similar to $\gamma - Pu$ and $\alpha - U$ where the correlation effects are reduced.

VOLUME 85, NUMBER 14 PHYSICAL REVIEW LETTERS 2 OCTOBER 2000

Pressure Induces Major Changes in the Nature of Americium's 5f Electrons

S. Heathman,[1] R. G. Haire,[2] T. Le Bihan,[3] A. Lindbaum,[1] K. Litfin,[1] Y. Méresse,[1] and H. Libotte[3]

[1]*European Commission, Joint Research Center, Institute for Transuranium Elements, Postfach 2340, D-76125 Karlsruhe, Germany*

[2]*Oak Ridge National Laboratory, P.O. Box 2008 MS-6375, Oak Ridge, Tennessee 37831-6375*

[3]*European Synchrotron Radiation Facility (ESRF), B.P. 220, F-38043 Grenoble, France*

(Received 13 June 2000)

Americium occupies a pivotal position in the actinide series with regard to the behavior of 5f electrons. High-pressure techniques together with synchrotron radiation have been used to determine the structural behavior up to 100 GPa. We have resolved earlier controversial findings regarding americium and find that our experimental results are in discord with recent theoretical predictions. We have two new findings: (1) that there exists a critical, new structural link between americium under pressure and its near neighbor, plutonium; and (2) that the 5f electron delocalization in americium occurs in two rather than one step.

PACS numbers: 61.50.Ks, 64.70.Kb

Over the past decade there have been several studies of lanthanide metals pursuing the occurrence of f electron delocalization by pressure, where these new investigations employ advancements in experimental techniques. The reader is referred to reviews [1,2], as well as recent efforts on cerium [3] and neodymium [4] metals. Some early lanthanide ($4f$) metals in the first half of this series delocalize under pressure and can adopt low-symmetry structures exhibited by the early actinide metals.

The involvement of f electrons in bonding, at normal or high pressure, is a function of the extension of the wave functions and the comparable energies of hybrid states relative to electronic levels without f character. These conditions change with increasing nuclear charge, type of f orbital (e.g., $4f$ or $5f$), etc. The $5f$ electrons of americium (the element following plutonium) are nonbonding (localized) at normal pressure, as are the $5f$ electrons for the remaining elements in the actinide series. In this sense, americium occupies an important pivotal position in the $5f$ series, which is in part reflected in the sudden change in atomic volume in going from plutonium, which has itinerant $5f$ electrons, to americium (see Fig. 1 inset) at atmospheric pressure. The smaller atomic volumes of the protactinium through plutonium metals result from the additional bonding supplied by $5f$ electrons.

Americium also displays significant structural differences at atmospheric pressure between its near neighbor, plutonium and its lanthanide homolog, europium. Its localized $5f$ electrons and special nonmagnetic $5f^6$ ($J = 0$) configuration lead to superconducting properties at low temperatures [5].

Previous results with americium were obtained at lower pressures [6–8] than here. Our data are in general agreement with the fact that the double hexagonal close-packed phase (dhcp, Am I phase) transforms at low pressure to a face-centered cubic phase (fcc, Am II phase). However, important differences are found at higher pressures, both in structural assignments and more importantly, in the interpretation of electronic behavior for the structures at higher pressure.

The intent of the present study was to understand correctly the behavior of americium up to 100 GPa. This is the first time the structural behavior of americium under pressure using synchrotron radiation has been reported.

Foils of americium [^{243}Am isotope ($t_{1/2} = 7 \times 10^3$ yr)] metal were prepared by vacuum vapor deposition after reduction of americium dioxide with lanthanum metal. Mass spectrographic analysis indicated purity of $>99.9\%$ and x-ray analysis showed the metal exhibited a double hexagonal close-packed structure [$a_0 = 3.467(4)$ and $c_0 = 11.240(8)$ Å, where 10 Å = 1 nm] in excellent accord with literature values [6–8]. Small pieces (5–10 μg each) were taken for the studies.

Diamond anvil cells are now widely used for studying minute quantities (a few μg) of materials up to and beyond the megabar range [9]. In our experiment both Syassen-Holzapfel (up to 60 GPa) and Cornell-type (up to 100 GPa) pressure cells have been used. The experiments were performed at room temperature at the European Synchrotron Radiation Facility (ESRF) ID30 beam line in the angular dispersive mode. Nitrogen was

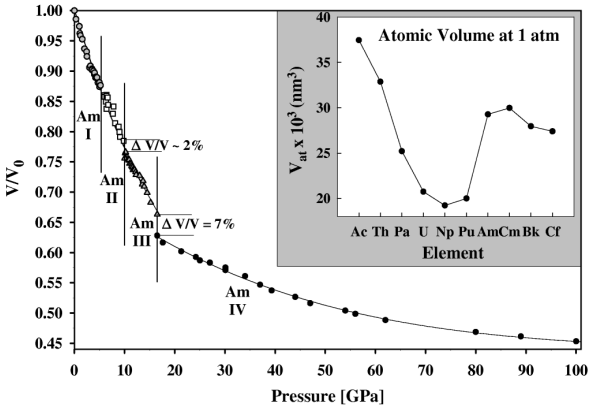

FIG. 1. Relative volume vs pressure curve for americium. The inset shows the atomic volume at ambient pressure across the actinide series.

0031-9007/00/85(14)/2961(4)$15.00

used as the pressure transmitting medium in the Syassen-Holzapfel cells enabling hydrostatic conditions between 0 to 18 GPa where the first three high-pressure phases were observed. Silicone oil was used as the pressure medium for the Cornell cells in the experiments up to 100 GPa. Pressure markers were ruby (fluorescence technique [9]) or platinum metal (via its equation of state [9]). Diffraction images were captured with a Fastscan image plate detector [10]. The diffraction images were then processed using the ESRF FIT2D program [11] and interplanar distances for the data collected were calculated. Indexing programs were employed to suggest possible structures, which were then refined with Rietveld analysis [12].

With the application of pressure, the dhcp form ($P6_3/mmc$, Am I) of americium converts to a fcc structure ($Fm3m$, Am II) at 6.1(2) GPa. This fcc phase is identical to the high-temperature phase reported for americium metal above 650 °C. This dhcp to fcc transformation requires little energy and probably indicates an increase in the d character of the bonding. In Fig. 1, one observes a smooth transition for the Am I to Am II structural change and that the fcc compression curve is a continuous extension of the dhcp compression curve, which suggests each phase has a comparable bulk modulus.

With additional pressure, the fcc Am II phase transforms to a third Am III phase at 10.0(2) GPa. The structure of this phase has been most controversial in past studies of americium. It has been assigned previously as a monoclinic structure [7] and a distorted, face-centered cubic structure [8]. In neither of these earlier works was delocalization of americium's f electrons considered in conjunction with this Am III phase.

As a result of the larger number of high quality diffraction data, we successfully arrived at the correct assignment for the Am III phase. The structure has a face-centered orthorhombic cell (space group $Fddd$, Am on the 8a sites, all position parameters fixed by symmetry) and exists between 10 and ~17 GPa (see later section on the Am IV phase). A Rietveld refinement of the data is shown in Fig. 2.

A crucial, and new, aspect is that this Am III structure is the same as is known for the gamma phase of plutonium metal, which is a slightly distorted hexagonal, close-packed structure considered to have 5f electrons involved in its metallic bonding. Thus, under pressure the electronic energy levels of americium are altered sufficiently so that it adopts one of the structures established for its near neighbor, plutonium, and the bonding in americium now has f electron character. This finding provides new insight into the role of the 5f electrons in americium as pressure is applied. A small "collapse" (~2%) in relative volume can be extracted from the data shown in Fig. 1.

The next phase, Am IV, was observed as early as 16(1) GPa but was the exclusive phase by 17.5 GPa. It was retained up to 100 GPa, the highest pressure for which we report data. Both of the previous groups reporting an Am IV phase assigned it to an alpha-uranium structure, and suggested that the appearance of this structure reflected itinerant 5f electrons in the metallic bonding.

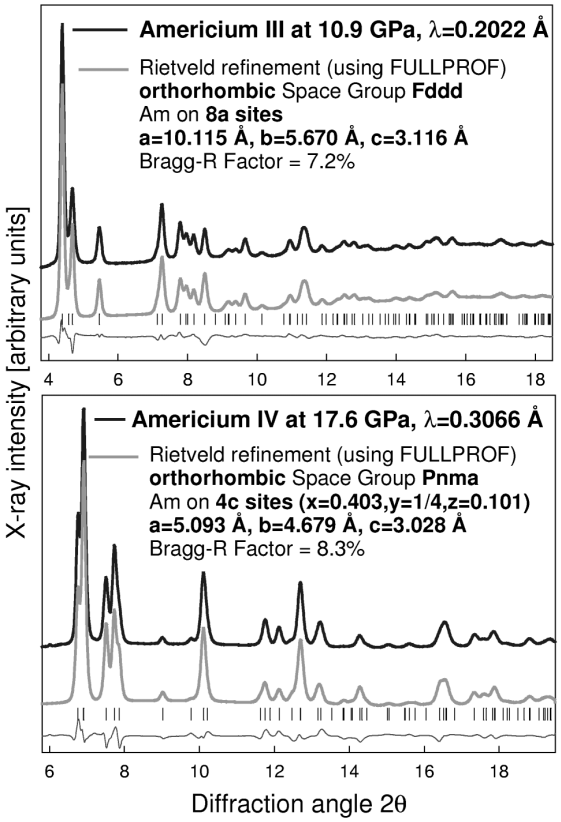

FIG. 2. Rietveld fits for the Am III and Am IV structures at 10.9 and 17.6 GPa showing the observed (top lines) and calculated (center lines) diffraction patterns, reflection tick marks, and difference profiles (lower trace).

A Rietveld refinement for our Am IV data (Fig. 2) establishes that Am IV has an orthorhombic structure similar to the base-centered alpha-uranium structure ($Cmcm$), but with a different space group ($Pnma$, primitive orthorhombic). The lattice parameters and atomic positions at 17.6 GPa are given in the figure.

Our Am IV structure represents a modified alpha-uranium structure. If the z value of the 4c sites in the $Pnma$ structure is placed at zero, one then obtains the higher-symmetry, alpha-uranium structure with the base-centered orthorhombic unit cell. This is depicted in Fig. 3, where the change in structure is demonstrated. Given the excellent quality of our data and the Rietveld fit (Fig. 2), we believe that the $Pnma$ structure is the correct assignment for the Am IV phase.

The four different structures observed for americium in this study are shown in Fig. 4. The structural transformations can be envisioned as occurring from a shift and distortion of the planes and a change in stacking sequence. This structural progression, which results from

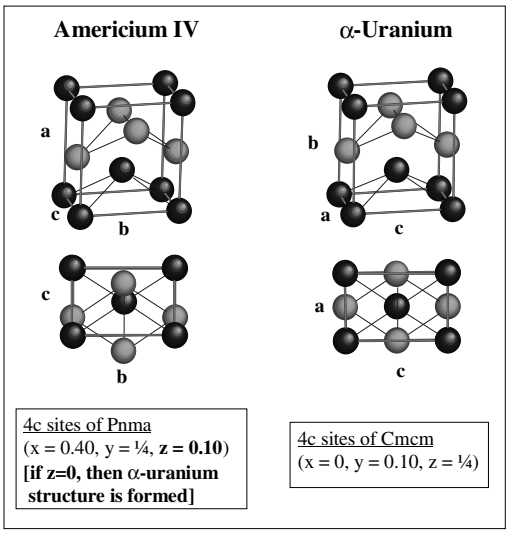

FIG. 3. Orthorhombic cells for the Am IV and alpha-uranium structures. Setting the z value of the 4c sites in the *Pnma* structure (left) to 0 means a shifting of the planes with the light atoms relative to the dark ones in the c direction so that one obtains the alpha-uranium structure (right).

changes in the metallic bonding, provides an increase in the crystal density.

In Fig. 1 a plot of the relative volumes (V/V_0, where V_0 is the volume at atmospheric pressure) versus pressure is shown, where the different structural regions and the relative volume changes are shown. We attribute both the 2% Am II to Am III transition and the 7% Am III to Am IV transition to f electron delocalization processes.

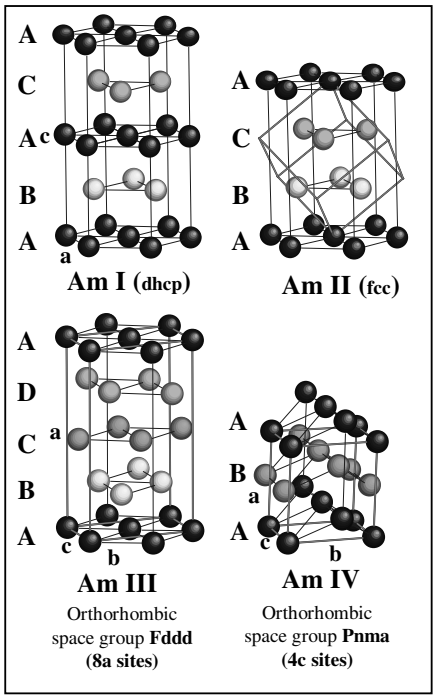

FIG. 4. The four structures observed for americium under pressure.

The collapse of 7% observed here is lower than the 25% change suggested in the recent theoretical predictions for americium metal under pressure [13]. The theoretical treatment also assigns the volume collapse as being due to the incorporation of f electrons in the metallic bonding of americium. Two conclusions were reached in this theoretical work: (1) that the high-pressure phase of americium was predicted to be the monoclinic alpha plutonium structure; and (2) that a volume collapse of 25% should accompany the incorporation of f electrons into the metallic bonding. Our experimental findings are in discord with both of these suggestions.

The isothermal bulk moduli and their pressure derivatives were obtained by fitting the Birch and Murnaghan equations of state [14,15] to the low-pressure phases (regions of localized f electrons) to obtain the bulk modulus B_0 and its pressure derivative B_0'. Both calculations gave similar values, which were $B_0 = 29.7 \pm 1.5$ GPa and $B_0' = 3.7 \pm 0.2$, and $B_0 = 29.9 \pm 1.5$ GPa and $B_0' = 3.5 \pm 0.2$, respectively. These americium moduli are in line with values for the light lanthanide metals [1], but considerably smaller than the modulus of alpha plutonium (45 GPa), which has additional bonding from its itinerant f electrons.

Obtaining high quality experimental data for the structural behavior of americium metal under pressures up to 100 GPa (one megabar) permits the proper identification of the Am III and Am IV phases. New insights into the behavior of americium's $5f$ electrons under pressure and a mechanistic picture for the sequential conversion of americium from one phase to another under pressure are also obtained.

In addition to resolving the controversy regarding the structural behavior of americium in the 10–30 GPa region, this work has established two critical findings about the Am III and the Am IV structures. First, that the Am III phase is a face-centered orthorhombic structure (space group *Fddd*), which is the same structure displayed by gamma plutonium (atmospheric pressure between 206 and 319 °C), and the bonding now involves itinerant $5f$ electrons. Second, the Am IV structure appears to be a primitive orthorhombic structure (*Pnma*), rather than the base centered alpha-uranium structure as reported previously [1,16]. The Am IV structure shows a smaller compressibility with pressure (being more similar to that of uranium), as expected for a metal with appreciable $5f$-electron character in its bonding.

This work provides important new insights for understanding the pivotal position of americium in the actinide series with regard to the involvement of $5f$ electrons in metallic bonding. The quality of these data establishes firmly the experimental behavior of americium under

pressure, and should promote the convergence of experimental and theoretical views regarding the volume collapse and the $5f$ electron delocalization in americium under pressure.

This work was supported by the European Commission and by the Division of Chemical Sciences, Geoscience and Biosciences, Office of Basic Energy Science, USDOE, under Contract No. DE-ACO5-00OR22725 with Oak Ridge National Laboratory, managed by UT-Battelle, LLC. The ^{243}Am isotope used in the study was supplied by the DOE Transuranium Production Program at Oak Ridge National Laboratory. A. L., K. L., and Y. M. wish to thank the "Training and Mobility of Researchers" program of the European Union and the Austrian Science Foundation FWF (Project No. P-11581-PHY). The authors acknowledge useful discussions with G. H. Lander of ITU.

[1] U. Benedict and W. B. Holzapfel, in *Handbook on the Physics and Chemistry of the Rare Earths,* edited by K. A. Gschneidner, Jr., L. Eyring, G. H. Lander, and G. R. Choppin (Elsevier Science, Netherlands, 1993), Vol. 17, Chap. 113, pp. 245–300, and references therein.

[2] R. G. Haire, in *Resources, Science, Technology and Applications,* edited by R. Bautista and N. Jackson (TMS, Pennsylvania, 1991), pp. 449–462, and references therein.

[3] M. I. McMahon and R. J. Nelmes, Phys. Rev. Lett. **78**, 3884 (1997).

[4] G. N. Chesnut and Y. K. Vohra, Phys. Rev. B **61**, 3768 (2000).

[5] J. L. Smith and R. G. Haire, Science **200**, 535 (1978).

[6] J. Akella, Q. Johnson, and R. N. Schock, J. Geophys. Res. B **85**, 7056 (1980).

[7] R. B. Roof, J. Appl. Crystallogr. **14**, 447 (1981); Z. Kristallogr. B **15**, 307 (1982).

[8] U. Benedict, J. P. Itié, C. Dufour, S. Dabos, and J. C. Spirlet, Physica (Amsterdam) **139B/140B**, 284 (1986).

[9] See, for example, K. Brister, Rev. Sci. Instrum. **68**, 1629 (1997).

[10] M. Thoms *et al.,* Nucl. Instrum. Methods Phys. Res., Sect. A **413**, 175 (1998).

[11] A. P. Hammersley, ESRF Report No. ESRF97HA02T, 1997.

[12] J. Rodriguez-Carvajal, Physica (Amsterdam) **192B**, 55 (1993).

[13] Per Söderlind, R. Ahuja, O. Eriksson, B. Johansson, and J. M. Wills, Phys. Rev. B **61**, 8119 (2000).

[14] F. Birch, Phys. Rev. **71**, 809 (1947).

[15] F. D. Murnaghan, Am. J. Math. **49**, 235 (1937).

[16] R. B. Roof *et al.,* Science **207**, 1353 (1980).

PHYSICAL REVIEW B, VOLUME 63, 214101

High-pressure studies of americium metal: Insights into its position in the actinide series

A. Lindbaum,* S. Heathman, K. Litfin, and Y. Méresse
Joint Research Center, European Commission, Institute for Transuranium Elements, Postfach 2340, D-76125 Karlsruhe, Germany

R. G. Haire
Chemical and Analytical Sciences, Oak Ridge National Laboratory, P.O. Box 2008, Oak Ridge, Tennessee 37831-6375

T. Le Bihan and H. Libotte
European Synchrotron Radiation Facility, Boite Postale 220, F-38043 Grenoble, France
(Received 24 November 2000; published 26 April 2001)

Americium metal occupies a pivotal position in the actinide series, displaying localized f electron bonding while the four preceding members are recognized for their itinerant f electron behavior. Important insights into the nature of americium's f electrons with regard to metallic bonding and the relationship to that in the γ form of plutonium have been acquired through studies of americium up to 100 GPa. Synchrotron radiation and other experimental advances were used to obtain data of high quality and resolution to resolve fully the high-pressure crystal structures of americium metal. We have resolved controversial findings reported earlier for americium in the 10–30 GPa region, and also addressed the significant differences that exist between the reported theoretical and experimental volume collapses. In this work we found that the normal pressure double hexagonal close packed ($P6_3/mmc$) structure transforms at 6.1 GPa to a face centered cubic ($Fm3m$) phase. At 10.0 GPa, the latter converts to a face centered orthorhombic ($Fddd$) structure, which with additional pressure undergoes a further transformation to form a primitive orthorhombic structure ($Pnma$) at 16 GPa. The $Pnma$ structure is stable up to at least 100 GPa, the maximum pressure reported here. By identifying correctly the structural forms of the Am III and IV phases, the mechanisms for sequential conversion of the structures with pressure have been established. A critical aspect of these data is that the Am III phase is now believed to reflect the first involvement of americium's f electrons in the metallic bonding; additional involvement occurs in the Am IV phase. This work provides important insights for understanding the pivotal position of americium in the actinide series and should bring about the convergence of experimental and theoretical views regarding its pressure behavior.

DOI: 10.1103/PhysRevB.63.214101 PACS number(s): 61.10.Nz, 61.50.Ks, 61.66.Bi

I. INTRODUCTION

In recent years there has been an increased interest in the effect of high pressure on materials. Geologists have probed the behavior of materials under pressure and/or temperature for learning the physicochemistry of materials near the center of the earth. There has been a continued advancement and interest in studies involving the lanthanide and actinide (the two f electron series) metals under pressure. The advancement has been due to the development of different designs of diamond anvil pressure cell (DAC), detectors, use of synchrotron radiation, and, in the case of the actinides, authorization to perform studies at synchrotron sites with elements more radioactive than thorium or natural uranium. With a modern DAC, it is possible to reach pressures of 100 GPa routinely, and pressures of 500 GPa or higher are achievable. At such pressures, materials are reduced to fractions of their original volumes. With this reduction in interatomic distances, significant changes in bonding and structure as well as other properties take place. Given this potential, there has been significant scientific interest in investigating pressure-induced changes in the chemistry and physics of the two f series of elements. A central point of interest in this regard is whether pressure can force delocalization of f electrons in metals where they are normally not involved in the metallic bonding.

Over the past few decades there have been several studies of lanthanide metals designed to pursue the above question, and investigations continue. The reader is referred to reviews[1–4] in this regard, and to a recent study of cerium metal.[5] There is strong evidence that the $4f$ electrons of some early lanthanide metals do indeed delocalize under pressure and the metals then adopt low-symmetry structures, exhibited by the early actinide metals having itinerant $5f$ electrons. There have been significant disagreements about the high-pressure structures formed. It is clear that the pressure required for delocalizing the $4f$ electrons rapidly increases across the series, and in the region of neodymium or samarium 100 GPa or more is required. This delocalization phenomenon has not been reported for members in the second half of the $4f$ series. In contrast, the spatial extension of the $5f$ electrons permits the delocalization and/or hybridization process to occur at lower pressures with transplutonium metals, even though they contain an even higher number of f electrons. For example, this process has been reported for californium metal, but not for dysprosium metal.[6]

The physicochemical properties of the actinide metals at normal pressure vary widely across the series, due largely to the changing nature of the $5f$ electrons. In principle, the filling of $5f$ orbitals begins after thorium. It is generally accepted that the $5f$ electrons are involved to varying degrees in the bonding (itinerant $5f$ electrons) for protactinium,

uranium, neptunium, and plutonium. These four elements display quite different properties from the transplutonium elements that have localized $5f$ electrons. Itinerant $5f$ electrons arise due to their more extended wave functions than those of the $4f$ electrons, and the comparable energies of hybrid states relative to other electronic levels without f character. With increasing nuclear charge the extension and energies of these $5f$ levels and/or hybridized states change. The $5f$ electrons of americium, the element following plutonium, are now nonbonding (localized) at normal pressure, as are the $5f$ electrons for the remaining elements of this series. In this sense americium occupies a pivotal position in the $5f$ series.

Given this pivotal position of americium, its behavior under pressure becomes especially interesting. Americium displays significant structural differences at atmospheric pressure both from its near neighbor plutonium and from its lanthanide homolog europium. Its localized f electron state and nonmagnetic $5f^6$ $(J=0)$ configuration, which lead to superconducting properties at low temperatures,[7] reflect a changing internal pressure for this element.

Several structural studies of americium have been performed previously at lower pressures[8–15] than obtained in the present work. Results from previous workers and this work are in agreement that the double hexagonal close packed phase (dhcp, Am I phase; $P6_3/mmc$ space group) transforms at a low pressure to a face centered cubic phase (fcc, Am II phase; $Fm3m$ space group). The latter phase is also obtained when the dhcp phase of americium is heated above 650 °C.[16] Differences are noted between previous structural assignments at increased pressures, especially for the Am III phase.[14] The Am IV structure has been assigned to be an α-uranium, orthorhombic structure, first by Roof *et al.*[11] and then by Benedict *et al.*[14] Both groups reported that delocalization of the $5f$ electrons of americium occurs in conjunction with the appearance of the Am IV phase.

There has also been one study to measure the resistivity of americium metal under pressure up to 25 GPa.[17] This experimental approach added another dimension in seeking an understanding of the pressure behavior of americium and its underlying causes. The main finding in this work was that the superconducting T_c of americium became elevated under pressure but the work provided additional evidence to support the onset of $5f$ delocalization due to the application of pressure.

The intent of the present study was to examine the behavior of americium under pressure using both synchrotron (angle dispersive mode) and conventional x-ray (energy dispersive mode) radiation sources in order to acquire the best possible data for resolving its pressure behavior. It is believed that this is the first time that americium has been studied under pressure using synchrotron radiation. The exceptional brilliance afforded by the European Synchrotron Radiation Facility, a third generation machine, allowed us to work with only a few micrograms of americium in each DAC. The companion studies using an energy dispersive mode allowed additional details of the behavior of americium to be obtained.

In the present structural study, we also observed the hexagonal $P6_3/mmc$ and the cubic $Fm3m$ phases, in accord with the structures reported in earlier work, but an important finding was that the Am III and Am IV structures previously reported were incorrect. We have now assigned structures for the Am III and Am IV phases, that provide additional understanding of the behavior of americium metal under pressure, as well as allowing a viable mechanistic picture for the structural progression under pressure. A very important finding was that under pressure americium adopts a known structural form of plutonium, its near neighbor in the series, considered to have itinerant $5f$ electrons. From our data we have also established transition pressures for the different structural forms and a more reasonable bulk modulus for Am. Major factors in obtaining these findings are the experimental advances employed in the work, which includes the use of synchrotron radiation. Given the lower symmetry of the structures encountered, especially at higher pressures, it is imperative that data of the highest quality be used in determining the behavior of americium.

The data obtained permitted us to resolve the previous controversy concerning the Am III and Am IV structures, while confirming that pressure forces the $5f$ electrons of americium to become itinerant. It was important to determine the correct structures obtained under pressure, and to acquire accurate relative volume data, to understand correctly the changes occurring with pressure. The insights obtained from these studies permit (1) interpretation and correct understanding of the behavior of americium under pressure; (2) a comparison of americium's structure/bonding behavior with that of its near neighbor plutonium; and (3) establishment of trends expected in future studies of transamericium metals and alloys under pressure.

These results also address differences noted between experiment and theory, especially regarding the magnitude of the volume collapses in americium. These data should now permit the convergence of experimental and theoretical concepts for the pressure behavior of americium. Reported here are the results of our experimental studies on americium and a discussion of the implications of the changes in structure and atomic volumes observed following the application of pressure. A short account of this work has recently been published elsewhere.[18]

II. EXPERIMENT

A. Materials

Foils of americium metal were prepared by vapor deposition following the reduction of americium dioxide by lanthanum metal. The ^{243}Am isotope ($t_{1/2}=7\times10^3$ years; specific heat generated by the radioactive decay$=6\times10^{-3}$ W/g) was employed in these studies. Mass spectrographic analysis indicated a high purity (99.94% based on metal ion content) and x-ray analysis showed that the metal exhibited the double hexagonal close packed structure ($a_0=3.467\pm0.004$ Å, $c_0=11.240\pm0.008$ Å), in excellent accord with the accepted literature values for it.[19] Small pieces (5–10 μg each) of this foil were cut in a helium atmosphere glove box for placing into the different diamond anvil cells used in the studies.

B. Diamond anvil cells

The high-pressure studies of americium were performed at room temperature using two different diamond anvil cell designs. One was of the Syassen-Holzapfel design (lever-type design) capable of routinely reaching up to 60 GPa. The second was the Cornell-type cell (Ruoff design). The Syassen-Holzapfel cell is best suited for small pressure steps, while the Cornell cells are designed for megabar pressures.

The Syassen-Holzapfel cell was used both in the energy dispersive mode with tungsten radiation produced via a conventional x-ray generator and in the angle dispersive mode with synchrotron radiation. In this cell, the diamonds had a 400 μm flat and the Inconel gasket had a nominal 200 μm hole for the sample. Two Bragg angles (nominal 5° and 7°) were employed in the energy dispersive measurements. The method has been described in the literature.[15] The Cornell-type cells used diamonds with a 95–120 μm flat and a T-301 steel gasket with a 40–70 μm diameter hole for the sample. The Cornell cells were used only in the angle dispersive mode with synchrotron radiation.

The pressure transmitting medium in the cells was either nitrogen or silicone oil. Pressure markers were either ruby (ruby fluorescence technique[20]) or platinum metal using its equation of state.[21] For the synchrotron studies, the cells were prepared at Oak Ridge National Laboratory (ORNL) and shipped to the European Synchrotron Radiation Facility (ESRF) at Grenoble, France. Using in-house developed techniques, the closed cells (few kbar pressure) free of any radioactive contamination were double sealed and placed in special holders for use at the ESRF synchrotron. For additional confinement, beryllium foils and plastic films (Melinex® and/or Kapton®) were used. These plastic films were selected based on their transparency to x rays and the laser wavelength used for the ruby fluorescence technique. After the studies at the ESRF, the sealed cells were returned to ORNL for unloading. The emptied cells were found to be free of radioactive contamination and were reused for other experiments.

Studies involving the energy dispersive technique were performed at the European Institute for Transuranium Elements (ITU) in Germany. In this work, americium was transported from ORNL to ITU. The DAC's were loaded and studied in nitrogen atmosphere glove boxes at ITU.

C. Synchrotron diffraction

Several different experimental parameters were used in the diffraction work at the ESRF synchrotron (beamline ID30). A typical arrangement for the Syassen-Holzapfel cell was to use a 100×100 μm^2 monochromatic collimated beam in the 32-bunch machine mode (100 mA) with an exposure time of ≈1 min. For the Cornell cells, a microfocused beam of 25×25 μm^2 (two bent mirrors in conjunction with a 30 μm pinhole filter) was used. A 15 s exposure was sufficient (2/3 fill machine mode, 200 mA) to obtain excellent diffraction data. Diffraction images were captured with a Fastscan image plate detector[22] and the images viewed within seconds. This permitted making a number of diffraction images under different parameters (wavelength, sample to detector distance, etc.) in a short time frame. The diffraction images were then processed using the FIT2D program,[23] which produced the diffraction results used for data analysis.

III. RESULTS

A. Am I and II structures

The initial structure of the americium used in the high-pressure studies was the normal dhcp form ($P6_3/mmc$; Am I) that has been reported as the stable ambient temperature/pressure phase. This dhcp form is isostructural with several of the early lanthanide metals through neodymium.[4] Although the actinide metals display smaller lattice parameters than the lanthanide metals, the transplutonium metals through californium and most of the lanthanide metals (except europium and ytterbium) are considered as being trivalent metals having localized *f* electrons.

With the application of pressure, the dhcp form of americium converts to a fcc structure ($Fm3m$; Am II) at 6.1 $\pm$0.2 GPa. The lattice parameter at 6.5 GPa is $a=4.613$ Å. This fcc phase is identical to the high-temperature phase that has been observed for americium metal above 650 °C. Benedict *et al.*[14] reported this dhcp $\rightarrow$fcc transition to occur at 9.5 GPa, a higher pressure than observed in this work. A third high-temperature phase, believed to be a body centered cubic phase but not confirmed by x-ray analysis,[24] has not been observed as a pressure phase.

Combined results from both angle and energy dispersive mode studies in the form of interplanar distances versus pressure are plotted in Fig. 1 (up to 15 GPa) and Fig. 2 (10 to 65 GPa). Four distinct phases were observed in the work and these are shown as dhcp (Am I), fcc (Am II), Am III, and Am IV in Fig. 1 and Fig. 2.

B. Am III structure

With additional pressure, we observed that the fcc Am II phase transformed to the Am III phase at 10.0 ± 0.2 GPa, which was retained up to 16 ± 1 GPa. In the work of Benedict *et al.*[14] the Am III phase is reported to start at 13.5 GPa and was retained up to 23 GPa. It is the structure of this phase that has been controversial in past studies of americium under pressure.[9,12–14] Knowledge of the exact structure of the Am III phase is critical in order to understand correctly its behavior under pressure.

The Am III phase has been assigned previously as a monoclinic structure,[12,13] a triple hexagonal closed packed structure,[9] and a distorted, face centered cubic structure.[14] The highest pressure obtained with Am prior to our work (52 GPa) was reported by Benedict *et al.*,[14] while other efforts were limited to 20 GPa. Benedict *et al.*[14] argued that the monoclinic indexing reported in Refs. 12 and 13 was incorrect, and would require an expansion of the volume with pressure. The assignment of a trigonal distortion[14] (distorted fcc) of the cubic Am II phase removed this contradiction and provided a 6% volume collapse when the Am III phase converted to a proposed α-uranium Am IV phase. Theoretical

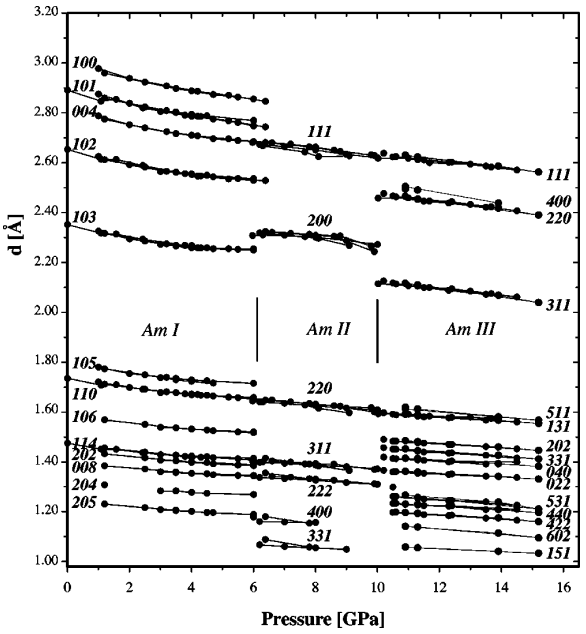

FIG. 1. Interplanar distances in americium metal as a function of pressure up to 15 GPa. (Miller indices *hkl* are indicated for the phases.)

calculations[25,26] at that time suggested a volume collapse of 22%. Subsequent estimations suggest that a collapse of 34% (Ref. 27) or 25% (Ref. 28) would be observed. A significant difference exists between these earlier experimental findings and the theoretical expectations.

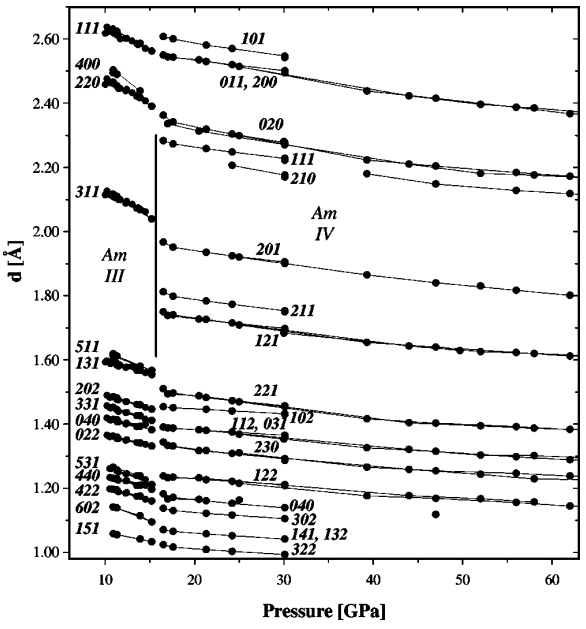

FIG. 2. Interplanar distances for the Am III and Am IV high-pressure phases of americium as a function of pressure from 10 to 65 GPa. (Miller indices *hkl* are indicated for the phases.)

In our study, extensive efforts were made to determine correctly the structure of this Am III phase. Nine diffraction spectra were collected at different pressures and multiple indexing programs, TREOR,[29] DICVOL91,[30] and ITO,[31] were employed to extract the structure type. Initial attempts suggested a monoclinic symmetry (e.g., $I2/m$, $C2/m$, etc.) but it was not possible to assign unequivocally all the diffraction peaks observed for the americium III phase. Deviations were especially notable at the higher diffraction angles for the $I2/m$ assignment and Rietveld refinements with the $C2/m$ space group indicated an unsatisfactory correlation with intensities at lower diffraction angles.

Given the quality and reproducibility of our diffraction data collected from multiple samples of Am and different DAC's, we were finally successful at arriving at the correct assignment of the structure of the Am III phase. We have determined that the structure has an unexpectedly high symmetry with a face centered orthorhombic cell (space group $Fddd$, Am on the $8a$ sites, all position parameters fixed by symmetry). The lattice parameters at 10.9 GPa are $a=10.115$, $b=5.670$, and $c=3.116$ Å ($\rightarrow b/c \approx \sqrt{3}$, i.e., the structure consists of slightly distorted close packed hexagonal planes; this is discussed in detail in a later section). Our findings for the Am III phase do not agree with the previous structural assignments[12–14] or pressure range for this Am III phase. A trigonal distorted Am III phase[14] was reported to exist between 13.5 and 23 GPa, while Roof[12,13] suggested that a monoclinic Am III phase started at 10 GPa. We observed the orthorhombic $Fddd$ structure between 10 and 16 GPa.

C. Am IV structure

In our work the Am IV phase was observed to form at 16 ± 1 GPa and was retained up to 100 GPa, the highest pressure for which we report data. Close examination of our data suggested evidence for the beginning of the Am IV phase already at 13 GPa ($\approx$10% Am IV) and that Am IV was the exclusive phase by 17.5 GPa. We also observed a gradual separation of the first three diffraction lines for this structure with pressure, and a definite separation was noted at 60 GPa. Roof *et al.*[11] first reported the appearance of the Am IV phase at 15.2 ± 0.2 GPa and assigned it as being an α-uranium structure (orthorhombic), while Benedict *et al.*[14] found that the phase formed at 23 GPa and reported it was stable up to 52 GPa.

Using Rietveld refinement (see below) we were able to assign this Am IV structure as being primitive orthorhombic (space group $Pnma$, Am on $4c$ sites with $x=0.403$, $y=1/4$, $z=0.101$ at 17.6 GPa, and $x=0.406$, $y=1/4$, $z=0.118$ at 89 GPa), in contrast to the base centered orthorhombic α-uranium structure (space group $Cmcm$, U on $4c$ sites with $x=0$, $y=0.102$, $z=1/4$). The lattice parameters for the Am IV structure are $a=5.093$, $b=4.679$, $c=3.028$ Å at 17.6 GPa and $a=4.607$, $b=4.288$, $c=2.737$ Å at 89 GPa.

This structure for Am IV is closely related to the α-uranium structure. If the atomic position parameter z of the $4c$ sites of the $Pnma$ structure is placed at zero, one obtains the higher-symmetry α-uranium structure with the

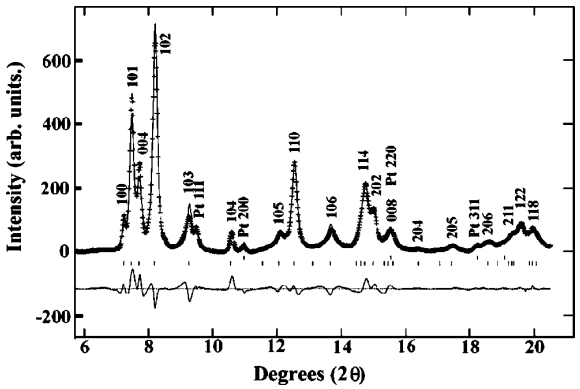

FIG. 3. Rietveld fit of the dhcp (space group $P6_3/mmc$) Am I phase at 1.2 GPa ($\lambda = 0.3738$ Å, pressure transmitting medium nitrogen) showing the observed (crosses) and calculated (line) diffraction patterns, reflection tick marks, Miller indices of the principal reflections, and difference profile. (Pt pressure calibrant used.)

base centered orthorhombic unit cell (only the definition for the three lattice parameters is different). We have found that the fit of the data is better with the $Pnma$ structure type and propose this as the correct identification of the Am IV phase.

D. Rietveld analyses of data

The Rietveld analyses of the angle dispersive synchrotron data were made using FULLPROF and GSAS.[32,33] It is often difficult to make a Rietveld analysis for very small samples, since bad grain statistics lead to unrepresentative intensities of the integrated diffraction lines. However, the grain size of our polycrystalline Am samples was small enough to produce perfect diffraction rings and reproducible intensities of the integrated patterns. It was only necessary to take into account the potential for preferred orientation. The Rietveld fits are shown in Figs. 3–7 for the observed phases of americium, where Figs. 6 and 7 represent two pressures for the Am IV phase. The refinements for the Am III and Am IV

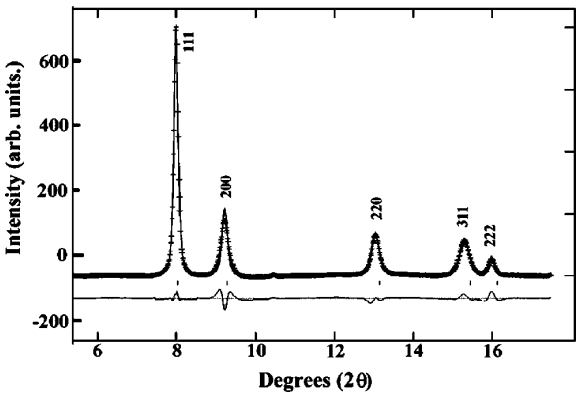

FIG. 4. Rietveld fit of the fcc (space group $Fm3m$) Am II phase at 6.5 GPa ($\lambda = 0.3738$ Å, pressure transmitting medium nitrogen) showing the observed (crosses) and calculated (line) diffraction patterns, reflection tick marks, Miller indices of the principal reflections, and difference profile.

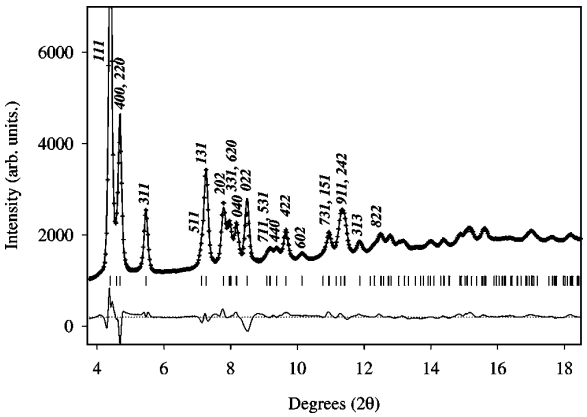

FIG. 5. Rietveld fit of the orthorhombic (space group $Fddd$) Am III phase at 10.9 GPa ($\lambda = 0.2022$ Å, pressure transmitting medium nitrogen) showing the observed (crosses) and calculated (line) diffraction patterns, reflection tick marks, Miller indices of the principal reflections, and difference profile.

phases are especially important in this regard, as the first two phases were already well established. Figures 5–7 show very good agreement between the experimental and calculated data points. The Bragg R values of the Rietveld refinements shown are 7.2% for Am III at 10.9 GPa, 8.3% for Am IV at 17.6 GPa, and 4.9% for Am IV at 89 GPa.

IV. DISCUSSION

A. Volume and bulk modulus

In Fig. 8 the relative volumes (V/V_0, where V_0 is the volume at normal pressure) are plotted against pressure. The changes occurring when changing from one pressure to another for the different phases are evident in the figure. Two abrupt changes in volume can be observed: one small one ($\approx 2\%$) at the Am II to Am III transition and a larger change ($\approx 7\%$) at the Am III to Am IV transition. These distinct

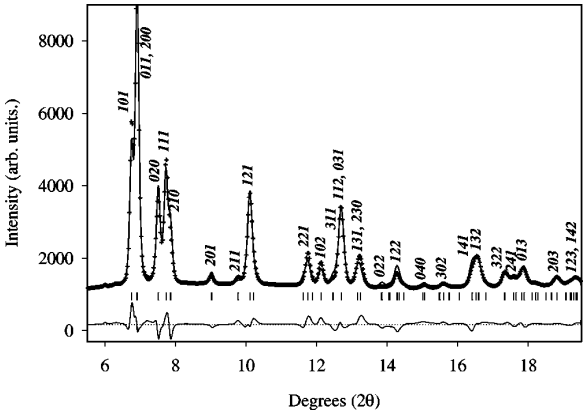

FIG. 6. Rietveld fit of the orthorhombic (space group $Pnma$) Am IV phase at 17.6 GPa ($\lambda = 0.3066$ Å, pressure transmitting medium: nitrogen) showing the observed (crosses) and calculated (line) diffraction patterns, reflection tick marks, Miller indices of the principal reflections, and difference profile.

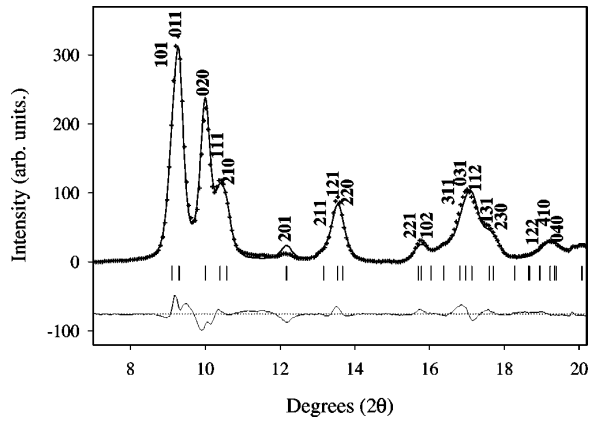

FIG. 7. Rietveld fit of the orthorhombic (space group *Pnma*) Am IV phase at 89 GPa ($\lambda = 0.3738$ Å, pressure transmitting medium silicone oil) showing the observed (crosses) and calculated (line) diffraction patterns, reflection tick marks, Miller indices of the principal reflections, and difference profile.

volume ''collapses'' are attributed to the onset of *f* electron contribution to the metallic bonding. A major difference in this work compared to former studies is the assignment of *f* electron character to the Am III phase, rather than only to the Am IV phase, and a second volume change for the Am III to Am IV transition. However, the change in volume is lower than the 25% change predicted by the most recent theory.[28] This onset of *f* electron itinerancy in americium metal due to pressure is discussed further in a subsequent section.

The isothermal bulk moduli and their pressure derivatives were obtained by fitting the Birch[34] and Murnaghan[35] equations of state to the experimental curve of the lower-pressure phases Am I and Am II (localized *f* electrons) to obtain the bulk modulus B_0 and its pressure derivative B_0' (the subscript zero indicates ambient pressure). The following values were obtained: Birch equation, $B_0 = 29.7 \pm 1.5$ GPa, $B_0' = 3.7 \pm 0.2$, and Murnaghan equation, $B_0 = 29.9 \pm 1.5$ GPa, $B_0' = 3.5 \pm 0.2$. These moduli are consistent with values reported for the light lanthanide metals.[1] The modulus reported by Benedict *et al.* for americium metal is 45 GPa,[14] appreciably higher and close to the value of 43 GPa reported for α-plutonium.[36] The modulus for plutonium with itinerant *f* electrons would be expected to be higher than that for americium metal with three non-5*f* conduction electrons. That is, the lattice for α plutonium should be ''stiffer'' than that of the dhcp form of americium metal.

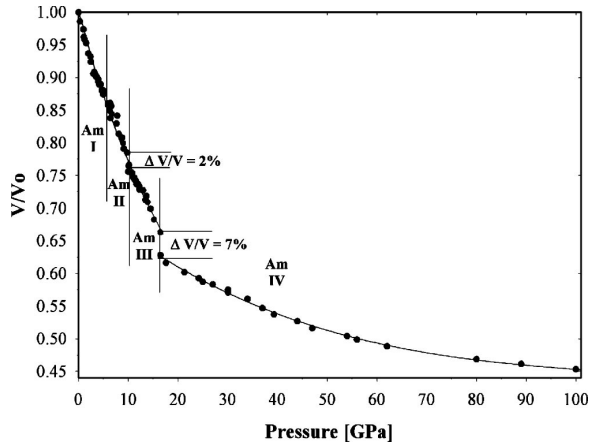

FIG. 8. Relative volume of americium metal as a function of pressure up to 100 GPa.

Another point is that some hysteresis is observed upon the release of the applied pressure (not shown). In the energy dispersive studies, the Am IV phase was retained down to ≈ 11 GPa and a mixture of Am III and Am IV was observed down to ≈ 6 GPa. The Am II phase was retained after the total release of the pressure. The retention of the fcc phase has been observed before[9,37] and was used to obtain ''pressure quenched'' lattice parameters for this cubic phase. However, the retention of the Am III and Am IV phases was surprising, as it was expected that *f* bonded structures forced by pressure would quickly revert back to stable, localized *f* electron structures with the release of pressure.

B. Compressibility of the Am IV phase

In the previous section the bulk modulus of americium metal obtained from this pressure study was discussed. The modulus can be obtained via the compression behavior of the Am I and Am II phases using established equation of state relationships. The bulk modulus of 30 GPa found for americium in this work is consistent with moduli established for several lanthanide metals that have localized *f* electrons.[2] The steep portion of the compression curve for Am I and Am II in Fig. 8 is in accord with a smaller bulk modulus—that is, a metal with a softer lattice that can be readily compressed. In contrast, the modulus of α uranium is much larger (reported as 100 to 152 GPa by various methods[2]) and under pressure uranium shows a much ''flatter'' compression curve.

In Fig. 8 it can be observed that the compression of the Am IV curve is also much ''flatter'' than for the Am I, Am II, or Am III phases, which suggests, that the Am IV phase has a much higher bulk modulus. It is not fully appropriate to calculate a bulk modulus for the Am IV phase using our data, but a pseudomodulus can be extracted from it by extrapolation. By this approach, we obtained a bulk modulus for the Am IV phase and estimate a value approaching 100 GPa. Such a value is in full accord with a rather ''stiff'' or ''rigid'' lattice, which has 5*f* electron involvement in the metallic bonding. This pseudo bulk modulus for the Am IV phase suggests that this phase's compressibility falls between those of α uranium and α neptunium, two actinide metals with itinerant 5*f* electrons. The difference in compressibility for the Am III and the Am IV phases (e.g., the compression curves in Fig. 8) also supports the contention that the Am IV phase has a higher degree of 5*f* involvement in its bonding.

C. Relationship between structures

The four different americium structures observed in this work are shown in Fig. 9, which permits one to envision the

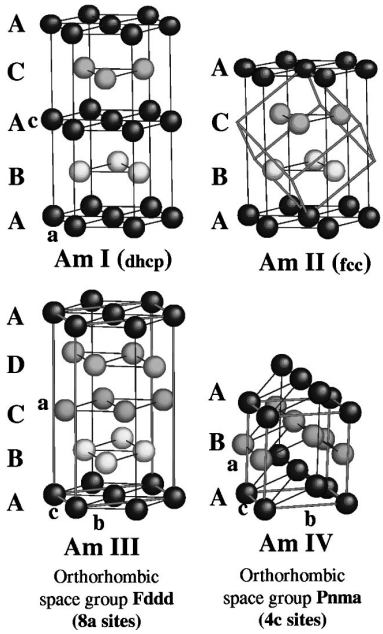

FIG. 9. Models for the four structures of americium metal under pressure.

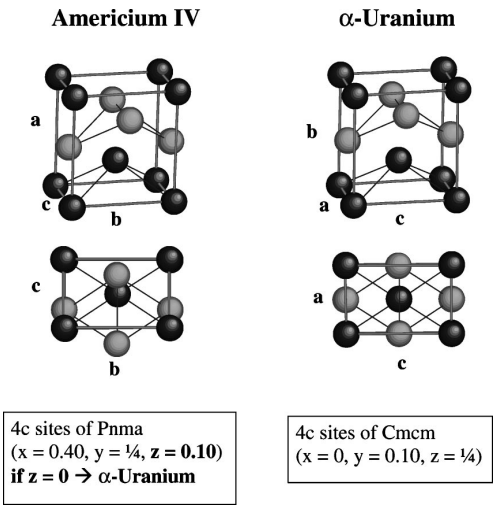

FIG. 10. Orthorhombic cells for the Am IV and α-U structures. Setting the z value of the $4c$ sites in the $Pnma$ structure of Am IV (left) to 0 means a shifting of the planes with the light atoms relative to the dark ones in the c direction so that one obtains the α-U structure (right).

transformation process occurring under pressure. In principle, the structures can be viewed as being composed of close packed hexagonal (Am I, Am II) or distorted close packed hexagonal planes (Am III, Am IV) with a stacking sequence that changes in going from one structure to the next. Thus, for the dhcp Am I structure, the sequence is (*A*-*B*-*A*-*C*-*A*), which changes to (*A*-*B*-*C*-*A*) for the fcc Am II phase by shifting planes. The fcc then converts to an (*A*-*B*-*C*-*D*-*A*) arrangement by a shift and distortion of planes to produce the Am III phase (b/c differs only by 5% from the ideal $\sqrt{3}$ value for close packed hexagonal planes). Finally, a shift, distortion, and zigzag bending of the hexagonal planes yields (*A*-*B*-*A*) for the Am IV phase. As shown in Fig. 9, this bending requires a shifting of the planes parallel to the *a*-*c* faces, which are perpendicular to the close packed hexagonal planes.

For the Am I and Am II structures, there are 12 nearest neighbors with the same interatomic distances (six in the same plane, three in the plane above, and three in the plane below). For the Am III phase there are also six neighbors in the same plane, but now four in the plane below and four in the plane above. Two of these four are the nearest neighbors, whereas the other two have the largest distance of all neighbors. This means that the Am III structure provides 14 neighbors with distances between 3.0 and 3.72 Å (at 10.9 GPa). There is then a distance gap and the next atom is at 4.85 Å.

The Am IV structure also has 14 neighbors with distances between 2.61 and 3.51 Å (at 17.6 GPa). Then there is again a gap with the next atom being at 4.44 Å. The atomic sites in the Am III structure have high point symmetry 222, while the sites in the Am IV structure have a lower point symmetry *m*.

What is most significant here is that this Am III structure is the same as that known for the γ phase of plutonium,[38] considered to have $5f$ electron involvement in its metallic bonding. Thus, under pressure the electronic nature of americium is altered and the metal adopts one of the structures established for its preceding neighbor, plutonium.

As discussed earlier, the structure proposed here for the Am IV phase is similar to the α-uranium structure previously assigned to the Am IV phase.[11–14] The orthorhombic cells of the two structures are shown in Fig. 10. If the atomic position parameter z (≈ 0.10) of the $4c$ sites of the Am IV $Pnma$ structure is set to zero, the second zigzag like bent plane (light colored atoms) of Am IV in Fig. 9 or Fig. 10 is shifted in the c direction so that one obtains centered rectangular *a*-*c* planes, i.e., the base centered orthorhombic α-uranium structure ($Cmcm$) is formed. The latter has a higher symmetry than the $Pnma$ structure (only the definition of the lattice parameters is different in the $Cmcm$ space group). If the α-uranium structure were the right structure of Am IV, then it would be possible to identify these centered rectangular planes as distorted close packed hexagonal planes. This means that the α-uranium structure could be obtained from the Am III structure by only shifting (without bending) the distorted close packed hexagonal planes. This argument leads also to a second possibility for the transformation path from Am III to the right Am IV structure: Instead of bending the close packed hexagonal planes of Am III one must shift the atoms within the plane, so that one no longer has hexagonal planes. This means that the *a*-*c* faces of Am IV in Fig. 9 have to be assigned to the *b*-*c* faces of Am III.

Evolution of the lattice parameters for the four Am pressure phases is shown in Fig. 11. These parameters have been multiplied by the factors shown in the figure and assigned to each other in a way which enables the changes in pro-

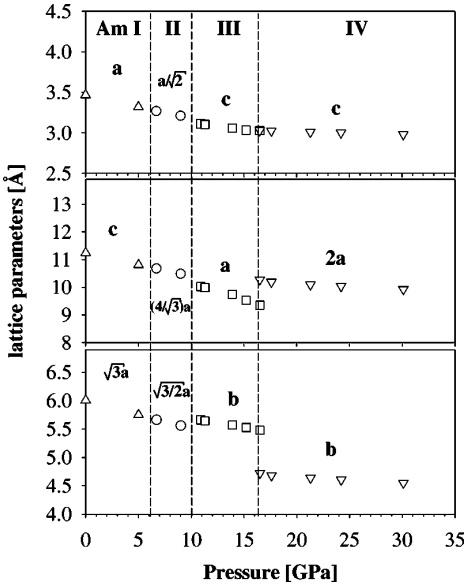

FIG. 11. Evolution of the lattice parameters for the four Am pressure phases with pressure. (See text for detailed explanation.)

gressing from one phase to another to be followed. Figure 11 helps to illustrate the mechanism of the structural changes which are shown in Fig. 9. Let us take, for instance, the first lattice parameter in Fig. 11, which shows the evolution of the interatomic distance defined by the hexagonal lattice parameter a of Am I through all the structural transitions. It is clearly evident that there is a smooth evolution of this parameter, which one would expect from looking at Fig. 9. On the other hand, the third parameter in Fig. 11 shows the evolution of the interatomic distance defined by the orthorhombic lattice parameters b of Am III and Am IV. This parameter shows a sharp pronounced decrease at the transition between Am III and Am IV, which is due to the bending of the hexagonal plane in the case of Am IV.

D. Discussion of structure and bonding

The involvement of $5f$ electrons in the metallic bonding of the actinides gives rise to several special physicochemical properties. The unique behavior of plutonium, the near neighbor of americium, is an example of the effects brought about by having itinerant $5f$ electrons. Plutonium is perhaps the most complex metal in the periodic table, displaying six structural forms between ambient temperature and its melting point of 640 °C. Below 155 °C, the pure metal displays a complex monoclinic (α phase, simple monoclinic, $P2_1/m$) structure, rather than the more symmetrical structures (cubic, hexagonal, etc.) found for most metals in the periodic table; for the transition metals it is the *d*, *s*, and *p* electrons that are responsible for the metallic bonding and hence the structures.

For americium and the subsequent actinide metals in the series that have localized f electrons, symmetrical crystal structures and a simpler phase behavior is observed. In this regard, the transplutonium metals are similar in their behavior to the lanthanide metals, the $4f$ series of elements. In essence, plutonium is trying to become a trivalent metal but its situation is complicated by a number of electronic states of similar energy. On the other hand, americium is a trivalent metal but not far removed from the electronic situation of plutonium. Perturbations like pressure therefore may alter its electronic nature more readily than for a higher member of the actinide series.

For the actinides, based only on atomic volume, α neptunium could be considered as having the maximum degree of f bonding, whereas the complex phase behavior of plutonium metal suggests a maximum multiplicity of energy levels of similar stability. The more complex behavior of actinide metals with itinerant f electrons is due to the latter's involvement in the metallic bonding. These different electronic configurations can yield atoms of different sizes, which affects packing and can give rise to denser metallic structures. For example, the ambient temperature form of plutonium (monoclinic α phase) has a calculated density of 19.86 g/cm^3, whereas the dhcp form of americium under comparable conditions has a density of 13.61 g/cm^3.

The important point is that there is a potential for generating multiple electronic levels of similar energy by incorporating f character in the bonding. This often leads to distorted structures of low symmetry. It is the symmetry of the f electrons' orbitals that disfavors the traditional close packed, high-symmetry structures and produces the distorted plutonium structures instead of a hexagonal-type structure. The appearance of such low-symmetry structures can be used to infer the partial infusion of f electron character into the metallic bonding. A low-symmetry structure, especially one displayed by the early actinide metals known to have itinerant f electrons, then becomes a ''fingerprint'' for the involvement of f electrons in metallic bonding. In conjunction with the formation of a low-symmetry structure, the appearance of a volume collapse (sharp decrease in relative volume at a given pressure) is also taken as a sign that f electrons may have been forced into the metallic bonding.

Given that americium is the near neighbor of plutonium, it seems reasonable that by adding f character Am would adopt one of the plutonium structures, a neptunium structure, or the α-uranium structure. There may be only small differences in the f electron character and energy levels between these structures. It is significant that the γ phase of plutonium has the same structure cited here for the Am III phase formed under pressure. The facts that plutonium is the near neighbor of americium and that Am adopts under pressure the γ-Pu structure make it worthwhile to note some specific characteristics about the behavior of plutonium.

The behavior of the crystal structure of plutonium with temperature is well established.[39,40] Beginning with the α phase of plutonium and increasing the temperature (which should increase the interatomic distances, as opposed to the effect of pressure), there are six reported phases, the third being the γ phase (the same structure as the Am III structure). With expansion there may be some reduction in f electron involvement in the bonding. However, there seems to be little question that f electron bonding is still present in these higher-temperature phases—it is likely that some f character even remains in the molten state.[40]

There are some important aspects of plutonium with reference to americium. One is that the largest atomic radius for plutonium metal[40] (1.64 Å calculated for both the δ and the δ' phases at 25 °C)[40] is smaller than the atomic radius of americium at the same temperature (1.73 Å). This is as expected given the type of bonding present in each metal at atmospheric pressure (plutonium, at least partial *f* character; americium, localized *f* electrons). Second, the atomic radius of americium near the Am II →Am III transition point is close to that for *f* electron bonded plutonium. The shortest distance of the Am III phase just after the transition is 1.50 Å and it is accepted that *f* bonding is still present in δ-plutonium at 25 °C, where the calculated radius is as large as 1.64 Å.[40] Further, the atomic radius for curium, the other near neighbor of americium in the series (for the fcc, Cm II phase), just before the onset of delocalization of its $5f$ electrons occurs, is $\approx$1.52 Å.[41] The important point of these comparisons is that they show the interatomic distances for americium III are (1) smaller than those in plutonium where *f* interactions are present; and (2) close to the value where *f* interactions take place in curium. The existence of localized versus itinerant *f* electron states is important in defining/understanding chemical and/or physical properties. The above comparisons of interatomic distances for Am and Pu also support the concept proposed here that, given the smaller interatomic distances in Am, the bonding in the Am III phase has acquired *f* electron character.

The above discusses americium's pressure behavior in conjunction with aspects of its neighbors plutonium and curium and it is worthwhile to make some more comparisons with the behavior for curium under pressure. Curium is reported to undergo two phase transitions with pressure.[41] The sequence is dhcp→fcc→orthorhombic, α-uranium structure (which is presumed to have itinerant $5f$ electrons). The transitions occur at much higher pressures and an intermediate phase is not observed between the fcc and the α-uranium phases. The volume collapse at the fcc to orthorhombic transition is 21%, much greater than observed for americium. The 21% for curium is much more in line with the theoretical estimates of 25–34 % for the volume collapse in americium.[27,28] If the overall volume change for americium between the fcc Am II structure (at 10 GPa) and the orthorhombic Am IV structure (at 16 GPa) is taken, without compensation for compression, the volume change appears to be 20%. Thus, the appearance of the additional Am III phase makes an important difference in the apparent behavior of americium. Americium appears to change in multiple steps rather than one much larger collapse, as observed for curium. Whether the Cm III phase is truly an α-uranium structure, or perhaps a *Pnma* structure as found here for Am IV, must be determined in future studies of curium with synchrotron techniques.

V. CONCLUSIONS

Obtaining high-quality experimental data for the structural behavior of americium metal under high pressure up to 100 GPa permitted the proper identification of the Am III and Am IV phases. It was possible to acquire these data by using synchrotron radiation and other experimental advances. The findings provide important insights into the behavior of americium's $5f$ electrons under pressure and permit a mechanistic picture for the sequential conversion of americium from the Am I phase through the Am IV phase.

In addition to resolving a previous controversy regarding the structural behavior of americium in the 10–30 GPa region, this work has established two critical findings about the Am III and Am IV structures formed under pressure. First, the Am III phase is now properly identified as a face centered orthorhombic structure (space group *Fddd*, Am on $8a$ sites), which is the same structure displayed by the γ phase of plutonium where the bonding involves itinerant $5f$ electrons. Second, the Am IV structure is now shown to be a primitive orthorhombic (space group *Pnma*, Am on $4c$ sites) structure, rather than the very similar base centered orthorhombic α-uranium structure as reported previously, and it is stable up to at least 100 GPa.

An important finding in this work is that the delocalization of americium's $5f$ electrons forced by pressure occurs in two rather than a single step. The first process involves partial delocalization and an accompanying 2% volume collapse (Am II→Am III transition). The belief that the bonding in the Am III phase has $5f$ electron character is supported by both the magnitude of the interatomic distances in this phase (relative to those in *f* electron bonded Pu structures) and the fact that Am III is isostructural with γ-Pu. This is based on the concepts of critical distances for *f* electron involvement and that *f* bonding is responsible for the formation of lower-symmetry structures. In the second delocalization step the involvement of $5f$ electrons becomes more prominent and this change is accompanied by a larger collapse in volume (Am III→Am IV transition). It is not known if all or just a greater portion of americium's $5f$ electrons are now involved in the Am IV phase. The Am IV phase is a more ''rigid'' structure, as evident by its apparent lower compressibility that reflects the behavior of α-uranium. The lower compressibility also supports the concept that the Am IV phase has a greater involvement of its $5f$ electrons in the metallic bonding than the Am III phase.

These experimental findings are not in accord with theoretical projections suggested recently for the pressure behavior of americium,[28] where the α-plutonium structure was believed to represent the high-pressure structure of americium.

Overall, this work provides important insights for understanding the pivotal position of americium in the actinide series, especially with regard to the involvement of its $5f$ electrons in metallic bonding. The quality of these data firmly establish the experimental behavior of americium under pressure up to 100 GPa. It is hoped that these findings for americium will promote the convergence of experimental and theoretical views regarding the volume collapse and $5f$ electron delocalization in americium metal under pressure.

ACKNOWLEDGMENTS

This work was supported by the European Commission and by the Division of Chemical Sciences, Geosciences and Biosciences, OBES, and U.S. DOE under Contract No. DE-

ACO5-00OR22725 with Oak Ridge National Laboratory, managed and operated by UT-Batelle, LLC. The ^{243}Am isotope used in the study was supplied by the DOE Transuranium Production Program at Oak Ridge National Laboratory. A.L., K.L., and Y.M. wish to thank the ''Training and Mobility of Researchers'' program of the European Union and the Austrian Science Fund FWF (Project No. P-11581-PHY) and the Austrian Academy of Sciences (APART 10739). The authors acknowledge useful discussions with G.H. Lander of ITU.

*Present address: Vienna University of Technology, Institute for Experimental Physics, Wiedner Hauptstrasse 8-10/131, A-1040 Wien, Austria. Email address: lindbaum@xphys.tuwien.ac.at

[1] U. Benedict and W.B. Holzapfel, in *Handbook on the Physics and Chemistry of the Rare Earths*, Vol. 17, edited by K.A, Gschneidner, Jr., L. Eyring, G.H. Lander, and G.R. Choppin (Elsevier Science, Amsterdam, 1993), Chap. 113, pp. 245–300.
[2] U. Benedict, in *Handbook on the Physics and Chemistry of the Actinides*, edited by A.J. Freeman and G.H. Lander (Elsevier Science, Amsterdam 1987), Vol. 5, Chap. 3, pp. 227–269.
[3] R.G. Haire, in *Resources, Science, Technology and Applications*, edited by R. Bautista and N. Jackson (TMS, Pittsburgh, 1991), pp. 449–462.
[4] K.A. Gschneidner, Jr. and F.W. Calderwood, in *Handbook on the Physics and Chemistry of the Rare Earths*, Vol. 8, edited K.A. Gschneidner, Jr. and L. Eyring (North-Holland, New York, 1986), Chap. 54, pp. 156–160.
[5] M.I. McMahon and R.J. Nelmes, Phys. Rev. Lett. **78**, 3884 (1997).
[6] J.R. Peterson, U. Benedict, C. Dufour, I. Birkel, and R.G. Haire, J. Less-Common Met. **93**, 353 (1983).
[7] J.L. Smith and R.G. Haire, Science **200**, 535 (1978).
[8] J. Akella, Q. Johnson, W. Thayer, and R.N. Schock, J. Less-Common Met. **68**, 95 (1979).
[9] J. Akella, Q. Johnson, and R.N. Schock, J. Geophys. Res. B **85**, 7056 (1980).
[10] R.L. Reichlin, J. Akella, G.S. Smith, and M. Schwab (unpublished).
[11] R.B. Roof, R.G. Haire, D. Schiferl, L.A. Schwalbe, E.A. Kmeto, and J.L. Smith, Science **207**, 1353 (1980).
[12] R.B. Roof, Z. Kristallogr. **B15**, 307 (1982).
[13] R.B. Roof, J. Appl. Crystallogr. **14**, 447 (1981).
[14] U. Benedict, J.P. Itié, C. Dufour, S. Dabos, and J.C. Spirlet, in *Americium and Curium Chemistry and Technology*, edited by N.M. Edelstein, J.D. Navratil, and W.W. Schultz (Reidel, Dordrecht, 1985), pp. 221–224.
[15] U. Benedict, J.P. Itié, C. Dufour, S. Dabos, and J.C. Spirlet, Physica B & C **139B/140B**, 284 (1986).
[16] R.G. Haire, *Metals Handbook*, 10th ed. (ASM, Materials Park, OH, 1990), Vol. 2, pp. 1198–1201.
[17] P. Link, D. Braithwaite, J. Wittig, U. Benedict, and R.G. Haire, J. Alloys Compd. **213/214**, 148 (1994).
[18] S. Heathman, R.G. Haire, T. Le Bihan, A. Lindbaum, K. Litfin, Y. Méresse, and H. Libotte, Phys. Rev. Lett. **85**, 2961 (2000).
[19] D.B. McWhan, J.C. Wallmann, B.B. Cunningham, L.B. Asprey, F.H. Ellinger, and W.H. Zachariasen, J. Inorg. Nucl. Chem. **15**, 185 (1960).
[20] R.A. Forman, G.J. Piermarini, J.D. Barnett, and S. Block, Science **176**, 284 (1972).
[21] R.S. Hixson and J.N. Fritz, J. Appl. Phys. **71**, 1721 (1992).
[22] M. Thoms, S. Bauchau, D. Häusermann, M. Kunz, T. Le Bihan, M. Mezouar, and D. Strawbridge, Nucl. Instrum. Methods Phys. Res. A **413**, 175 (1998).
[23] A.P. Hammersley, ESRF Internal Report No. ESRF97HA02T, 1997 (unpublished).
[24] W.W. Schultz and R.A. Penneman, in *The Chemistry of the Actinide Elements*, edited by J.J. Katz, G.T. Seaborg, and L.R. Morss (Chapman and Hall, New York, 1986), Vol. 1, p. 900.
[25] B. Johansson, H.L. Skriver, and O.K. Anderson, in *Physics of Solids under High Pressure*, edited by J.S. Schilling and R.N. Shelton (North-Holland, Amsterdam, 1981), pp. 245–262.
[26] M.S.S. Brooks, J. Phys. F: Met. Phys. **13**, 103 (1983).
[27] O. Eriksson and J.M. Wills, Phys. Rev. B **45**, 3198 (1992).
[28] Per Söderlind, R. Ahuja, O. Eriksson, B. Johansson, and J.M. Wills, Phys. Rev. B **61**, 8119 (2000).
[29] P.E. Werner, L. Eriksson, and M.J. Westdahl, J. Appl. Crystallogr. **18**, 367 (1985).
[30] A. Boultif and D.J. Louer, J. Appl. Crystallogr. **24**, 987 (1991).
[31] J.W. Ito and J.W. Visser, J. Appl. Crystallogr. **2**, 89 (1969).
[32] J. Rodriguez-Carvajal, Physica B **192**, 55 (1993).
[33] A. Larson and B. Von Dreele, computer code GSAS, Los Alamos National Laboratory, 1994.
[34] F. Birch, Phys. Rev. **71**, 809 (1947).
[35] F.D. Murnaghan, Am. J. Math. **49**, 235 (1937).
[36] S. Dabos-Seignon, J.P. Dancausse, E. Gering, S. Heathman, and U. Benedict, J. Alloys Compd. **190**, 237 (1993).
[37] R.G. Haire, U. Benedict, J.R. Peterson, C. Dufour, and S. Dabos, Physica B & C **144B**, 19 (1986).
[38] W.H. Zachariasen and F.H. Ellinger, Acta Crystallogr. **8**, 431 (1955).
[39] *Plutonium Handbook*, edited by O.J. Wick (Gordon and Breach, New York, 1967), Chap. 3, pp. 33–36.
[40] F. Weigel, J.J. Katz, and G.T. Seaborg, in *The Chemistry of the Actinide Elements* (Ref. 24), Vol. 1, pp. 595–614.
[41] U. Benedict, R.G. Haire, J.R. Peterson, and J.P. Itié, J. Phys. F: Met. Phys. **15**, L29 (1985).

5.5 Conclusion

The interest of americium lies in its pivotal position in the actinide series, between the light and heavy actinides, at the borderline between the high-symmetry and low-symmetry structures. Under pressure it switches from a localized f-electron system to an itinerant f-electron system. Our evidence relies on the distribution of distances that have been carefully measured thanks to the high pressure dedicated setup of ID30[3] at the ESRF.

We identified the final structures of Am-III and Am-IV by X-ray diffraction and the $5f$ electron delocalization is found to be a two-step process. We have shown that the phase Am-III is very similar to the γ-Pu. The primitive orthorhombic structure of Am-IV is a slight distortion of the $\alpha - U$. Thus, when pressure is increased, a delocalization of the f-electrons takes place and the structure of Am first mimics the structure of $\gamma - Pu$ and then the structure of $\alpha - U$.

Our simple theoretical discussion shows that the two behaviours observed in the actinide series can be described within the Friedel model taking into account the correlation effects. However further work is required in order to obtain a unified model for the whole actinide family.

[3]Now moved to ID27 and still improved.

Chapter 6

Clathrates

6.1 Introduction

The clathrates, from the Greek *klathron* meaning *enclosed*, are known from the beginning of the XIX^{th} century in the hydrated chlorine crystals[115]. The most famous clathrate is the methane hydrate contained in the deep substratum of the oceans. However its structure was only identified in 1951[116]. Moreover it was also found in many other compounds ($G_8(H_2O)_{46}$, $G_{24}(H_2O)_{136}$ and $G_{16}G_8(H_2O)_{46}$ where G= Ar, Kr, Xe, H_2S, Cl_2 or CH_4). Generally speaking, the term *clathrate* describes compounds where cages enclose another component, either atomic or molecular.

Among the clathrate structures, three of them have shown to be particularly important in group-14 clathrates. They are called type I (labeled Si-46 or Si_{46}), II (labeled Si-34 or Si_{136}) and III (labeled Si_{100}). The related structural details are given in section 6.2.

In 1965, the first silicon clathrates endohedrally doped with alkali atoms, $Na_8@Si_{46}$ and $Na_x@Si_{136}$, were synthetized[117, 118]. Other clathrate compounds are now based on different group-IV elements such as carbon, germanium, tin and lead. These works first succeeded in 1969 with $K_8@Ge_{46}$ and $K_8@Sn_{46}$ [119]. In parallel with the experimental synthesis, DFT *ab initio* calculations have shown [120, 121] that the diamond structure is slightly more stable than the clathrate by 0.08, 0.07 et 0.05 eV per C, Si, Ge atom, respectively [121, 120].

The technological interest of these artificial nanomaterials is continuously growing. Depending on the type and concentration of the dopant atom, the electrical, thermal and even mechanical properties of clathrates are widely tunable. So clathrates are good candidates for various applications[122, 123, 124, 125, 126] such as ultrahard materials[1], thermoelectric materials and wide-band-gap semiconductors.

On one hand this low-density structure has a remarkable bulk modulus in comparison to the diamond structure [122, 127]. The $Si-34$ bulk modulus is 90 GPa, 10% lower than silicon in the diamond structure. Cohen [128] gave a relationship between the interatomic distance of tetrahedral semiconductors, d (in Å) and their bulk modulus, B_0 (in GPa).

$$B_0 = 1971 d^{-3.5} \tag{6.1}$$

This formula is working very well for column-IV elements : B_0 is predicted to be 96 GPa and 99 GPa for silicon clathrate and diamond structures respectively. When compressed the silicon clathrate structure, $Si-34$, directly transforms to the β-Sn structure at about 11 GPa at

[1] B_0 has not to be confused with the hardness of the material, determined by the Mohs scale. There is no theoretical definition of the hardness. In the quest of ultrahard materials, B_0 is taken as a rough approximation of the hardness.

ambient temperature[2]. Another interesting point is that the filled clathrates, $Na_x@Si-34$ for example, seems to be more stable under pressure than empty clathrates. Indeed, the study of the electrical conductivity of doped clathrates under pressure[129] underlined that the transition to the metallic state occurs at about 11 GPa for $x = 3$ and only between 15 and 18 GPa for $x = 11$. These values are higher than the diamond-to-β-Sn transition pressure (11 GPa). This is linked to the structural support induced by the endohedral alkali atoms. The stability of the clathrate structure can be pushed even further with convenient intercalation (K, Rb, Ba or I) [130].

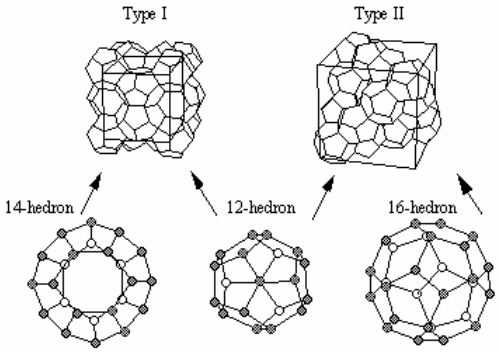

Figure 6.1: Structure of the type I and type II clathrates.

On the other hand, the guest atoms simultaneously act as electronic dopant and localized phonon scattering centers[126]. Clathrates thus have a phonon glass and electron crystal behaviour, i.e. low thermal conductivity and high electric conductivity. As explained by Slack [131], this is the ideal candidate for thermoelectric materials [132, 133]. Further details and references can be found in very complete review papers [134, 130]

In this chapter we focus on the structural properties of endohedrally-doped group-IV clathrates. Alkali atoms included within the clathrate cages are displaced with respect to the central position of the cages as observed by EXAFS [135]. A possible explanation for this experimental evidence is the symmetry breaking of the alkali diamond sublattice and the resulting formation of alkali pairs. This displacement is illustrated in figure 6.2 with the related EXAFS spectra. This distortion seems to be a dynamical pairing [136].

The critical effect of the expansion factor of the alkali structure will be highlighted using both semi-empirical models and *ab initio* calculations. We will give the theoretical description of the electronic instability driving the off-centering of the alkali atoms included within clathrate cages when there are sufficiently expanded.

Such an expanded structure allows to explore the area of the alkali phase diagrams corresponding to the expanded metals [137] or what Hemley even calls 'negative' pressures [138]. The stability under pressure of this distorted structure will be studied using both semi-empirical and *ab initio* calculations. Moreover the variation of the distortion amplitude as a function of the atomic nature of the dopant atoms will be considered. Based on these results, the systematics of the alkali doped group-IV clathrates will be discussed.

[2]The diamond structure appears at high temperature

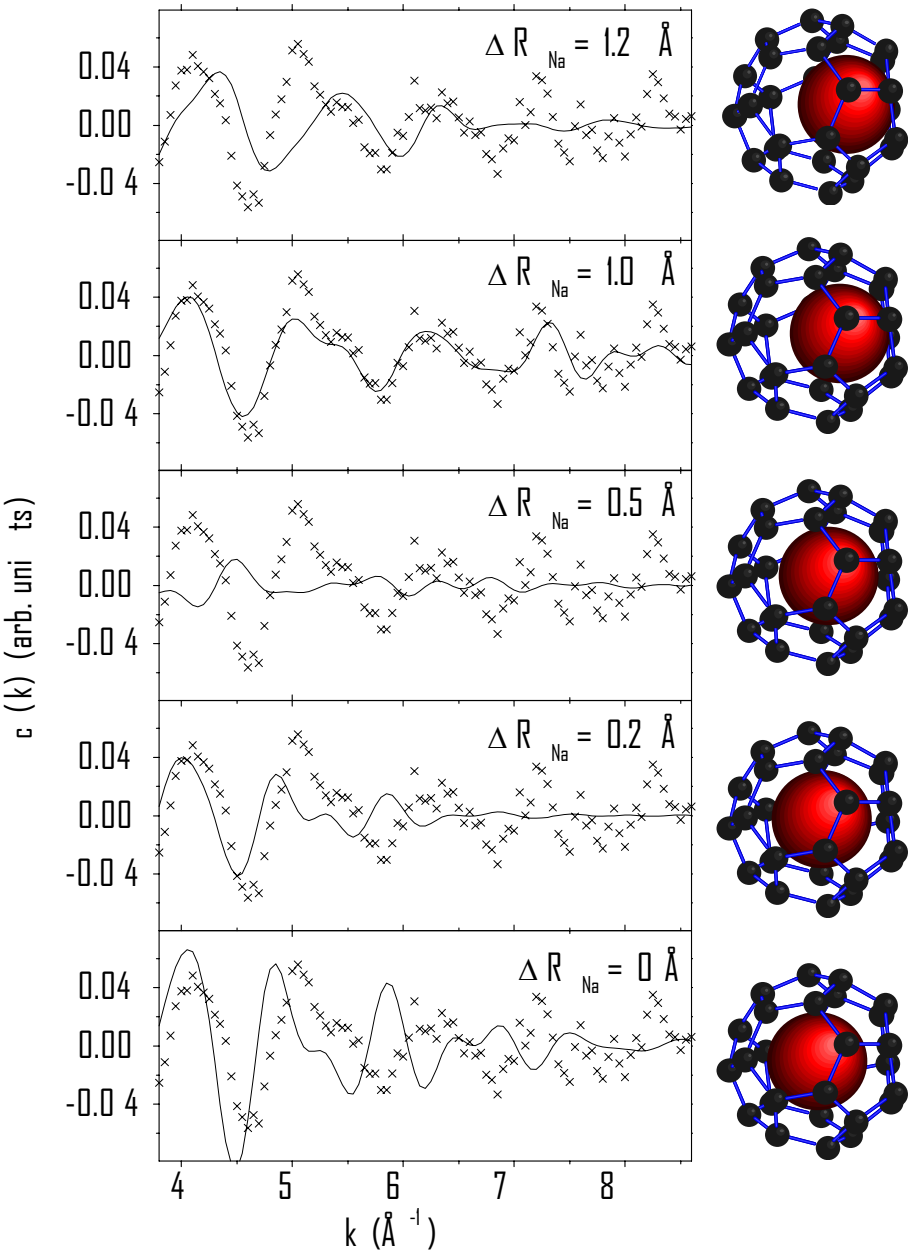

Figure 6.2: Figure (fig. 7) extracted from the paper of Brunet *et al.* [135] which illustrates the EXAFS signal linked to the displacement of the sodium atoms inside the silicon clathrate cages.

6.2 Description of the crystallographic structures

6.2.1 Cage structure

The prototype of the type-I clathrate is G_8X_{46} with space group $Pm\bar{3}n$ (n^o 233) where G = Na, Ba, ...and X = Si, Ge, Sn, ...Within this simple cubic structure, the atoms of the unit cell give rise to two types of cages : a dodecahedron ($[5^{12}]$) made with 20 atoms[3] and

[3]This cage is built with 12 pentagons which writes $[5^{12}]$. It obviously follows the Euler-Poincaré law, $F-A+S=2$, where F, A and S are the number of faces, edges and vertex, respectively.

a tetrakaidecahedron made with 24 atoms ($[5^{12}6^2]$). This cage assembly allows two possible positions for the intercalated atoms, i.e. 2a (0,0,0) and 6d ($\frac{1}{4}$,$\frac{1}{2}$,0). The cage arrangement defines channels in the three space directions, perpendicular to each other. Nowadays, Na_8Si_{46}, K_8Si_{46}, K_8Ge_{46}, K_8Sn_{46}, Cs_8Sn_{46}, $Rb_8Sn_{44.6}$, $K_{1.6}Cs_{6.4}Ge_{46}$ among others, are also known to exhibit this structure.

Structure	Lattice parameter (Å)	Space group	Atomic position
Si_{46}	10.36	$Pm\bar{3}m$	6c, 16i and 24k ($\frac{1}{4}$,0,$\frac{1}{2}$), (x,x,x) and (0,y,z) with $x \approx 0.183$, $y \approx 0.31$ and $z \approx 0.12$
Si_{136}	14.62	$Fd\bar{3}m$	8a, 32e and 96g ($\frac{1}{8}$,$\frac{1}{8}$,$\frac{1}{8}$), (x,x,x) and (y,y,z) with $x \approx 0.217$, $y \approx 0.068$ and $z \approx 0.370$
Ge_{46}	10.66	$Pm\bar{3}m$	6c, 16i, 24k
Ge_{136}	15.48	$Fd\bar{3}m$	96g, 32e, 8a
Sn_{46}	12.04	$Pm\bar{3}m$	6c, 16i, 24k
Sn_{136}	17.34	$Fd\bar{3}m$	96g, 32e, 8a

Table 6.1: Clathrate structural parameters.

The structure of type-II clathrates is based on the space group $Fd\bar{3}m$ (n^o 227). The prototype structures are $G_{24}(H_2O)_{136}$ and $G_8G_{16}(H_2O)_{136}$ where G=$H_2S, CO_2, \ldots$ In this case, the second type of cages is hexakaidecahedrons ($[5^{12}6^4]$). These cages are linked by their hexagonal faces giving rise to a super-diamond network where the cages are located on the nodes of the lattice. There are two typical positions for the endohedral atoms, i.e. 8b ($\frac{3}{8}$,$\frac{3}{8}$,$\frac{3}{8}$) and 16c (0,0,0).

Within both these structures, the cage atoms are all fourfold coordinated with bond angles close to the perfect tetrahedral sp_3 arrangement, i.e. $\approx 109.5^o$.

6.2.2 Alkali-doped silicon clathrates

Under ambient conditions, it is well-known that alkaline elements crystallize into compact structures and are electrical conductors. In contrast, hydrogen, H_2, is a molecular insulator, except at very high pressure where it becomes metallic. In both cases the atomic species have the same electronic configuration of their outer shells ns^1. They only differ by their inner shell structure: alkali's have complete core shell(s), whereas hydrogen has none. The complete core shells make the interatomic repulsion harder (by Pauli exclusion principle). In the case of a soft repulsion, it has been shown[139] that a Peierls distortion occurs for a partially-filled band. Moreover, the formation of alkali dimers in the expanded fluid regime[140] is supported by experiments and calculations. In the solid state, it was recently observed by Brunet *et al.*[135] in clathrates of silicon endohedrally doped with Na atoms.

If the case of filled clathrates, the endohedral atoms also have their own sub-structure within the cage assembly. Obviously this is widely constraint by the clathrate structure but few freedom degrees are still available. As mentioned in the previous sections, the sodium atoms are located within the Si_{28} and form a diamond sublattice. The *Fd3m* symmetry only occurs when the guest atom position coincides with the center of the cages. Both X-ray photoemission (XPS) and X-ray absorption spectroscopy (XANES and EXAFS) were performed by Brunet *et al.* and conclude that the sublattice of Na atoms is not an expanded diamond structure with Na atoms at the center of the Si_{28} cages. Instead, a symmetry-breaking mechanism occurs driven by an electronic instability: the Peierls distortion. From the EXAFS measurements, a displacement of the Na atoms of (0.9 ± 0.2) Å is evidenced. As a consequence, two situations are possible. First,

the Na atoms form a static structure made of dimers similar to hydrogen or to halogen molecules [141]. Second, there is a dynamical pairing as suggested by tunneling of the off-centered guest evidenced by Hermann *et al.* [136].

The distorted structure of the endohedral alkali atoms is obviously influenced by pressure. The symmetry recover under pressure is studied by both tight-binding and *ab initio* calculations. A Landau's model of this phenomenon is also discussed.

6.3 Systematics of alkali-doped silicon clathrates

It is interesting to go deeper in the study of the combined influence of the nature of the dopant atom and the size of the cage on the distortion amplitude in order to confirm the trend underlined in our theoretical study. The following cases are considered: $G_8@X-46$ where G is Li, Na or K and X is C, Si, Ge and Sn.

In order to make the link with our study of the Peierls distortion, two geometrical factors are introduced. First the expansion factor, f_e, is the direct image of how much the alkali atoms are pulled away from each other[4]. It is defined by

$$f_e = \frac{r_{clat}}{r_{met}} \tag{6.2}$$

where r_{met} and r_{clat} are the interatomic distances in the metallic and clathrate structures without distortion at zero pressure respectively. The second coefficient is the relative distortion amplitude, Δ_r.

$$\Delta_r = \frac{\Delta}{r_{clat}} \tag{6.3}$$

The calculated lattice parameters of the clathrates and the interatomic distances in the metallic structures at ambient pressure are given in tables 6.3 and 6.4, respectively.

The results of our *ab initio* calculations are summarized in figure 6.3. The distortion disappears if the alkali atoms are not expanded enough. This is in agreement with our theoretical approach of the Peierls distortion where we predict that materials which are not distorted under ambient conditions may undergo a symmetry-breaking if their atomic volume is sufficiently increased.

Another interesting point is to compare alkaline metals and hydrogen, all of them lying in the same column of the periodic table. Depending on the volume available for each atom, it is possible to induce a dimerization process to an alkali such as sodium. The existence of diatomic hydrogen molecules under ambient conditions and the molecular dissociation of H_2 under pressure has to be related to this dimerization of alkaline metals in clathrates. Clathrates can be considered as a means of expanding the usual compact alkaline structure letting the distortion process take place. Moreover the model underlines the fact that alkaline metals behave in the same way as hydrogen and halogens do. This is schematically described in table 6.5.

[4] In comparison with their metallic state under ambient conditions.

Structure	C	Si	Ge	Sn
Type II	379	90	67	38
Diamond	446	98	77	-

Table 6.2: Bulk moduli of the clathrate and diamond structures of group-IV elements[130].

Compound	a (Å)	r_{clat}
C-46	11.9	5.16
Si-46	14.6	6.34
Ge-46	15.4	6.67
Sn-46	17.3	7.50

Table 6.3: Calculated lattice parameters for type-II clathrates. The distance between the centers of two cages, r_{clat}, are also given.

Atom	r_{met} (Å)
Li	3.023
Na	3.659
K	4.525

Table 6.4: Interatomic distances in the alkali metals at ambient pressure.

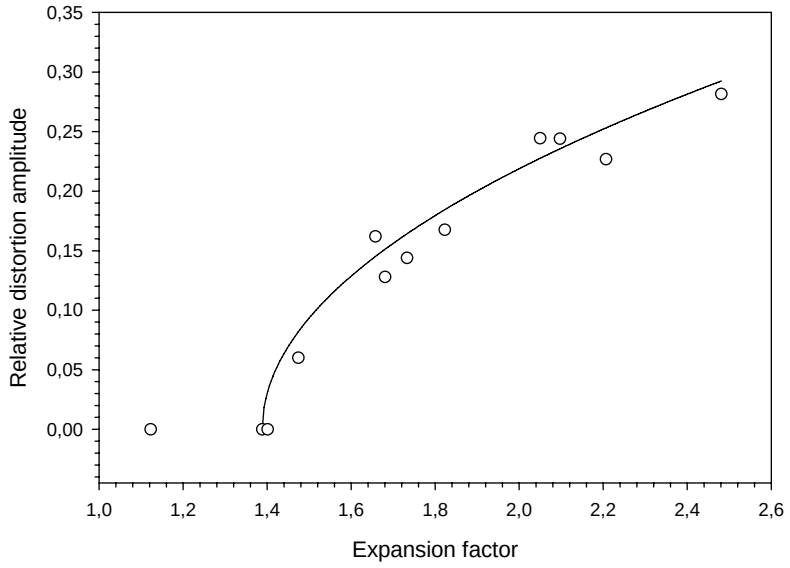

Figure 6.3: Relative distortion amplitude, Δ_r, as a function of the expansion factor, f_e. When the expansion factor is low enough, the alkali atoms stay at the center of the clathrate cages. As soon as the expansion factor reaches a critical value of 1.4, the alkali atoms become off-center with an amplitude roughly proportional to the square root of the expansion factor.

Our results are compared with the previous works concerning the potential of the alkali atoms within the clathrate cages [141, 133, 142]. Dong *et al.* and Conesa *et al.* did not directly assume a pairing of the alkali atoms. They studied the potential of different atoms included in the cages. They found a very flat potential for the sodium which is compatible with EXAFS results [135]. Tournus *et al.* directly focused on the possible existence of alkali dimers. They conclude to the possibility of the existence of dimers in alkali doped clathrates.

In our approach we assume that the alkali atoms are moving in the direction of each other giving rise to a set of diatomic molecules. The *ab initio* calculations clearly shows an energetic gain for such a structure. Our approach is compatible with both a static and dynamic structure. However, if the relative stability of those two structures is evaluated, an entropic contribution

$\frac{V}{V_0}$	H	Na
< 1	Atomic	Atomic
1	Molecular	Atomic
> 1	Molecular	Molecular

Table 6.5: The existence of diatomic hydrogen molecules under ambient conditions and its dissociation under pressure is related to the dimerization of sodium in type-II clathrate cages. The ratio $\frac{V}{V_0}$ appears to be a good parameter to describe the sequence of the *molecular* and *atomic* state. V_0 is the atomic volume of sodium or hydrogen under normal conditions.

has to be calculated.

EUROPHYSICS LETTERS 15 December 2003

Europhys. Lett., **64** (6), pp. 757–762 (2003)

A comparative theoretical study of the Peierls distortion in type-II alkaline-doped clathrates

H. LIBOTTE[1], J.-P. GASPARD[1], A. SAN MIGUEL[2] and P. MÉLINON[2]

[1] *Condensed Matter Physics Lab., (B5) Physics Institute, University of Liège B-4000 Sart-Tilman, Belgium*

[2] *Département de Physique des Matériaux, Université Claude Bernard-Lyon 1 F-69622 Villeurbanne, France*

(received 20 January 2003; accepted in final form 9 October 2003)

PACS. 61.48.+c – Fullerenes and fullerene-related materials.
PACS. 71.15.Nc – Total energy and cohesive energy calculations.
PACS. 71.30.+h – Metal-insulator transitions and other electronic transitions.

Abstract. – We show that a Peierls distortion may occur in expanded metals. When the sodium is expanded it undergoes a symmetry breaking and diatomic molecules are formed. This phenomenon is a result of an electronic instability mechanism. As shown by recent EXAFS experiments, sodium atoms included in chlathrate cages do not stay at the center of the cages. We describe this distortion by two very different methods: an *ab initio* study based on the local density approximation of the density-functional theory and a tight-binding description. This study is also extended to the other alkaline-doped silicon clathrates. This dimerization process is related to hydrogen dimer existence.

Under ambient conditions, it is common sense that alkaline elements crystallise into compact structures and are metallic conductors. In contrast, hydrogen, H_2, is a molecular insulator, except at very high pressure ($> 140\,\mathrm{GPa}$), where it becomes metallic [1, 2]. In both cases, the atomic species have the same electronic configuration of their outer shells ns^1. They only differ in their inner shell structure: alkalis have complete core shell(s), whereas hydrogen has none. The complete core shells make the interatomic repulsion harder (by Pauli exclusion principle). In the case of a soft repulsion, it has been shown [3] that a Peierls distortion occurs for a partially filled band. The formation of alkali dimers in the expanded fluid regime [4] is supported by experiments and calculations. In the solid state, it was recently observed by Brunet *et al.* [5] in clathrates of silicon [6] endohedrally doped with Na atoms. The clathrate Si-34 lattice ($Fd3m$ space group, 34 atoms per unit cell) is made with covalent tetrahedrally bonded Si atoms. This results in sharing-face Si_{28} and Si_{20} polyhedra [7]. The sodium atoms are located at the center of the Si_{28} and form a diamond sublattice. The $Fd3m$ symmetry only occurs when the guest atom position coincides with the center of the cages. Both X-ray photoemission (XPS) and X-ray absorption spectroscopy (XANES and EXAFS) were performed by Brunet *et al.* and conclude that the sublattice of Na atoms is not an expanded diamond structure with Na atoms at the center of the Si_{28} cages. Instead, a symmetry-breaking mechanism occurs driven by an electronic instability, the Peierls distortion. From

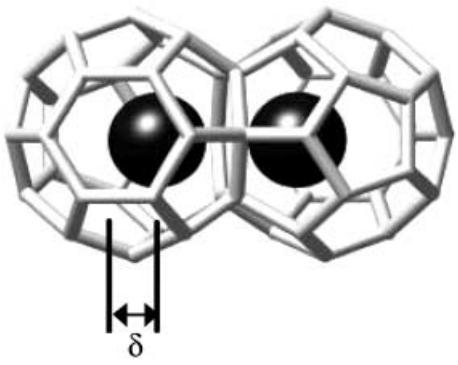

Fig. 1 – δ is the atomic displacement from the cage center. Na atoms form diatomic molecules separated by the silicon cage.

the EXAFS measurements, a displacement of the Na atoms of (0.9 ± 0.2) Å is evidenced. As a consequence, the Na atoms form dimers similar to hydrogen or to halogen molecules. This is in agreement with the poor screening of the photoelectrons observed in XPS and XANES [5].

The aim of this letter is twofold. First, in the case of expanded Na in silicon clathrate we performed *ab initio* calculations in order to confirm the experimental observation of Brunet *et al.* We also generalize the calculations to two other alkali-doped silicon clathrates. Secondly, we develop a tight-binding model in order to describe all this compound family in a semi-empirical way.

The *ab initio* calculations presented here were performed with the AbInit package [8] within the framework of the density-functional theory (DFT). The pseudopotentials of Hartwigsen, Goedecker and Hutter [9] were used with the Ceperley-Alder [10] form of the local-density approximation (LDA). A complete numerical convergence study was performed: an energy cut-off of 30 Ha is chosen for the plane-wave expansion of the wave functions and the Brillouin zone is sampled by a $2 \times 2 \times 2$ grid [11]. When Na atoms move away from the cage center, the size of the unit cell size increases by symmetry reduction.

In order to determine the stable distortion amplitude, LDA-DFT energy calculations are performed for different values of Δ. Δ is the fractional atomic coordinate change of the Na atom in the Na-Na direction in the clathrate as illustrated in fig. 1. Therefore, the distance between two Na atoms, $d_{\text{Na-Na}}$ is given by relation (1):

$$d_{\text{Na-Na}} = \sqrt{3}\left(\frac{1}{4} - 2\Delta\right)a_{\text{cl}}, \tag{1}$$

where a_{cl} is the lattice parameter of the clathrate. The distortion amplitude, δ, is then given by relation (2),

$$\delta = \sqrt{3}\Delta a_{\text{cl}}. \tag{2}$$

The equilibrium lattice parameter is computed by relaxation of the internal atomic forces and is independent of Δ. The calculated value of Na_8@Si-34 is 14.51 Å which is only 1% lower than the experimental value of 14.65 Å [5]. Figure 2 shows the evolution of the cohesive energy of the doped clathrate as a function of the internal sodium displacement. It is clear from this $E(\Delta)$ curve that the stable structure is a collection of sodium dimers instead of a

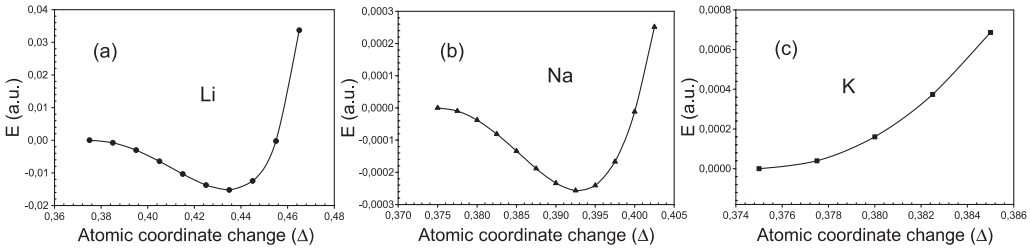

Fig. 2 – Cohesive energy of the doped clathrates ((a) Li_8@Si-34, (b) Na_8@Si-34 and (c) K_8@Si-34) as a function of the alkali atom displacement, Δ, within the LDA approximation. The origin is chosen to be the energy of the non-distorted structure. The minimum is located at $\Delta = 0.018$ for sodium. The resulting distortion amplitude is $\delta = 0.456$ Å.

simple diamond lattice. This simulation method was also applied for Li_8@Si-34 and K_8@Si-34. The calculated distortion amplitudes are summarized in table I.

The distortion amplitude found for Na_8@Si-34, 0.456 Å, is much lower than the experimental value. The resulting Na-Na distance is 5.37 Å. However it is a very shallow minimum and a small correction could give quite different results. LDA approach is known to give too short distances. In this case it does not seem to be the case. However, the Na-Na distance is not the first-neighbour distance. Na atoms are surrounded by silicon atoms. When a sodium atom is moving from the center of the clathrate cage, a complex combination of attractive and repulsive interactions between the sodium atom and the silicon atoms takes place and masks the distance shortening due to LDA. Moreover, it is clear that in such a situation long-range interactions play a role. However, it is well known from LDA studies on graphite that LDA-DFT *ab initio* simulations do not correctly reproduce the dispersion forces [12]. Intuitively, if a long-range attractive interaction is added, the distortion amplitude should increase. More complex methods [13] could be used to describe this kind of compounds where long-range interactions have a clear influence. LDA approach is a very good first step in the theoretical study of distorted sodium structures.

In comparison with *ab initio* methods, the tight-binding approach allows the tuning of each interaction parameter separately. Only the energy of the diamond sublattice of Na atoms inside the clathrate cages is considered, as these cages are proved to be rigid by previous LDA calculations. The tight-binding technique using a second-moment approximation is well adapted to describe systems where a Peierls distortion occurs [3]. Alkali atoms are treated as hydrogen-like atoms linked by $ss\sigma$ resonant interactions. An additive pairwise repulsive potential is also added in order to simulate effects of the Pauli principle and electrostatic repulsion. Moreover, electronic correlation effects are taken into account using a simple description given by Friedel [14, 15]. As silicon atoms are fourfold coordinated with no dangling bonds, they behave like a rare-gas atom from the point of view of Na atoms. This

TABLE I – *Distortion amplitude predicted for the endohedrally doped-clathrates considered here using DFT-LDA calculation.*

Clathrate formula	Δ	δ (Å)
Li_8@Si-34	0.061	1.55
Na_8@Si-34	0.018	0.456
K_8@Si-34	0	0

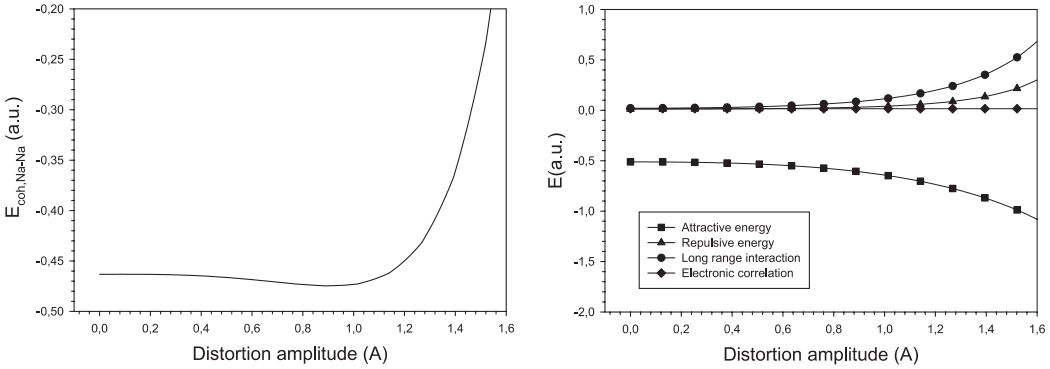

Fig. 3 – $E_{\mathrm{coh,Na\text{-}Na}}$ curve calculated using the tight-binding model for Na_8@Si-34 (continuous line). The amplitude distortion is in fair agreement with the experimental value. All the contributions to the cohesive energy are also represented below: attractive part (square), repulsive part (triangle), long-range interaction between sodium and silicon cages (circle), electronic-correlation energy (diamond).

is supported by the fact that the Na atoms can be extracted by pumping [16], while this is not possible in other situations where a strong hybridization occurs between dopant atoms and the cage atoms [17]. Our model applies when the hybridization between the cages and the dopant atoms is weak. We now consider the diamond sublattice of Na atoms inside the clathrate cages. As the Na atoms try to form dimers, each Na atom has one neighbour at a short distance, r_c, and three others at a long distance, r_l. Both r_c and r_l are easily related to the atomic displacement, Δ. The tight-binding cohesive energy, $E_{\mathrm{coh}}(\Delta)$, of the alkali sublattice is given by relation (3) [18],

$$\begin{aligned} E_{\mathrm{coh,Na\text{-}Na}}(\Delta) \; = \; & \\ & -\sqrt{\beta_0^2\left(r_c^{-2q}+3r_l^{-2q}\right)}+ \\ & +\frac{V_{0,\mathrm{Na\text{-}Na}}}{2}\left(r_c^{-p_{\mathrm{Na\text{-}Na}}}+3r_l^{-p_{\mathrm{Na\text{-}Na}}}\right)+ \\ & +\frac{U}{4}-\frac{U^2}{16W}+ \\ & +\frac{V_{0,\mathrm{Na\text{-}Si}}}{2}\left(\overline{r}_{l,\mathrm{Na\text{-}Si}}^{-\frac{p_{\mathrm{Na\text{-}Na}}+p_{\mathrm{Si\text{-}Si}}}{2}}+\overline{r}_{c,\mathrm{Na\text{-}Si}}^{-\frac{p_{\mathrm{Na\text{-}Na}}+p_{\mathrm{Si\text{-}Si}}}{2}}\right). \end{aligned} \tag{3}$$

The first and second terms of eq. (3) are, respectively, the electronic attractive and repulsive parts of the Na-Na interaction. The third term takes into account the correlation contribution [14,15] depending on the electronic bandwidth, W. W is approximated from our tight-binding electronic model. The last term takes into account the dispersion forces between

TABLE II – *Distortion amplitude predicted for the endohedrally doped clathrates considered here using our tight-binding model.*

Clathrate formula	Δ	δ (Å)
Li_8@Si-34	0.076	1.93
Na_8@Si-34	0.036	0.91
K_8@Si-34	0	0

TABLE III – *The existence of diatomic hydrogen molecules under ambient conditions and the metallization of* H_2 *under pressure is related to the dimerization of sodium in type-II clathrate cages. The ratio* $\frac{V}{V_0}$ *is a good parameter to describe the succession of the metallic or insulator state.* V_0 *is the atomic volume of sodium or hydrogen under normal conditions.*

$\frac{V}{V_0}$	H	Na
< 1	metal	metal
1	insulator	metal
> 1	insulator	insulator

the alkali atoms and the clathrate cages. All the parameters of this model are directly calculated from experimental data [21–24] relative to alkali diatomic molecules and bulk metals.

This models gives good insight into the alkaline-doped clathrate systematics. In the case of Na_8@Si-34, the calculated distortion amplitude is 0.91 Å. This result is in very good agreement with the experimental value of (0.9 ± 0.2) Å. Figure 3(a) shows the variation of $E_{\mathrm{coh,Na\text{-}Na}}$ as a function of Δ. This model is then used to establish a systematics of the endohedrally doped Si-34 clathrates. Table II shows the distortion amplitudes found for all clathrates considered here. Our model shows that the distortion should disappear when the interaction between the dopant atom and the cage increases. This occurs when the dopant atom becomes bigger, *i.e.* going down in the column I of the periodic table or when the cage diameter decreases. Figure 3(b) shows the different contributions to the total energy as a function of the atomic displacement. The correlation contribution has a very weak dependence as a function of the atomic displacement.

It is interesting to compare alkaline metals and hydrogen, all of them lying in the same column of the periodic table. Depending on the volume available for each atom, it is possible to induce a dimerization process to any alkali. The existence of diatomic hydrogen molecules under ambient conditions and the metallization of H_2 under pressure has to be related to this dimerization of alkaline metals in clathrates. Clathrates can be considered as a means of expanding the usual compact alkaline structure, the absence of distortion occurring when the distances between alkali atoms can be further reduced, *i.e.* outside any host structure. This universality of behaviour through the first column of the periodic table is summarized in table III.

In summary, the dimerization process of alkali atoms included in chlatrate is a new example of the Peierls distortion. DFT-LDA calculations show that the long-range interactions play a role for the exact description of this distortion process. In addition, a semi-empirical tight-binding model was developed in order to find out the general trends through the doped clathrate family. We clearly show that the interaction between the dopant atom and the cage is one of the most important parameters in distortion amplitude determination. Moreover, the model underlines the fact that alkaline metals behave as a function of atomic volume in the same way as hydrogen does.

* * *

We gratefully thank Prof. B. LEIH (University of Liège, Belgium) for invaluable discussions. This work was supported by FNRS Grant No. 9.4565.96F.

REFERENCES

[1] WEIR S. T., MITCHELL A. C. and NELLIS W. J., *Phys. Rev. Lett.*, **76** (1996) 1860.
[2] CELLIERS P. M., COLLINS G. W., DA SILVA L. B., GOLD D. M., CAUBLE R., WALLACE R. J., FORD M. E. and HAMMEL B. A., *Phys. Rev. Lett.*, **84** (2000) 5564.
[3] GASPARD J.-P., PELLEGATTI A., MARINELLI F. and BICHARA C., *Philos. Mag. B*, **77** (1998) 727.
[4] PILGRIM W.-C., ROSS M. and YANG L. H., *Physica B*, **241-243** (1998) 935.
[5] BRUNET F., MÉLINON P., SAN MIGUEL A., PEREZ A., FLANCK A. M., RENY E., CROS C. and POUCHARD M., *Phys. Rev. B*, **61** (2000) 16550.
[6] SAN-MIGUEL A., KÉGHÉLIAN P., BLASE X., MÉLINON P., PEREZ A., ITIÉ J.-P., POLIAN A., RENY E., CROS C. and POUCHARD M., *Phys. Rev. Lett.*, **83** (1999) 5290.
[7] KASPER J. S., HAGENMULLER P. and POUCHARD M., *Science*, **3704** (1965) 1715.
[8] The AbInit code is a common project of the Université Catholique de Louvain, Corning Incorporated, University of Liège and other contributors (URL: `http://www.abinit.org`).
[9] HARTWIGSEN C., GOEDECKER S. and HUTTER J., *Phys. Rev. B*, **58** (1998) 3641.
[10] CEPERLEY D. M. and ALDER B. J., *Phys. Rev. Lett.*, **45** (1980) 556.
[11] MONKHORST H. J. and PACK J. D., *Phys. Rev. B*, **13** (1976) 5188.
[12] GIRIFALCO L. A. and HODAK M., *Phys. Rev. B*, **13** (2002) 125404.
[13] RAPCEWICZ K. and ASHCROFT N. W., *Phys. Rev. B*, **44** (1991) 4032.
[14] FRIEDEL J., *Microclusters*, edited by SUGANO S., NISHINA Y. and OHNISHI S., *Springer Ser. Mater. Sci.*, Vol. **4** (Springer-Verlag, Berlin) 1986.
[15] FRIEDEL J., *Physics and Chemistry of Electrons and Ions in Condensed Matter*, edited by ACRIVOS J. V., MOTT N. F. and YOFFEE A. D., *ASI Ser. C Math. Phys. Sci.*, Vol. **130** (Dreidel Publ., Dordrecht) 1984.
[16] CROS C., POUCHARD M. and HAGENMULLER P., *J. Solid State Chem.*, **2** (1970) 570.
[17] CONNÉTABLE D., ARTACHO E. and BLASE X., *Phys. Rev. Lett.*, **87** (2001) 206405.
[18] All the details of the tight-binding model will be given in a forthcoming paper. Actually, this model seems to be able to describe a wide variety of distortion situations in a semi-quantitative way (non-hydrostatic effects in silicon under pressure [19] and bromine metallization mechanism under pressure [20], for example).
[19] LIBOTTE H. and GASPARD J.-P., *Phys. Rev. B*, **62** (2000) 7110.
[20] SAN MIGUEL A., LIBOTTE H., GASPARD J.-P., GAUTHIER M., ITIÉ J.-P. and POLIAN A., *Eur. Phys. J. B*, **17** (2000) 227.
[21] GSCHNEIDNER K. jr., *Solid State Phys.*, **16** (1964) 275.
[22] BERRY R. S., RICE S. A. and ROSS J., *Physical Chemistry*, Vol. **4** (Wiley, New York) 1980.
[23] MAJEWSKI J. A. and VOGL P., *Phys. Rev. B*, **35** (1987) 9666.
[24] SANDERSON R. T., *Chemical Bonds and Bond Energy* (Academic Press, New York) 1971.

High Pressure Research, Month 2004, Vol. 00, pp. 1–9

Taylor & Francis
Taylor & Francis Group

STUDY OF THE PEIERLS DISTORTION IN Na_8@Si-34 UNDER PRESSURE

H. LIBOTTE* and J.-P. GASPARD

Condensed Matter Physics Lab., (B5) Physics Institute, University of Liége, B-4000 Sart-Tilman, Belgium

(Received 28 May 2003; Revised 9 December 2003; In final form 15 December 2003)

Recent EXAFS experiments have shown that a Peierls distortion can occur in alkali sublattices [Brunet *et al.*, Phys. Rev. B 61, 16550 (2000)]. This shows that even though all the alkali metals crystallise under ambient conditions in compact structures, the sodium sublattice in Na_8@Si-34 undergoes a symmetry-breaking transition and forms dimers. In this article, the evolution of this distortion under pressure is predicted within the local density approximation of the density–functionnal theory. We find a transition from a distorted structure to a regular diamond sublattice at 3.9 GPa, which is also discussed using a semi-empirical model.

Keywords: Clathrate; Peierls distortion; Expanded metals; Tight-binding model

INTRODUCTION

Clathrates are of considerable technological interest [1–7]. Indeed they are considered as super hard materials, measured by X-ray diffraction under pressure. They are also good candidates for high-T_c superconductors and for advanced thermoelectric materials. In the case of the endohedrally doped clathrates, the behaviour of the alkali atoms included in clathrate cages has a major influence on the thermoelectric and structural properties of these new materials.

Under ambient conditions, alkali metals have close-packed structures, *i.e.* hexagonal close-packed, face centered cubic or body centered cubic. However, when expanded, alkali atoms may form dimers as it is shown by experiments and calculations as well in the expanded fluid regime [8]. In the solid state, the same kind of behavior was recently observed in type-II clathrates of silicon endohedrally doped with Na atoms [9] under ambient pressure.

The Si-34 clathrate lattice (*Fd3m* space group, 34 atoms per unit cell) is made with covalent tetrahedrally bonded Si atoms. This results in face sharing Si_{28} and Si_{20} polyhedra [10]. The Si_{28} cages are made of 12 pentagons and 4 hexagons whereas the Si_{20} cages contain 12 pentagons and no hexagon. This obviously follows the Euler–Poincaré law, $F - A + S = 2$, where F, A and S are the number of faces, edges and vertex, respectively.

* Corresponding author. E-mail: h.libotte@ulg.ac.be

ISSN 0895-7959 print; ISSN 1477-2299 online
DOI: 10.1080/08957950410001661981

The Si_{28} cages are linked together through the four hexagons. If the sodium atoms are located at the center of these Si_{28} cages, they form a diamond sublattice with the *Fd3m* symmetry. Both X-ray photoemission (XPS) and X-ray absorption spectroscopy (XANES and EXAFS) were performed by Brunet *et al.* [9] and conclude that the sublattice of Na atoms is not an expanded diamond structure with Na atoms at the center of the Si_{28} cages. Instead, a symmetry-breaking mechanism occurs driven by an electronic instability, the Peierls distortion. From the EXAFS measurements, a displacement of the Na atoms of (0.9 ± 0.2) Å is evidenced. As a consequence, the Na atoms form dimers, similar to hydrogen or halogen molecules. This is in agreement with the poor screening of the photoelectrons observed in XPS and XANES [9].

The aim of this article is to predict the evolution of the distortion amplitude as a function of pressure. In the next section, a semi-empirical description of the electronic structure of the sodium sublattice is given. Then, the equilibrium atomic position of the sodium atoms inside the clathrate cage is studied within the local–density approximation (LDA) of the density–functionnal theory (DFT).

SEMI-EMPIRICAL DESCRIPTION OF THE PEIERLS DISTORTION IN Na_8@Si-34

In this section, only the sodium sublattice is considered. Indeed, it was observed that the hybridisation between the sodium atoms and clathrate cages is weak [11]. Therefore in order to illustrate the electronic instability at the origin of the Peierls distortion, we only consider the electronic density of states (eDoS) of the sodium sublattice as a function of the distortion amplitude.

The eDoS is calculated using the continued fraction method [12]. Here the continued fraction is truncated after 10 stages and a constant prolongation is used.

$$R(z) = \cfrac{1}{z - a_1 - \cfrac{b_1}{z - a_2 - \cfrac{b_2}{z - \cfrac{\ddots}{z - a_\infty - \cfrac{b_\infty}{z}}}}} \tag{1}$$

The (a_i, b_i) parameters are calculated using the recursion method [13] applied to a tight-binding electronic hamiltonian. Δ is the atomic displacement of the Na atom in the Na–Na direction in the clathrate as illustrated on Figure 1. δ is defined as the atomic coordinate change induced by the atomic displacement. Therefore, $\Delta = \sqrt{3}\delta a$ where a is the clathrate lattice parameter.

The electronic energy gain is clear from the eDoS figures (see Fig. 2). The electronic attractive energy gain is due to the displacement of the filled valence band to the negative

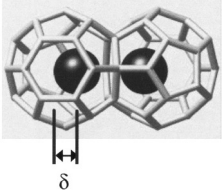

FIGURE 1 Δ is the atomic displacement from the cage center. Na atoms form diatomic molecules separated by one face of the Si_{28} cage.

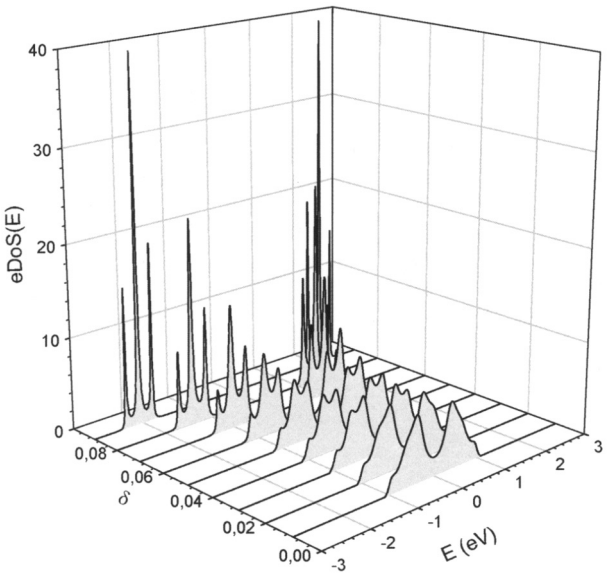

FIGURE 2 Electronic density of states of the sodium sublattice calculated using the continued fraction method. The density is given for different value of δ. It is clear that the dimer formation is electronically favorable. Indeed the center of gravity of the filled valence band shifts to low energy. The energy origin is chosen at the Fermi level.

energies of the gravity center. However, if only this electronic attractive contribution is taken into account, the alkali should always be distorted. Obviously, the repulsive contribution has to be taken into account and plays a major role.

Using a tight-binding model based on the second-moment approximation and a pairwise repulsive potential, the energy of the sodium sublattice is given by the expression (2). This model succeeded in the description of the Peierls distortion for elements of groups Va, VIa and VIIa [14, 15].

$$E_{\mathrm{Na}} = -\beta_0\sqrt{3r_{\mathrm{L}}^{-4} + r_{\mathrm{C}}^{-4}} + V_0(3r_{\mathrm{L}}^{-p} + r_{\mathrm{C}}^{-p}), \tag{2}$$

where β_0, V_0 and p are the attractive and repulsive parameter of the model. They can be numerically determined using the experimental data of the diatomic molecule, Na_2. r_{L} and r_{C} are respectively the long and short bonds inside the distorted diamond Na sublattice. The existence of a distortion can be determined using a serie expansion of the relation (2) at constant volume as a function of the distortion amplitude, ε. Using the lattice parameter, a, the undistorted bond length, $(\sqrt{3}/4)a$, is introduced and the short and long bond lengths can be written:

$$d_1^2 = \frac{3}{16}a^2(1 - 16\varepsilon + 64\varepsilon^2), \tag{3}$$

$$d_{2,3,4}^2 = \frac{3}{16}a^2\left(1 - \frac{16}{3}\varepsilon + 64\varepsilon^2\right). \tag{4}$$

The series expansion of the total energy of the sodium sublattice (2), gives the following relation

$$E_{\mathrm{Na}}(\varepsilon) = 2V_0\left(\frac{\sqrt{3}a}{4}\right)^{-p} - 2\beta_0\left(\frac{\sqrt{3}a}{4}\right)^{-2} + 2V_0\left(\frac{\sqrt{3}a}{4}\right)^{-p} 32\frac{p(2p+1)}{3}\varepsilon^2 - 2\beta_0\left(\frac{\sqrt{3}a}{4}\right)^{-2} 96\varepsilon^2. \tag{5}$$

Considering the sign of the ε^2 term, it is possible to say that the distortion occurs when

$$a > a_{\text{lim}} = \frac{4\sqrt{3}}{3}\left(\frac{V_0 p(2p+1)}{9\beta_0}\right)^{1/(p-2)}. \tag{6}$$

If the accessible volume of the atoms is not constraint, the equilibrium atomic volume is given by the minimum of the total energy (2).

$$a_{\text{eq}} = \frac{4\sqrt{3}}{3}\left(\frac{pV_0}{\beta_0}\right)^{1/(p-2)}. \tag{7}$$

As $a_{\text{lim}} > a_{\text{eq}}$, it is clear that when an alkali metal is expanded, it undergoes a symmetry-breaking but not under ambient conditions. Considering the doped clathrate structure, the resulting structure is then a collection of diatomic molecules. If a pressure is applied on the structure, *i.e.* if the accessible volume is reduced, our simple model predicts that the distortion will disappear. Using this semi-empirical model, the volume reduction at the transition is found to be 12%. This point is addressed in the next section using *ab initio* method.

METHOD OF CALCULATION

The *ab initio* calculations presented here were performed with the AbInit package [16] in the framework of the DFT. The pseudopotentials of Troulliers and Martins [17] were used with the Ceperley–Alder [18] form of the LDA. An energy cut-off of 30 Ha is chosen for the plane wave expansion of the wavefunctions. The Brillouin zone is sampled using a $2 \times 2 \times 2$ k-point grid [19]. A complete convergence study was performed and confirmed that these parameters allow to get a precision of 0.1 Å on the stable sodium position inside the clathrate cages.

The total energy calculations were performed for given atomic positions as a function of the clathrate lattice parameter. For a given sodium position, the energy–volume curve is fitted using the third-order Murnaghan equation of states.

$$P(V) = \frac{3B_0}{2}\left[\frac{3}{4}\left(\frac{V_0}{V}\right)^{7/3} - \left(\frac{V_0}{V}\right)^{5/3}\right]\left[1 + \frac{3}{4}(B_0' - 4)\left[\left(\frac{V_0}{V}\right)^{2/3} - 1\right]\right]. \tag{8}$$

Using these equations, it is then possible to get the evolution of the free enthalpy as a function of the atomic displacement at a given pressure. The minimum of this curve for a given pressure gives the equilibrium distortion amplitude at that pressure.

RESULTS AND DISCUSSION

The first step of this study is the LDA–DFT calculation of the total energy of Na_8@Si-34 as a function of both the sodium atomic displacement, Δ, and the clathrate lattice parameter, a_{cl}.

This atomic displacement is related to the atomic coordinate change, δ, by the relation $\Delta = \sqrt{3}\delta a_{cl}$. Therefore the distance between two Na atoms, d_{Na-Na} is given by relation (9)

$$d_{Na-Na} = \sqrt{3}\left(\frac{1}{4} - 2\delta\right)a_{cl}. \tag{9}$$

The DFT–LDA calculations were performed for 10 different values of the lattice parameter and 12 values of the atomic displacement. First of all, the equilibrium structure at zero pressure is determined using the fitted $E(V)$ curves. This study underlines that the equilibrium lattice parameter is not influenced by the atomic displacement of the alkali atom. The third-order Birch–Murnaghan equation of states is presented on Figure 3.

Figure 4 shows the evolution of the enthalpy of the doped clathrate as a function of the internal sodium displacement at different pressure. It is clear from this $H(\Delta)$ curve that the stable structure is a collection of sodium dimers instead of a simple diamond lattice.

The calculated equilibrium distortion found using this method is 0.454 Å, is in fair agreement with the experimental value. The second step is the study of this distortion amplitude as a function of pressure. Using the calculated Murnaghan equation of states, the enthalpy for given pressure values is calculated as a function of the sodium atomic displacement. Collecting all the minimum values from these curves, it is easy to obtain the evolution of the distortion amplitude as a function of pressure. This final curve is presented in Figure 5.

Our theoretical considerations predict that the distortion disappears at 3.9 GPa. This point needs to be confirmed by experimental approaches such as EXAFS. When the distortion disappears, the volume is 96% of the volume under ambient conditions. Combining all these results, the final equation of states of Na_8@Si-34 is calculated. The parameter values of the third-order Birch–Murnaghan are given in Table I.

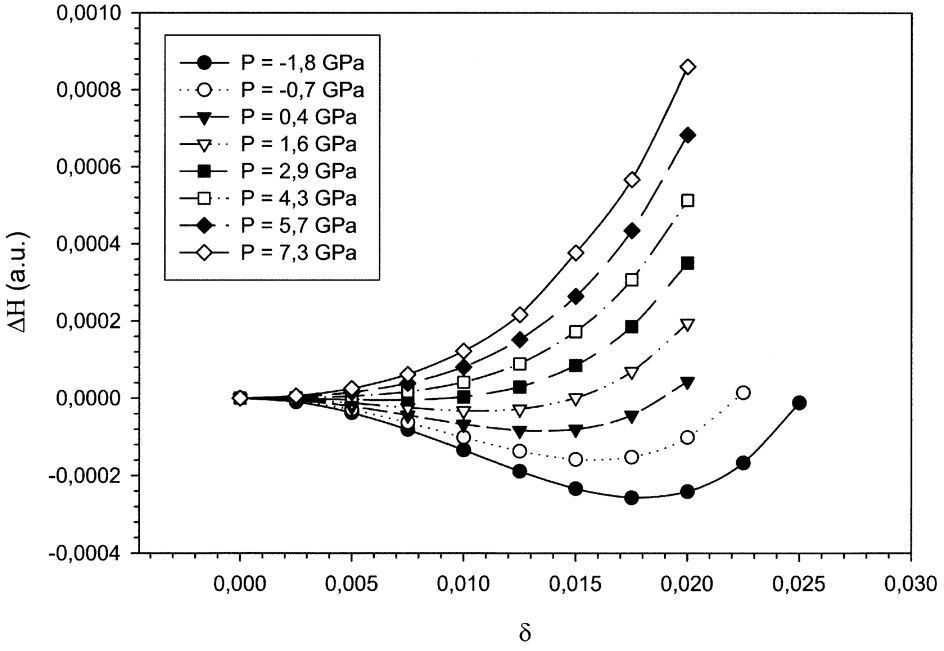

FIGURE 3 Volume–pressure curve of Na_8@Si-34.

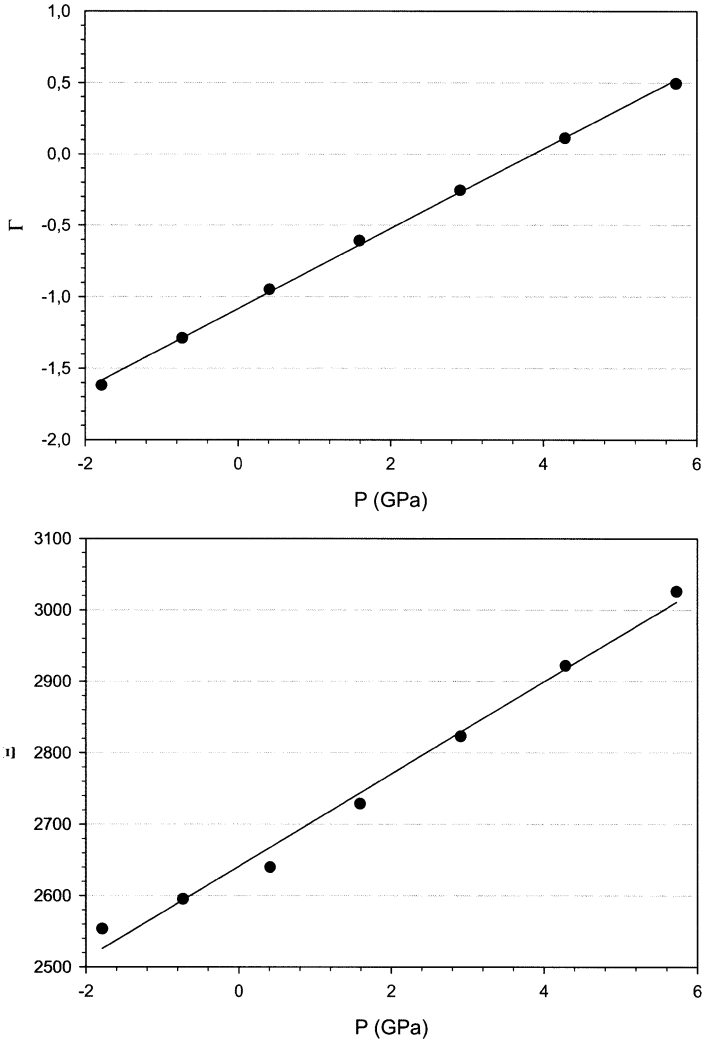

FIGURE 4 Enthalpy of Na_8@Si-34 as a function of the internal sodium displacement, Δ within the LDA approximation at different pressures. The origin is chosen to be the energy of the non-distorted structure. The resulting distortion amplitude is $\Delta = 0.454$ Å at ambient pressure.

A simple Landau development can also be performed on the different energy curves (see relation (6)) as a function of the pressure.

$$E(P, \delta) = \Gamma(P)\delta^2 + \Xi(P)\delta^4. \tag{10}$$

Figure 6 shows the evolution of these parameters as a function of pressure. The transition is clearly underlined when the the sign of $\Gamma(P)$ changes. In both of the graphs, the linear regression line is given. All the parameters of this developement are given in Table II.

The fit is excellent for $\Gamma(P)$ which can be written $\Gamma(P) = \gamma_\Gamma(P - P_0)$. In the case of $\Xi(P)$, the fit quality is a little lower, however, the linear approximation is still very good, $\Xi(P) = \Xi_0 + \gamma_\Xi P$. As $\Xi(P)$ is positive, the transition is a very good example of a structural

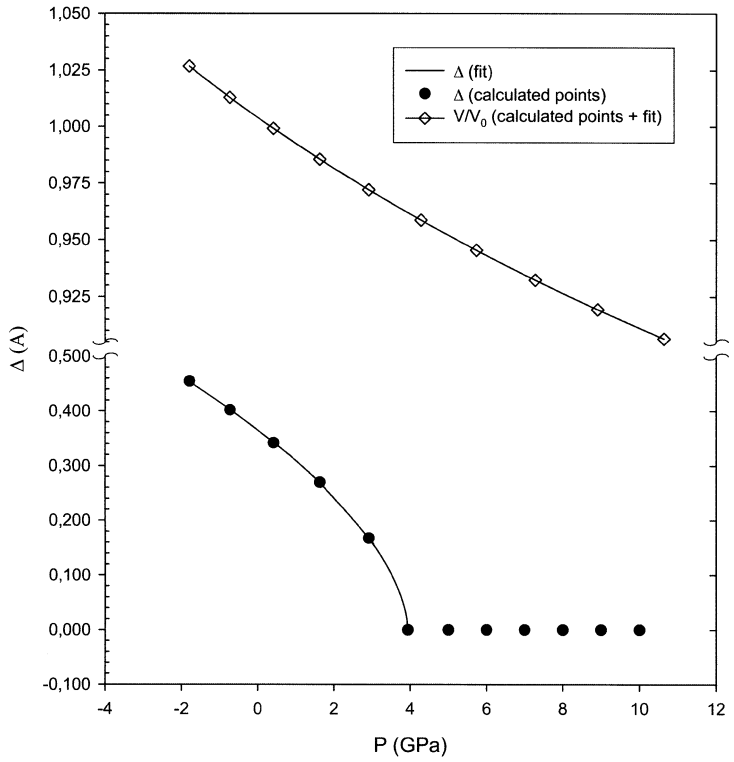

FIGURE 5 The distortion amplitude as a function of pressure. Moreover, the V/V_0 is also given for Na_8@Si-34. The distortion disappears for a volume reduction of the cage of 3.8%. No discontinuity is observed on the $V(P)$ curve.

second order phase transition. The minimum of the relation (10) as a function of pressure, P, is simply given by

$$\frac{\partial E(P,\delta)}{\partial \delta} = 0 = 2\Gamma(P)\delta + 4\Xi(P)\delta^3. \tag{11}$$

Taking into account that $\Xi(P)$ is positive and of the linear expression of the Landau coefficients, the relation (11) can be simplified and gives

$$\delta(P) = \sqrt{\frac{\gamma_\Gamma(P - P_0)}{2(\Xi_0 + \gamma_\Xi P)}}. \tag{12}$$

TABLE I Parameters calculated from the LDA calculations are compared with previous experimental and theoretical results.

Parameter	*This work*	*Previous work [9]*
a (Å)	14.51	14.57
B_0 (GPa)	84	90 ± 5
B'_0	4.07	3.6

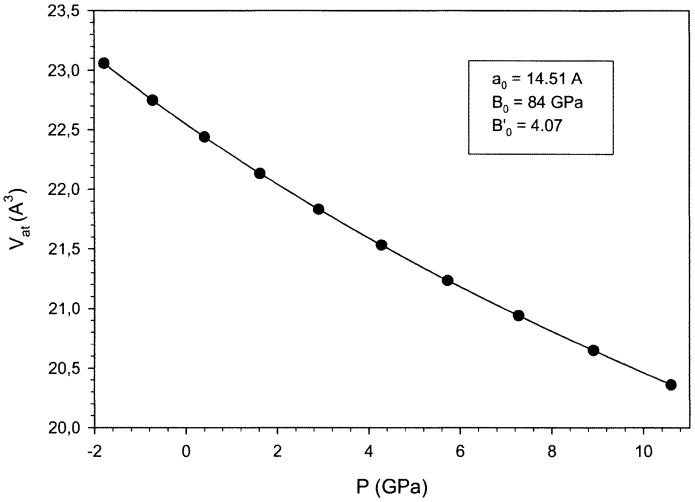

FIGURE 6 The parameters of the Landau development as a function of pressure. The results of the linear regression are represented by the continuous straight lines.

TABLE II Summary of the parameters of the Landau development.

Parameter	*Value*	*Parameter*	*Value*
γ_Γ	0.28 Ha GPa^{-1}	P_0	3.9 GPa
γ_Ξ	65 Ha GPa^{-1}	Ξ_0	2640 Ha

Another interesting point is to compare alkaline metals and hydrogen, all of them lying in the same column of the periodic table. Depending on the volume available for each atom, it is possible to induce a dimerisation process to an alkali such as sodium. The existence of diatomic hydrogen molecules under ambient conditions and the molecular dissociation of H_2 under pressure has to be related to this dimerisation of alkaline metals in clathrates. Clathrates can be considered as a mean of expanding the usual compact alkaline structure letting the distortion process to be possible. This universal behaviour through the first column of the periodic table is schematically summarised in Table III.

TABLE III The existence of diatomic hydrogen molecules under ambient conditions and the metallisation of H_2 under pressure is related to the dimerisation of sodium in type-II clathrate cages.

V/V_0	*H*	*Na*
<1	Metal	Metal
1	Insulator	Metal
>1	Insulator	Insulator

Note: The ratio V/V_0 is a relevant parameter to describe the succession of the metallic or insulator state. V_0 is the atomic volume of sodium or hydrogen under normal conditions.

CONCLUSION

In conclusion, the dimerisation process of alkali atoms included in clathrate is a new example of the Peierls distortion. This study is the first theoretical study of the distortion amplitude as a function of pressure. As in all distorted structures, the distortion disappears when pressure is applied, in this case at 3.93 GPa. This study can be further applied to other alkali doped clathrate in order to make a link between the volume accessible to the alkali atom and the distortion amplitude. A complete description of the distortion phenomenon in column I elements will be given in a forthcoming paper.

Acknowledgements

We gratefully acknowledge Dr. A. San Miguel (University Claude Bernard, Lyon, France) for invaluable discussions. This work was supported by FNRS Grant No. 9.4565.96F.

References

[1] A. San-Miguel, P. Kéghélian, X. Blase, P. Mélinon, A. Perez, J. -P. Itié, A. Polian, E. Reny, C. Cros and M. Pouchard, *Phys. Rev. Lett.*, **83**, 5290 (1999).
[2] M. Schluter, M. Lannoo, M. Needels, G. A. Baroff and D. Tomanek, *Phys. Rev. Lett.*, **68**, 526 (1992).
[3] M. Lannoo, G. A. Baroff and M. Schluter, *Phys. Rev. B*, **44**, 12106 (1992).
[4] G. B. Adams, O. F. Sankey, J. B. Page and M. O'Keefe, *J. Chem. Phys.*, **176**, 61 (1993).
[5] G. S. Nolas, J. L. Cohen, G. A. Slack and S. B. Schujman, *Appl. Phys. Lett.*, **73**, 178 (1998).
[6] J. L. Cohen, G. S. Nolas, V. Fessatidis, T. H. Metcalf and G. A. Nolas, *Phys. Rev. Lett.*, **82**, 779 (1999).
[7] B. C. Sales, B. C. Chakoumakos, D. Mandrus and J. W. Sharp, *J. Solid State Chem.*, **146**, 528 (1999).
[8] W. -C. Pilgrim, M. Ross and L. H. Yang, *Physica B*, 241–243, **935** (1998).
[9] F. Brunet, P. Mélinon, A. San Miguel, A. Perez, A. M. Flanck, E. Reny, C. Cros and M. Pouchard, *Phys. Rev. B*, **61**, 16550 (2000).
[10] J. S. Kasper, P. Hagenmuller, M. Pouchard and C. Cros, *Science*, **150**, 1713 (1965).
[11] A. A. Demkov *et al.*, *Phys. Rev. B*, **50**, 17001 (1994).
[12] T. J. Stieltjes, *Ann. Fac. Sci. Toulouse Sci. Math. Sci. Phys.*, **8**, 1 (1894).
[13] R. Haydock, *Solid State Phys.*, **35**, 215 (1980).
[14] A. San Miguel, H. Libotte, J. -P. Gaspard, M. Gauthier, J. -P. Itié and A. Polian, *Eur. Phys. J. B*, **17**, 227 (2000).
[15] J. -P. Gaspard, A. Pellegatti, F. Marinelli and C. Bichara, *Phil. Mag. B*, **77**, 727–744 (1998).
[16] The AbInit code is a common project of the Université Catholique de Louvain, Corning Incorporated, University of Liège and other contributors (URL: http://www.abinit.org).
[17] N. Troulliers and J. L. Martins, *Phys. Rev. B*, **43**, 1993 (1991).
[18] D. M. Ceperley and B. J. Alder, *Phys. Rev. Lett.*, **45**, 556 (1980).
[19] H. J. Monkhorst and J. D. Pack, *Phys. Rev. B*, **13**, 5188 (1976).

6.4 Conclusion

We show that a pairing - either static or dynamic - of the alkali atoms in clathrate structures is energetically possible. Our systematic study shows that the distortion amplitude is highly correlated with the expansion factor of the alkali structure. As soon as the expansion factor is higher than a critical value, the distortion appears and is proportional to the square root of this expansion factor.

Type-II alkali-doped clathrates are an interesting case of Peierls distorted materials. By varying the nature of the guest and host atoms, it is possible to tune the distortion amplitude of the structure. As the link between structural and thermoelectric properties of such compounds is very tight, the systematic study may allow to determine the best material for a given application.

This distortion is destroyed when pressure is applied. As far as I know this study is the first theoretical approach of the evolution of the distortion in doped clathrates under pressure. An experimental confirmation of this mechanism would be required.

Chapter 7

Symmetry and stability

7.1 Introduction

Understanding the structure of condensed matter is the most fundamental issue in condensed matter. It is a complex problem although the cohesion relies only on two well established physical theories: **electromagnetism** and **quantum physics**. The nature of the chemical bond and its calculation is far from being obvious as many electrons and nuclei are in interaction. The Schrödinger equation cannot be solved analytically, not even numerically without severe approximations about the electron-electron interaction [143, 144, 145, 146]. Hence the theory of the chemical bond [44] is still a subject of discussion and controversy.

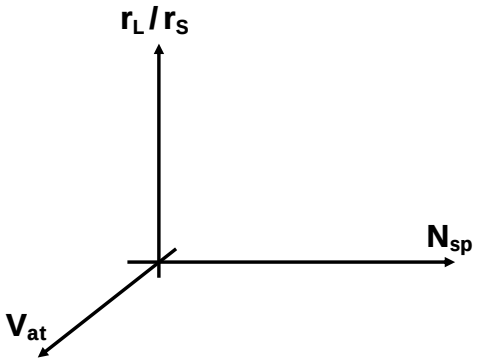

Figure 7.1: This bare figure illustrates the three axes of our work : the distortion amplitude is studied as a function of the number of valence s and p electrons, N_{sp}, and the accessible atomic volume, V_{at}. The atomic volume is modified either by an external pressure or by a structural constraint.

Numerous and strong approximations are made to render the equations tractable. Firstly, the electron-electron interactions are taken as an average: an electron is assumed to behave in the average potential of the nuclei and the other electrons. The dynamical correlations between the electrons are then neglected. As a consequence, the electrons are independent: the wavefunction of the N electrons is the product of N wavefunctions of single electrons. Fortunately, the independent electron model is a satisfactory approximation in most cases, the electron-electron correlation being of importance in a limited number of cases, such as the Mott insulators.

In condensed matter, the valence electrons are neither totally free nor strongly bound to

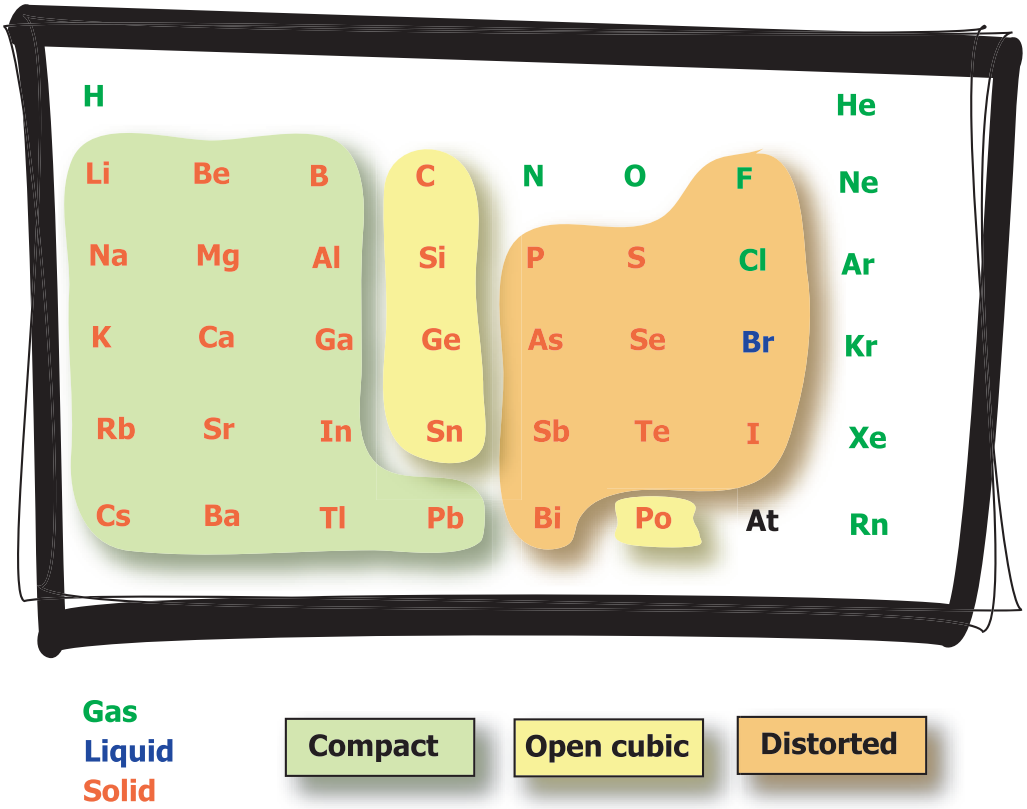

Figure 7.2: Simplified periodic table describing the main structural characteristics of the elements under ambient conditions. The colored area illustrates if the structure is compact (green), open and cubic (yellow) or distorted (orange). The physical state at room temperature is given by the color of the characters. Green: gas, blue: liquid and red: solid. H, N and O form diatomic molecules induced by strong electron-electron correlation.

the nuclei : they are extended through the structure with an appreciable delocalisation of the wavefunction. Practically, the wavefunction - as it cannot be computed exactly - has to be expanded in a basis of functions, assumed to be complete[1].

Schematically, the basis set is either a collection of plane waves or a collection of atomic orbitals (LCAO). We then have the nearly free electron approximations and the tight binding schemes respectively. The former is dressed in several approximations under the generic name of "*ab initio*" such as LDA or GGA[2] which are basically numerical methods to deal with the hamiltonian. They benefited from the incredible progress both of the speed of the computers and the size of the memories. This opened the way to quantitatively accurate calculation of the total energy of solids. The relative stability of competing structures can be computed as well as the energy variation of a given structure as a function of external parameters like pressure. The success of the density functional theory was recognized by the Nobel prize awarded to Walter Kohn in 1998.

Besides the success of the *ab initio* numerical experiments, semi-empirical quantum models are of great relevance not only because of their relative simplicity, allowing to handle large systems or relatively long averaging time, but also because they are of great value to understand the underlying physical mechanisms.

Our main concern in this thesis is to find systematic behaviours in the periodic table and to describe their evolution under pressure. The periodic table, considered as a whole, shows a striking feature: on the left hand side[3], the elements are close packed and metallic (except hydrogen) whereas on the right hand side including column IV, but *Pb*, the structures are open, loosely packed with a low coordination number that depends on the number of valence electrons per atom (the celebrated **octet rule**). This is illustrated in figure 7.2 and raises the questions

Are the most coordinated structures the most stable ?
Are the most symmetric structures the most stable ?

One can think that the most symmetric structure are likely to be the most stable but the answer to this general question is not obvious. It depends on the symmetry of the electrons involved in the chemical bond, the number of electrons per atom and critically depends on the relative strength of the repulsive interactions as we will show.

Our work is focused on the understanding of the deep nature of symmetry breaking and recovering throughout the periodic table, in particular under the effects of pressure. Following René Descartes, we simplify the problem to the extreme. What we keep is the quantum mechanical nature of the problem and an order parameter that reflects the symmetry breaking. The distorted structure is described by the two first neighbour distances, r_s and r_l, where s and l stands for *short* and *long*. We choose as an order parameter the ratio between the long, r_l, and short, r_s, bond lengths, $\frac{r_l}{r_s}$ that we call the Peierls ratio, R_P. We consider its evolution as a function of the band filling and the accessible atomic volume, i.e. the pressure (see figure 7.1). The analysis of this evolution allows to draw our unified model of the *sp*-bonded elements.

After a brief description of the structural trends within the *sp*-bonded elements, the fundamental electronic interactions are introduced. In this chapter, a semi-empirical quantum model of the *sp*-bonded elements is described. Using parametrized interaction energies, we study the structural systematics observed through the periodic table and their evolution under pressure.

[1] The completeness is usually approximate and not in the strict mathematical sense e. g. in the basic treatment of the hydrogen molecule H_2, the basis is made of two 1s orbitals!

[2] Local Density Approximation (LDA) and Generalized Gradient Approximation (GGA)

[3] Including transition metals.

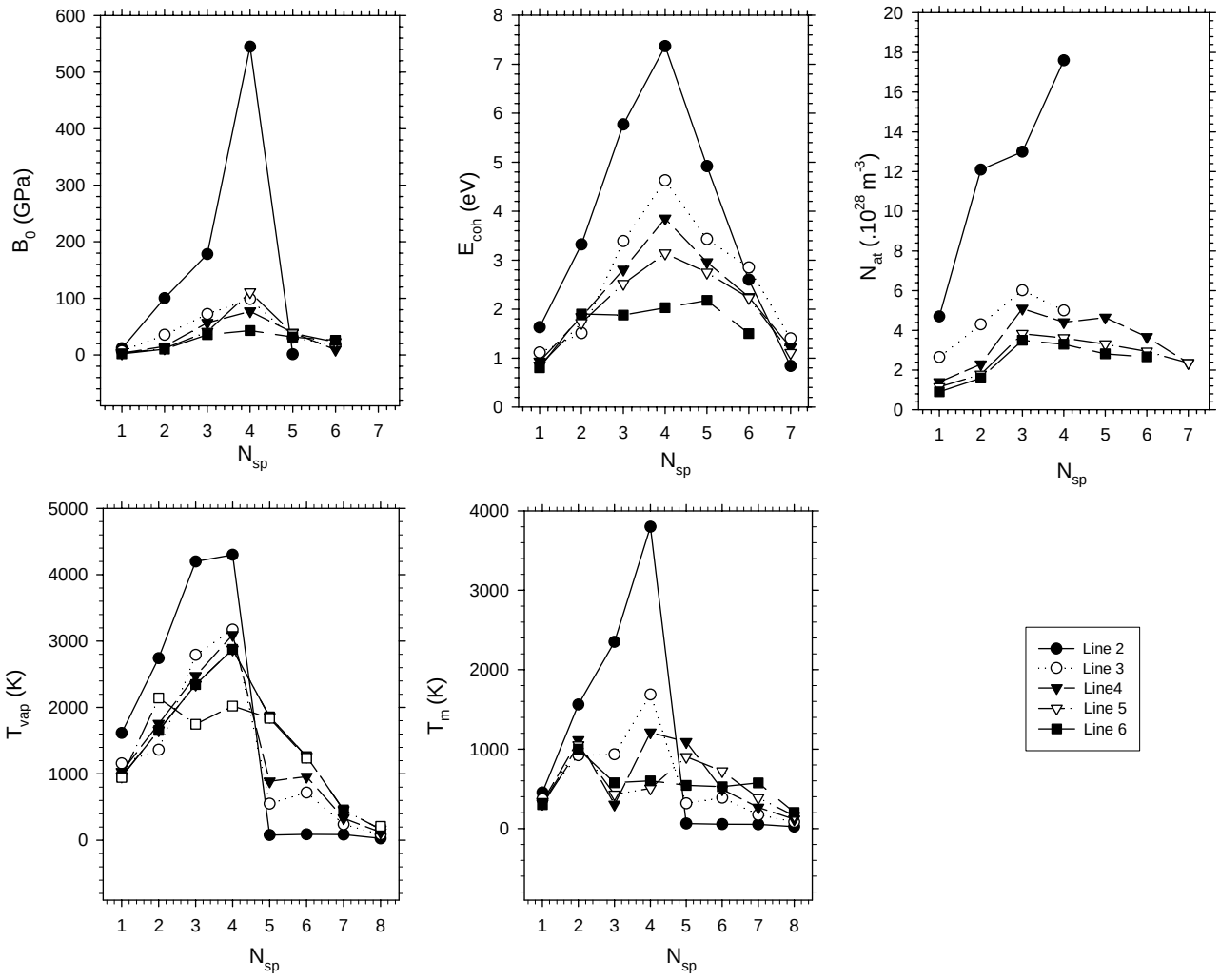

Figure 7.3: Evolution of the properties of the *sp*-bonded elements as a function of the number of *sp* electrons, N_{sp} :the zero pressure bulk modulus, B_0, the cohesive energy, E_{coh}, the atomic concentration, N_{at}, vaporization, T_{vap}, and melting, T_m, temperatures taken from reference [147] for each line of the periodic table. The maximum values of both B_0, E_{coh}, T_m and T_{vap} are located at $N_{sp} \approx 4$. . The atomic density reaches its maximum at $N_{sp} = 3$ except for the second line of the periodic table for which it is reached at $N_{sp} = 4$.

7.2 Structural trend

We start this chapter by having a look on the periodic table (see figure 7.2) from the structural point of view. The related structural data are summarized in table 7.1. Under ambient pressure, the *sp*-bonded elements [148] exhibit a systematic evolution of their cohesive energies, atomic densities, bulk moduli, melting and vaporization temperatures as a function of the *sp* valence electron number as shown in figure 7.3. We also present some of the structures that we consider in this thesis and their relatives.

From the left to the right of the periodic table, the structural behaviour of elements is progressively evolving from an "atomic" behaviour (e. g. alkali metals) with isotropic environment, to a molecular character (e. g. halogens) with a directional bonding. We show that the right hand side of the periodic table (covalent elements) can be understood as a distortion of a reference simple cubic structure.

Elements of groups 1, 2 and 13 have compact structures (FCC, HCP, BCC) with a high symmetry but in very special circumstances they may also be Peierls distorted when their accessible atomic volume is artificially increased, e.g. in clathrate cages as described in chapter 6. In addition, alkali metals are known to undergo surprising symmetry breaking and restoring at high pressures [149, 150]. Some of these structures are similar to the structures of halogens under pressure.

Elements of group 14 and their isoelectronic compounds, $A^N B^{8-N}$ with $N=$ 5 or 6 have four nearest neighbors and crystallize in the diamond ($Fd\bar{3}m$), zinc-blende ($F\bar{4}3m$) or würtzite ($P6_3mc$) structures . Lead is an exception to this rule with its face-centered cubic structure (FCC). At higher temperatures (Sn) or under pressure (Si, Ge), they increase their coordination number to 6. As illustrated in figure 7.4, it is possible to continuously move from the diamond or zinc-blende structures to the monoatomic ($I4_1/amd$) or the diatomic β-tin ($I\bar{4}2m$) [151] structure. Their respective orthorhombic distortions, i.e. the monoatomic ($Imma$) or its diatomic equivalent ($Immm$), results from a displacement along the z axis of the atoms located in the x-z and y-z planes.

A similar distortion process occurs between the $NaCl$ and $Cmcm$ structures. In this case, two zig-zag chains are generated by plane sliding as illustrated in figure 7.5. $CsCl$ may also undergo structural distortion. Two candidate structures were suggested by *ab initio* identification of soft phonon modes : $AuCd$ and $InBi$. The mechanism of such a distortion is illustrated in figure 7.6.

An extensive study of the displacive mechanisms occurring in the high pressure diagrams of these semiconductors has been conducted by Katske and co-workers [152]. It underlines the possibility of continuous transition from one structure to the other.

As shown in chapter 3, such distortions are not related to an electronic instability : symmetry breaking is induced either by parasitic effects in the experimental surroundings or by a mechanical instability similar to the Euler buckling.

Elements of groups 15, 16, 17 and even 18 exhibit a structure which can be considered as distortion of the simple cubic structure as illustrated in figure 7.7. It is an alternation of shortening and elongation of the bonds along each direction x, y z giving rise to a succession $(SL\ldots)^n$ of short, S, and long, L, bonds. The relative evolution of the Peierls ratio and the transition pressure is illustrated in figure 7.8.

In arsenic and black phosphorus, the resulting structure, $(SL)^n$, is a stacking of corrugated planes where each atom is covalently bonded to three neighbors. Selenium and tellurium

show helical chains resulting from a $(SLL)^n$ structure.

Finally, the halogens (fluorine, chlorine, bromine and iodine) are made of parallel planes of diatomic molecules loosing the x, y and z symmetry. This structure originates from a $(SLLL)^n$ distortion scheme in the plane. The experimental evolution of this structure under pressure is documented in chapter 4.

The expected effect of an external pressure on a distorted structure is to reduce the distortion amplitude up to total disappearance at some transition pressure, P_T. The longer interatomic distance is more sensitive to pressure effects than the shorter one. The disappearance of the distortion at P_T is often accompanied by a semiconductor-to-metal transition. Nearly all elements show this behaviour (e. g. arsenic, selenium, ...). The phase transition under pressure is accompanied by an increase of the coordination number. The effect on symmetry is not obvious: the symmetry can be either increased - in most cases - or decreased as illustrated by the $NaCl$-to-$Cmcm$ transition described in section 3.5. The case studies described in the previous chapters testify the richness and complexity of the field of symmetry breaking phenomena.

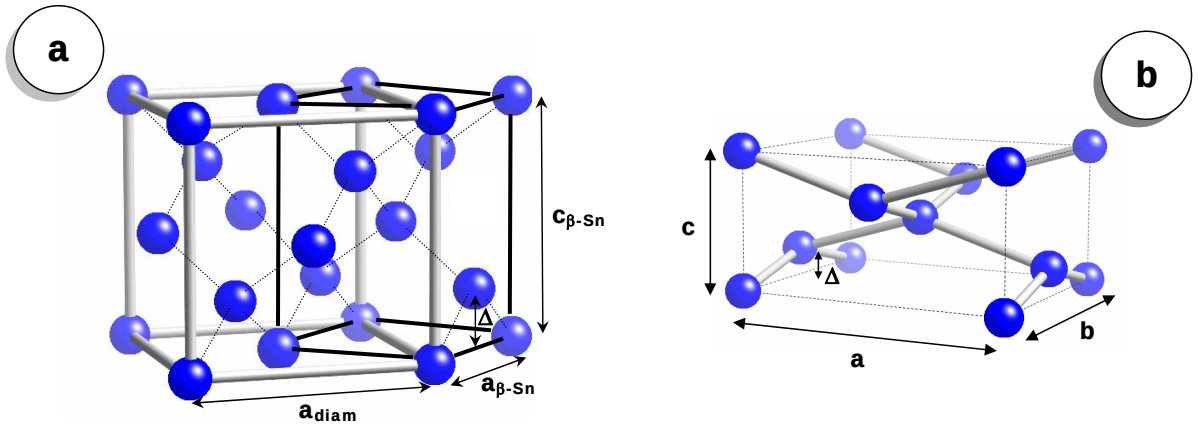

Figure 7.4: Illustration of the geometrical distortion from the diamond (a) to the $\beta - Sn/Imma$ (b) structures. This mechanism allows to study those couple of structures within a common set of structural parameters. The β-Sn unit cell is directly obtained from the diamond structure by a compression along the z axis. If Δ becomes different from $\frac{1}{2}$ and if an orthorhombic distortion occurs, the β-Sn structure becomes the $Imma$ structure.

7.3 Mechanisms of the Jahn-Teller and Peierls distortions

Due to their bonding through the p-electrons, elements of groups 15, 16 and 17 should exhibit a sixfold coordinated structure. However, this structure is unstable due to an electronic instability, the Peierls distortion, leading to the famous octet rule. The distortion processes are discussed in this section depending on the repulsive hardness and the band filling.

7.3.1 Localized systems

Symmetry breaking is known for a long time in structural chemistry and in physics. The famous **Jahn-Teller distortion** in molecules was described as early as in 1937[153]. It is a spontaneous **symmetry breaking** mechanism driven by quantum effects. It occurs when a degenerate

Group	Element	Space group	Interatomic distances (Å) and coordination number	$\frac{r_L}{r_S}$
1	Li	CC ($Im\bar{3}m$)	3.51 Å	
	Na	CC ($Im\bar{3}m$)	4.29 Å	
	K	CC ($Im\bar{3}m$)	5.33 Å	
	Rb	CC ($Im\bar{3}m$)	5.58 Å	
	Cs	CC ($Im\bar{3}m$)	6.14 Å	
2	Be	hcp ($P6_3mmc$)	a=b=2.29 Å; c=3.58 Å $\alpha = \beta = 90^o$; $\gamma = 120^o$	
	Mg	hcp ($P6_3mmc$)	a=b=3.21 Å; c=5.21 Å $\alpha = \beta = 90^o$; $\gamma = 120^o$	
	Ca	CFC ($Fm\bar{3}m$)	5.59 Å	
	Sr	CFC ($Fm\bar{3}m$)	6.08 Å	
	Ba	CC ($Im\bar{3}m$)	5.03 Å	
13	B	Rhomb. ($R\bar{3}mr$) S.G. 166	a=b=c=5.06 Å $\alpha = \beta = \gamma = 58.1$	
	Al	CFC ($Fm\bar{3}m$)	4.08 Å	
	Ga	Orthorh. (Cmca)	a=4.52Å, b=7.66Å, c=4.53Å	
	In	Tetrag. (I4/mmm)	a=b=3.25Å, c=4.95Å	
	Tl	hcp ($P6_3mmc$)	a=b=3.46Å, c=5.52Å $\alpha = \beta = 90^o$; $\gamma = 120^o$	
14	C	hcp ($P6_3mmc$)	a=b=2.46Å, c=6.71Å $\alpha = \beta = 90^o$; $\gamma = 120^o$	
	Si	CFC ($Fm\bar{3}m$)	5.43 Å	
	Ge	CFC ($Fm\bar{3}m$)	5.66 Å	
	Sn	Tetrag. ($I4_1/amd$)	a=b=5.83Å, c=3.18Å	
	Pb	($Fm\bar{3}m$)	4.95Å	
15	N	hcp ($P6_3mmc$)	a=b=3.86Å, c=6.27Å $\alpha = \beta = 90^o$; $\gamma = 120^o$	
	P (black)	(S.G. 2)	2.22 (2), 2.24(1), 3.68 (2)	1.68
	As	$R\bar{3}m$	2.51 (3), 3.25 (3)	1.25
	Sb	$R\bar{3}mh$	2.87 (3), 3.37 (3)	1.17
	Bi	C2/m	3.10 (3), 3.47 (3)	1.12
16	O	$C1_2m1$ (S.G. 12)		
	S	(S.G. 70)	2.04 (2)	1.8
	Se (α)		2.32 (2), 3.47 (4)	1.5
	Se (Rhomb)	S.G. 14	2.37 (2), 3.44 (4)	1.45
	Te	$P3_12_1$	2.84 (2), 3.49 (4)	1.31
	Po	$Pm\bar{3}m$	3.34 (6)	1
17	Cl	Cmca (S.G. 64)	2.02 (1), 3.34 (2)	1.65
	Br	Cmca (S.G. 64)	2.27 (1), 3.30 (2)	1.45
	I	Cmca (S.G. 64)	2.68 (1), 3.55 (2)	1.32

Table 7.1: Structures of the elements of groups 1, 2 and 13 to 17 observed at ambient conditions.

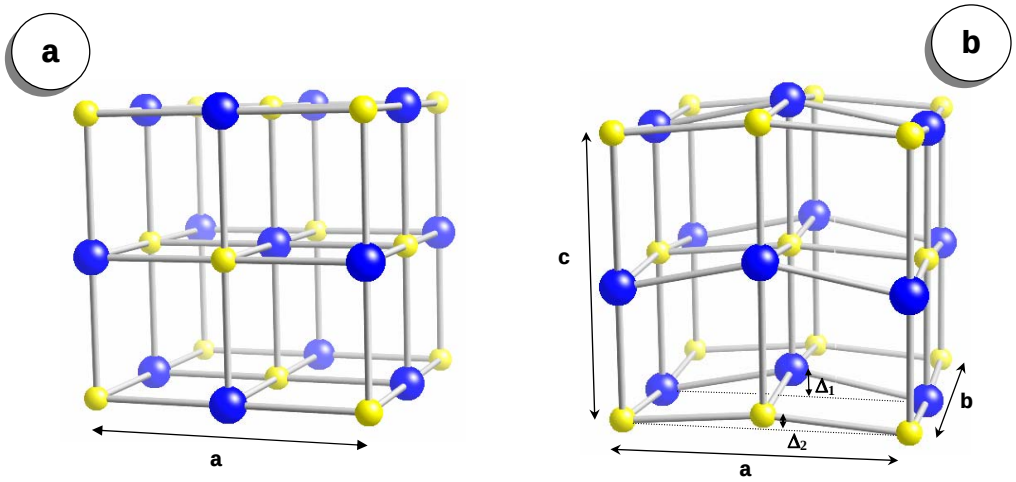

Figure 7.5: Illustration of the geometrical distortion from the $NaCl$ (a) to the $Cmcm$ (b) structures. This mechanism allows to study those couple of structures within a common set of structural parameters. $Cmcm$ is a slightly distorted $NaCl$ unit cell : the x-y planes are sliding on each other to create a zig-zag chain along the z direction. A second zig-zag chain also appears along the x direction.

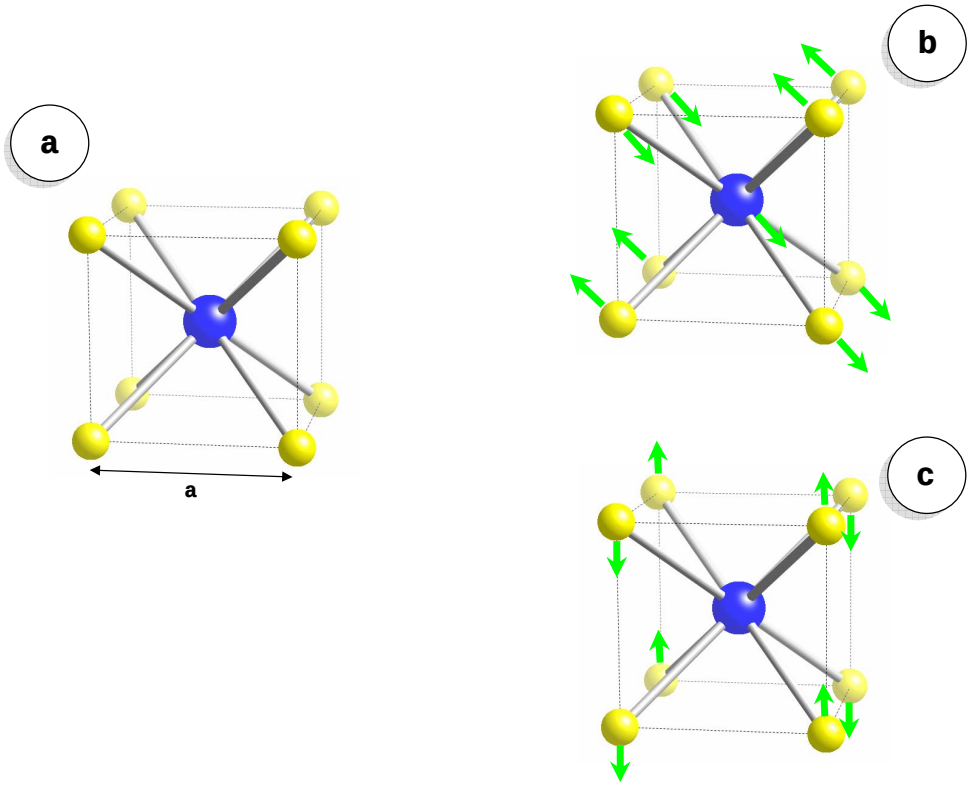

Figure 7.6: Illustration of the geometrical distortion from the $CsCl$ (a) to the $AuCd$ (b) and $InBi$ (c) structures. This mechanism allows to study both structures within a common set of structural parameters. The plane translations are illustrated by the green arrows which are oriented along the $(1\bar{1}0)$ and (001), respectively.

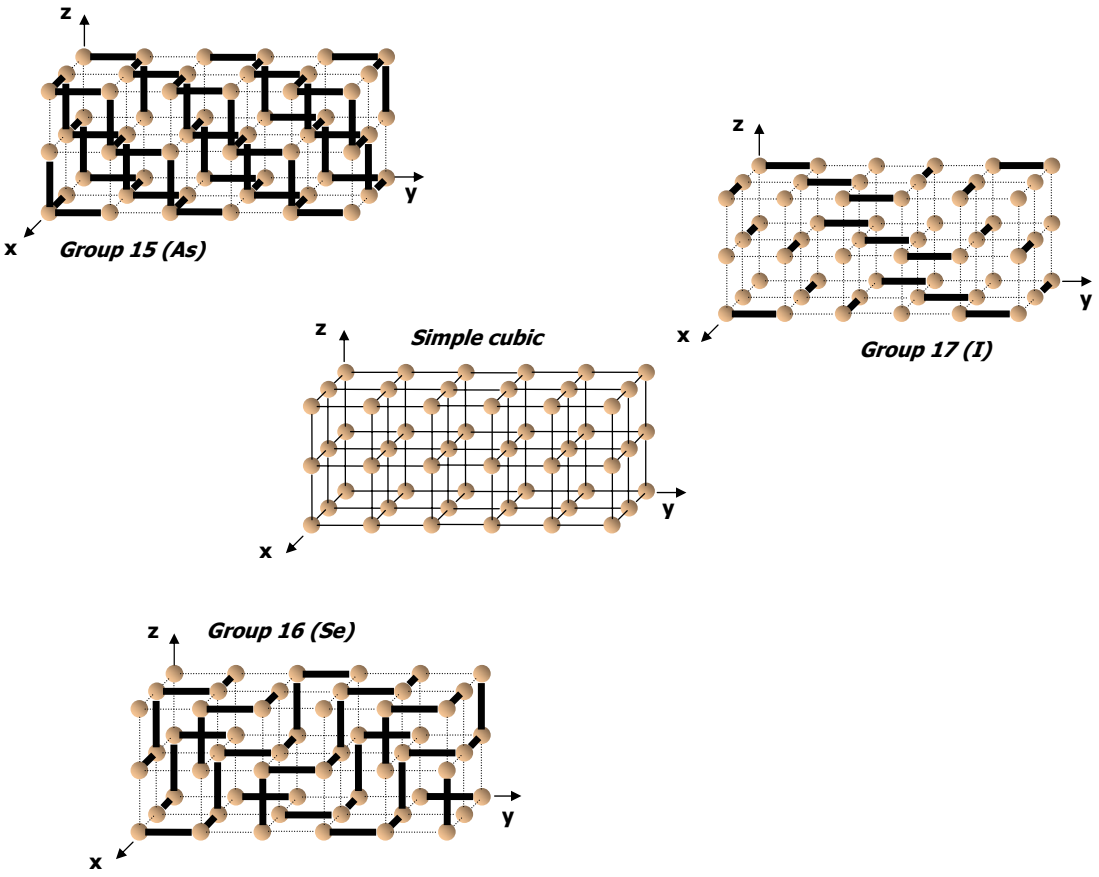

Figure 7.7: Illustration of the distortion mechanisms of the simple cubic structure. The thick and thin lines mimic the short and long bonds, respectively. The resulting angular distortions are not shown in the figures. Three geometrical arrangements are corrugated planes for group 15-elements, helical chains for group 16-elements, diatomic molecules lying in parallel planes for group-17 elements.

energy level is partially filled. This distortion lifts the degeneracy of these levels (see figure **??**). The degenerate levels split into two (or more) sublevels, preserving the center of gravity. The lowering of the occupied level gives rise to a gain of energy, the upward move of the unoccupied level has no consequence on the total electronic energy. This phenomenon is only based on local considerations and applies to localized systems such as molecules (cyclobutadiene, ...), vacancies and dopant atoms in semiconductors. The Jahn-Teller effect is a local distortion driven by an electronic instability, in finite systems.

7.3.2 Extended systems

The Jahn-Teller effect extended to infinite systems is called the **Peierls distortion**. Instead of levels we have a band of states and, for adapted static distortion of the lattice a gap appears at the Fermi level. It is the driving force for the octet rule that occurs in the right hand side of the periodic table. In addition, the insulating character of polymers such as polyacetylene is due to a Peierls distortion. The energetic gain due to this gap opening is possible as the electronic density of states is reduced at the Fermi level. This original mechanism imagined by Sir Rudolf Peierls is illustrated in figure 7.10 for a linear chain with a half band filling. When the linear

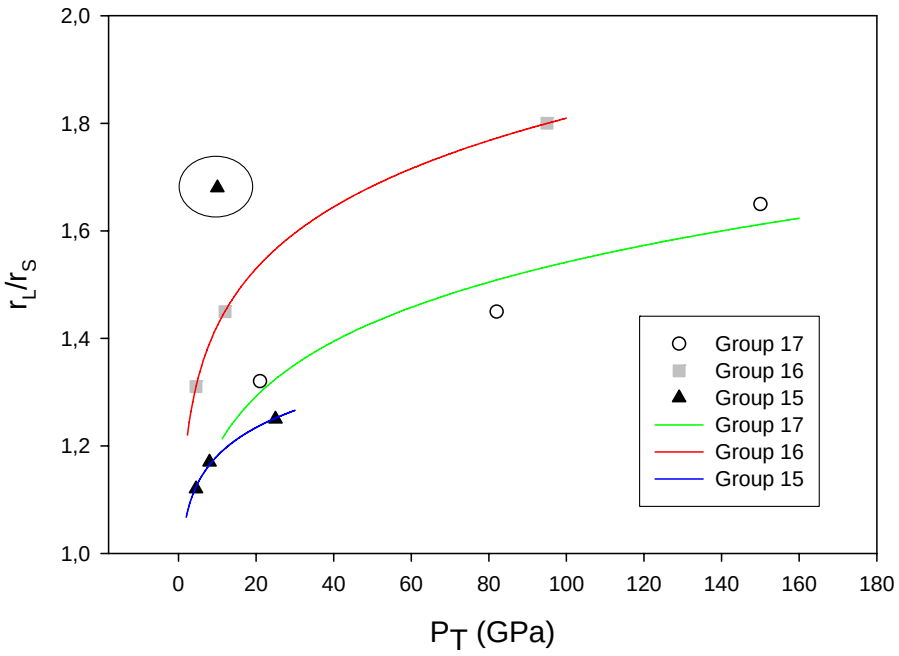

Figure 7.8: Peierls ratio, R_P, as a function of the transition pressure for the elements of groups 15, 16 and 17. There is some degree of correlation between these two parameters - except for phosphorus which is the isolated triangle. Phosphorus (illustrated by the surrounded black triangle) has a specific molecular structure at room temperature.

chain is distorted, the highest bonding levels are lowered with respect to the undistorted linear chain because the dispersion relations have to be orthogonal to the border of the Brillouin zone.

This phenomenon is general and should occur for any system with partially-filled bands. However conducting metals exist! In close packed structures encountered in metallic crystals, there is no way to produce a displacive distortion that produces a gap opening. Close packed structures are too much entangled[4]. By contrast, in open structures, such as the simple cubic structure, a large variety of distortions may occur. Indeed, the linear chain may have distortions of any periodicity and the simple cubic structure alike as it is the direct product of three chains that behave independently if we neglect the valence angle modifications. For a band filling ratio $\rho = \frac{m}{n}$, m, n being prime integers) a gap opens at the Fermi energy, when the unit cell is m-merized in the three orthogonal directions [139].

This electronic instability of the simple cubic structure is the physical origin of the octet rule for the p-bonded elements.

Finite system (*Jahn-Teller*)	**Extended system** (*Peierls*)
Degenerate level	Band
Partially filled	E_F inside the band
Lifting of	Opening of
the degeneracy	a gap

Table 7.2: Finite and extended distorted systems.

[4]The BCC structure, that occur for a half filled d-band could be considered as a relative of a Peierls distortion as its density of states has a dip at the Fermi energy, unlike the FCC or HCP structures[154]

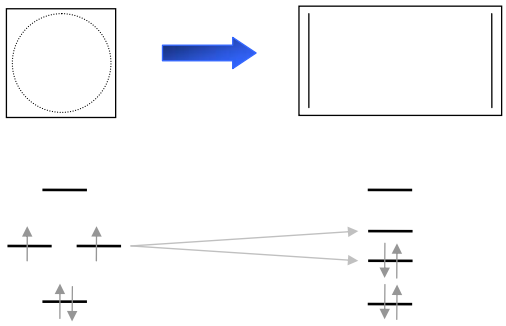

Figure 7.9: Jahn-Teller effect in cyclobutadiene C_4H_4 (H are not represented). The symmetry lowering from the square to the rectangle lifts the twofold degeneracy of the electronic levels at $E = 0$. The resulting structure is more stable as the occupied level are more bonding.

Remarks

1. The octet rule is also satisfied for compounds (e. g. As_2Te_3) where the periodicity of the Peierls distortion depends on the average band filling [155].

2. Whether the octet rule is satisfied individually or collectively in the alloys or compounds depends on the line number in first instance. For light elements (e. g. SiO_2), the individual behaviour prevails whereas for the heavier elements (e. g. $GeTe$) the important parameter is the average number of electrons [156].

3. Despite the fact that the demonstration of R. Peierls is based on the periodicity, non periodic structures (liquid, amorphous) do show Peierls-like behaviour. In particular, the octet rule is satisfied the same way provided the entropic term does not dominate.

7.4 High or low coordination? The one-distance model

7.4.1 Tight binding method

There are many different methods to model the properties of matter. They differ from each other by the transferability and the number of particles that can be included in the model:

Empirical potentials allows to study large systems (10^6 particles) but their transferability is very limited.

Tight-binding or semi-empirical approaches allow to describe reasonable system size (up to 10^5 particles). However the transferability highly depends on the parametrization method. These parameters have to be determined by fitting either experimental data or results of *ab initio* calculations.

Ab initio calculations insure a good transferability but they are limited to small systems (less than 10^3 particles).

In this thesis, a tight binding model is preferred in order to give a physical description of matter keeping the accessibility of the fundamental parameters of the interactions (hardness of the repulsive potential, number of valence electrons, ...).

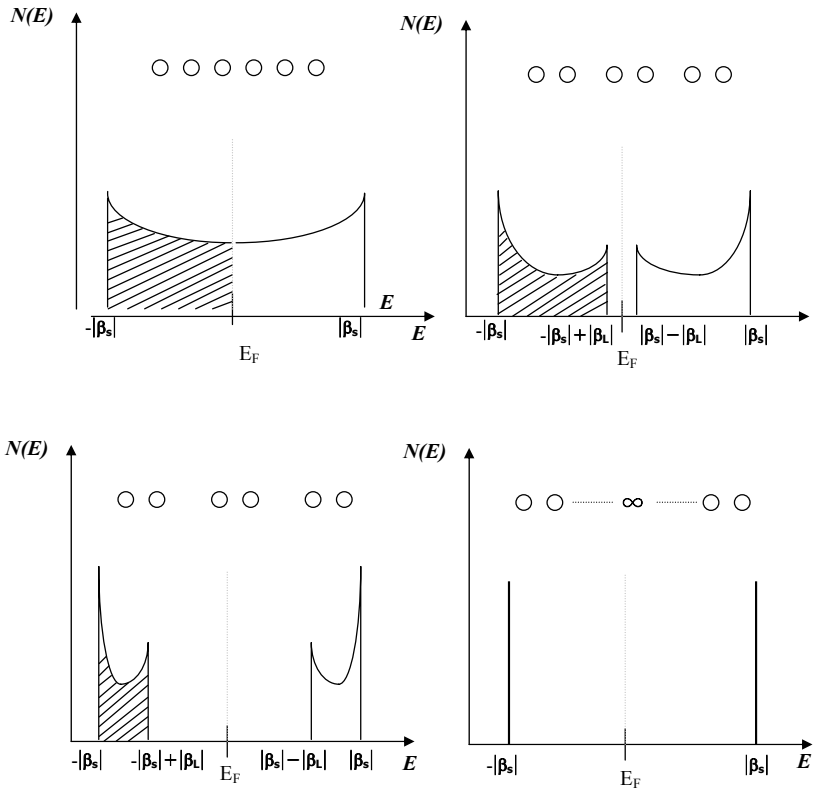

Figure 7.10: Schematic evolution of the electronic density of states of a distorted linear chain of atoms. The density of states is reduced at the Fermi level and thus a gap opening allows to increase the cohesive energy of the system as the gravity center of the filled band is left shifted.

Interactions	Resonance $\beta(r)$	Repulsion $V(r)$	Parameters	Relation
Inverse power	$\frac{\beta_0}{r^q}$	$\frac{V_0}{r^p}$	$p = -\frac{d\ln V}{d\ln r}$	
			$q = -\frac{d\ln \beta}{d\ln r}$	
Exponential	$\beta_0 e^{-qr}$	$V_0 e^{-pr}$	$p = -\frac{d\ln \beta}{dr}$	$\frac{p}{q} = \frac{d\ln V}{d\ln \beta}$
			$q = -\frac{d\ln V}{dr}$	
Generalization	$f(r)$	$f^{\frac{p}{q}}(r)$		

Table 7.3: Particular and generalized models of resonance integrals and repulsive potentials.

Using this simple model, another light can be shed on the symmetry breaking mechanism. The answer to our initial question about *stability* requires the description of the basic interactions

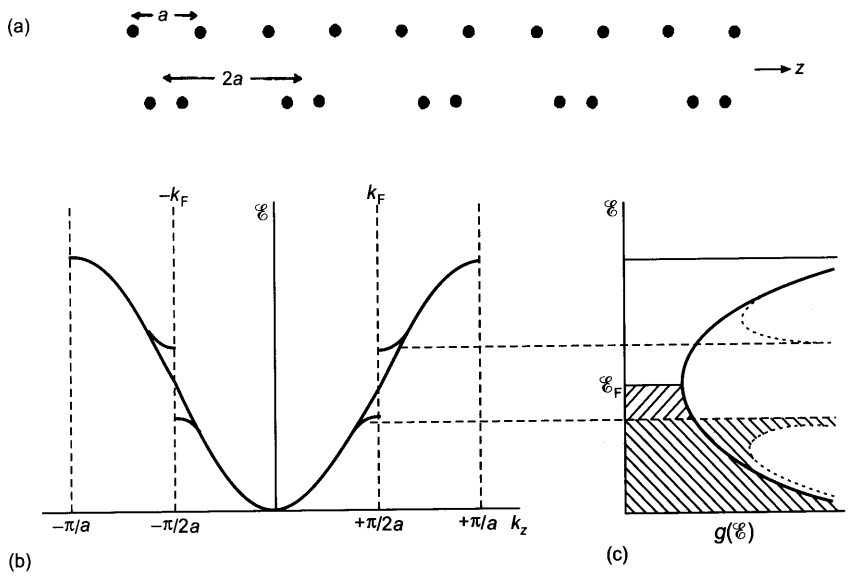

Figure 7.11: Figure adapted from reference [157]. Schematic evolution of the electronic density of states of a distorted linear chain of atoms. The density of states is reduced at the Fermi level and thus a gap opening allows to increase the cohesive energy of the system as the gravity center of the filled band is left shifted.

that we consider through this thesis : the attractive and repulsive interactions. The latter is often neglected in the literature [158, 159, 160] but we underline its major role in the structural behaviour of the elements.

The one-distance model introduced in this section is based on the assumption that the long interactomic distance results in a resonance integral which can be neglected. In other words, only the short distances are considered in the calculation of the energy and the long one is assumed to be infinite. Even if the one-distance modeling can be considered as crude, it gives valuable insight of the qualitative symmetry trends through the periodic table.

Let us assume that the total energy, E_{tot}, can be written as the sum of an attractive quantum resonance energy, E_a proportional to the resonance integral $\frac{\beta_0}{r^q}$, and a repulsive contribution, E_r, described using a pairwise additive potential.

On one side, we can simply write the repulsive energy as

$$E_r = Z\frac{V_0}{r^p} \tag{7.1}$$

The repulsive potential originates from the Coulomb repulsion, and, more importantly, from the Pauli principle. We are not aware of any theoretical description of the repulsive potential [158, 160, 159] and, in the rare papers where it is considered [148], it is represented by an effective potential, in the form of an exponential or inverse power of the interatomic distance, r. The parameter p of the repulsive potential is known to increase with the number of closed shells. When there is no Peierls distortion, the ratio $\frac{p}{q}$ is given by the relationship (7.54). As it appears that only the number of closed shells matters, this relative evolution can be extended to the right hand side of the periodic table. The evolution of the p parameter is given in figure 7.12 for the elements of the first column of the periodic table. This is calculated using relation (7.54). This behaviour is quite general and is also relevant to the liquid state as exemplified in

JY Raty's thesis [161].

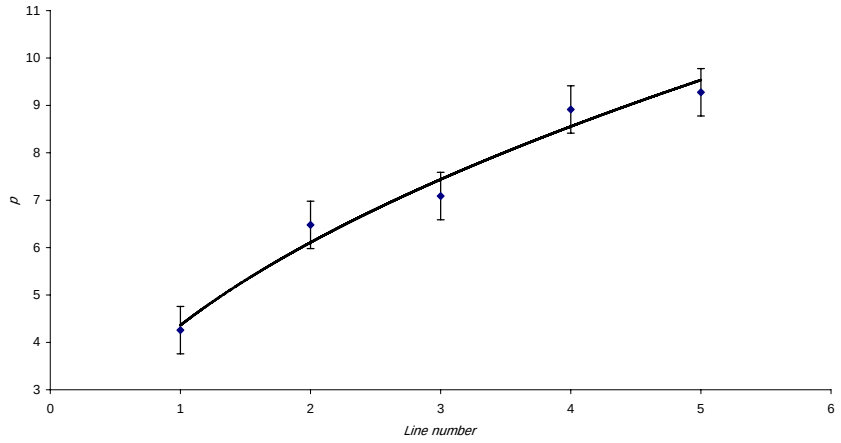

Figure 7.12: Evolution of the parameter of the repulsion p within the first column of the periodic table. It illustrates that the repulsion becomes harder when the number of inner closed shells increases. The error bars illustrates the uncertainty on the p value induced by the experimental uncertainties on the bulk modulus. The line is a guide for the eye.

On the other side, the attractive energy of a system characterized by an electronic density of states, $n(E)$, is given by the following general expression.

$$E_a = \int_{-\infty}^{E_F} En(E)dE \tag{7.2}$$

where E_F is the Fermi level. The total number of sp electrons, N_{sp} is simply given by

$$N_{sp} = \int_{-\infty}^{E_F} n(E)dE \tag{7.3}$$

As an integral quantity, the total energy is efficiently computed using the gaussian integration method. Using a limited number of moments of the electronic density of states (DOS) is thus very efficient to calculate the total energy of a given structure. The calculation of E_a usually relies on an explicit expression of the covalent interaction as a function of the interatomic distance, r. The most common functions are the exponential $\beta_0 e^{-qr}$ or the inverse power, $\beta_0 r^{-q}$, ...(see table 7.3). Usually, an explicit expression of the attractive and repulsive potential is used (see table 7.3). In a second moment approximation, the attractive and repulsive energies are simply given by

$$E_a = -\frac{\sqrt{Z}\beta_0}{r^q} \tag{7.4}$$

where Z is the number of neighbours. The resulting potentials are illustrated in figure 7.13.

Here we generalize the attractive potential (or resonance integral) with the general expression

$$E_a = Af(r) \tag{7.5}$$

where $f(r)$ is a monotonic decreasing function of the interatomic distance, r. By comparison with the standard expressions, we also assume

$$\frac{p}{q} = \frac{d\ln V_r(r)}{d\ln \beta(r)} \tag{7.6}$$

where V_r is the repulsive potential. This expression is valid not only for the standard inverse power and exponential expressions of the covalent interaction but also for different potentials such as gaussian or more complex potentials. Finally, we simply have

$$E_r(r) = K f^{\frac{p}{q}}(r) \tag{7.7}$$

where K is a constant. The ratio $\frac{p}{q}$ remains the relative hardness of the repulsive and attractive potentials[5] which is the fundamental parameter of the one-distance model.

7.4.2 Isotropic interactions : s-electron bonding

In the case of s electrons, the resonance interaction is isotropic. Assuming that each atom has Z neighbours, the total energy writes

$$E_{tot} = -\sqrt{Z} f(r) + Z K f^{\frac{p}{q}}(r) \tag{7.8}$$

The square root dependence on the coordination number, Z, in (7.8) originates from the usual second moment approximation of the covalent bonding[111] [6]. Indeed, the covalent bonding comes from the band broadening of a partially filled band. The bandwidth depends on the number of resonance channels between bonding orbitals. The band broadening is not the sum of the contributions of the nearest neighbors, instead, using the variance addition theorem, we deduce that the bandwidth is proportional to the square root of the coordination number.

The differentiation of the total energy with respect to the interatomic separation, r, gives the equilibrium interatomic spacing, r_{eq}. As a functional expression is used for the covalent potential $f(r)$, we only obtain a relation between the potential and the model parameters, p and q.

$$f^{\frac{p}{q}-1}(r_{eq}) = \frac{q}{p} \frac{1}{K\sqrt{Z}} \tag{7.9}$$

As $f(r)$ is a monotonic decreasing function, we observe that the equilibrium interatomic separation r_{eq} increases with the coordination number Z as it should be in covalent bonding[7]. On the contrary, if both the attractive and the repulsive energies are pairwise additive, like the Lennard-Jones potential, the equilibrium interatomic separation r_{eq} is independent of Z[8].

At the equilibrium distance r_{eq}, the total energy[9] is then

$$E_{tot} \propto Z^{\frac{p-2q}{2(p-q)}} \tag{7.10}$$

- When $p < 2q$, i. e. in the case of a soft repulsion, the structure with the lowest coordination number are the most stable; molecular structures are expected with Z=1.
- At the opposite if $p > 2q$ i. e. in the case of a hard repulsion, the highest the coordination, the more stable the structure. The coordination number Z is limited by the steric hindrance. Compact structures are expected with $Z = 12$ or $Z = 8 + 6$.

A remarkable illustration of the relation (7.10) is column 1 where H, with no inner closed shell, makes diatomic molecules both in the liquid and solid phases[10] while Li, Na,... make

[5] The value of the p parameter is the image of the hardness of the repulsive potential. Roughly, we have p=4 for soft potentials and p=7 for medium ones. Lennard-Jones interactions is characterized by p=12 and finaly, p=∞ corresponds to hard-sphere repulsion.

[6] When a higher-order moment approximation is preferred, the dependence becomes $\sqrt[\alpha]{Z}$

[7] $p>q$ is required for stability reasons, otherwise matter collapses.

[8] At least if only first neighbour interactions are involved

[9] As mentionned above, if a higher-order moment approximation is chosen, the previous expression is generalized by $E_{tot} \propto Z^{\frac{p-\alpha q}{\alpha(p-q)}}$.

[10] Except at extremely high pressures

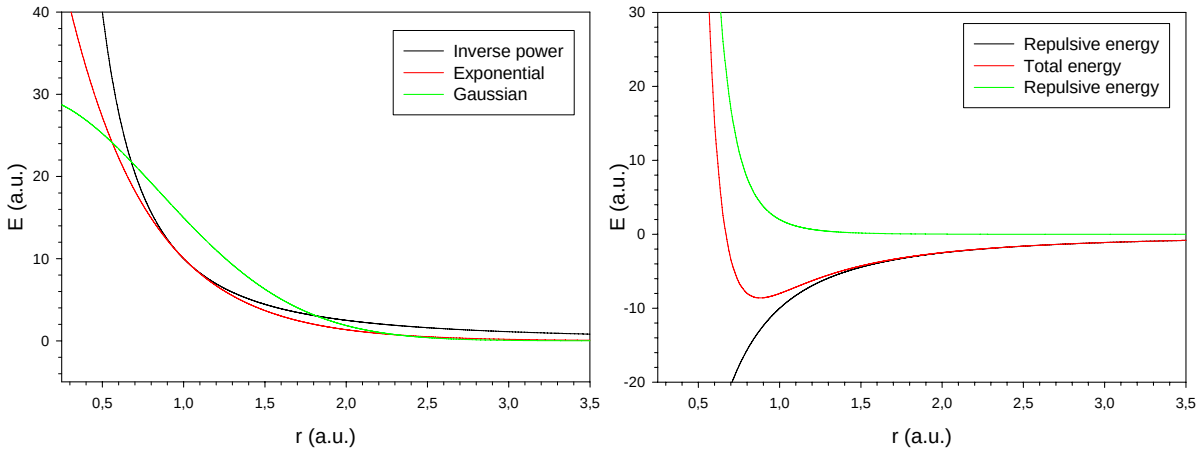

Figure 7.13: Schematic view of the attractive contribution to the total energy for different analytical expressions of $f(r)$. repulsive and total energy for the inverse potential.

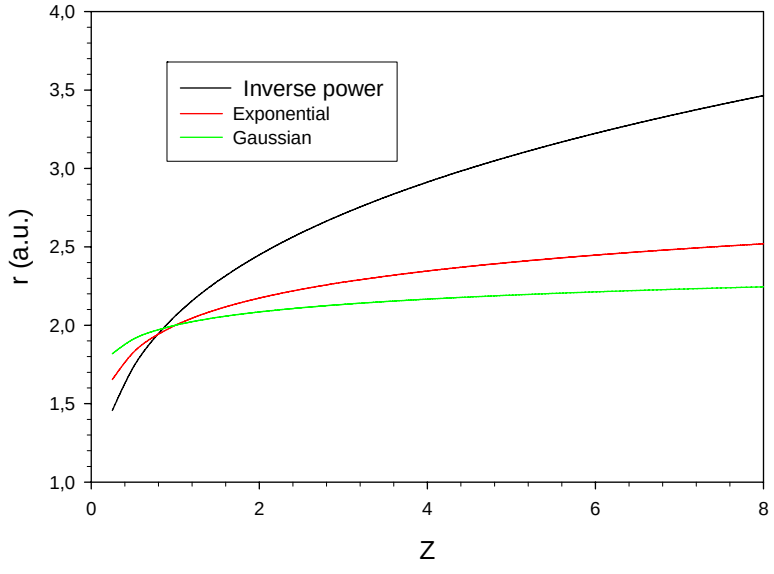

Figure 7.14: Schematic evolution of interatomic distance as a function of the coordination number for three potential types.

compact phases (BCC).

Let us underline that most - if not all - theories of the chemical bond do not include the repulsive term - except the *ab initio* calculations. They use the experimental interatomic separation and consider only the attractive potential to compare the stability of phases. This methodology can lead to qualitatively wrong results.

$$H_2 + H \overset{?}{\leftrightarrows} H_3 \tag{7.11}$$

The equilibrium (7.11) is totally displaced towards the right if the repulsive term is not taken into account whereas it is displaced to the left if the repulsion is included in the calculation.

7.4.3 Directional interactions: p versus sp^3 bonding

As illustrated in the previous section, open structures with low coordination numbers are preferred when the repulsive potential is soft enough ($\frac{p}{q} < 2$). In this section, we discuss the competition between fourfold coordinated and sixfold coordinated structures. The internal and external parameters that influence this competition are analyzed.

The aim of this section is to find guidelines on the structure of covalent systems. The key parameters are the average number of electrons per atom, N_{sp}, the promotion energy, $\varepsilon_p - \varepsilon_s$, and the resonance energy, $f(r)$. The difference in energy levels of the components of a compound (ionicity) and the relative size of the atoms play also a secondary role. The two competing structures we consider are the fourfold coordinated structures (e. g. blende or würtzite) and the octahedral structures (simple cubic, $\beta - Sn$, $NaCl$). This simple semi-empirical study with parameters that can be varied at will is complementary to the *ab initio* calculations [162]. In particular we consider the effect of external parameters such as the pressure.

If the number of electrons per atom is in between 4 and 5, the system could be either fourfold or sixfold coordinated. We analyze this competition in a simple model that is local i. e. it involves only nearest neighbour interactions and, as such, can be applied to crystalline structure as well as amorphous or liquid structures.

Simple cubic structure (N=6)

The total energy of a simple cubic structure with N_{sp} electrons ($2 \leq N_{sp} \leq 5$), is computed in the second moment approximation of the p band. The resonance integral decay is again characterized by a parameter q. In the simplest cases, it is the q^{th} inverse power of the distance[11]. Following Harrison [48], $q = 2$. We consider a more general case of the interaction energies described above. The higher the p value, the harder the repulsive potential.

The bonding mechanism is insured by the p electrons ($pp\sigma$ bonding), the number of which is $N_{sp} - 2$, as the 2 electrons in the filled s band do not contribute to the bonding mechanism. Within the second moment approximation, the electronic density of states is approximated by two peaks. The resulting cohesive energy is given by

$$E_{tot}^{(6)} = -(N_{sp} - 2)\sqrt{2} f_{pp\sigma}(r) + K_{pp\sigma} f_{pp\sigma}^{\frac{p}{q}}(r) \qquad 2 \leq N_{sp} \leq 5 \tag{7.12}$$

At the equilibrium distance, $r_{eq}^{(6)}$, the cohesive energy is given by

$$E_{tot,\,eq}^{(6)} = -(N_{sp} - 2)\sqrt{2} f_{pp\sigma}\left(r_{eq}^{(6)}\right)\left(1 - \frac{q}{p}\right) \tag{7.13}$$

[11] An exponential variation with distance would give analogous results.

Diamond structure (N=4)

The total energy of a diamond structure with N_{sp} electrons ($4 \leq N_{sp} \leq 8$) electrons can be computed to the first approximation in the molecular model approximation [48, 163]. Let us call β_{sp^3} the resonance integral between sp^3 orbitals and let us assume that it decays with the same q^{th} inverse power of the distance.

$$\beta_{sp^3,0} = \frac{1}{4}(\beta_{ss\sigma,0} - 2\sqrt{3}\,\beta_{sp\sigma,0} - 3\,\beta_{pp\sigma,0}) \tag{7.14}$$

Let us remark that $pp\pi$ does not enter into the formula. The total energy per atom is the sum of a (positive) promotion energy (promotion of an electron from the s level to the p level) and an attractive (negative) bonding term and the pairwise repulsive term.

$$E_{tot}^{(4)} = (\varepsilon_p - \varepsilon_s) - N_{sp} f_{sp^3}(r) + K_{sp^3} f_{sp^3}^{\frac{p}{q}}(r) \qquad 0 \leq N_{sp} \leq 4 \tag{7.15}$$

The equilibrium distance, $r_{eq}^{(4)}$, is independent of the promotion energy $\varepsilon_p - \varepsilon_s$. The resulting total energy is given by

$$E_{tot}^{(4)} = (\varepsilon_p - \varepsilon_s) - (8 - N_{sp}) f_{sp^3}\left(r_{eq}^{(4)}\right)\left(1 - \frac{q}{p}\right) \tag{7.16}$$

The evolution of the difference between the s and p levels is illustrated in figure 7.15. The difference $\varepsilon_p - \varepsilon_s$ increases with the column number as the ε_s level goes down faster than the ε_p level.

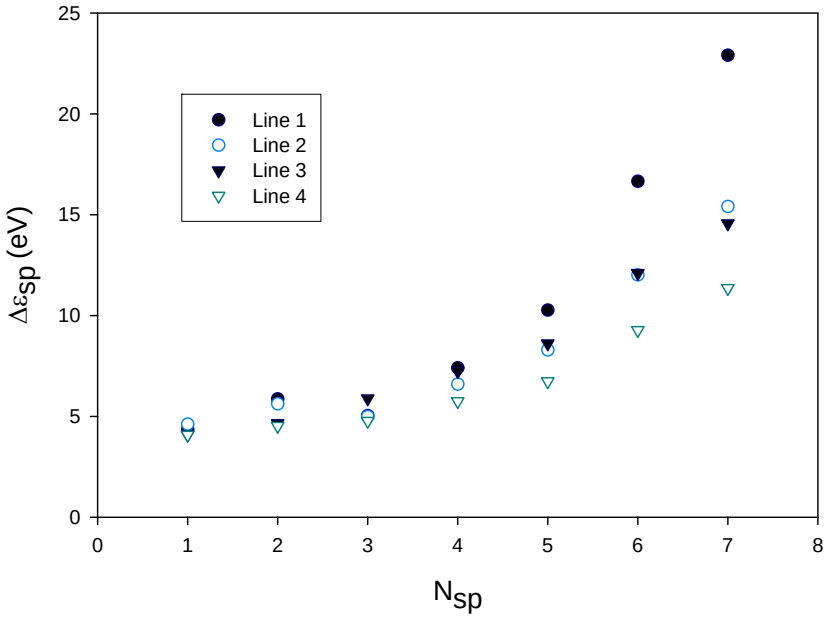

Figure 7.15: Difference between the electronic s and p levels for the sp-elements of the periodic table for the different lines of the periodic table.

On figure 7.16 the crossing point between fourfold- and sixfold-coordinated structural energies is around $N_{sp} = 4.2$. Indeed, in the region $4 \leq N_{sp} \leq 5$, the total energy curve for fourfold-coordinated structures is increasing and the total energy curve for sixfold-coordinated is decreasing. As a consequence, the crossing point is well defined and is largely independent

of the parameters. The result is not too sensitive to the parameters as the crossing is done at high angles. One important conclusion is that the repulsive term does not play an important role in this case. To a first approximation, we can neglect the repulsive term assuming a given interatomic distance, r_{eq}. The curved lines of figure 7.16 are then replaced by straight lines. The crossing is obtained by equating the energies $E^{(6)}$ and $E^{(4)}$ of the two structures (equations (7.13) and (7.16).)

$$-(N_{sp}-2)\sqrt{2}f_{pp\sigma}\left(r_{eq}^{(6)}\right) = (\varepsilon_p - \varepsilon_s) - (8-N_{sp})f_{sp^3}\left(r_{eq}^{(4)}\right)r_4^q \tag{7.17}$$

And the resulting critical value of the number of sp electrons is

$$N_{sp}^* = -\frac{\varepsilon_p - \varepsilon_s}{f_{sp^3}\left(r_{eq}^{(4)}\right) + \sqrt{2}f_{pp\sigma}\left(r_{eq}^{(6)}\right)} + \frac{8f_{sp^3}\left(r_{eq}^{(4)}\right) + 2\sqrt{2}f_{pp\sigma}\left(r_{eq}^{(6)}\right)}{f_{sp^3}\left(r_{eq}^{(4)}\right) + \sqrt{2}f_{pp\sigma}\left(r_{eq}^{(6)}\right)} \tag{7.18}$$

The numerical analysis of this result is now considered using the inverse power expression for the general potentials $f_{sp^3}(r)$ and $f_{pp\sigma}(r)$. Assuming that the ratio of $\frac{\beta_{pp\sigma,0}}{\beta_{sp^3,0}} = 0.74$ and taking into account the 6% increase of the interatomic distance $\frac{r_{eq}^{(6)}}{r_{eq}^{(4)}}$ and $q=2$, one finds a value of N_{sp}^*

$$N_{sp}^* = 5.1 - 0.52\frac{\varepsilon_p - \varepsilon_s}{\left|\beta_{sp^3,0}{r_{eq}^{(4)}}^{-2}\right|} \tag{7.19}$$

Typical values for Ge are $\varepsilon_p - \varepsilon_s = 7eV$ and $\beta_{sp^3,0}{r_{eq}^{(4)}}^{-2} = 6.5eV$. The critical value of N_{sp}^* is 4.5. Stabilizing the fourfold coordinated structure up to $N_{sp}=5$ requires a ratio $\frac{\varepsilon_p-\varepsilon_s}{\beta_{sp^3,0}} = 2$.
At the opposite, if $\varepsilon_p - \varepsilon_s = 0$, the fourfold-coordinated structure is stable up to $N_{sp} = 5.1$. Of course, the higher the value of $\varepsilon_p - \varepsilon_s/\beta_{sp^3}$, the more difficult it is to hybridize the s and p electrons and the less stable the fourfold-coordinated structure.

If we include the repulsive potential, the above formula transforms into

$$N_{sp}^* = 5.1 - \frac{0.52}{1-\frac{q}{p}}\frac{\varepsilon_p - \varepsilon_s}{\left|\beta_{sp^3,0}{r_{eq}^{(4)}}^{-2}\right|} \tag{7.20}$$

A simple but approximate formula could be drawn

$$N_{sp}^* = 5 - \frac{\varepsilon_p - \varepsilon_s}{\left|\beta_{sp^3,0}{r_{eq}^{(4)}}^{-2}\right|} \tag{7.21}$$

The reference value for the separation between fourfold coordination and sixfold coordination is N^*=5; a higher value of the promotion energy decrease the N^* value as it favors the sixfold coordination for which this promotion energy has not to be payed.

If, in addition, we take into account the approximate linear dependence of $\varepsilon_p - \varepsilon_s$ on the column number (=N_{sp}), i. e.

$$\varepsilon_p - \varepsilon_s = a * N_{sp} + b \tag{7.22}$$

then we have

$$N_{sp}^* = \frac{5 - \frac{b{r^{(4)}}^2}{\beta_{sp^3,0}}}{1 + \frac{a{r^{(4)}}^2}{\beta_{sp^3,0}}} \tag{7.23}$$

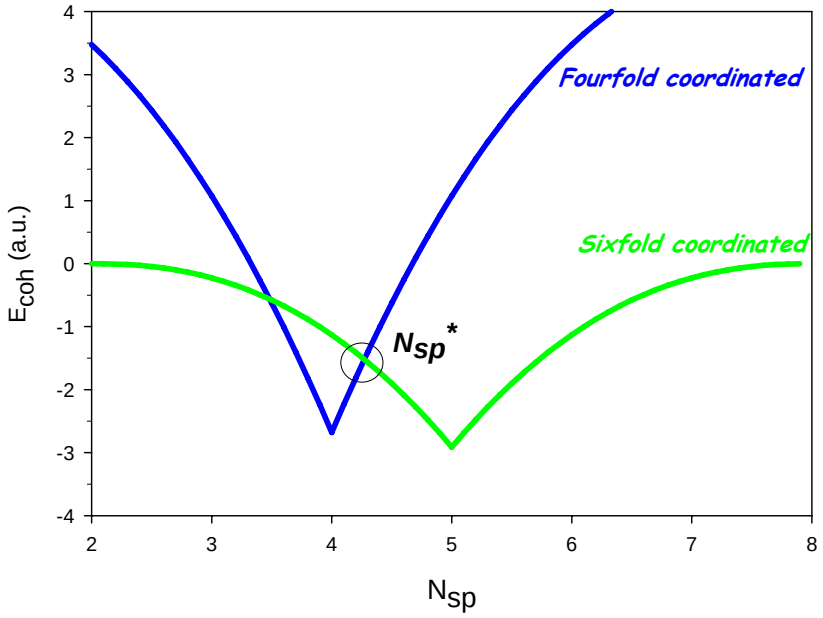

Figure 7.16: Schematic evolution of the cohesive energies of the fourfold and sixfold coordinated structures as a function of the electron number, N_{sp}. The crossing point of the two curves gives the critical value of the electron number, $N_{sp}*$, for which the fourfold structure becomes unstable in favour of the sixfold coordinated structure.

Coming back to the generalized expression of the attractive potential, $f(r)$, the evolution of the critical value, N^*_{sp}, as a function of promotion energy, $\varepsilon_p - \varepsilon_s$, is deduced from (7.17).

$$\frac{dN^*_{sp}}{d(\varepsilon_p - \varepsilon_s)} = \frac{-1}{\sqrt{2}\left|f_{pp\sigma}(r^{(6)})\right| + \left|f_{sp^3}(r^{(4)})\right|} \tag{7.24}$$

Let us notice that the repulsive term does not contribute to relation (7.24).

The following trends are observed:

- The larger the interatomic separation, the smaller the N^*_{sp} value.
- The higher the promotion energy ($\varepsilon_s - \varepsilon_p$ separation), the lower the N^*_{sp} (number of electrons at the crossover).
- The crossing point of the two curves is well defined as the two curves crosses sharply. The critical value of the distances is $r \approx 2.63$ Å, which is between Ge and Sn interatomic distance.
- The curvature of the total energy curves reflects the softness of the repulsive potential. The softer the potential, the larger the curvature. Hard core repulsion gives straight lines. The repulsive term plays a minor role here by contrast to the demonstration of the octet rule [139]. If the repulsive term is not taken into account, i. e. if the calculations are done at fixed bond length, the curved lines are replaced by straight lines and the crossing point is weakly altered.

An important issue is the variation of N* with the pressure. The enthalpies of structures, $H^{(4)}$ and $H^{(6)}$, need to be considered.

$$H^{(6)} = -(N_{sp} - 2)\sqrt{2} f_{pp\sigma}(r^{(6)}) + K_{pp\sigma} f^{\frac{p}{q}}_{pp\sigma}(r^{(6)}) + P{r^{(6)}}^3 \qquad 2 \leq N_{sp} \leq 5 \tag{7.25}$$

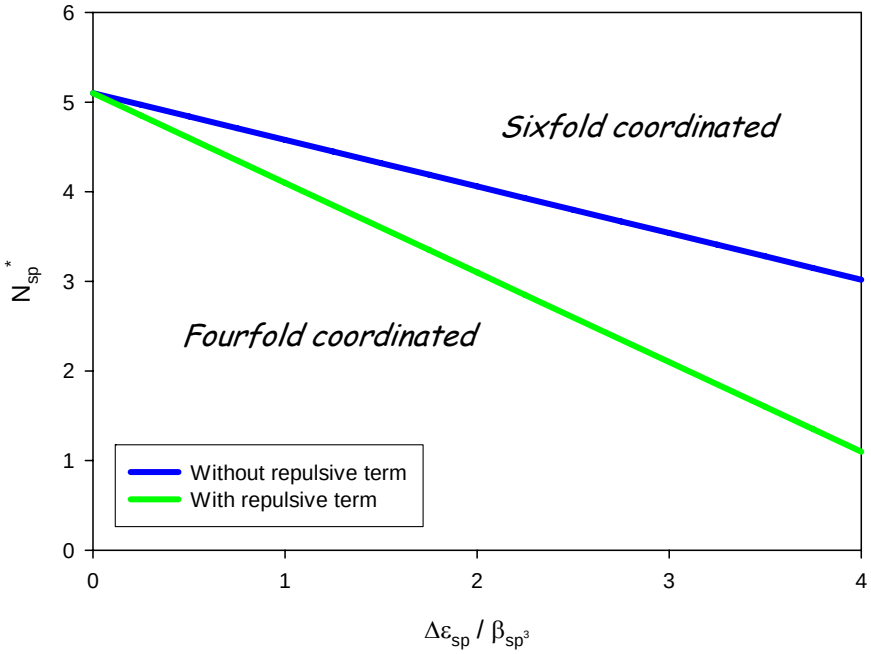

Figure 7.17: Evolution of N_{sp}^{*} with the promotion energy (see relations (7.19) and (7.20)). When the energy difference between the s and p electronic levels becomes higher and higher, the sixfold coordinated structure is progressively stabilized.

and

$$H^{(4)} = (\varepsilon_p - \varepsilon_s) - (8 - N_{sp}) f_{sp^3}(r^{(4)}) + K_{sp^3} f_{sp^3}^{\frac{p}{q}}(r^{(4)}) + P{r^{(4)}}^3 \qquad 4 \leq N_{sp} \leq 8 \qquad (7.26)$$

The equations no longer have an analytic solution and we have to perform a numerical analysis. Once again, the inverse power expression is selected for the $f(r)$ interaction potential. Pressure allows to decrease the crossing point below $N_{sp} = 4$: all group-14 elements and isoelectronic compounds are no longer fourfold coordinated as illustrated in figure 7.18.

7.4.4 The octet rule

Let us now focus on the p-bonded systems: the directionality of the bonds is important and the resulting structures becomes open. As the p orbitals have six orthogonal lobes, in order to maximize the orbital resonance and hence the cohesion, a sixfold coordinated structure (e. g. a simple cubic lattice) is expected (Z=6). But nature does not confirm our expectations, for instance in arsenic we have three nearest neighbors and three next-nearest neighbors: the right hand side of the periodic table is governed by the well-known octet rule if only the nearest neighbors are counted. This writes

$$Z = 8 - N_{sp} \qquad (7.27)$$

where N_{sp} is the number of s and p electrons and Z the number of first neighbours.

Only the p_x, p_y and p_z orbitals are considered in this section as the cohesive properties are dominated by the p electrons contribution for groups 15, 16 and 17. Indeed the s-p separation increases with number of p-electrons : the sp hybrids are less energetically favourable than for the group-14 elements. Moreover, as the bond angles are assumed to be right, the three space directions can be considered to be independent as demonstrated by Kanamori [164].

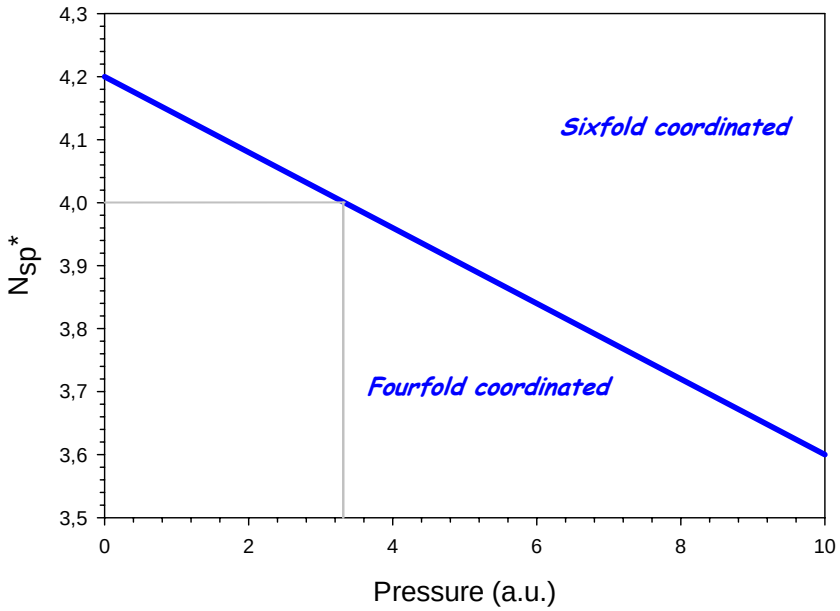

Figure 7.18: Schematic evolution of the critical number of electrons, $N_{sp}*$ when pressure is applied.

Various works about the prediction of the structural trend through the periodic table have been already published. However, only few of them take care of the repulsive contribution in an explicit way. In this section, the importance of such a contribution is highlighted. We generalize a model of Gaspard *et al.* [139] initially applied to the octet rule in the groups 15, 16 and 17 of the periodic table. We extend their approach using a functional expression for the attractive and repulsive potentials. Afterwards the Pettifor structural energy difference theorem is described. It only gives the energy difference between two structures but this is an intermediate stage to take into account the repulsive contribution. Besides the semi-empirical methods, it is also possible to exploit the empirical Landau's point of view to describe the structural distortions through the periodic table. The evolution of these distortions under pressure is finally tackled using the approaches previously introduced.

Taking into account that the model is limited to a second-moment approximation and that the long bonds are assumed to give negligible resonance integral, the total energy per atom of the linear chain with a band filling, ρ, is given by

$$\begin{cases} E = -\rho f(r) + \frac{c}{2} K f^{\frac{p}{q}}(r) & \text{if} \quad \rho \leq \frac{c}{2} \\ E = -\frac{c}{2} f(r) + \frac{c}{2} K f^{\frac{p}{q}}(r) & \text{if} \quad \frac{c}{2} \leq \rho \leq 1 - \frac{c}{2} \\ E = -(1-\rho) f(r) + \frac{c}{2} K f^{\frac{p}{q}}(r) & \text{if} \quad 1 - \frac{c}{2} \leq \rho \end{cases} \tag{7.28}$$

where c is the proportion of atoms involved in diatomic molecules. $1 - c$ is the proportion of lone atoms. In the framework of a second-moment approximation, the electronic levels of this linear chain described by a weighted average of these configurations. The resulting sketches of the electronic levels are illustrated in figure 7.19.

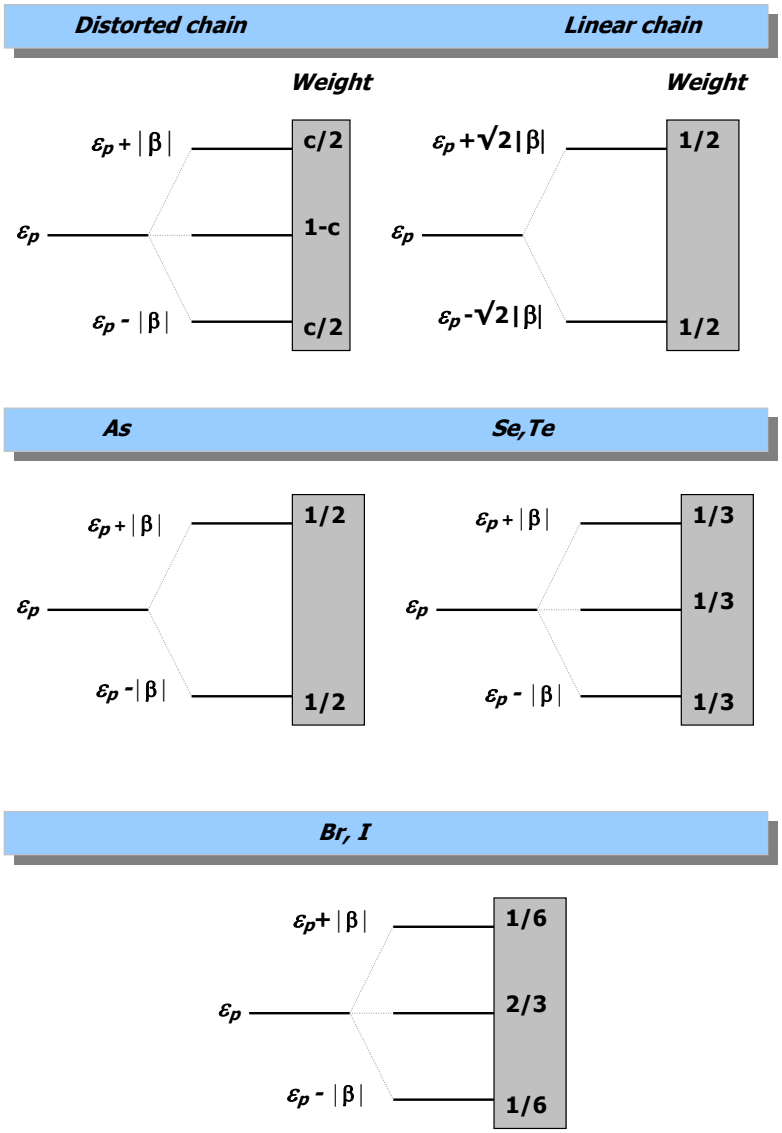

Figure 7.19: Schematic description of the electronic levels of the distorted structures. The structure is characterized by a proportion of c atoms involved in diatomic molecules.

The set of equations (7.28) can be interpreted if they are written in the following form

$$\begin{cases} E &= A\dfrac{\rho^{\frac{p}{p-q}}}{c^{\frac{q}{p-q}}} & \text{if} \quad \rho \leq \frac{c}{2} \\ E &= cA' & \text{if} \quad \frac{c}{2} \leq \rho \leq 1-\frac{c}{2} \\ E &= A\dfrac{(1-\rho)^{\frac{p}{p-q}}}{c^{\frac{q}{p-q}}} & \text{if} \quad 1-\frac{c}{2} \leq \rho \end{cases} \tag{7.29}$$

where A, A' and A'' are independent of ρ and c. As shown in figure 7.20, the attractive energy

is not depending on the structure itself for a given band filling. As soon as the repulsive contribution is taken into account this degeneracy is removed : the straight sections are bend as illustrated in figure 7.21.

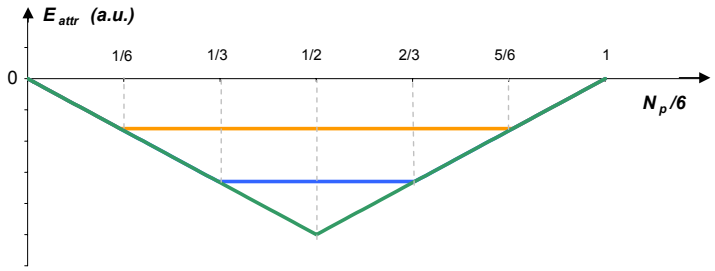

Figure 7.20: Attractive contribution to the total energy of the idealized distorted structures as a function of the band filling (the interatomic separation is kept constant).

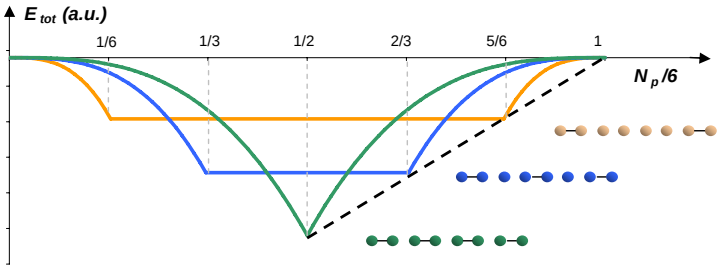

Figure 7.21: Total energy of the distorted structures as a function of band filling. The repulsive term is included and the calculations are done at the equilibrium distance. The dashed line is the locus of the stable phases given by relation (7.30).

The most stable structure is then easily determined as a function of the band filling, ρ, in the following way :

$$c = 2 - 2\rho \tag{7.30}$$

Taking into account the three dimensions, c becomes the number of neighbours, Z, and the previous relation writes

$$Z = 3c = 6 - 6\rho = 6 - N_p = 8 - N_{sp} \tag{7.31}$$

where N_p is the number of p electrons. $N_{sp} = 2 + N_p$ is simply the total number of electrons in the valence band.

As c is the proportion of atoms involved in diatomic molecules, it is possible to deduce the structural assembly, i.e. the order , n, of the n-merization by simply writing c as the ratio $\frac{2}{n}$.

Considering only the p-electrons, the stable structure for a half band filling is a 2-merized structure resulting in corrugated planes. For a 2/3 filled band, a 3-merized structure is energetically favoured giving rise to helical chains. Finally, for a 5/6 filling, the stable structure is a 6-merized chain. However, in this particular case, the diatomic molecules are lying in parallel planes within the actual structure. Along the z-axis, there is absolutely no short bond and the 6-merized structure calculated for an isotropic three-dimensionnal behaviour becomes a 4-merized structure along the x- and y- directions. This modification is mainly due to effects not included in the model such as Van der Waals interactions.

By averaging, the prediction of the model are qualitatively correct also in this case. Indeed if the three dimensions, i, are independently considered we have $c_i = 2 - 2\rho_i$. Of course the

octet rule is verified for the three-dimensionnal assembly, i.e. $c_1 + c_2 + c_3 = 6 - N_p$. In the case of iodine, there is no bond in the z direction and thus $c_3 = 0$. As the remaining dimensions are equivalent, i.e. $c_1 = c_2$, we simply have $c_1 = \frac{2}{4}$: in the x-y plane, a 4-merized structure must occur.

Using our functional description of the attractive potential, the relative stability of the distorted, (1), and undistorted, (2), structures is discussed as a function of the hardness of the repulsive potential, $\frac{p}{q}$. Thus, if the total energy of the system writes

$$E = -Af(r) + Bf^{\frac{p}{q}}(r) \tag{7.32}$$

The relative stability of two phases, (1) and (2), is driven by the ratio

$$\frac{E^{(2)}}{E^{(1)}} = \left(\frac{A^{(1)}}{A^{(2)}}\right)^{\frac{p}{p-q}} \left(\frac{B^{(2)}}{B^{(1)}}\right)^{\frac{q}{p-q}} \tag{7.33}$$

The stability boundary between the two structures is simply given by the equality of the two total energies, i.e. $\frac{E^{(2)}}{E^{(1)}} = 1$. This expression combined with 7.30 allows to obtain the critical value for the $\frac{p}{q}$ ratio, $\left(\frac{p}{q}\right)^*$, giving the stability limit between the distorted and the simple cubic (undistorted) structures:

$$\left(\frac{p}{q}\right)^* = \frac{ln(1-\rho)}{ln\sqrt{2}} \tag{7.34}$$

In conclusion, the octet rule only occurs when the repulsive potential is soft enough. When the ratio $\frac{p}{q}$ is higher than the critical value, $\left(\frac{p}{q}\right)^*$, i.e. when the repulsive interaction is hard enough, the distorted structure becomes unstable in favour of the undistorted simple cubic structure.

Let us consider the particular case of the inverse power interactions : the total energy writes

$$E_{tot} = -Ar^{-q} + Br^{-p} \tag{7.35}$$

The equilibrium interatomic distance, r_{eq}, is obtained by the minimization of the total energy E_{tot}

$$r_{eq} = \frac{pB}{qA}^{\frac{1}{p-q}} \tag{7.36}$$

Even if this model ignores how the short and long bonds alternate, it underlines the influence of the band filling, ρ, and of the hardness of the repulsive potential - through the ratio $\frac{p}{q}$ - on the existence - or not - of the distortion. This is directly linked to the fact that the description of the attractive potential is based on quantum-mechanical considerations and not on a classical additive pairwise attractive potential. Indeed, the classical attractive contribution is proportional to Z. As $\frac{p}{q} \leq 1$ is not physical for stability reasons, a classical system is not allowed to become spontaneously distorted.

This method is based on second moment expansion and thus on the local order with no reference to the long range crystalline order. Our conclusions are thus wider : if no important entropic effects arise, our conclusions can be generalized to liquids and amorphous systems.

Let us note that we could describe the occurrence of an incommensurate structure. Indeed if the band filling ratio, ρ, is irrational, the resulting structure becomes incommensurate. In the case of halogens, electrons of the in-plane p-bands could be transfered to the p_z band when this one is broadened by the pressure[12].

[12]The distance between the molecular planes is strongly influenced by the pressure as the related interactions are weak.

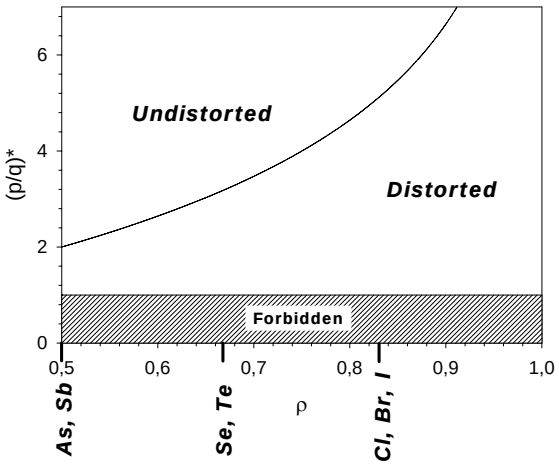

Figure 7.22: Simple phase diagram illustrating the distorted and undistorted areas as a function of the band filling and of the hardness of the repulsive potential. The cases of As, Se, Te, Br and I is illustrated.

7.4.5 The Pettifor structural energy difference theorem

In his structural energy difference theorem, Pettifor[165, 158] shows that total energy difference between two structures is the difference of their attractive energies, calculated at distances for which both repulsive terms are equal.

$$\Delta E = [\Delta E_a]_{\Delta E_r = 0} \tag{7.37}$$

This expression is exact up to the second order in $\tilde{r}_{eq}^{(2)} - r_{eq}^{(2)}$ where $r_{eq}^{(2)}$ and $\tilde{r}_{eq}^{(2)}$ are respectively the equilibrium interatomic distance in structure (2) and the interatomic distance for which the structure (2) has the same repulsive energy as structure (1).

In practice, in order to calculate the difference in energy between two phases, we calculate the distance, $\tilde{r}_{eq}^{(2)}$, for which the repulsive energy of the second structure is equal to the repulsive energy of the first structure, i. e. $E_r^{(2)}(\tilde{r_{eq}^{(2)}}) = E_r^{(1)}(r_{eq}^{(1)})$. Then

$$\Delta E = E_a^{(2)}(\tilde{r}_{eq}^{(2)}) - E_a^{(1)}(r_{eq}^{(1)}) \tag{7.38}$$

The usefulness of this theorem is not obvious but it makes a link between the numerous approaches that neglect the repulsive term and our approach that takes it into account.

We have shown that, astonishing enough, (7.38) gives the exact value of the critical ratio $\left(\frac{p}{q}\right)^*$, given by (7.34). Indeed

$$\Delta E = -A^{(2)} f(\tilde{r}_{eq}^{(2)}) + A^{(1)} f(r_{eq}^{(1)}) \tag{7.39}$$

The equality of the repulsive terms gives the relation

$$\frac{f(\tilde{r}_{eq}^{(2)})}{f(r_{eq}^{(1)})} = \left(\frac{B^{(1)}}{B^{(2)}}\right)^{\frac{q}{p}} \tag{7.40}$$

and we finally have

$$\Delta E = -A^{(1)}(r_{eq}^{(1)}) \left[-1 + \frac{A^{(2)}}{A^{(1)}} \left(\frac{B^{(2)}}{B^{(1)}}\right)^{\frac{q}{p}} \right] \tag{7.41}$$

From that, the critical ratio $\left(\frac{q}{p}\right)^*$, is given by

$$\left(\frac{q}{p}\right)^* = \frac{ln\frac{A^{(1)}}{A^{(2)}}}{ln\frac{B^{(2)}}{B^{(1)}}} \tag{7.42}$$

This gives the same expression as (7.34). Cressoni and Pettifor [166] applied this theorem to the relative stability of the structures of the *sp*-elements. The structural maps obtained with this methods are in good agreement with the experimental data.

The octet rule for the elements of the groups 15 (Va), 16 (VIa) and 17 (VIIa) of the periodic table is discussed using the Pettifor theorem. The resulting energy differences are given by the following relations depending on the band filling, ρ, and the number of neighbours, Z. If $\rho > 1 - \frac{c}{2}$, we have

$$\Delta E_Z \propto 2\left[\sqrt{2} - \left(\frac{6}{Z}\right)^{\frac{q}{p}}\right](1-\rho) \tag{7.43}$$

and if $\rho < 1 - \frac{c}{2}$

$$U_Z \propto -\left[\frac{Z}{3}\left(\frac{6}{Z}\right)^{\frac{q}{p}} - 2\sqrt{2}(1-\rho)\right] \tag{7.44}$$

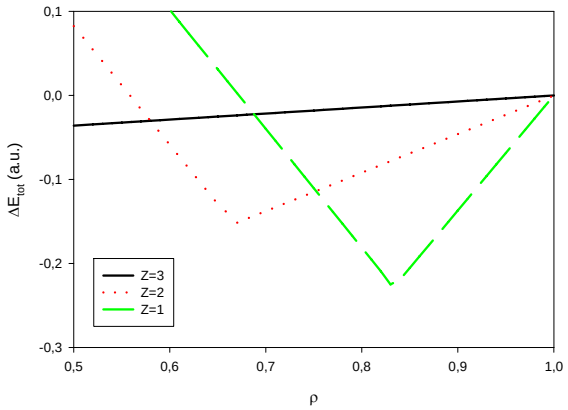

Figure 7.23: Energy differences for the distorted structures in the case of groups 15 (Z=3), 16 (Z=2) and 17 (Z=1). It shows that the octet rule is also observed through the application of the Pettifor's theorem.

The curves illustrated in figure 7.23 are the difference between the distorted structures and the reference structure. This reference structure is the simple cubic structure. In this case we have

$$E_{CS} \propto (1-\rho)^{\frac{p}{p-q}} \tag{7.45}$$

7.4.6 From a microscopic model to a macroscopic behaviour

Based on relation (7.8), it is possible to describe the macroscopic behaviour of matter under hydroscatic pressure, P. The pressure itself is defined by

$$P = -\frac{dE}{dV} \tag{7.46}$$

where V is the atomic volume defined by $V = \gamma r^3$. γ is a geometrical parameter taking into account of the actual structure. Two thermodynamical variables have to be defined: the bulk modulus, B, and its first derivative, B'.

$$B = -V\frac{dP}{dV} \tag{7.47}$$

$$B' = \frac{dB}{dP} = \frac{dB}{dV}\frac{dV}{dP} \tag{7.48}$$

In the macroscopic description of matter, the bulk modulus at zero pressure is used. Based on our general potential, $f(r)$, we have

$$B_0 = \frac{1}{9\gamma r_{eq}}\left(\frac{p}{q} - 1\right)\frac{f'^2(r_{eq})}{f^2(r_{eq})} \tag{7.49}$$

If the inverse power potential is chosen, more explicit results are obtained using $E(r) = Ar^{-p} - Br^{-q}$:

$$B_0 = \frac{1}{9\gamma r_{eq}}\frac{\partial^2 E}{\partial r^2}\bigg|_{r_{eq}} \tag{7.50}$$

where r_{eq} is the interatomic equilibrium distance, $r_{eq} = \left(\frac{Ap}{Bq}\right)^{\frac{1}{p-q}}$. If this expression is included in (7.50), the simple following relations can be obtained assuming $V_{eq} = \gamma r_{eq}^3$.

$$E_{eq} = Ar_{eq}^{-p}\left(1 - \frac{p}{q}\right) \tag{7.51}$$

$$B_0 = \frac{Ap}{9\gamma}r_{eq}^{-p-3}(p-q) \tag{7.52}$$

$$B_0' = \frac{p+q}{3} + 2 \tag{7.53}$$

$$\frac{B_0}{\left|\frac{E_{eq}}{V_{eq}}\right|} = \frac{pq}{9} \tag{7.54}$$

This last relation was demonstrated by Ducastelle on a more specific basis [167]. Relation (7.54) is valid for non Peierls distorted structures, essentially the metals.

$$B' = \frac{p+3}{3} + \frac{q+3}{3}\frac{(p-q)b}{p(p+3)aV^{\frac{p-q}{3}} - q(q+3)b} \tag{7.55}$$

If $P = 0$, we simply have

$$B_0' = \frac{p+q}{3} + 2 \tag{7.56}$$

At the opposite, $P \to \infty$

$$B_\infty' = \frac{p+3}{3} \tag{7.57}$$

The related equation of state, i.e. the $P(V)$ relation, is simply given by

$$P = V_0^{-\frac{q}{3}-1}\frac{q\beta_0}{3}\gamma^{-\frac{p}{3}}\left[\left(\frac{V_0}{V}\right)^{\frac{q}{3}+1} - \left(\frac{V_0}{V}\right)^{\frac{q}{3}+1}\right] \tag{7.58}$$

which becomes the Murnaghan equation of state for $p = 4$ and $q = 2$.

A general expression for the equation of states based on the generalized energy writes simply

$$P = \left[-1 + \left(\frac{f}{f_0}\right)^{\frac{p}{q}-1}\right]\frac{f'}{3\gamma r^2} \tag{7.59}$$

This formula can be helpful to obtain a generalized equation of states.

7.5 Distortion amplitude and pressure : the two-distance model

7.5.1 The linear chain

The previous demonstration of the octet rule is non quantitative as the long bonds are assumed to be infinitely long. The next step is to take into account of the second neighbour by introducing a second distance, r_l. If we go further in the description of the Peierls distortion using a long and a short bond within a second-moment approximation, it is possible to describe the relative evolution of the short and long bonds through the periodic table, i.e. as a function of the ratio $\frac{p}{q}$. This ratio is the image of the relative hardness of the repulsive potential. The total energy of a distorted atomic chain with a succession of long and short bonds is given by

$$E = -\sqrt{f(r_s) + f(r_l)} + K\left(f^{\frac{p}{q}}(r_s) + f^{\frac{p}{q}}(r_l)\right) \tag{7.60}$$

It is convenient to define two new geometrical parameters, $\bar{r}$ and η, as follows

$$\bar{r} = \frac{r_s + r_l}{2} \tag{7.61}$$

$$\eta = \frac{r_l - r_s}{2\bar{r}} \tag{7.62}$$

$\bar{r}$ is the average interatomic distance, i.e. the unidimensional analogue of the atomic volume. η illustrates the relative importance of the distortion. This coordinate change is illustrated in figure 7.24. The ratio $\frac{r_l}{r_s}$ is linked to the new variable, η, by

$$\frac{r_l}{r_s} = \frac{1+\eta}{1-\eta} \tag{7.63}$$

The equilibrium interatomic value when no distortion is assumed, $\bar{r}_{eq}$, is given by $f(r_{eq}) = \frac{q}{pK}$. The distortion appears when the sign of the coefficient of the η^2 term changes from positive to negative in the following equation:

$$E(\bar{r}_{eq}, \eta) = -\frac{\beta_0}{\bar{r}_{eq}^q}\left[\left(1 - \frac{q}{p}\right) - \left(\frac{f'}{f}\right)^2\left(\frac{p}{q} - 2\right)\frac{\bar{r}_{eq}\eta^2}{2}\right] \tag{7.64}$$

It is clear from (7.64) that if p is lower than $2q$, a distortion occurs whereas, when p is greater than $2q$, i.e. when the repulsive potential becomes harder, the undistorted structure is stable.

The study of the fourth order shows that the total energy can be written

$$E(\bar{r}_{eq}, \eta) = -\frac{\beta_0}{\bar{r}_{eq}^q}\left[\left(1 - \frac{q}{p}\right) - \alpha\eta^2 - \beta\eta^4\right] \tag{7.65}$$

where β has a constant sign. The resulting distortion is

$$\eta = \sqrt{-\frac{\alpha}{2\beta}} \tag{7.66}$$

The ratio $\frac{p}{q}$ is once again identified as a driving parameter of the distortion process in the one-distance model. The variation of η as a function of the ratio, $\frac{p}{q}$ is illustrated in figure 7.25.

The evolution of the distortion under pressure is studied by calculating the minimum of the enthalpy, $H = E + PV$. As relation (7.60) is related to the linear chain, it has to be adapted to the take into account the three dimensions. $\bar{r}^3$ is the atomic volume related to this structure. The fourth-order development of the enthalpy is then simply given by

$$H(\bar{r}, \eta, P) = E(\bar{r}, \eta) + P\bar{r}^3 \tag{7.67}$$

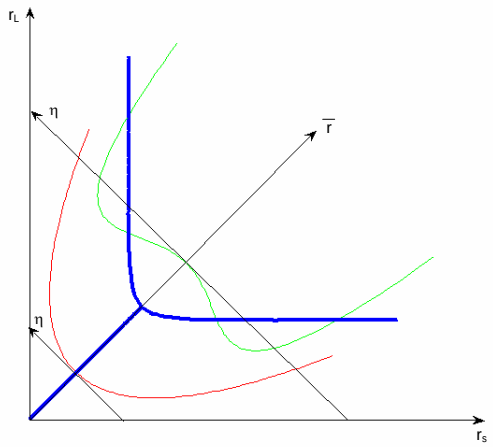

Figure 7.24: Schematic view of the potential for the two distance model. The blue line illustrates the position of the energy minima for any fixed value of $\bar{r}$. The red curve shows the potential appearance when there is no distortion. The minima of the green curve give the amplitude of the distortion parameter, η, for a given value of $\bar{r}$.

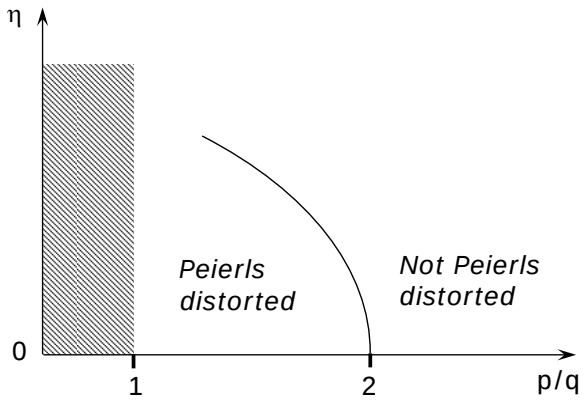

Figure 7.25: Schematic evolution of the distortion amplitude as a function of the $\frac{p}{q}$ ratio for a half-filled band.

It is important to note that the study of the distortion amplitude under pressure is usually not possible analytically due to the additional pressure term. We first calculate numerically the enthalpy surfaces illustrated in figure 7.26. The minimum of the enthalpy is illustrated by red stars. They correspond to the long and short distances.

7.5.2 Landau's approach

Empirical description of the total energy

To complete the study, we introduce an empirical Landau's model, in direct line or similar to (7.65). The following expression is assumed to describe the energy evolution of the distorted linear chain with two interatomic distances, r_l and r_s. The parameters η and $\bar{r}$ are defined by (7.61) and (7.62).

$$E(\bar{r},\eta) = E_0 + \frac{k}{2}(\bar{r} - r_0)^2 + \alpha(P - P_0)\eta^2 + \beta\eta^4 \tag{7.68}$$

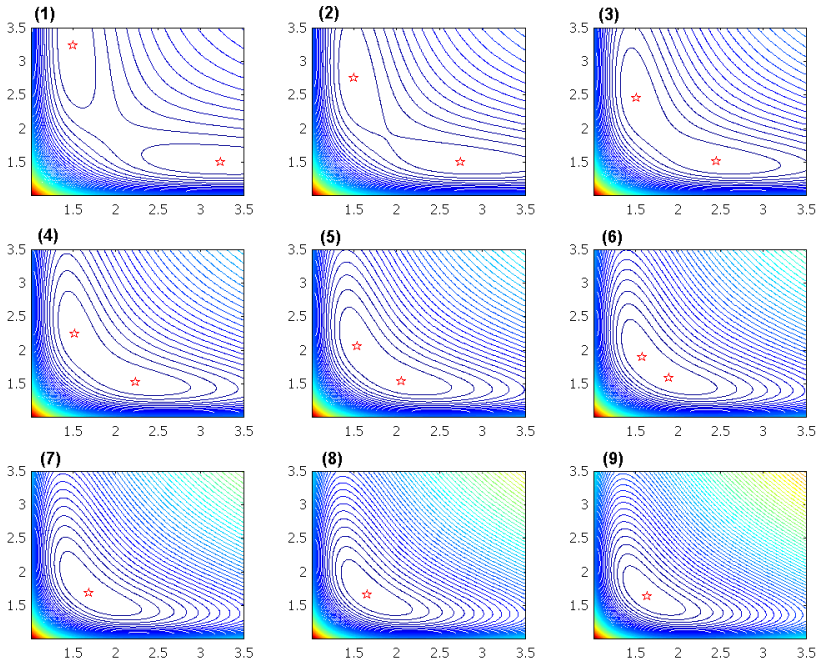

Figure 7.26: Evolution of the isoenthalpic curves of the distorted structure under pressure. Pressure increases from graph (1) to (9). The axes are the long and short interatomic distances, r_L and r_S. The red stars illustrate the minimum of the enthalpy which correspond to the stable (r_l,r_s) interatomic distances. (1)-(6) show a Peierls distorted structure whereas (7)-(9) fit with an undistorted structure.

where both α and β are positive and P_0 is the transition pressure. We choose P as an external parameter for simplicity. Then the distortion amplitude η, has no influence on the equilibrium interatomic distance $\bar{r}$. Had we replaced $(P - P_0)$ by $(V_0 - V)$, then a coupling between η and $\bar{r}$ arises.

In this case, the enthalpy has to be used

$$H = E + \gamma P \bar{r}^3 \tag{7.69}$$

where γ is related to the structure (filling factor).

The evolution of the mean interatomic distance $\bar{r}$ and the distortion amplitude η is simply given by calculating the zero of both the partial derivatives of the enthalpy.

$$\bar{r} = \frac{r_0}{2}\left(-\frac{P_n}{P} + \sqrt{\frac{P_n^2}{P^2} + 4\frac{P_n}{P}}\right) \tag{7.70}$$

$$\eta = \sqrt{\frac{P_0 - P}{P_P}} \tag{7.71}$$

where P_n is defined as a normal pressure, $P_n = \frac{k}{3r_0}$.

The pressure effect on the distortion can be described by the study of the enthalpy, $H(\bar{r}, \eta, P)$, as a function of $\bar{r}$, η and P

$$H(\bar{r}, \eta, P) = E_0 + \frac{k}{2}(\bar{r} - r_0)^2 + \alpha(P - P_0)\eta^2 + \beta\eta^4 + P\gamma\bar{r}^3 \tag{7.72}$$

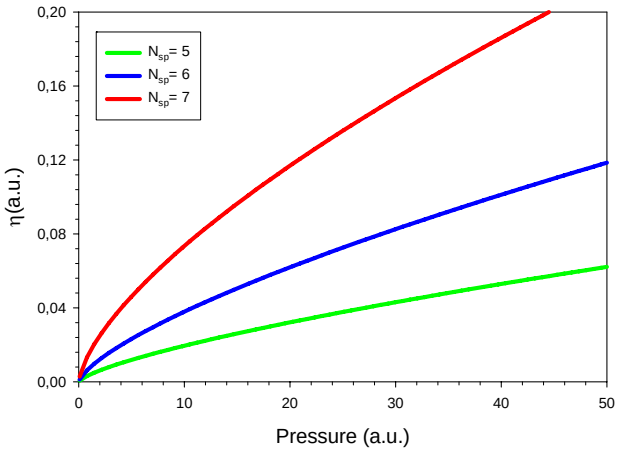

Figure 7.27: Evolution of distortion amplitude, η, as a function of the transition pressure, P_T, given by our model. The shape of the curve is similar to the experimental curve.

The first point is to establish the existence - or not - of the distortion under ambient conditions. The partial derivative, $\frac{\partial H}{\partial \eta}$ is of fundamental interest. The edge between distorted and non-distorted structures is simply given by $\frac{\partial H}{\partial \eta} = 0$ which writes

$$\eta^2 = -\frac{\alpha}{2\beta}(P - P_0) \tag{7.73}$$

As we first consider the zero-pressure case, we have $\eta^2 = \frac{\alpha P_0}{2\beta}$ and the distortion only occurs if $P_0 > 0$. P_0 is the transition pressure. It is the driving parameter of the distortion as summarized in table 7.4. When pressure is increased on a distorted structure, the distortion amplitude is reduced as the square root of $(P - P_0)$. This is what happens in the expanded sodium included in clathrate cages as discussed in chapter 6. Once again the transition is a second-order transition.

If we consider the evolution of the average interatomic distance, $\bar{r}$, we simply have to calculate $\frac{\partial H}{\partial \bar{r}}$. In this case, this leads to two independent expressions for the η and $\bar{r}$ variables. Their evolution as a function of pressure is illustrated in figure 7.28

$$\eta = \sqrt{-\frac{\alpha}{2\beta}(P - P_0)} \tag{7.74}$$

$$\bar{r} = \frac{-k + \sqrt{k^2 + 12kr_0P}}{6P} \tag{7.75}$$

Symmetry breaking and restoring

We finally show that Landau's approach allows to extend the description of the distortion to reentrant distortion as it happens in the case of alkaline metals. A description of the total

P_0	Distortion
≥ 0	No
$= 0$	Critical
≤ 0	Yes

Table 7.4: Structures observed under ambient conditions depending on the value of P_0.

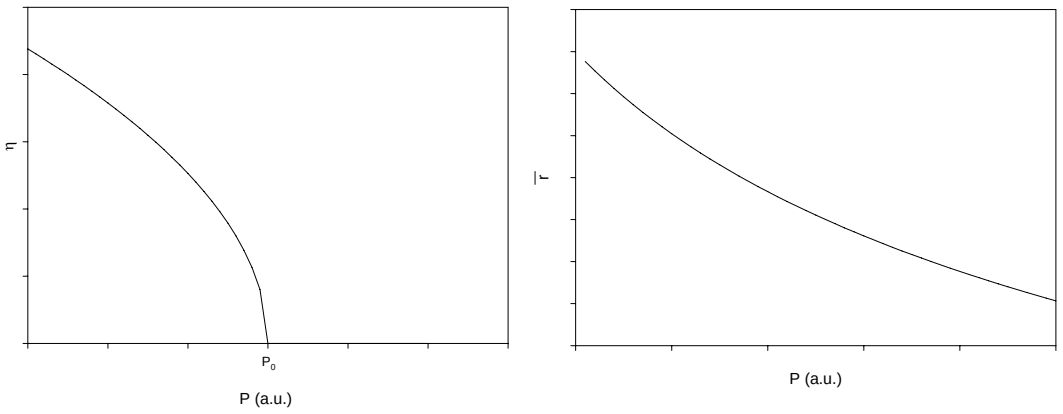

Figure 7.28: Evolution of the two geometrical variables of the Landau model as a function of the external pressure (arbitrary units).

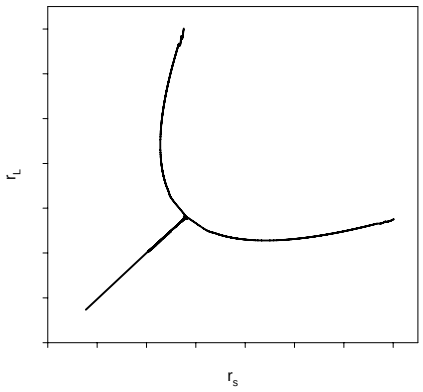

Figure 7.29: Interatomic distances within the Landau's model (arbitrary units).

enthalpy is based on the following equation.

$$H(\bar{r},\eta,P) = E_0 + \frac{k}{2}(\bar{r}-r_0)^2 + \alpha(P^2+\chi P+\xi)\eta^2 + \beta\eta^4 + P\gamma\bar{r}^3 \tag{7.76}$$

In this case, it is possible to describe symmetry breaking and restoring under pressure. Assuming that $\chi^2 - 4\xi \geq 0$, the zero values of the η^2 term are now the two new transition pressures, P_1 and P_2, given by

$$P_{1,2} = \frac{\chi \pm \sqrt{\chi^2-4\xi}}{2} \tag{7.77}$$

The partial derivative of the enthalpy is given by relation (7.78).

$$\frac{\partial H}{\partial \eta} = 2\eta\left[\alpha(P-P_1)(P-P_2) + 2\beta\eta^2\right] \tag{7.78}$$

It is clear from this expression that for pressure below P_1 and higher than P_2, $\frac{\partial H}{\partial \eta}$ is positive and thus no distortion occurs. In the $[P_1, P_2]$ range, the distortion is stable and its amplitude is simply deduced from (7.78). Thus it leads to the evolution of the distortion amplitude driven by the relation (7.79).

$$\eta^2 = -\frac{\alpha}{2\beta}(P-P_1)(P-P_2) \tag{7.79}$$

7.6 Conclusion : structural trend in the periodic table

A unified description of structural trends through the periodic table can be deduced from the previous discussions. We identify three main types of behaviours:

Compact structures (FCC, HCP, BCC, ...) are observed in the left hand side of the periodic table, due to the spherical symmetry of the s orbitals. In the compact structures, a distortion is more difficult and arises only for very soft repulsive potentials (e. g. H_2).

Open cubic structures (diamond) with a tetrahedral environment are observed in group-14 elements. $\beta-Sn$ and Pb are exceptions to this rule. Based on our p-sp^3 competition model, we show that the existence of sixfold coordinated structures (simple cubic or $\beta - Sn$) are favored by an increase of the pressure or an increase of the electron/atom ratio. Pb is a special case as the d electrons enter in the game and favor a compact structure.

Distorted structures (from the simple cubic) are experimentally observed in the right hand side of the periodic table. Polonium is an exception as it is not distorted (simple cubic structure) because of the hardness of the repulsive potential. In general, when the repulsive potential becomes harder (i. e. when one moves down in the periodic table, the $\frac{p}{q}$ ratio becomes larger, the distortion is lowered or destroyed).

In general, pressure reduces or destroys the distortion but, as we have shown in previous chapters, it may, on the contrary, produce a symmetry breaking by "buckling" effect.

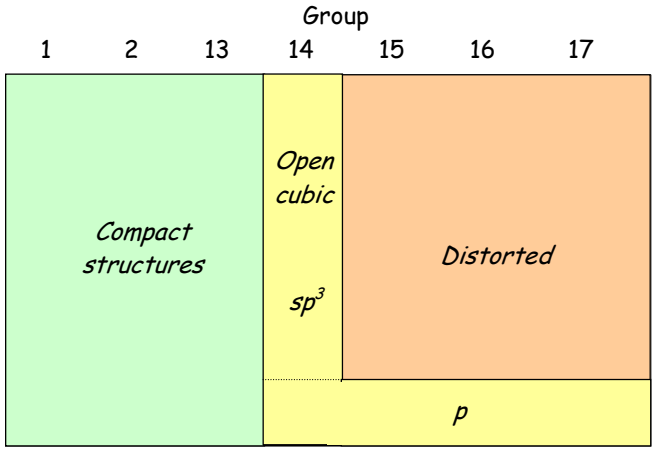

Figure 7.30: General trends observed in the periodic table (see figure 7.2).

Our theoretical approach of the distortion explicitly takes into account the repulsive interaction which is the key point in the description of the octet rule. The initial questions about low or high symmetry is thus addressed depending on only few basic parameters. Analytical developments are described as far as possible but as soon as pressure is included in the problem, a numerical approach is mandatory. The evolution of the distortion under pressure is thus considered using a two-distance model.

Our understanding of the symmetry breaking mechanism can be summarized by figure 7.31. Increasing pressure, or equivalently reducing the atomic volume, induces the fading of the distortion. At the opposite, increasing the atomic volume allows to induce distortion in initially undistorted materials such as sodium atoms included in clathrate cages (see chapter 6).

Finally, the aim of this approach is to draw systematics but certainly not to obtain quantitative results. As soon as a quantitative study is required, we switch to accurate methods such as *ab initio* calculations as illustrated in previous chapters.

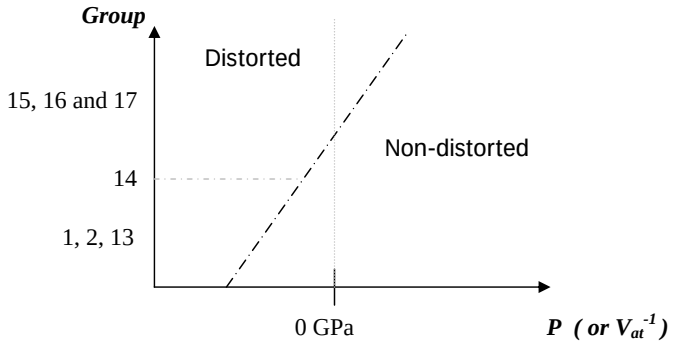

Figure 7.31: Schematic description of the occurrence of a distortion in a "phase" diagram (N_e, P) (N_e= the number of valence electron, P= pressure). The driving parameter of the distortion is the atomic volume, or the pressure. At ambient pressure, elements from the left-hand side of the periodic table are not distorted. However, if the accessible volume is increased, distortion may occur. At the opposite, the elements from the right-hand side of the periodic table are mainly distorted structures. This distortion disappears under pressure.

Chapter 8

Conclusion

The science of high pressures is now mature, technologically and scientifically, and a considerable amount of data has been collected. It is timely to exploit them and uncover systematic behaviours that would be the guide for future progress. The science of high pressures gives invaluable information into the nature of the chemical bond.

In this thesis, through experiments on several systems, apparently unrelated, we identified a systematics on the structure of covalent systems and their evolution under pressure. We used X-ray absorption spectroscopy and X-ray diffraction as tools with setups dedicated to very high pressures at the synchrotron ESRF: beamline ID24 for EXAFS in the energy dispersive mode with a diamond anvil cell and beamline ID30 for diffraction with a large volume Paris-Edinburgh cell.

Our contribution is in three complementary domains of high pressure science: metrology, experiment and theory.

III-V semiconductors : we studied the room temperature phase diagrams of $GaSb$, $InAs$ and GaP for which uncertainties and discrepancies appeared in previous experiments.

We first focus on the occurrence of the $\beta - Sn$ structure in $GaSb$ and GaP. The $\beta - Sn$ structure is found to occur in the III-V semiconductors only if the charge transfer is very low, i.e. only in $GaSb$.

In a second step we analyzed the stability range of the $NaCl$ structure in GaP and $InAs$ by EXAFS. Once again, it is shown to be highly dependent on the charge transfer. Finally we describe the symmetry lowering of $InAs$ under pressure as a mechanical "buckling" effect.

From the point of view of metrology, on $GaSb$ and Si, we have shown both experimentally and theoretically that the pressure transmitting medium has to be carefully chosen as phases may appear because of nonhydrostatic conditions.

Halogens : on the basis of EXAFS measurements, we identified a new phase transition in Bromine under pressure that precedes the incommensurate structure. Even if the structure still remains to be identified, this point modifies the currently accepted scaling rule of the halogens.

Actinides : Americium occupies a pivotal position in the actinide series, at the borderline of light and heavy actinides. We studied in detail its phase diagram. The $Am - III$ and $Am - IV$ structures are resolved. We discuss the high pressure phase in terms of the delocalization of the f-electrons and we show that these high pressure structures are distorted.

Alkali doped clathrates : clathrates produce negative pressures -in some sense- as they expand the spacing between alkali atoms and, as a result, "low density Na" undergoes a distortion. We performed a systematic study of the off-centering of the alkali atoms contained in the clathrate cages. The expansion factor is shown to be the driving parameter of the distortion amplitude. We also studied the reduction of the distortion amplitude when pressure increases. This again confirms that the atomic volume plays a central role in the occurrence -or not- of the Peierls distortion.

In the theoretical analysis we tried to put forward very simple models that grasp the essential of the physics with tunable parameters. Our leading theme is the symmetry or more specifically the symmetry breaking and restoring mechanisms. To the two questions:

1. Is the most symmetrical structure the most stable?
2. Does pressure increase or lower the symmetry?

the answer is sometimes yes, sometimes no, a scientifically untenable answer. The rationale is the following. Depending on the relative hardness of the repulsive potential, elements exhibit a low or a high coordination number. Moreover, the covalent low coordinated structures show a spontaneous symmetry breaking towards a more "molecular" structure with an alternation of short and long bonds and are electrically insulating. This is the celebrated octet rule or the Peierls distortion. Pressure shortens the long bonds more than the short bonds and at a transition pressure, usually of the order of tens of GPa, the structure recovers a high symmetry. At a finer scale, complex structures may occur at intermediate pressures. This is more difficult to comprehend and needs a recurse to numerical calculations. The relative hardness of the repulsive and attractive potentials is shown to be the driving parameter of the existence - or not- of the distortion under ambient conditions.

The volume is a key parameter in the occurrence of the Peierls distortion. We show that under «*negative pressure*» conditions i. e. an artificial expansion, compact structures may exhibit a symmetry breaking (e. g. Na in silicon clathrates). This is the general trend.

We have shown, also theoretically, that an uniaxial stress may induce a low symmetry phase and this is a trap for high pressure studies. The risk to induce phases by non hydrostaticity exists! Our study of $GaSb$ underlines that uniaxial stresses induces structural artefacts: the $Imma$ structure is not observed under hydrostatic conditions. More specifically the unaxial stress is responsible of a huge change of transition pressure in the case of silicon.

Finally, pressure may induce both a symmetry reduction or an increase depending on the conditions. In all these cases, our tight binding model is able to reproduce and even to predict the behaviour of the whole compound family. When quantitative results are required, *ab initio* calculations are performed. This thesis underlines that both methods are complementary. On one hand, the tight binding approach allows physical interpretations and to uncover systematic evolutions. On the other side, *ab initio* calculations give accurate results without any direct access to the physics of the related phenomena. The combined used of these methods is an efficient way to describe and understand a structural systematics.

In conclusion, the atomic volume, the band filling and the hardness of the repulsion are identified to be the most important parameters in the occurrence - or not - of the Peierls distortion. On this basis a systematics can be drawn on the whole periodic table, at least for the general trends.

The story is far from being finished, fortunately. The Peierls distortion is rich of future developments. Our experiments have been done done at room temperature. However the anharmonicity of the potential leads to astonishing thermal properties: negative thermal expansion, anomalous vibration properties, phase transitions in the liquid state, ...

Appendix A

X-ray basics

A.1 History

X-rays were discovered in 1895 by W.C. Röntgen using a Rhumkoff induction coil to supply a modified Crookes tube. The very first image obtained with X-rays was the hand of Mrs Röntgen (see figure A.1). The original tube imagined by Röntgen was replaced in 1913 by the tube design of Coolidge using a hot tungsten filament and a high vacuum in the tube (see figure A.2). This was the first efficient X-ray tube. It is still the base of the classical modern X-ray tubes.

Figure A.1: The first X-ray image taken by W.C. Röntgen is the radiography of his hand's wife. It took 15 minutes to take this exposure. Nowadays, such an image needs few tenths of a second for much better results.

The X-ray emission in such tubes is usually based on the Bremsstrahlung radiation of very fast electrons. These electrons are emitted by a hot filament (thermo-ionic emission) and they are accelerated by an electric field between the cathode and the anode. The power of the tube is limited by the heat load on the target material. In order to further increase the power of such tubes, rotating anode were developed in the 60's. They allow to make huge progress in the medical field mainly with scanners.

After being strange and amazing, scientists understood that they could use X-rays as a very efficient probe of matter at the atomic scale. Nowadays, X-rays are daily used in the scientific, industrial and security worlds. Few examples are given in figure A.3.

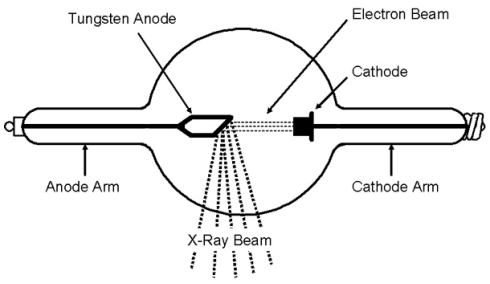

Figure A.2: Coolidge tube design.

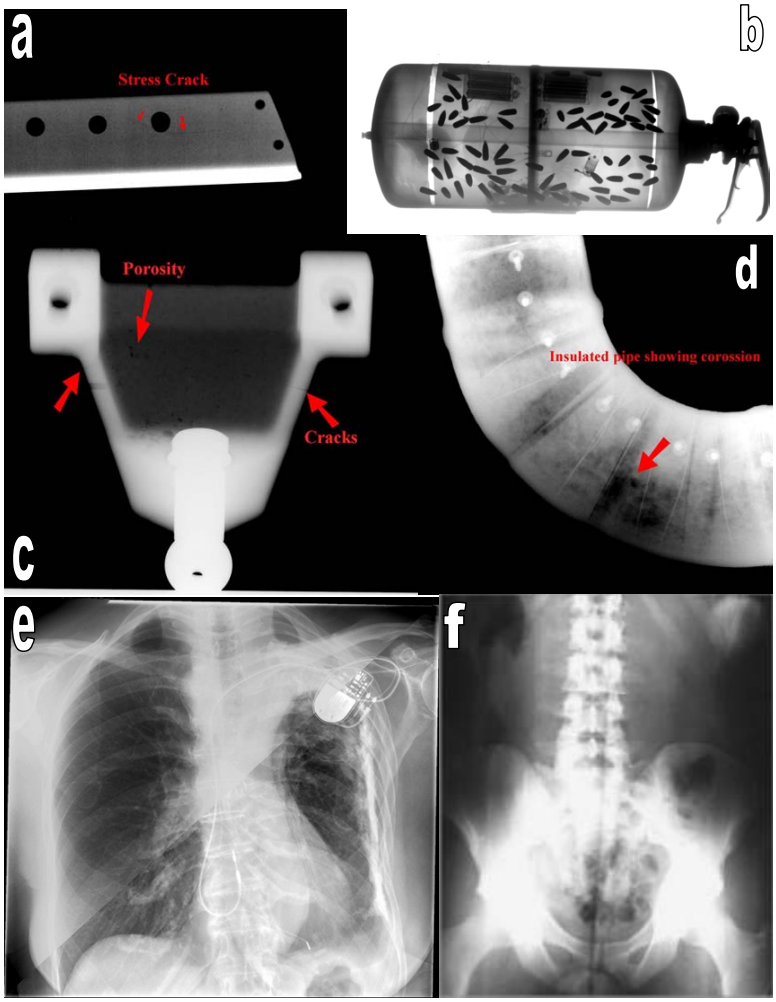

Figure A.3: X-ray images relative to the different applications.

The first diffraction patterns were recorded using the Laue method as soon as 1912. In 1913, the Braggs, father and son, published their explanation for diffraction by crystal planes which is the fundamental milestone of X-ray diffraction (XRD). After studying *simple* structures, scientists begin to study organic molecules in the 30's. One of the most striking results of X-ray diffraction is the determination of the structure of DNA. In any case, the information collected in such experiments is not easily interpreted. Nowadays, efficient algorithms exist in order to speed up the structure analysis. This will be discussed in the next section.

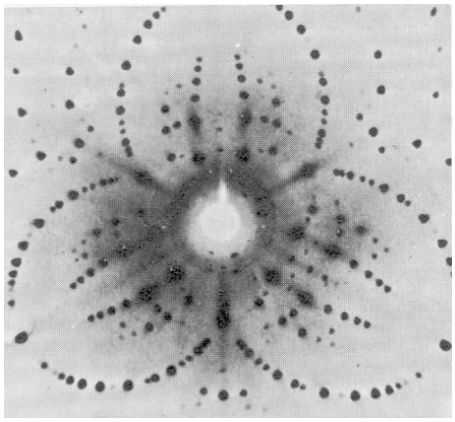

Figure A.4: The result of the Laue experiment of 1912.

X-ray absorption spectroscopy (XAS) begins in 1913 with the first evidence of an absorption edge given by Maurice De Broglie[168]. In 1920, Fricke and Hertz obtained the first structured spectra around the absorption edge. The theoretical contributions to the understanding of X-ray absorption begin with the works of Kronig [169] in 1931. In 1971, finally, the Fourier processing of the basic equations allows Sayers, Lytle and Stern [170] to write down the basic equation of EXAFS.

As mentioned above the spectrum emitted by a classical X-ray tube is resulting from a bremsstrahlung phenomenon. Sharp radiation peaks are also emitted when the electrons hit the target: they are the fluorescence peaks characteristic of the target material, as illustrated in figure A.5. Many experiments need a collimated and monochromatic beam. This drastically reduces

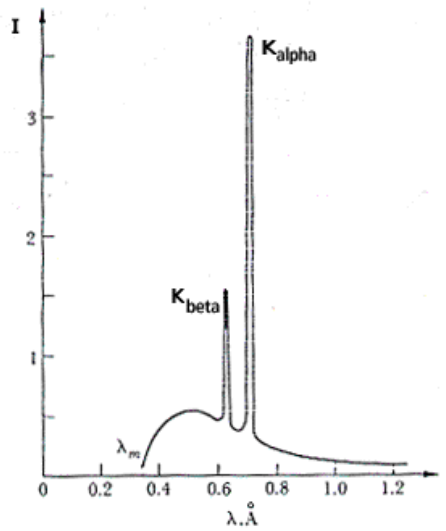

Figure A.5: Experimental spectrum from a X-ray tube

the number of photons available for the experiment. This is the reason why the fluorescence peaks of the target material are usually selected to work with : the choice of the wavelength is obviously limited in classical X-ray tubes. In order to improve the quality of data (signal to noise ratio, time resolved experiment, ...) it is also important to increase the intensity of the beam.

During the 70's, a very important step occured to produce an intense flux of collimated photons. The first generation synchrotron appeared. Synchrotron radiation is a generic term used to refer to an electromagnetic wave emitted by a relativistic electron placed in a magnetic field. This field induces a curvature of the electron trajectory which induces the emission of an electromagnetic wave. In synchrotron radiation facilities, bending magnets are used to produce such a magnetic field. Moreover, in third-generation synchrotrons, wigglers and undulators (complex periodic assemblies of magnets) are also used to produce such a radiation with even more efficiency and specific properties. Further details will be given in the next section. It is worth to note that new X-ray sources are now under development : the free electron laser should be applicable to also generate X-rays with a brilliance even higher than a third-generation undulator. They are based on the coherent emission of photons like in a classical laser.

A.2 Synchrotron radiation

Synchrotron radiation is currently the most efficient method to produce X-ray photons with a high brilliance. The basic principle of synchrotron radiation is simply the acceleration of an electron or a positron within a magnetic field. In such conditions the beam emitted by relativistic electrons is much more collimated than the one emitted by non-relativistic particles (see figure A.6). If the particles have an energy of $E = \gamma m_e c^2$, the curvature radius of the electron trajectory, ρ, is given by $\rho = \frac{m_e \gamma c}{eB}$. m_e is the rest mass of the electron. The typical opening angle of the instantaneous X-ray beam is $\frac{1}{\gamma}$.

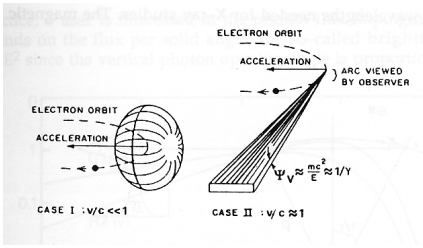

Figure A.6: Radiation shape from a non relativistic and relativistic particle. From the HERCULES courses.

Different parameters are used to describe the technical specifications of a synchrotron. The most important ones are introduced here. Characteristic values are given for the ESRF in the next section. Mathematical developments concerning the beam properties can be found in [171].

Brilliance Brilliance is one of the key parameters of synchrotron radiation. It is defined as the number of photons per second, per mrad^2 (i.e. vertical and horizontal angular divergence), per mm^2 (i.e. the source surface), per 0.1% of the bandwidth. This brilliance is maximised using third-generation undulators (see figure A.7). The ratio with the bandwidth is used to allow comparison between X-ray sources with a continuous spectrum and X-ray sources with a peak-structured spectrum. The divergence angle is defined by $\frac{1}{\gamma} = \sqrt{1 - \left(\frac{v_e}{c}\right)^2}$. Due to the electron trajectory, the radiation emitted from a bending magnet is only collimated in the direction perpendicular to the orbit plane (see figures A.8 and A.9).

In the case of wigglers, the electron oscillations within the device are quite large : the resulting radiation is the incoherent sum of the radiation emitted by the individual magnets ($I \approx 2N$ where N is the number of magnet magnet periods). In the undulator, the oscillation angle is close to or around the opening angle. In this case, the radiation emitted at

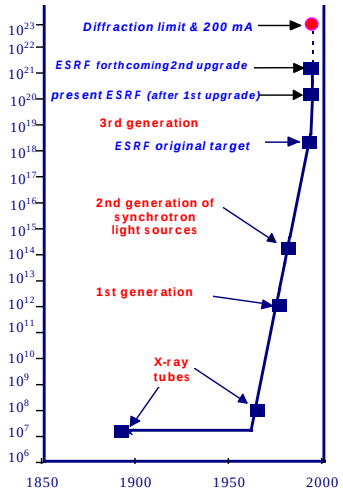

Figure A.7: Evolution of the brilliance since the X-ray discovery.

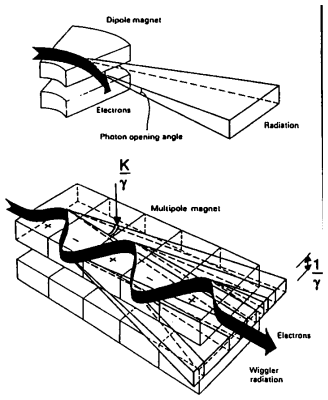

Figure A.8: Radiation shape from a bending magnet and wiggler.

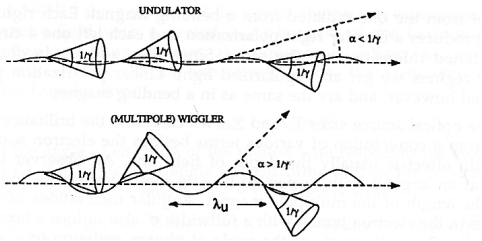

Figure A.9: Radiation shape from a wiggler and undulator.

each magnet interacts coherently resulting in a peak-shaped spectrum where the intensity of the radiation is proportional to N^2.

Critical wavelength , λ_c. Its expression is $\lambda_c = \frac{4\pi}{3}\frac{\rho}{\gamma^3}$. This critical value is defined as the value for which half of the total radiated power is radiated at higher frequencies and half at lower frequencies [1].

Electron lifetime The lifetime of the electrons, τ, in the storage ring is also important for the

[1] At the ESRF with a 6 GeV electrons : $\lambda_c = 0.5$.

user (it has a direct influence on the flux evolution with time $F(t) = F_0 e^{-t/\tau}$).

Polarization The X-ray beam produced by synchrotrons is polarized. This polarization allows to use X-rays for magnetic studies of matter. The X-ray beam from a bending magnet is polarized linearly in the orbital plane and elliptically below and above this plane. Insertion devices can be specifically designed to produce circular polarization allowing to perform circular dichroism experiments.

A.3 Interaction with matter

X-ray photons interact with electrons in matter using different basic principles. The X-ray energy considered in this work is lower than 100 keV. In this range, the following processes may occur.

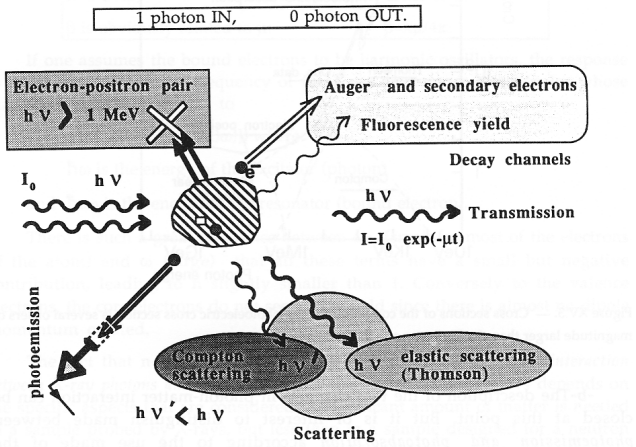

Figure A.10: Scheme of the interaction between X-rays and matter.

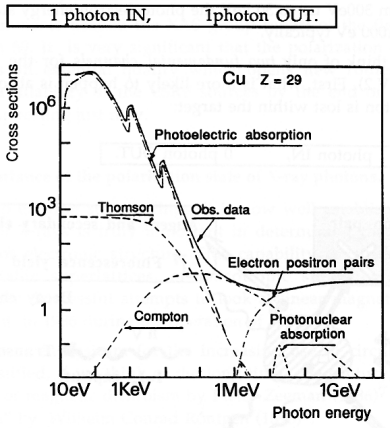

Figure A.11: Evolution of the components of the total cross sections (case of Cu) as a function of the incident photon energy.

Absorption X-ray photons can be absorbed by the electrons using different mechanisms. We can distinguish the photoelectric effect and pair production. During the photoelectric

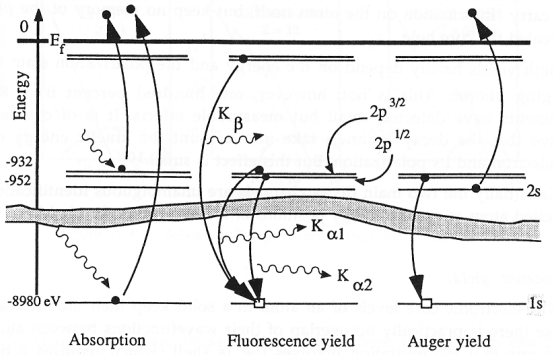

Figure A.12: Schematic diagram of the absorption process and decay channels.

absorption, one electron from the K, L, ... shell absorbs the incident photon energy and leaves the atomic shell with an energy ($E = E_{phot} - E_{K,L,...}$). The resulting hole in the atom is filled by an electron from the higher shells. This phenomenon also induces fluorescence. The fundamental parameter for the absorption process is the linear absorption coefficient, $\mu(E)$. Several discontinuities are observed in the evolution of the absorption coefficient as a function of incident energy; these discontinuities are called edges. The absorption coefficient around these edges can be modulated by an EXAFS signal depending on the structural environment of the atoms. This point is discussed later. The absorption process can be also accompanied by Auger electron production (see figures).

Scattering Scattering can be elastic (Thomson scattering) or inelastic (Compton scattering). As the wavelength of the X-ray is of the order of Angström, $\lambda[] = \frac{hc}{E} = \frac{12.398}{E[keV]}$, it is possible to obtain structural information at the atomic scale. Elastic scattering is the base of many different methods depending on the subject of interest (small angle scattering, diffraction, diffuse scattering, ...). Inelastic scattering between X-rays and electrons was originally described by Compton. The inelastic scattering of X-rays by phonons may also occur but these interactions uses very small energy differences. It is currently a challenging method to study crystal dynamics with X-rays.

Refraction As X-rays can be considered as a wave, they can be reflected and refracted. The refraction index of X-rays is imaginary and very close to 1. $n = 1 - \delta + i\beta$ where δ is about 10^{-5} in solids and only 10^{-8} in air. β is generally much lower than δ. These properties are the base of refractive optics (multilayer monochromator and focusing lenses). Reflection is also possible based on the classical total reflection process. The critical angle is simply given by $\alpha_c = \sqrt{2\delta}$.

Magnetic interaction The interaction of the magnetic field of the X-ray wave with the spin of the electrons is weak in comparison to the interaction with their charge (i.e. in the ratio $\frac{A_{mag}}{A_{elec}} = \frac{\hbar\omega}{mc^2}$). This is the reason why magnetic studies were for a long time limited to neutron experiments. However using the effect of the polarization state of the incident beam, X-rays become complementary to neutrons because they give rise to different selection rules. Linear and circular dichroism experiments are now daily performed at synchrotron facilities. Linear dichroism is the preferential absorption of one of the two orthogonal polarization states (such as polaroid sheets in the optical world). There is also the circular dichroism occurring in magnetic materials at X-ray wavelengths. XMCD is the study of

the absorption difference of right and left handed circularly polarized light. Working at the absorption edge makes the method element specific.

A.4 X-ray optics

At the beginning of X-ray discovery, it was thought that X-rays can not be refracted. Very soon, Von Laue discovered diffraction by monocrystals. This is the first step to Bragg optics. The goal of optics is to make the X-ray beam monochromatic and to focus it. Among the different optical elements we can find mirrors, monochromators (single crystals or multilayer) and lenses.

Mirrors Mirrors are flat or bent reflective surfaces. They are used as high energy cut-off and focusing device. By this way they allow to reduce the heat load (initially 100 W/mm^2) on the next single crystal monochromators. A coating is applied at the surface in order to improve the critical angle, $\theta_c(mrad) = 1.6\lambda()\rho^{\frac{1}{2}}(g/cm^3)$, 2.6 mrad for Pt. More complex designs, i.e. toroidal mirrors, allow to focalize along two axes.

Single crystal monochromators Single oriented crystals are used to select a single wavelength based on Bragg reflection.

Multilayer monochromators Multilayer monochromators are nanostructured assemblies of thin films based on Bragg's law to reflect a selected wavelength. It is a succession (period d) of different materials having very different density but low absorption coefficients. As this structure has a nanometer periodicity , it is possible to use them in the low energy X-ray range. Very complex designs (graded multilayer and curved graded multilayer) allow to also operate some optical manipulation on the beam such as divergence correction.

Lenses for X-rays can be based either on diffraction or refraction. Kumakhov and Snigirev designs are two illustrations of these techniques

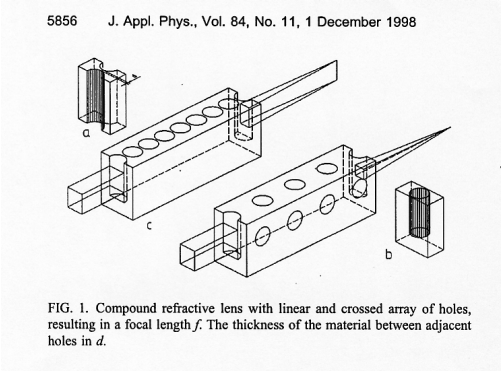

Figure A.13: Refractive lens.

A.5 X-ray diffraction

Crystals are invariant by translation. Each node is determined by a positional vector, $\vec{R_n} = n\vec{a_1} + m\vec{a_2} + l\vec{a_3}$. The three-dimensional structure of a crystal can be described using one of the 14 Bravais lattices. At each node of this network, we can associate a unit cell containing the minimal set of atoms. The complete symmetry information is summarized by the spacegroup associated with the structure. 230 different spacegroups do exist.

Diffraction can be performed either on monocrystals or on powders. In the first case, two methods exist : the Laue method and the rotating crystal method. The Laue method uses an incident white beam. The diffraction pattern obtained is thus made of points which give valuable information about the symmetry of the crystal. This method is still used to orient crystals. For the second method a monochromatic beam is used and the crystal is rotated around a given axis. During this rotation, reciprocal lattice nodes progressively enter in the Ewald sphere (1912) and diffraction peaks appear. In the framework of this thesis, powder diffraction is preferred as using monocrystals in high pressure cells is very complicated. Moreover, phase transitions usually induce the destruction of the crystal due to the large volume variation occurring at the transition.

Powder diffraction can be used either in the angular diffraction or in the energy dispersive method. The angular dispersive method is preferred. In this case, if the powder is well done (not to many preferential orientations and well grinded), the resulting spectra are made of diffraction rings. These rings are integrated in order to obtain the theta diagram. These diagrams are the signature of a given compound in a given structural phase.

Even if this method is basically less complete than monocrystal diffraction, it gives valuable information about structure, internal constraints, texture, ... Using the Rietveld method, it is possible to adjust a structural model to the experimental data using a minimization method (least-square method). If the energy-dispersive method is used, it is impossible to use the peak intensities. Thus the information collected is much more limited. In the 90's, image plates were introduced in high pressure experiments at synchrotron radiation facilities. These give impressive results : the angle dispersive method now allows to get high quality data (improved signal-to-noise ratio, preferred orientation studies, ...).

In 1912, the reciprocal lattice, $\{\vec{G}\}$, was introduced by Ewald in the diffraction description. If $\vec{k}$ and $\vec{k}'$ are respectively the incident and diffracted wave vectors, the diffraction condition is simply given by $\Delta\vec{k} = \vec{k}' - \vec{k} = \vec{G}$. The scattered amplitude is given by

$$A_{\vec{G}} = \sum_j \int_{unitcell} n_j(\vec{\rho}) e^{-i\Delta\vec{k}.\vec{\rho}} dV \tag{A.1}$$

where $\vec{\rho} = \vec{r} - \vec{r}_j$ is the positional vector related to the atom j and $n_j(\vec{\rho})$ is the electron density of each atom j in the periodic structure. If we define the atomic form factor, f_j,

$$f_j = \int n_j(\rho) e^{-i\vec{G}.\vec{\rho}} dV \tag{A.2}$$

and if the atoms are assumed to be at rest the diffracted amplitude becomes

$$S_{\vec{G}} = \sum_j f_j e^{-i\vec{G}.\vec{r}_j} \tag{A.3}$$

This structural factor clearly explains that some diffraction peaks are extinguished. The atomic form factor takes into account the electronic density but also thermal effects (Debye-Waller). It is thus necessary to add a factor that takes into account the uncertainty on the atomic positions due to the thermal motion. The structural factor is damped by an exponential factor. The corrective factor for the diffracted intensity is simply $e^{-\frac{1}{3}G^2<u^2>}$.

The diffracted intensity collected from a powder sample is thus the combination of this theoretical value and other instrumental parameters. The shape of the diffraction peaks is the convolution of three contributions

- distribution of the wavelength in the incident beam

- the technical specification of the optics
- the sample itself

Indeed some imperfections may induce modifications in the shape of the diffraction peaks

- Crystallite size : As the diffracting particles have a finite size, the nodes of the reciprocal lattice are no more punctual but they have a finite size. This induces a broadening of the diffraction peaks. The smaller the particles the wider are the peaks.
- Internal strain
- Crystalline defects

It is not an easy task to extract the complete structure. A systematical procedure is usually set up. The peak position is directly linked to the symmetry and the lattice parameters. The peak intensities allow to extract the atomic positions. Unfortunately overlapping of peaks and preferential orientations induce some complications. The R ietveld refinement method allows to extract the best-fitted set of structural parameters. It is based on the minimization of the following target function

$$M = \sum_{spectra} w_i (y_i - y_{ci})^2$$

using the least square method where

- w_i is the weight associated to the point i
- y_i is the observed intensity to the point i
- y_{ci} is the calculated intensity to the point i

This calculated intensity is given by

$$y_{ci} = y_{bi} + \sum_{\Phi=1}^{N_{phase}} S_\Phi j_{\Phi,hkl} L_{p,\Phi,hkl} O_{\Phi,hkl} \left|F_{\Phi,hkl}\right|^2 \Omega_{i,\Phi,hkl}$$

where

- y_{bi} is the intensity of the background at the point θ_i
- S_Φ is a scale factor proportional to the volume of the different phases
- $j_{\Phi,hkl}$ is the multiplicity of the diffraction related to the plane hkl of the phase Φ
- $L_{p,\Phi,hkl}$ is the common factor to the Lorentz and the polarization
- $O_{\Phi,hkl}$ takes into account of the preferred orientation
- $F_{\Phi,hkl}$ is the structural factor (Debye-Waller included)
- $\Omega_{i,\Phi,hkl}$ describes the peak profile (take into account of the instrumental aspects and the sample)

Different convergence parameters can be used in order to estimate the convergence but usually, we use

$$R_p = \frac{\sum_i |y_i - y_{ic}|}{\sum_i y_i} or R_{wp} = \sqrt{\frac{\sum_i w_i (y_i - y_{ci})^2}{\sum_i w_i y_i^2}}$$

It is important to have a sufficient amount of crystallites in order to obtain a good statistical distribution of the crystallites. In this case continuous rings are obtained In the case of the dispersive energy method, the incident beam is polychromatic. Depending on the energy, the reflective angles are depending on this incident energy. In this case, the reflections are collected in only one direction. Thus, preferred orientation is absolutely not taken into account.

EXAFS and XANES

The EXAFS[171] [2] and XANES[3] methods allow to study the local structure of matter. This can be understood by the basic principle of EXAFS. A core photoelectron is emitted by the absorption of an X-ray photon. This electron is scattered by the neighbouring atoms of the emitting atom. The interference between the emitted and scattered wavefunction is visible in the experimental absorption spectrum in the region just after the absorption edge. To be fully correct, the energy region close to the absorption edge is called XANES followed by the EXAFS region. XANES gives information about multiple scattering events. Indeed the free mean path of electrons in matter decreases with kinetic energy. These methods are thus a very efficient method to look at the local structure. Moreover due to the use of absorption edges, it is possible to select the target-atom in the structure.

Within the approximation of one electron, the absorption in a solid μ is defined by the Golden Fermi rule

$$\mu \approx \sum_f | < \phi_f | \epsilon.\mathbf{r} | \phi_\mathbf{i} > |^\mathbf{2} \delta(\mathbf{E_f} + \mathbf{E_i} - \hbar\omega) \tag{A.4}$$

where ϕ_i and ϕ_f are respectively the initial and final states with energies, E_f and E_i ϵ is the polarization vector of the X-ray beam used.

The basic EXAFS signal is defined by

$$\chi(k) = \frac{\mu(k) - \mu_0(k)}{\mu_0(k)} \tag{A.5}$$

where μ_0 is the absorption due to an isolated atom. From experimental data, the $\chi(k)$ can be extracted by quite simple mathematical operations.

The basic equation used to analyze the EXAFS spectra is

$$\chi(k) = -\frac{1}{k} \sum_j 3cos^2(R_j, \epsilon) \frac{|f_j(\pi, k)|}{R_j^2} sin(\Phi_j) e^{-2\sigma^2 k^2} e^{-\frac{r_j}{\lambda(k)}} \tag{A.6}$$

where $\Phi_j = 2kR_j + 2\delta_l + \theta_j$ and $\theta_j = arg(f(\pi, k))$. j is the index of each neighbour located at R_j and which contribute to the EXAFS signal. Moreover $f_j(\pi, k)$ is the intensity of the back-scattered radiation; it is a complex number

$$f_B(\pi, k) = \frac{1}{2ik} \sum_l (2l+1)(e^{i2\delta_l} - 1) P_l(cos\theta = -1) \tag{A.7}$$

[2] Extended X-ray Absorption Fine Structure

[3] X-ray absorption Near-Edge Structure

δ_l is the phase shift and P_l is a Legendre polynomial.

After few developments, the EXAFS formula can be established :

$$\chi(k) = \frac{m}{2\pi h^2 k^2} \sum_i N_i \frac{t_i(2k)}{R_i^2} e^{-2k^2\sigma_i^2 - 2\frac{R_i}{\lambda}} sin[2kR_i + \delta_i(k)] \tag{A.8}$$

The fit of the experimental data with a structural model gives the values of structural parameters. The information that EXAFS allows to give is mainly : local interatomic distances, number of first (up to second in good conditions) neighbours and their chemical nature and Debye-Waller factors. XANES gives more qualitative information. Indeed no exact theory exists to directly extract structural information from this signal. Usually, simulated spectra are calculated using candidate structures. The resulting spectra are compared with the actual ones. It allows to distinguish different oxydation states and to obtain a qualitative picture of the electronic density of states.

A.6 Experimental set-up

A.6.1 The ESRF

The ESRF was the first third-generation synchrotron built in the world. It was opened to the experimental users in 1994. Nowadays, other similar sources exist in the world: APS (Advanced Photon Source) in the USA, Spring8 in Japan, ...

The annual budget of the ESRF is 74.000 kEUR in 2004. Belgium takes part to this budget within the Benesync consortium. The annual contribution is 6%. The other countries which are members of the ESRF project are France (27.5 %), Germany (25.5 %), Italy (15 %), United Kingdom (14 %), Spain (4 %), Switzerland (4 %) and Nordsync composed of Denmark, Finland, Norway and Sweden (4 %). Several other countries gives small contributions (Portugal, Israel, Austria, Poland, Czech Republic and Hungary).

The electrons are first accelerated in a linear accelerator. After they enter in a booster which gives them their final energy, 6 GeV before injection in the storage ring. The electrons in the storage ring are grouped in bunches. The arrangement of these bunches along the storage ring depends on the filling mode.

- single bunch : 20 mA for a lifetime of 6 hours. In this mode, a single electron bunch is inserted in the storage ring. This is interesting for time-resolved experiments.
- 16 bunches : 90 mA for a lifetime of 9 hours
- continuous : 200 mA for a lifetime of 75 hours; 992 electron bunches uniformly placed around the storage ring
- 2 times one-third filling mode : 200 mA 75 hours
- hybrid mode : one third filling and a single bunch diametrally opposed

A.6.2 ID24

ID24 is designed mainly for the dispersive EXAFS method. In this case, it is possible to collect a complete EXAFS spectrum simultaneously. The complete spectrum is concentrated in a single point (the sample position) and then dispersed on a linear detector (see beamline schematics). ID24 was developed for two main applications : studies of sub-second chemical reactions (about

50 % of the application time), for high-pressure studies using diamond anvil cells and for magnetic circular dichroism (both of these are the other part of the application time).

The optics of ID24 is composed of a succession of a vertical focalization mirror, a demagnification mirror, a Bragg or Laue polychromator and a vertical re-focalisation mirror [172]. The sample is placed at the focal spot which is determined by the choice of the polychromator crystal Si(111), Si(220) or Si(311). It can be as small as 5 μm by 5 μm FWHM. The energy resolution is of the order of $\frac{\Delta E}{E} = 10^{-4}$. The energy range available on this beamline is between 5 and 28 keV.

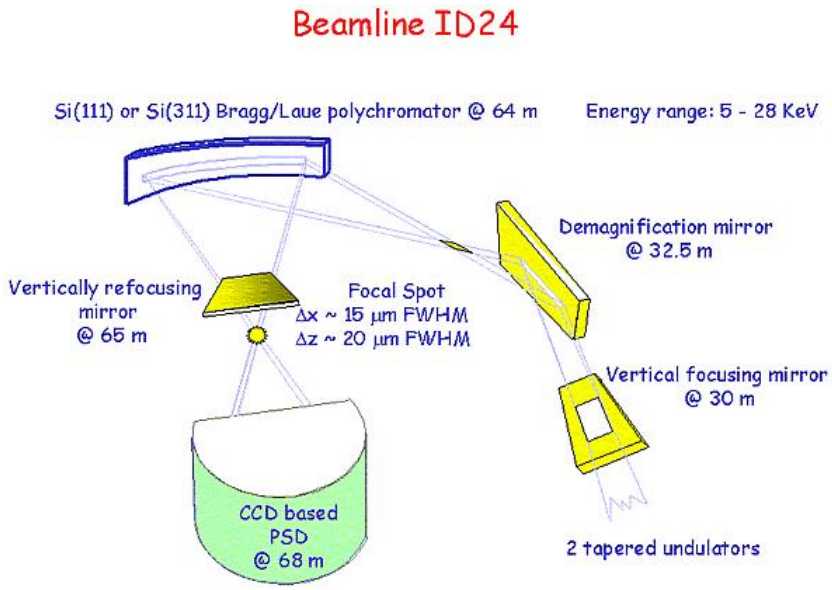

Figure A.14: Layout of the ID24 beamline optics.

ID24 is located on a undumator straight section of the storage ring. Usually XAS[4] uses bending magnet thanks ot the intrinsic large beam divergence. Indeed it is important to have a large beam footprint on the curved polychromator in order to obtain a dispersion in a wide energy range for EXAFS studies.

However, the advantages of the undulator are clear, leading to a small spot to a more efficient reduction of the unwanted harmonics, and to higher brilliance.

A.6.3 ID27

ID27 beamline - formerly ID30 - is created for extreme condition studies. The main properties of the beam in this special case are the high collimation and the high flux. This is the reason why three insertion devices were used. The resulting beam is 15 μm x 15μm. This is particularly well suited for the study of very small samples with "heavy" sample environment. The typical applications are : geophysics studies (Fe, Ni alloys, ...), synthesis of materials under pressure, low temperature experiments, light element studies (hydrogen), ultrahard materials(BN, C_{60}, ...), ...

ID27 uses 3 insertion devices : 2 undulators (in this case, is it possible to increase further more the flux by using resonance phenomena occuring between these two undulators) and a wiggler. The two undulators are mainly used for ADX at 30 keV. The wiggler is more used for higher

[4] X-ray Absorption Spectroscopy

energies, up to 150 keV. After these insertion devices, a water-cooled silicon monochromator and two curved mirrors allows to focalize the beam in the two planes. The detector is based on an image-plate inducing to us a two dimensional view of the diffraction rings : this allows a much better intergration along the rings but also the study of preferred orientations, ...

The methods used on this beamline are mainly high resolution powder angular diffraction using diamond anvil cells (75 %) or the large volume press (25 %).

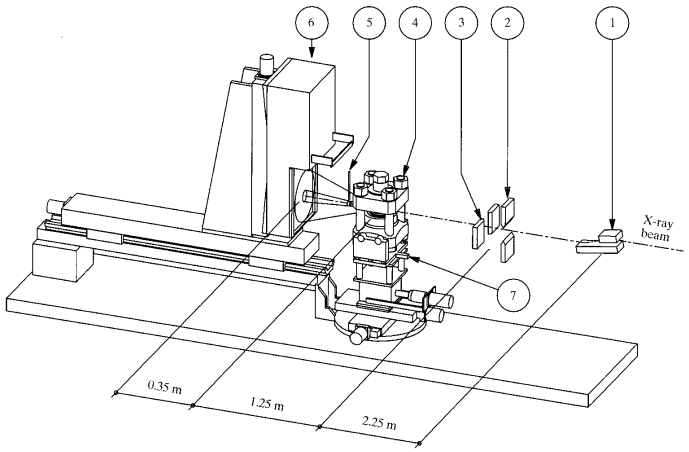

Figure 1
Layout of the high-pressure beamline ID30 at the European Synchrotron Radiation Facility (ESRF) in large-volume press configuration. 1: Si(111) channel-cut monochromator; 2–3: tungsten carbide slits, horizontal and vertical limits; 4: Paris–Edinburgh large-volume press; 5: beam stop; 6: fast-scan detector.

Figure A.15: Layout of the ID30 beamline: (1) Si(111) channel-cut, (2)-(3) tungsten carbide slits - horizontal and vertical limits, (4) Paris-Edinburgh large-volume press, (5) beam stop and (6) Fast-scan detector.

Appendix B

Low-order moment method.

B.1 Fundamental approximations

The models presented all along this thesis are mainly based on a set of approximations related to the tight binding method. They can be summarized as follows:

- *The Born-Oppenheimer approximation* : no electron-phonon interactions are taken into account;
- *The one-electron approximation* : the correlation effects are thus ignored. As it will be shown later, a correction term can be added in order to take into account of these effects if necessary. The electrons are moving in an effective potential which is simply the addition the kinetic energy and of atomic potentials, V_i.

$$H_{el} = T + \sum V_i(\vec{r} - \vec{R}_i) \tag{B.1}$$

  These potentials will not be determined self consistently : the parametrization of the related matrix elements is discussed below;
- The electronic wavefunction of the system is expanded on *a basis of atomic orbitals* (s and/or p in the considered cases):

$$\psi_n = \sum_{i,\lambda} a^n_{i,\lambda} \Phi_{i,\lambda} \tag{B.2}$$

  where λ is the degenerancy of the atomic orbital and i the atomic site. The coefficients $a^n_{i,\lambda}$ are solutions of the following equation set.

$$det|H_{i\lambda,j\mu} - E_n S_{i\lambda,j\mu}| = 0 \tag{B.3}$$

  where

$$H_{i\lambda,j\mu} = < \Phi_{i,\lambda}|H_{el}|\Phi_{j,\mu} > \tag{B.4}$$
$$S_{i\lambda,j\mu} = < \Phi_{i,\lambda}|\Phi_{j,\mu} > \tag{B.5}$$

- The atomic orbitals are supposed to *be orthogonal to each other*;
- *The two-center approximation* : the matrix elements involving more than two sites (i and j) are neglected, i.e. terms similar to $< \Phi_{i,\lambda}|V_j|\Phi_{i,\mu} >$ is supposed to be 0;

- *the spin-orbit interaction is neglected.*

The last three approximations are used to improve the transparency of the model but they are obviously not mandatory to perform any LCAO studies.

Using the above approximations, the hamiltonian of the system is now simply given by

$$H = -\frac{\hbar^2}{2m}\Delta + V_j(\vec{r} - \vec{R}_j) + \sum_{k \neq j} V_k(\vec{r} - \vec{R}_k) \tag{B.6}$$

If you consider the atomic orbital located in j, the first two terms are related to its atomic state and the latter is related to the effect of the lattice. The potentials v_i can be different at each atomic site i. As the atomic orbitals $\Phi_{j,lambda}(\vec{r} - \vec{R}_j)$ are the solutions of the free atoms. This allows to define the electronic levels $E^0_{j\lambda}$ using

$$\left[-\frac{\hbar^2}{2m_e}\Delta + V_j\right] |\Phi_{j,\lambda}> = E^0_{j\lambda}|\Phi_{j,\lambda}> \tag{B.7}$$

It is also important to define two kinds of hamiltonian matrix elements :

$$\alpha_{i\lambda,i\mu} = <\Phi_{i,\lambda}| \sum_{j \neq i} V_j |\Phi_{i,\mu}> \tag{B.8}$$

$$\beta_{i\lambda,j\mu} = <\Phi_{i,\lambda}|V_i|\Phi_{j,\mu}> \tag{B.9}$$

The first one is called crystal field integral and the second the resonance (or hopping or transfer)integrals. $\alpha_{i\lambda,i\mu}$ make the atomic levels deeper. As they are much weaker than the resonance integrals, they usually can be neglected in the cases tackled in this thesis.

$\beta_{i\lambda,j\mu}$ integrals are also neglected if sites i and j are not first neighbours. The mathematical description of $\beta_{i\lambda,j\mu}$ is obviously very important as it is one of the main contributions to the cohesive energy. Salter and Koster describes the $\beta_{i\lambda,j\mu}$ terms as a function of the nature of orbital overlap, i.e. $ss\sigma$, $pp\pi$, ... As we only study $s-p$ orbital based solids, the set of possible interactions is limited. The related mathematical expressions are given in the table B.1.

Based on these expressions it is now necessary to describe to coefficients $\beta_{..}$. They are obviously dependant on the interatomic distance. Harrison set up a simple relation concerning the distance dependance of the resonance integral :

$$\beta_{..}(r) = \eta_{..}\frac{\hbar^2}{m} r^{-2} \tag{B.10}$$

where $\frac{\hbar^2}{m} = 7.62\ eV/\ \text{Å}^2$. Heine demonstrates a similar result : $\beta_{..}(r) \approx r^{-l+l'+1}$ where l and l' are the degenerancy of the orbitals. The values of the $\eta_{..}$ coefficients can be extracted from the electronic band structures, for example. Nevertheless in this thesis we prefer to use the universal parameters determined by Harrison (see table B.2) as our goal is to study trends within the whole periodic table. However, when we have experimental results in hand, we will fit the theoretical model in order to evaluate the difference between the actual and universal values of the coefficients.

$E_{s,s}$	$\beta_{ss\sigma}$
E_{s,p_x}	$\beta_{sp\sigma}$
$E_{p_xp_x}$	$l^2\beta_{pp\sigma} + (1-l^2)\beta_{pp_\pi}$
$E_{p_xp_y}$	$lm\beta_{pp\sigma} - lm\beta_{pp_\pi}$
$E_{p_xp_z}$	$ln\beta_{pp\sigma} - ln\beta_{pp_\pi}$

Table B.1: Slater and Koster description [173] of the resonance integral for s and p interactions. l, m and n are the coefficients of the vector between the site of the two orbitals.

$\eta_{ss\sigma}(eV^2)$	$\eta_{sp\sigma}(eV^2)$	$\eta_{pp\sigma}(eV^2)$	$\eta_{pp\pi}(eV/^2)$
-1.40	1.84	3.24	-0.81

Table B.2: Tight-binding parameters following Harrison

B.2 Harrison's description of diamond and zinc-blende structures

Harrison gave a very efficient tight-binding description of tha band structure of the tetrahedral semiconductors [174, 175]. As this model is one of the starting points of our own work, it is very interesting to describe it with more attention.

Group-IV and III-V semiconductors exhibit a fourfold coordinated under ambient conditions. This geometrical configuration can be efficiently described using sp^3 hybrids. These hybrid orbitals are simply a linear combination of the s and p orbitals in order to obtain the directionality of the bond which is observed experimentally :

$$|sp^3,1> = \frac{1}{2}\left(|s>+|p_x>+|p_y>+|p_z>\right) \quad \text{(B.11)}$$

$$|sp^3,2> = \frac{1}{2}\left(|s>-|p_x>+|p_y>-|p_z>\right) \quad \text{(B.12)}$$

$$|sp^3,3> = \frac{1}{2}\left(|s>-|p_x>-|p_y>+|p_z>\right) \quad \text{(B.13)}$$

$$|sp^3,4> = \frac{1}{2}\left(|s>+|p_x>-|p_y>-|p_z>\right) \quad \text{(B.14)}$$

The hybrid energy level is also defined to be $\epsilon_h = \frac{\epsilon_s+3\epsilon_p}{4}$. As we consider two different atomic species, two sets of the previous sp^3 orbitals exist. To be concise, they will be written $|aj>$ and $|cj>$, for the anion and cation respectively. j is related to the direction of the orbital.

As the hybrid sp^3 levels of the anion and cation are not similar a charge transfer from the cation (c) to the anion (a) occurs. The parameter set is thus

$$\epsilon_a = <aj|H|aj> \quad \text{(B.15)}$$

$$\epsilon_c = <cj|H|cj> \quad \text{(B.16)}$$

$$V_1^a = -<aj|H|aj'> \quad \text{(B.17)}$$

$$V_1^c = -<cj|H|cj'> \quad \text{(B.18)}$$

$$V_2 = -<cj|H|aj> \quad \text{(B.19)}$$

$$V_3 = \frac{1}{2}(\epsilon_h^c - \epsilon_h^a) \quad \text{(B.20)}$$

Based on this description, Harrison defined the metallic energy, $V_1^{a,c}$, the hybrid covalent energy, V_2, and the hybrid polar energy, V_3. It is easy to show that

$$V_1^{a,c} = -\frac{1}{4}(\epsilon_p^{a,c} - \epsilon_s^{a,c}) \quad \text{(B.21)}$$

$$V_2 = \frac{-\beta_{ss\sigma} + 2\sqrt{3}\beta_{sp\sigma} + 3\beta_{pp\sigma}}{4} \quad \text{(B.22)}$$

The separation of the bonding and anti-bonding hybrid levels is given by $2\sqrt{V_2^2+V_3^2}$.

If the bonding orbital is assumed to be $|b>= u_a|aj> + u_c|cj>$, we can calculate the stable state by minimizing $<b|H|b>$:

$$u_a = \sqrt{\frac{1}{2}(1+\alpha_p)} \tag{B.23}$$

$$u_c = \sqrt{\frac{1}{2}(1-\alpha_p)} \tag{B.24}$$

$$\tag{B.25}$$

with the polarity, α_p, defined by

$$\alpha_p = \frac{V_3}{\sqrt{V_2^2 + V_3^2}} \tag{B.26}$$

Moreover, Harrison showed that the ionicity of the Philips and Van Vechten, f_i, can be related to the polarity, α_p using

$$f_i = 1 - (1-\alpha_p^2)^{\frac{3}{2}} \tag{B.27}$$

Taken into account the expression of $u_{a,c}$, the charge on the electronegative atom writes $4\alpha_p - \Delta Z$ with $\Delta Z = 0$, 1, 2 or 3 for IV, V, VI and VII column element, respectively.

B.3 Cohesive energy calculation

Competition between structures when pressure is applied is driven by their enthalpy, $H = E + PV$. The calculation of the energy, E, as a function of volume is thus the very first step to the theoretical high pressure studies. In our tight-binding description of covalent and low ionic materials, the main contributions are :

1. *promotion energy*, E_{promo} : one of the s electron has to be promoted to the p level in order to form the sp_3 orbital. This induces an energetic cost, E_{promo}.

2. *atomic repulsion*, E_{rep} : this term takes into account of the Pauli principle and the electrostatic interactions of the electrons

3. *orbital interaction*, E_{attr} : this is energy coming from the creation of the electronic bands depending on the filling factor.

$$E_{tot} = E_{promo} + E_{rep} + E_{attr} \tag{B.28}$$

The repulsive contribution is chosen to arise from a simple additive pairwise repulsive potential, V_r, varying like an inverse power of the interatomic distance:

$$V(r_{ij}) = V_0 r_{ij}^{-p} \tag{B.29}$$

where p is directly linked to the hardness of the repulsive interaction. The repulsive energy is thus simply given by the addition of the repulsion contributions arising from the first shell of neighbours.

$$E_{rep} = \frac{1}{2}\sum_{i \neq j} V(r_{ij}) \tag{B.30}$$

From the Harrison's model, the promotion energy in a tetrahedral semiconductor is given by

$$\left(1 + \frac{\Delta Z}{4}\right) V_1^c + \left(1 - \frac{\Delta Z}{4}\right) V_1^a \tag{B.31}$$

If we consider only the discrete levels induced by the bonding (see the second moment approximation described in the next section), the cohesive energy per bond is then given by the following equation for the diamond and zinc-blende

$$E_{coh} = 2\sqrt{V_2^2 + V_3^2} - \frac{\Delta Z}{4}(2V_3 + \delta_a - \delta_c) - \delta_a - \delta_c + E_{rep} \tag{B.32}$$

where $\delta_{a,c} = \epsilon_p^{a,c} - \epsilon_s^{a,c}$ Within this approximation level, the calculation of E_{attr} is quite simple. This is obviously not always the case and a more accurate description of the electronic density of states is often necessary. This point is addressed in the next section.

B.4 Description of the electronic density of states

In the present work, we will focus on the cohesive energy calculation in order to study competitive structures. As stated in the previous section, one of the most important contribution is comes from the resonant electronic interactions between atoms generating the electronic band structure.

$$E_{attr} = \int_{-\infty}^{E_F} n(E) E dE \tag{B.33}$$

The band structure is efficiently described within the reciprocal space which often induces quite a lot of computational effort. As we are only interested in integral expression of the electronic density of states, $n(E)$, it would be interesting to use a method which does not require to calculate the complete density of states first.

It can be shown that the Green's function of the Hamiltonian defined by

$$R(z) = (z - H)^{-1} \tag{B.34}$$

is directly linked to the electronic density of states

$$n(E) = -\frac{1}{\pi} \lim_{\substack{\epsilon \to 0+ \\ z = E + i\epsilon}} \Im Tr(R(z)) \tag{B.35}$$

Reciprocally, it is possible to get the trace of the Green's function of the Hamiltonian using the Hilbert transform of the density of states

$$TrR(z) = \int_{-\infty}^{+\infty} \frac{n(E)}{z - E} dE \tag{B.36}$$

Moreover, if we focus on the local density of states to get information about charge transfer, for example, the same relations still exists for the atomic orbital $|\Phi_{i,\lambda}>$.

$$n_{i,\lambda} = -\frac{1}{\pi} \lim_{\substack{\epsilon \to 0+ \\ z = E + i\epsilon}} \Im < \Phi_{i,\lambda} | R(z) | \Phi_{i,\lambda} > \tag{B.37}$$

$$< \Phi_{i,\lambda} | R(z) | \Phi_{i,\lambda} > = \int_{-\infty}^{+\infty} \frac{n_{i,\lambda}(E)}{z - E} dE \tag{B.38}$$

It is now clear that the calculation of the Green's function of the Hamiltonian is the solution in order to avoid the step within the reciprocal state. Two methods exist to perform such a task: the method of moments and the recursion method. The first is very convenient when physical mechanism are under study whereas the latter is the most suited method for computational processing. Both of them allows to get successive approximations of the electronic density of states.

B.4.1 Method of moments

Come back first on the definition of the n^{th} order moment of a function $f(t)$:

$$\mu_n = \int t^n f(t) dt \tag{B.39}$$

If the whole set of moments of a function is know, the function is completely defined

$$f(t) = \sum_{n=0}^{\infty} \frac{(-it)^n}{n!} \mu_n \tag{B.40}$$

At a large distance from the eigenvalues of the Hamiltonian, it is possible to develop diagonal elements of its Green's function as a function of the inverse powers of z.

$$R_i(z) = \left\langle i \left| \frac{1}{z - H} \right| i \right\rangle = \frac{1}{z} + \frac{H_{ii}}{z^2} + \frac{H_{ii}^2}{z^3} + \dots \tag{B.41}$$

If this expression is compared to the following expansion of equation B.38

$$R(z) = \int_{-\infty}^{+\infty} \left(\frac{1}{z} + \frac{E}{z^2} + \frac{E^2}{z^3} + \dots \right) n_{i,\lambda}(E) dE = \frac{\mu_0}{z} + \frac{\mu_1}{z^2} + \frac{\mu_2}{z^3} + \dots \tag{B.42}$$

From these two expressions, it is clear that the p^{th} moment of the local density related to $|\Phi_{i,\lambda}>$, $\mu_{(p,i\lambda)}$, is simply the the diagonal element of the p^{th} power of the Hamiltonian related to the orbital λ on site i.

$$\mu_{p,i\lambda} = \int_{-\infty}^{+\infty} E^p n_i(E) dE = (H^p)_{i\lambda,i\lambda} = \sum_{i_1,\dots,i_{p-1}} H_{ii_1} H_{ii_2} \dots H_{ii_{p-1}} \tag{B.43}$$

This last expression gives the geometrical interpretation of the p^{th} moment : the sum of the whole set of closed pathes of length p starting and ending at site i. Each of the first moments have their physical meaning:

- μ_0 is the norm of the density of states, $n(E)$. It is often equal to 1 which is usually the normalization of the density of states.
- μ_1 gives the gravity center of the density of states; if the origin is chosen cleverly, it is possible to get $\mu_1 = 0$.
- $\mu_2 - \mu_1^2$ is the variance of $n(E)$ which is proportional to the width of the electronic density of states (eDOS);
- $\frac{\mu_3}{\mu_2^{\frac{3}{2}}}$ gives a measurement of the asymmetry of the eDOS; it is zero if the density is symmetrical;
- $\frac{\mu_4\mu_2 - \mu_3^2 - \mu_2^3}{\mu_2^3}$ says if the density of states is unimodal or bimodal;
- ...

The very first moments allows to get a very good knowledge of the cohesive energy as it is an integral function of the electronic density of states. However, it is more complicated to get the density of states itself. Indeed relation B.42 is not practical as the series expansion of $R(z)$ is not convergent for values of z around the eigenvalues of the hamiltonian. This series is thus written as a continued fraction. This is a way to perform an analytical continuation within the complex plane.

$$R(z) = \cfrac{b_0^2}{z - a_1 - \cfrac{b_1^2}{z - a_2 - \cfrac{b_2^2}{z - a_3 - \dots}}} \tag{B.44}$$

where (a_i, b_i) are given by

- $a_1 = \mu_1$
- $b_1 = \mu_2 - \mu_1^2$
- $a_2 = \frac{\mu_3 - \mu_2 a_1 - \mu_1 b_1}{b_1}$
- $b_2 = \frac{\mu_4 - \mu_3(a_1+a_2) - (b_1 - a_1 a_2)\mu_2}{b_1}$
- $\dots$

or more generally

- $a_i = \frac{1}{\Delta'_{i-2}\left[\frac{\Delta_{i-2}\Delta'_{i-1}}{\Delta_{i-1}} + \frac{\Delta_{i-1}\Delta'_{i-3}}{\Delta_{i-2}}\right]}$
- $b_i = \frac{\Delta_i \Delta_{i-2}}{\Delta_{i-1}^2}$

where

$$\Delta_i = \begin{vmatrix} \mu_0 & \mu_1 & \cdots & & \mu_i \\ \mu_1 & \mu_2 & \cdots & & \mu_{i+1} \\ \vdots & & & & \vdots \\ & & & \ddots & \ddots & \\ & & & \ddots & \\ \mu_i & \mu_{i+1} & & & \mu_{2i} \end{vmatrix}$$

and

$$\Delta'_i = \begin{vmatrix} \mu_0 & \cdots & & \mu_{i+1} \\ \mu_1 & \cdots & & \mu_{i+2} \\ \vdots & & & \vdots \\ & & \ddots & \ddots & \\ & & \ddots & \\ \mu_{i+1} & \mu_{i+2} & & \mu_{2i+1} \end{vmatrix}$$

Therefore the a_i and b_i coefficients are directly linked to the moments of the density of states. The first moments of the density of states are quite easy to calculate "'by hand"' using their geometrical interpretation. Unfortunately, it is not so easy for moments of higher order. In the case of computational approach, it becomes interesting to switch to the recursion method described in the next section.

B.4.2 Recursion method

As mentioned in the previous section, it is possible to reconstruct the electronic density of states and its moments using a mathematical method : the recursion method. It allows to build up a tridiagonal matrix from the Hamiltonian by an recursive procedure, the Lanczos algorithm. The elements of the resulting tridiagonal matrix are the coefficients of the continued fraction.

$$H_{TD} = \begin{pmatrix} a_1 & \sqrt{b_1} & 0 & 0 & ... & 0 & 0 \\ \sqrt{b_1} & a_2 & \sqrt{b_2} & 0 & & & \\ 0 & \sqrt{b_2} & a_3 & \sqrt{b_3} & & & \\ 0 & 0 & \sqrt{b_3} & \ddots & \ddots & & \\ & & & \ddots & & & \\ & & & & & & \\ & & & & & & \end{pmatrix} \tag{B.45}$$

The H_{TD} is simply the original hamiltonian represented in a new basis. It is equivalent to a semi-infinite linear chain of atoms. The initial vector of the Lanczos process is chosen to be $|\psi_{i\mu}>$ which is the atomic orbital where we want to calculate the local density of states. The generated vectors are $|\Phi_j>$, thus the iterative vectors are

$$|\Phi_1> = |\psi_{0,0}> \tag{B.46}$$
$$\sqrt{b_1}|\Phi_2> = H|\Phi_1> - a_1|\Phi_1> \tag{B.47}$$
$$\dots \tag{B.48}$$
$$\sqrt{b_n}|\Phi_{n+1}> = (H - a_n)|\Phi_n> - \sqrt{b_{n-1}}|\Phi_{n-1}> \tag{B.49}$$

with

$$a_n = <\Phi_n|H|\Phi_n> \tag{B.50}$$
$$\sqrt{b_{n-1}} = <\Phi_{n-1}|H|\Phi_n> \tag{B.51}$$

These conditions allow to keep the new basis vectors orthogonal and normalized to each other.

B.4.3 Truncation of the continued fraction

In order to practically calculated the density of states, it is mandatory to truncate the continued fraction. This operation can be very delicate depending on the shape of the actual density of states. If the support of the density of states is connex, the coefficients of the continued fraction converge to a finite value and it is quite easy to manage the calculation of the density of states as illustrated in the appendix on the simple case of dimerized linear chain. At the opposite, if the support is not connex, i.e. if there is a gap, the convergence of the continued fraction coefficients is more complex. The continuation of continued fraction has an undamped oscillatory behaviour. A possible is to approximate the asymptotic behaviour of the continued fraction coefficients by suitable oscillatory functions. A complete study of the different methods of continuation of the continued fraction is presented by Turchi et al.[176]. In any case, the evaluation of the gap width has to be performed very carefully.

B.5 Linear chain of atoms

The electronic density of states can be easily determined in the case of a linear chain of atoms using the resolvant. If we consider the case of a distorted chain with one short and one long distance, the two interactions can be named β_s and β_l, respectively.

$$\Re(z) = \cfrac{1}{z - \cfrac{\beta_s^2}{z - \cfrac{\beta_l^2}{z - \cfrac{\beta_s^2}{z - \dots}}} - \cfrac{\beta_l^2}{z - \cfrac{\beta_s^2}{z - \cfrac{\beta_l^2}{z - \dots}}}} \tag{B.52}$$

As this fraction has a periodic part, it could also be written

$$\Re(z) = \cfrac{1}{z - \Sigma - \cfrac{\beta_l^2}{z - \Sigma}} \tag{B.53}$$

where

$$\Sigma = \cfrac{\beta_s^2}{z - \cfrac{\beta_l^2}{z - \Sigma}} = \frac{\beta_s^2 (z - \Sigma)}{z^2 - z\Sigma - \beta_l^2} \tag{B.54}$$

Thus Σ is simply given by the following second order equation

$$\Sigma = \frac{z^2 - \beta_l^2 + \beta_s^2 \pm \sqrt{(z^2 - \beta_l^2 + \beta_c^2)^2 - 4z^2\beta_s^2}}{2z} \tag{B.55}$$

As the density of states, $n(E)$, is defined by $n(E) = -\frac{1}{\pi} \Im \lim_{\epsilon \to 0} \Re(E + i\epsilon)$ it will be non-zero only if $\Re$ has an imaginary part. Based on the relation (B.55), this imaginary part exists if

$$\left| E^2 - \beta_l^2 + \beta_s^2 \right| < 2 \left| E \beta_s \right| \tag{B.56}$$

Therefore the density of states is non-zero between $-\beta_s - \beta_l$ and $-\beta_s + \beta_l$, and $\beta_s - \beta_l$ and $\beta_s + \beta_l$. Therefore as $\beta_s > \beta_l$, a gap exist in the electronic density of states as long as the structure is distorted. The gap value is simply given by $2(\beta_c - \beta_l)$.

Appendix C

Common crystallographic structures in III-V semiconductors

Group-IV and III-V semiconductors under pressure exhibit several different structures. In this section, these structures are described successively. We also present a theoretical powder diffraction pattern for each structure.

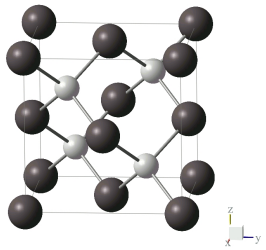

Diamond
Space group : $Fd\bar{3}m$ - O_h^7 Atomic positions : 8(a) at $(\frac{1}{8}, \frac{1}{8}, \frac{1}{8})$
Zinc-blende
Space group : $F\bar{4}3m$ - T_d^2 Atomic positions : 4(a) at $(0, 0, 0)$ and 4(c) at $(\frac{1}{4}, \frac{1}{4}, \frac{1}{4})$

Diamond and zinc-blende

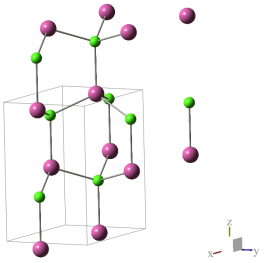

Lonsdaleite
Space group : $P6_3/mmc$ - D_{6h}^4 Atomic positions : 4(f) at $(\frac{1}{3}, \frac{2}{3}, z)$ with $z \approx \frac{1}{16}$
Würtzite
Space group : $P6_3mc$ - C_{6v}^4 Atomic positions : A specie at 2(b) at $(\frac{1}{3}, \frac{2}{3}, 0)$ and B specie at 2(b) position, $(\frac{1}{3}, \frac{2}{3}, u)$ with $u \approx \frac{3}{8}$. If we consider an ideal structure (i.e. perfect tetrahedron) we should have $\frac{c}{a} = \sqrt{8/3}$.

Würtzite et Londsdaleite

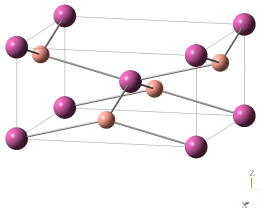

Monoatomic
Space group : $I4_1/amd$ - D_{4h}^{19}
Atomic positions : 4(a) at $(0, \frac{3}{4}, \frac{1}{8})$
Diatomic
Space group : $I\bar{4}m2$ - D_{2d}^{9}
Atomic positions : A specie at 2(a), $(0,0,0)$, and B specie at 2(c) $(0, \frac{1}{2}, \frac{1}{4})$

Monoatomic and diatomic β-Sn

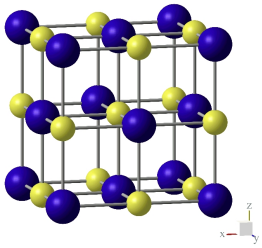

Space group : $Fm\bar{3}m$ - O_h^5
Atomic positions : A specie at 4(a), $(0,0,0)$, and B specie at 4(b), $(\frac{1}{2}, \frac{1}{2}, \frac{1}{2})$.

NaCl

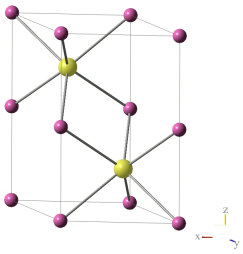

Space group : $P6_3mc$ - D_{6v}^4
Atomic positions : A specie at 2(a), $(0,0,0)$ and B specie at 2(b) $(\frac{1}{3}, \frac{2}{3}, u)$ where u is about $\frac{1}{4}$

NiAs

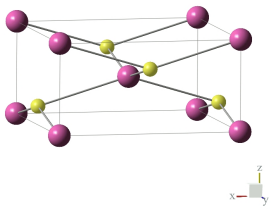

Imma (D_{2h}^{28}) is a distortion of the monoatomic β-Sn structure. Generally, the structure is represented with a shifted origin $(0, \frac{1}{4}, \frac{\Delta}{2})$. Thus the atoms are located at (0,0,0) and $(0, \frac{1}{2}, \Delta)$. If $a = b$ and $\Delta = \frac{1}{2}$, the β-Sn structure is recovered and if $b = c\sqrt{3}$ and $\Delta = \frac{1}{2}$, we find the simple hexagonal.
For the diatomic version of this structure, we have to use the Imm2 space group (C_{2v}^{20}) with atoms A at 2(a) (0,0,0) and B at position 2(b) at $(0, \frac{1}{2}, \Delta)$. If $\Delta = \frac{1}{4}$, Imm2 becomes diatomic β-Sn.
If $\Delta = \frac{1}{2}$, Imm2 becomes Immm with atoms A at 2(a) (0,0,0) and B at 2(b) $(0, \frac{1}{2}, \frac{1}{2})$.

Imm2, Imma and Immm

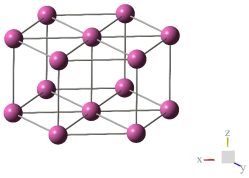

Space group : $P6/mmm$ - D^1_{6h}
Atomic positions : 1(a), $(0,0,0)$

Simple hexagonal

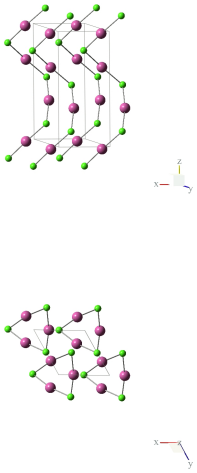

Space group : $P3_121$ - D^4_3
Atomic positions : atom A at 3(a) at $(u,0,\frac{1}{3})$ and $(v,0,\frac{5}{6})$

Cinnabar

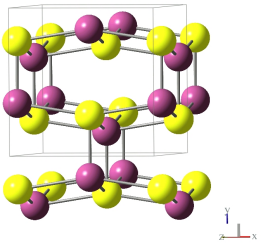

Space group : $Cmcm$ - D^{17}_{2h}
Atomic positions : 4(c) $(0,y_1,\frac{1}{4})$ and $(0,y_2,\frac{1}{4})$ where $\Delta y = y_2 - y_1 \approx 0.5$

Cmcm

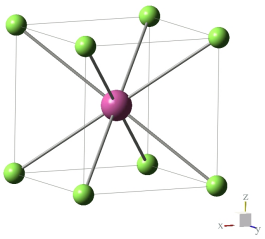

Space group : $Pm\bar{3}m$ - O^1_h
Atomic positions : A specie at 1(a), $(0,0,0)$ and B specie at 1(b), $(\frac{1}{2},\frac{1}{2},\frac{1}{2})$

CsCl

Appendix D

Publication list

- G. Aquilanti, H. Libotte, W.A. Crichton, S. Pascarelli, A. Trapananti and J.P. Itié, accepted for publication in *Physical Review B*.
- A San Miguel, H. Libotte, M. Gauthier, G. Aquilanti, S. Pascarelli and J.P. Gaspard, accepted for publication in *Physical Review Letters*.
- H. Libotte, G. Aquilanti, S. Pascarelli, W.A. Crichton, T. Le Bihan and J.P. Gaspard, submitted to *Journal of Physics C*.
- H. Libotte and J.P. Gaspard, *High Peessure Research*, **24**, 139 (2004).
- H. Libotte and J.P. Gaspard, *Europhysics Letters*, **63**, 545 (2003).
- H. Libotte, J.P. Gaspard, A. San Miguel and P. Mélinon, *Europhysics Letters*, **64**, 757 (2003).
- A. Lindbaum, S. Heathman, K. Liftin, Y Méresse, R.G. Haire, T. Le Bihan and H. Libotte, *Physical Review B*, **63**, 214101 (2001).
- H. Libotte and J.P. Gaspard, *Physical Review B*, **62**, 7110 (2000).
- A. San Miguel, H. Libotte, J.P. Gaspard, M. Gauthier, J.P. Itié and A. Polian, *European Physics Journal B*, **17**, 227 (2000).
- S. Heathman, R.G. Haire, T. Le Bihan, K. Liftin, Y Méresse and H. Libotte, *Physical Review Letters*, **85**, 2961 (2000).
- M. Mezouar, H. Libotte, S. Députier, T. Le Bihan and D. Häusermann, *Physica Status Solidii b*, **211**, 395 (1999).
- M. Mezouar, T. Le Bihan, H. Libotte, Y. Le Godec and D. Häusermann, *Journal of Synchrotron Radiation*, **6**, 1115 (1999).

Bibliography

[1] T. Andrews. *Phil. Trans. Roy. Soc. London*, 159:575, 1869.

[2] P. Bridgman. *Nobel Lecture*, 1946.

[3] M. Gauthier *et al. Phys. Rev. B*, 40, 1989.

[4] R.A. Stager and H.G. Drickhamer. *Phys. Rev.*, 132, 1963.

[5] R.C. Newton A. Jayaraman and J.M. McDonough. *Phys. Rev.*, 159, 1967.

[6] M. Bockowski, S. Krukowski, and B. Lucznik. *Semicond. Sci. Technol.*, 7, 1992.

[7] J. C. Jamieson. *Science*, 139:845, 1963.

[8] B. Weinstein and G.J. Piermarini. *Phys. Rev. B*, 12, 1975.

[9] P. Perlin *et al. Phys. Rev. B*, 45, 1992.

[10] R. J. Nelmes and M. I. McMahon. *Structural transitions in the group IV, III-V and II-VI semiconductors under pressure*, chapter 3. Academic press, 1998.

[11] A. Mujica *et al. Rev. Mod. Phys.*, 75, 2003.

[12] P.W. Bridgman. *Proc. Am. Acad. Arts Sci.*, 60, 1925.

[13] P.W. Bridgman. *Phys. Rev.*, 60, 1941.

[14] A. Jayaraman. *Rev. of Mod. Phys.*, 55:65, 1983.

[15] M.I. Eremets. *High pressure experimental methods.* Oxford Science Publisher, 1996.

[16] T. Yagi. *Trans. Am. Geo. Union*, 69:18, 1988.

[17] Y. Le Godec *et al. High Press. Res.*, 25:243, 2005.

[18] J.N. Johnson and R. Chéret. *Shock waves*, 9:193, 1999.

[19] C. E. Weir *et al. J. Res. Natl. Bur. Stand.*, 63A:55, 1959.

[20] J. Xu and H.K. Mao. *US patent 654329.*

[21] R. Chen and B. Weinstein. *US patent 5693345.*

[22] P. Bell and H.K. Mao. *US patent 4386950.*

[23] S.T. Weir *et al. Appl. Phys. Lett.*, 77:3400, 2000.

[24] W. Soller. *Phys. Rev.*, 24:158, 1924.

[25] M. Mezouar *et al. Rev. Sci. Instr.*, 73:3570, 2002.

[26] M. Mezouar *et al. J. Synchrotron Rad.*, 12:659, 2005.

[27] M. Mezouar *et al. J. Synchrotron Rad.*, 6, 1999.

[28] A. Dewaele, P. Loubeyre, and M. Mezouar. *Phys. Rev. B*, 70:094112, 2004.

[29] D.L. Decker. *J. Applied Phys.*, 42, 1971.

[30] *et al.* H.K. Mao. *J. Appl. Phys.*, 49:3276, 1978.

[31] J.A. Xu, H.K. Mao, and P.M. Bell. *Science*, 232:1404, 1986.

[32] G.J. Piermarini *et al. J. Appl. Phys.*, 46:2774, 1975.

[33] Holzapfel W.B., Hartwig M., and Sievers W. *J. Phys. Chem. Ref. Data*, 30, 2001.

[34] W. Crichton and M. Mezouar. *High Temperatures - High Pressures*, 34, 2002.

[35] M.I. McMahon *et al. Phys. Rev. B*, 50, 1994.

[36] M. Mezouar *et al. Phys. Stat. Sol. (b)*, 211, 1999.

[37] H. Libotte and J.-P. Gaspard. *Phys. Rev. B*, 62:7110, 2000.

[38] H.M. Rietveld. *J. Appl. Cryst.*, 2, 1969.

[39] S. Minomura and H.G. Drickhamer. *J. Phys. Chem. Solids*, 23, 1962.

[40] R. Zallen and W. Paul. *Phys. Rev.*, 134, 1964.

[41] K. Kim, V. Ozolins, and A. Zunger. *Phys. Rev. B*, 60:R8449, 1999.

[42] V. Ozolins and A. Zunger. *Phys. Rev. Lett.*, 82:767, 1999.

[43] J.C. Phillips. *Rev. Mod. Phys.*, 42:317, 1970.

[44] L. Pauling. *The nature of the chemical bond and the structure of molecules and crystals: an introduction to modern structural chemistry.* Cornell University Press, New-York, 1960.

[45] J.A. Van Vechten. *Phys. Rev. B*, 7:1479, 1973.

[46] J.C. Phillips. *Bonds and Bands in Semiconductors.* Academic Press New-York, 1973.

[47] J.R. Chelikowsky and J.K. Burdett. *Phys. Rev. Lett.*, 56:961, 1986.

[48] W. Harrison. *Electronic Structure and the Properties of Solids.* 3rd edition, 1980.

[49] J.C. Phillips. *Phys. Rev. Lett.*, 27:1197, 1971.

[50] R.J. Nelmes, M.I. McMahon, and S.A. Belmonte. *Phys. Rev. Lett.*, 79, 1997.

[51] S.T. Weir, Y.K. Vohra, and A.L. Ruoff. *Phys. Rev. B*, 36:4543, 1987.

[52] C. Vanpeteghem *et al. Phys. Stat. Sol. (b)*, 223:405, 2001.

[53] H. Libotte and J.-P. Gaspard. *Europhys. Lett.*, 63:545, 2003.

[54] S. T. Weir Y. Vohra and A. L. Ruoff. *Phys. Rev. B*, 31:7344, 1985.

[55] R. J. Nelmes *et al. J. Phys. Chem. Solids*, 56:539, 1995.

[56] A. Mujica and R.J. Needs. *Phys. Rev. B*, 55:9659, 1997.

[57] S. Pascarelli *et al. High Press. Res.*, 22, 2002.

[58] S. Pascarelli *et al. Europhys. Lett.*, 61, 2003.

[59] G. Aquilanti *et al. Nucl. Instr. and Meth. Phys. Res. B*, 200, 2003.

[60] G. Aquilanti and S. Pascarelli. *J. Phys. : Condens. Matter*, 17, 2005.

[61] H. Libotte *et al. submitted to J. Phys. : Condens. Matter*, 2007.

[62] A. Onodera and *et al. Solid State Commun.*, 14:803, 1974.

[63] S.C. Yu, I.L. Spain, and E.F. Skelton. *Solid State Commun.*, 25:49, 1978.

[64] M. Baublitz Jr and A.L. Ruoff. *J. Appl. Phys.*, 53, 1982.

[65] J.Z. Hu and I.L. Spain. *Sol. St. Commun.*, 51, 1984.

[66] J.-P. Itié *et al. Phys. Rev. B*, 40:9709, 1989.

[67] A. Mujica, A. Munoz, and R.J. Needs. *Phys. Rev. B*, 57:1344, 1998.

[68] G. Aquilanti *et al. accepted for publication in Phys. Rev. B*, 2007.

[69] M.C. Gupta and A.L. Ruoff. *J. Appl. Phys.*, 51:1072, 1980.

[70] A.K. Singh and G.C. Kennedy. *J. Appl. Phys.*, 45:4686, 1974.

[71] A. K. Singh. *J. Appl. Phys.*, 73:4278, 1993.

[72] J. Wang *et al. Phys. Rev. B*, 52:12627, 1995.

[73] W. H. Huang C. Cheng and H. J. Li. *Phys. Rev. B*, 63:153202, 2001.

[74] C. Cheng. *Phys. Rev. B*, 67:134109, 2003.

[75] K. Gaál-Nagy and D. Strauch. *Phys. Rev. B*, 73:134101, 2006.

[76] P. Loubeyre *et al. Nature*, 383, 1996.

[77] M. Metrangolo *et al. Acc. Chem. Res.*, 38, 2005.

[78] A.S. Balchan and H.G. Drickhamer. *J. Chem. Phys.*, 34:1948, 1961.

[79] K. Takemura *et al. Solid State Comm.*, 30, 1979.

[80] F. Siringo, R. Pucci, and N. H. March. *Phys. Rev. B*, 37, 1988.

[81] H. Fujihisa *et al. J. Phys. Chem. Solids*, 56, 1995.

[82] R.M. Martin. *Nature*, 400:117, 1999.

[83] M.S. Miao, V.E. Van Dooren, and J.L. Martins. *Phys. Rev. B*, 68:094106, 2003.

[84] P. Loubeyre *et al. High Press. Research*, 24, 2004.

[85] L. Zhang *et al. Solid State Comm.*, 141, 2007.

[86] I. Goncharenko and P. Loubeyre. *Nature*, 435:1206, 2005.

[87] R.W. Wyckoff. *Crystal Structures.* John Wiley, 1963.

[88] K. Takemura *et al. Nature*, 423, 2003.

[89] T. Kume *et al. Phys. Rev. Lett.*, 94, 2005.

[90] R. Bersohn. *J. of Chem. Phys.*, 36, 1962.

[91] B. M. Riggleman and H. G. Drickhamer. *J. Chem. Phys.*, 38, 1963.

[92] A. San-Miguel *et al. Eur. Phys. J. B*, 17:227, 2000.

[93] J. L. Rosenberg. *J. of Chem. Phys.*, 40, 1964.

[94] Y. Natsume and T. Susuki. *Solid State Comm.*, 44, 1982.

[95] F. Siringo, R. Pucci, and N. H. March. *Phys. Rev. B*, 38, 1988.

[96] F. Siringo, G. Piccitto, and R. Pucci. *High Press. Res.*, 3, 1990.

[97] K. Takemura *et al. Phys. Rev. Lett.*, 45, 1980.

[98] Y. Fujii. *et al.. Solid State Commun.*, 59, 1986.

[99] Y. Fujii. *et al. Phys. Rev. Lett.*, 58, 1986.

[100] Y. Ohishi *et al.* Y. Fujii., K. Hase. *Phys. Rev. B*, 63, 1989.

[101] K. Shimizu *et al.* page 498. World Scientific, River Edge, 1996.

[102] H.G. Drickhamer *et al. Solid State Phys.*, 19:135, 1966.

[103] R.W. Lynch and H.G. Drickhamer. *J. Chem. Phys.*, 45:1020, 1966.

[104] E. Düsing, W.A. Grosshans, and W. B. Holzapfel. *Journal de Physique*, 45, 1984.

[105] A. San Miguel *et al. Accepted for publication in Phys. Rev. Lett.*, 2007.

[106] S. van Smaalen and T.F. George. *Phys. Rev. B*, 35:7939, 1987.

[107] R.J. Nelmes *et al. Phys. Rev. Lett.*, 83:4081, 1999.

[108] O. Degtyareva, M.I. McMahon, and R.J. Nelmes. *Phys. Rev. B*, 70:184119, 2004.

[109] J. Friedel. *J. Phys. Chem. Solids*, 1:175, 1956.

[110] W.A. Harrison. *Phys. Rev. B*, 29:2917, 1984.

[111] J. Friedel. *Physics of Metals.* Cambridge University Press, New York, 1969.

[112] W.A. Harrison. *Solid State Comm.*, 124:443, 2002.

[113] J. Friedel and C.M. Sayers. *J. Phys.*, 38, 1977.

[114] J. Friedel. *J. Phys.*, 48:93, 1987.

[115] H. Davy. *Roy. Soc. London Phil. Trans.*, 101:1, 1811.

[116] W. F. Claussen. *J. Chem. Phys.*, 19:1425, 1951.

[117] C. Cros, M. Pouchard, and P. Hagenmuller. *C.R. Acad. Sci.*, 260, 1965.

[118] J.S. Kasper, P. Hagenmuller, and M. Pouchard. *Science*, 150, 1965.

[119] J. Gallmeier, H. Schäfer, and A. Weiss. *Z. Naturforsh.*, 24b:665, 1969.

[120] A.A. Demkov, W. Windl, and O.F. Sankey. *Phys. Rev. B*, 53:11288, 1996.

[121] M. O'Keeffe, G.B. Adams, and O.F. Sankey. *Phys. Rev. Lett.*, 68:2325, 1992.

[122] A. San-Miguel *et al. Phys. Rev. Lett.*, 83, 1999.

[123] G.B. Adams, M. O'Keeffe, and A.A. Demkov. *Phys. Rev. B*, 49, 1994.

[124] G.S. Nolas *et al. Appl. Phys. Lett.*, 73, 1998.

[125] B.C. Sales *et al. J. Solid State Chem.*, 146, 1999.

[126] H.P. Hermann, F. Grandjean, and G. Long. *American J. Phys.*, 73:110, 2005.

[127] A.K. Singh and G.C. Kennedy. *Phil. Mag. B*, 77, 1973.

[128] M. L. Cohen. *Phys. Rev. B*, 32, 1985.

[129] F. P. Bundy and J.S. Kasper. *High Temp.-High Press.*, 2, 1970.

[130] A. San-Miguel and P. Toulemonde. *High Press. Res.*, 25:159, 2005.

[131] G. A. Slack. Proceedings of the symposium. *Thermoelectric materials*, page 47, 1997.

[132] A. Demkov, O. Sankey, and K. E. Schmidt. *Phys. Rev. B*, 50:17001, 1994.

[133] J. Dong and O. F. Sankey. *J. Appl. Phys.*, 87:7726, 2000.

[134] S. Bobev and S. Sevov. *J. of Solid States Chemistry*, 153:92, 2000.

[135] F. Brunet *et al. Phys. Rev. B*, 61:16550, 2000.

[136] R. Hermann *et al. Mat. Res. Soc. Symp. Proc.*, 886, 2006.

[137] F. Hensel and H. Uchtman. *Annu. Rev. Phys. Chem.*, 40:61, 1989.

[138] R.J. Hemley and N.W. Ashcroft. *Physics Today*, 51, 1998.

[139] J.-P. Gaspard *et al. Phil. Mag. B*, 77, 1998.

[140] A.K. Singh and G.C. Kennedy. *Phil. Mag. B*, 77, 1973.

[141] F. Tournus *et al. Phys. Rev. B*, 69:035208, 2004.

[142] J.C. Conesa, C. Tablero, and P. Wahnon. *Phys. Rev. B*, 120:6142, 2004.

[143] P. Hohenberg and W. Kohn. *Phys. Rev.*, 136:B864, 1964.

[144] W. Kohn and L.J. Sham. *Phys. Rev.*, 140:A1133, 1965.

[145] D.M. Ceperley and B.J. Alder. *Phys. Rev. Lett.*, 45:556, 1980.

[146] J.P. Perdew, K. Burke, and M. Ernzerhof. *Phys. Rev. Lett.*, 77:3865, 1996.

[147] C. Kittel. *Physique de l'état solide.* Dunod, 1983.

[148] G. Allan and M. Lannoo. *J. Phys.*, 44:1355, 1983.

[149] J.B. Neaton and N.W. Ashcroft. *Nature*, 400:141, 1999.

[150] M. Hanfland *et al. Nature*, 408:174, 2000.

[151] M.J.P. Musgrave. *Proc. Roy. Soc. London - Serie A - Math and Phys. Siences*, 272:503, 1963.

[152] H. Katzke, U. Bismayer, and P. Tolénado. *Phys. Rev. B*, 73:134105, 2006.

[153] H.A. Jahn and E. Teller. *Proceedings of the Royal Society of London. Series A, Mathematical and Physical Sciences*, 161, 1937.

[154] J. Friedel. *J. Phys. F: Met. Phys.*, 3:785, 1973.

[155] J.-P. Gaspard *et al. Solid State Comm.*, 84, 1992.

[156] J.P. Gaspard *et al. Private communication.*

[157] S. Elliott. *Physics and Chemistry of Solids.* J. Wiley, Chichester, 1998.

[158] D.G. Pettifor. *Bonding structure of molecules and solids.* Clarendon PRess, Oxford, 1995.

[159] A. P. Sutton. *Electronic structure of materials.* Oxford University Press, 1993.

[160] J.K. Burdett. *Chemical Bonding in Solids.* Oxford University Press New York, 1995.

[161] J.-Y. Raty. *Thèse de Doctorat.* 2000.

[162] W. Welnick *et al. Sol. State Comm.*, 119, 2001.

[163] W. A. Harrison. *Phys. Rev. B*, 23, 1981.

[164] J. Kanamori. *Prog. Theor. Phys.*, 30:275, 1963.

[165] D.G. Pettifor. *J. Phys. C, Solid State Phys.*, 19, 1986.

[166] J. C. Cressoni and D.G. Pettifor. *J. Phys. : Condens. Matter*, 3:495, 1991.

[167] F. Ducastelle. *Thèse de Doctorat.* 1972.

[168] M. De Broglie. *Compte rendus*, 157, 1913.

[169] R. Kronig. *Zeit. Phys.*, 70, 1931.

[170] D. Sayers, E. Stern, and F. Lytle. *Phys. Rev. Lett.*, 27, 1971.

[171] A. Fontaine. *Interaction of X-rays with matter: X-ray absorption spectroscopy*, chapter XV. Les Editions de Physique - Springer Verlag, 1993.

[172] S. Pascarelli *et al. J. Synchr. Rad.*, 13:351, 2006.

[173] J.C. Slater and G.F. Koster. *Phys. Rev. B*, 94, 1954.

[174] W. Harrison. *Phys. Rev. B*, 8, 1973.

[175] W. Harrison and S. Ciraci. *Phys. Rev. B*, 10, 1973.

[176] P. Turchi, P. Ducastelle, and G. Tréglia. *J. Phys.*, 15:2891, 1982.

List of Figures

List of Tables